Kelemen, P.B., Kikawa, E., Miller, D.J., et al., 2004
Proceedings of the Ocean Drilling Program, Initial Reports Volume 209

10. SITE 1275[1]

Shipboard Scientific Party[2]

OPERATIONS SUMMARY

Site 1275

After a brief ~10-nmi transit west from Site 1274, we arrived at Site 1275 (Fig. F1). At 0445 hr on 19 June 2003, we began a camera survey on the top of a large dome, previously surveyed during 1998 *Shinkai* 6500 Dive 422. During that dive, gabbro and peridotite were recovered from the southern flank of the dome (Fig. F2); our first drilling target was smooth, slabby outcrops on the north end of the dome summit.

Hole 1275A

Our camera survey for Hole 1275A required <2 hr, and we selected a target on a bare rock outcrop. We initiated coring at 0815 hr at a water depth of 1563 meters below sea level (mbsl). In an attempt to recover the uppermost surface of the outcrop, we elected to recover the core barrel after only 5 m of penetration. Since we had to lift the pipe above seafloor in order to have the proper pipe spacing at the rig floor to extract the core barrel, Core 1R (Table T1) was the only core recovered from this hole.

Hole 1275B

In an attempt to remain on or at least very near the outcrop where we cored Hole 1275A, we moved in dynamic positioning mode only 4 m south to begin Hole 1275B. Core 1R was cored to a depth of 11.0 meters below seafloor (mbsf) and required >10 hr to drill. Coring continued through Core 22R (108.7 mbsf). Because our rate of penetration early in the hole was so low and the bit had been used for nearly 80 hr of coring, we chose to terminate coring to attempt logging while coring

F1. Bathymetric map and hole location for Site 1275, p. 45.

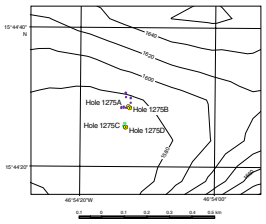

F2. Hole location and bathymetric section for Site 1275, p. 46.

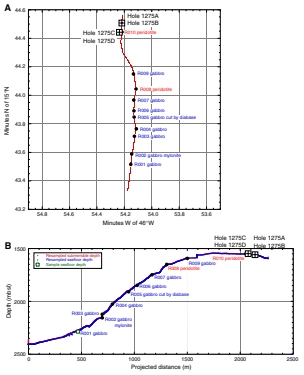

T1. Coring summary, Site 1275, p. 154.

[1]Examples of how to reference the whole or part of this volume.
[2]Shipboard Scientific Party addresses.

(LWC) at a nearby location. We did not release the bit in the bottom of the hole, so we would have the option to attempt a bare hole reentry and then deepen and log Hole 1275B if time allowed. The location of Hole 1275B was marked with a glass float deployed from the subsea camera frame prior to abandonment. The average rate of penetration for the hole was only 1.4 m/hr.

Hole 1275C

Our target for the LWC operation was, in our estimation, the most optimum location for high recovery occupied during Leg 209. We selected a drilling location at the site of an outcrop where the precruise dive survey had collected serpentinized peridotite. This site was ~90 m south of Holes 1275A and 1275B. Relatively high recovery in hard rock from nearby Hole 1275B (>43%), combined with shallow water and calm seas, should have made for ideal deployment conditions. We deployed a standard eight-collar bottom-hole assembly (BHA), as memory on the LWC tool (resistivity at the bit with coring [RAB-C]) is only 70 rotating hours in its current configuration and we did not expect to penetrate more than ~70 m in that time.

After conducting a brief (1 hr) subsea camera survey, we located an outcrop near the coordinates where peridotite was sampled during the *Shinkai* 6500 dive. Hole 1275C was initiated at 0445 hr on June 24, with the same slow rate of penetration we experienced in Hole 1275B. After three cores and nearly 20 hr of operations we had reached only 20.8 mbsf and the three core barrels we had recovered were either empty (Core 1R) or contained only one or two small, rounded cobbles of rock. Compared to recovery of initial cores from all our previous drilling locations, recovery with the RAB-C was significantly poorer than with our conventional rotary system. Based on poor recovery, we abandoned Hole 1275C.

Hole 1275D

In an attempt to ensure the deepest penetration possible in the time we had left, we deployed a 22-collar BHA in preparation for coring Hole 1275D. We offset 4 m west from Hole 1275C and began coring Hole 1275D at 1025 hr on 25 June. Coring in the same interval with the RAB-C (Cores 1R to 3R; 0 to 17.6 mbsf) yielded 32% recovery. This was the highest rate of recovery from the first three cores from any hole drilled during Leg 209 (Fig. F3). Coring continued through Core 43R to 209 mbsf (average recovery = >50%). We terminated coring at 0915 hr on 30 June in order to leave time for wireline logging. The average rate of penetration for Hole 1275D was 2.4 m/hr. Wireline logging failed to pass an obstruction at ~103 mbsf, but two tool strings (triple combination [triple combo] and Formation MicroScanner [FMS]-sonic) were deployed over the interval from 103 to 20 mbsf. The pipe was pulled clear of the seafloor at 0515 hr on July 1, ending operations for Leg 209, and after recovering the pipe, we began our transit to Bermuda.

F3. RAB-C and RCB recoveries, p. 47.

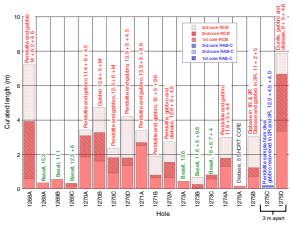

Transit to Bermuda

During the 5-day, 1410-nmi transit to Bermuda, all the cores recovered during Leg 209 were arranged throughout the upper two floors of the labstack for a postcruise research sampling party. Sample selection and resolution of the distribution of popular intervals were accom-

plished over 24 hr. Sample orientation and processing were completed prior to arrival in Bermuda.

Our transit speed averaged 11.6 kt. Leg 209 was completed with the first line ashore at Market Wharf, St. George, Bermuda, at 1715 hr on 6 July 2003.

IGNEOUS AND MANTLE PETROLOGY

Four holes were drilled at Site 1275, separated by a total lateral distance of 91 m. Holes 1275A and 1275C provided very little recovered material. Hole 1275A was drilled to a depth of 5 m, and a curated length of 0.13 m was recovered consisting of fine-grained mafic rock (diabase and limestone-cemented diabasic breccia). Hole 1275C was drilled to a depth of 20.8 m, and a curated length of 0.22 m was recovered consisting of diabase and troctolite. Holes 1275B and 1275D yielded substantial amounts of gabbroic rock and lesser amounts of other lithologies (Hole 1275B: troctolite [5.5%], gabbro [85.1%], diabase [8.6%], and granophyre [0.8%] and Hole 1275D: troctolite [18.3%], olivine gabbro [4.7%], gabbro [64.4%], diabase [10.5%], and granophyre [2.1%]). Therefore, in the following description of Site 1275 we focus on Holes 1275B and 1275D. We first define the stratigraphic variations and hand-sample characteristics of the lithologies in each hole. We then describe the rocks in detail, coupling hand-sample and thin section observations. Because many of the rocks from Holes 1275B and 1275D are similar, they are described together.

Lithology and Stratigraphy

Hole 1275B

Unit I

Interval: Sections 209-1275B-1R-1 through 6R-1
Depth: 0–28.13 mbsf
Lithology: diabase/oxide gabbro

Unit I includes the first five cores of the hole and a small part of the sixth, extending to 18 mbsf (Section 209-1275B-3R-2). It contains diabase (48.3%), gabbro and oxide gabbro (51.3%), and granophyre (0.4%) (Fig. F4). We use the term granophyre to refer to rocks that are composed mainly of plagioclase feldspar and quartz. According to formal igneous nomenclature (Streckeisen, 1974), these would either be trondjhemites if the plagioclase has anorthite ≥ 10 or alkali syenites or granites if the plagioclase is albitic (anorthite < 10). Since the proportion of quartz to feldspar is difficult to determine in hand sample and the feldspar composition is unknown, we use the more general term granophyre.

The remainder of Unit I is a mixture of variably altered microgabbro to fine-grained gabbro. The grain size of the gabbroic rocks varies on the millimeter scale. The different grain sizes define bands, lenses, and irregular blobs with sharp boundaries (Fig. F5). These rocks have a variable but, in many places, well-developed igneous foliation. Where sharp boundaries in grain size cut the core it can be seen that the igneous foliation parallels these boundaries. No reaction rims or chilling are evident at any of these boundaries. The granophyre in Unit I occurs exclusively as small irregular bodies that crosscut the gabbroic rocks of Section 209-1275B-5R-2.

F4. Lithostratigraphic summary, Hole 1275B, p. 48.

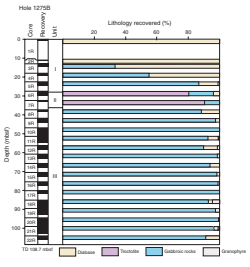

F5. Fine-grained gabbro patches in medium-grained matrix, p. 49.

Unit II

Interval: Sections 209-1275B-6R-1 through 7R-1
Depth: 28.13–32.6 mbsf
Lithology: troctolite

Unit II is a ~4.5-m-thick horizon composed of "troctolite" (96.4%) cut by a small number of diabase dikes (3.6%). The troctolite is medium grained with equant, rounded olivine surrounded by a gabbroic matrix (Fig. **F6**). The gabbroic material is heterogeneous and is composed of poikilitic pyroxenes as large as 1.5 cm (both clinopyroxene and orthopyroxene) and interstitial plagioclase, so rock types in this unit vary from plagioclase dunite and troctolite to plagioclase-harzburgite, plagioclase-wehrlite, and plagioclase-lherzolite at the thin section scale. For simplicity, we refer to all these olivine-rich, texturally similar rocks as "troctolites" throughout this report. Olivine makes up >75% of the troctolite and typically accounts for >85%. The troctolites are cut by gabbroic dikes and in many places these dikes appear to be continuous with gabbroic material interstitial to the olivine (Fig. **F6**).

Unit III

Interval: Sections 209-1275B-7R-1 through 22R-2
Depth: 32.6–108.7 mbsf
Lithology: oxide gabbro

Unit III is the last unit in Hole 1275B and is composed primarily of oxide gabbro with some oxide gabbronorite in the lower portions. Small intervals of gabbro and gabbronorite with <5% oxides can also be found. Gabbro is the dominant lithology (96.4%), cut by diabase (2.7%) and granophyre (0.9%).

Unit III makes up the bulk of Hole 1275B (76.1 m) and is extremely heterogeneous—the greatest extent of homogeneous material is <50 cm. Heterogeneity is defined by variations in mineralogy and modal proportions. Thus, this unit contains gabbro, gabbronorite, oxide gabbro, and oxide gabbronorite. Heterogeneity is also defined by variations in grain size (Figs. **F7**, **F8**) that may or may not be accompanied by changes in mineralogy and/or modal proportions. The style of the grain-size variation can be grouped into three loosely defined categories:

1. "Banded contacts" are flat and sharp, defining discrete intervals in the core (Fig. **F8**).
2. "Crenulate contacts" are curviplanar and sharp and in places do not cross the core width (Fig. **F9**).
3. "Mixed zones" are where there is no discrete boundary between grain-size domains that occur as patches. This texture is similar to that of most Unit I gabbros (Fig. **F5**).

The diabase in Unit III has sharp boundaries with the gabbroic rocks and is distributed throughout the unit with no particularly large concentrations. Grain sizes in the gabbros of Unit III increase downhole (Fig. **F10**).

Granophyre also occurs throughout Unit III, mostly as thin (2–3 mm) dikelets that compose <4% of the volume of any given section (Fig. **F11A**). About half of the granophyres and all the larger masses of granophyre are oriented subparallel to the drilling direction (Fig. **F11B**); more quantitatively, 49% of measured dips of granophyre/gabbro con-

F6. Typical troctolite, p. 50.

F7. Coarse-grained/fine-grained gabbro contact, p. 51.

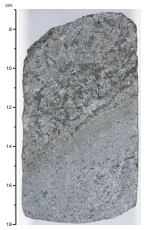

F8. Flat, sharp gabbro contact, p. 52.

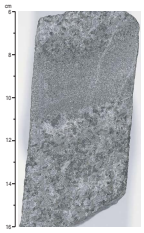

F9. Crenulate gabbroic contacts, p. 53.

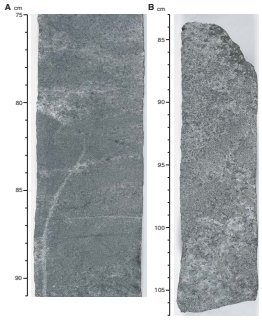

F10. Grain size variations, Hole 1275B, p. 54.

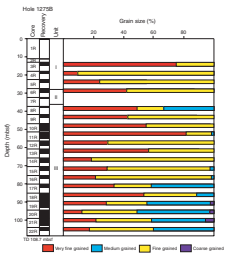

tacts have dips steeper than 60°. Because a vertical drill hole preferentially intersects subhorizontal features rather than near-vertical features, we infer that the near-vertical granophyres are, in fact, much more common than those with dips <60°. For more discussion, see "Structural Geology," p. 17. Section 209-1275B-18R-1 contains 18% granophyre, and in this section the granophyre includes pieces of the gabbro. The granophyre has reacted with the inclusions, generating large crystals of amphibole in the former gabbro (Fig. F12).

Hole 1275D

Unit I

Interval: Sections 209-1275D-1R-1 through 11R-2
Depth: 0–52.99 mbsf
Lithology: troctolite

Unit I includes the first ten cores of the hole and most of the eleventh (Fig. F13). Unit I is composed almost entirely of troctolite (85.4% of Unit I) with the exception of the very top of the hole in Section 209-1275D-1R-1, which contains diabase (5.5% of Unit I), and Core 7R, which contains a significant amount of gabbro (9.1% of Unit I). The troctolite is similar to that described in Hole 1275B, with rounded olivine crystals in a gabbroic matrix. As in Hole 1275B, the troctolite is cut by numerous gabbroic dikes and veins that vary in geometry and volume. In interval 209-1275D-9R-2, 27–40 cm, there is a poikilitic pyroxene crystal that is partially enclosed in the troctolite and partially enclosed in a crosscutting gabbro, suggesting co-crystallization of the gabbroic matrix in the troctolite and the crosscutting gabbroic dikes.

Unit II

Interval: Sections 209-1275D-11R-2 through 17R-1
Depth: 52.99–81.0 mbsf
Lithology: oxide gabbro(norite)

Unit II is gabbroic (86.6%) with some diabase (11.4%) and minor granophyre (2%). Unit II contains ~30 m of oxide-rich gabbro and gabbronorite sandwiched between troctolite-rich Units I and II. Unit II gabbros and gabbronorites are mineralogically and texturally similar to oxide-rich gabbroic rocks found in Unit III of Hole 1275B. Texturally they are extremely heterogeneous, with abrupt grain-size changes that define bands or parts of crenulate blobs. The attitude of the igneous foliation in Unit II is variable. Most foliations cross the core at small angles, but in certain places (e.g., Section 209-1275D-13R-1) the foliation is parallel to the drilling direction. The granophyre in Unit II occurs both as thin stringers and in larger, more irregular masses that are generally elongate parallel to the length of the core. In Section 209-1275D-13R-2 there is a granophyre that is ~8 mm wide where it first cuts the core but increases in width upward. As the granophyre widens, its color changes from white to gray and it ultimately becomes diffuse within the gabbro (Fig. F14).

Unit III

Interval: Sections 209-1275D-17R-1 through 19R-2
Depth: 81.0–90.94 mbsf
Lithology: troctolite and oxide gabbro

F11. Granophyre cutting gabbro, p. 55.

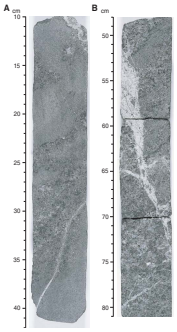

F12. Amphibole grains from gabbro-granophyre reactions, p. 56.

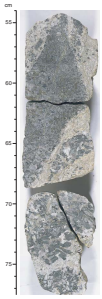

F13. Lithostratigraphic summary, Hole 1275D, p. 57.

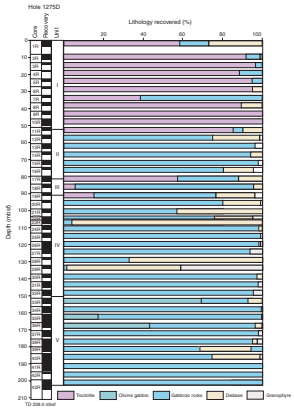

F14. Granophyre grading into gabbro, p. 58.

Unit III contains a mixture of the rock types found in Units I and II. Unlike Unit I, which contains 20-m sections of troctolite uninterrupted by oxide gabbro, the troctolite in Unit III is interspersed with oxide gabbro at the meter scale. The contacts between the two lithologies show clearly that the oxide gabbro postdates the troctolite, but no fragments of the troctolite are found as inclusions in the oxide gabbro. The oxide gabbro does not appear to be chilled against the troctolite, but alteration invariably obscures these relations. In addition to troctolite (40.7%) and gabbro (51.7%), Unit III contains diabase dikes or sills (6.3%), which cut both troctolite and gabbro, and granophyre (1.3%), which is exclusively associated with the gabbro.

Unit IV

Interval: Sections 209-1275D-19R-2 through 33R-1
Depth: 90.94–151.34 mbsf
Lithology: oxide gabbro(norite)

Unit IV is similar to Unit II in most respects. It contains slightly less gabbro (76.8%) but more diabase (18.6%) and granophyre (4.6%). The base of Unit IV corresponds to the first occurrence of olivine-bearing gabbroic rocks. The two main distinctions between Unit II and Unit IV are the larger proportion of granophyre and the larger average grain size in Unit IV compared to structurally higher gabbros. The granophyre in Unit IV is more massive than elsewhere in the core, and in some intervals (e.g., Section 209-1275D-29R-2) it constitutes a significant portion of the core (i.e., >75%). The grain size of the gabbros in Unit IV varies at small scales as in the upper part of the core but there is an overall increase downhole (Fig. **F15**). The maximum fraction of coarse-grained gabbro in Hole 1275D is found at the lower boundary in Unit IV, comprising >50% of Cores 209-1275D-31R and 32R. However, it should be noted that microgabbro is present throughout the core and most sections contain fine-, medium-, and coarse-grained gabbros.

Unit V

Interval: Sections 209-1275D-33R-1 through 43R-4
Depth: 151.34–209 mbsf
Lithology: olivine gabbro and oxide gabbro(norite)

Unit V consists of oxide gabbro and oxide gabbronorite (83.8%), olivine gabbro (7.3%), diabase (7.4%), and granophyre (1.5%). The olivine gabbros are more primitive than gabbroic rocks encountered elsewhere in Units I and II in Hole 1275B or Units II and IV in Hole 1275D. The olivine gabbros contain as much as 20% olivine, which is obvious in hand sample where altered to iddingsite (Fig. **F16**). In Section 209-1275D-35R-4, the olivine gabbro contains bands of coarse-grained euhedral orthopyroxene as wide as 2.5 cm (Fig. **F17A**). In Sections 209-1275D-36R-1, and 36R-2, the olivine gabbro is associated with an olivine and plagioclase phyric diabase that is mixed with granophyric material (Fig. **F17B**). The rest of Unit V is similar to the oxide gabbros elsewhere at Site 1275. There is a general decrease in maximum grain size in Unit V oxide gabbros downhole (Fig. **F15**).

F15. Grain size variations, Hole 1275D, p. 59.

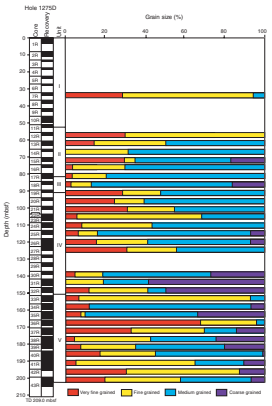

F16. Olivine gabbro texture, p. 60.

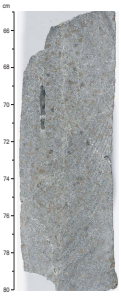

F17. Crystal phyric diabase mixed with granophyre, p. 61.

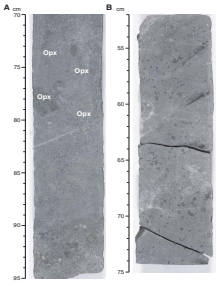

Lithologic Characterization

Troctolite

Significant proportions of troctolitic rocks were recovered in Holes 1275B and 1275D, and they are essentially identical in their characteristics in both hand sample and thin section. The troctolite-rich portions of the cores (Unit II in Hole 1275B and Units I and III in Hole 1275D) are cut by numerous gabbros. These gabbros tend to be rich in pyroxene relative to plagioclase and typically lack oxides. In hand sample, the troctolites can be seen to contain large (up to 4 cm) poikilitic pyroxenes that enclose olivine crystals. Plagioclase grains fill the interstitial space between the pyroxene-rich domains. Several of the thin sections studied sampled only interstitial clinopyroxene or orthopyroxene. Both pyroxenes were found together in a thin section, where clinopyroxene encloses olivine and rims orthopyroxene. It is clear from the hand samples that these thin sections do not provide an adequate sampling of the modal proportions in the rock. Some thin sections are classified as plagioclase-harzburgite (interstitial orthopyroxene) or plagioclase-wehrlites (interstitial clinopyroxene), but at the scale of the core the rocks are clearly troctolitic with plagioclase as the most abundant interstitial mineral.

In thin section, most of the olivine grains in these samples are isolated so that olivine/olivine contacts are scarce. Where olivine grains remain in contact it can be seen that the gabbroic material extends as thinning tendrils between the grains (Fig. **F18**). In these samples the olivine grains are rounded and embayed. Optically continuous, spatially separate grains of olivine are present within interstitial pyroxene or plagioclase (Fig. **F18**). Plagioclase, clinopyroxene, and orthopyroxene are all found in contact with olivine in various thin sections. No igneous reaction rims or corona textures are present between these phases. Subhedral to euhedral spinel is also found in these samples, and reflected-light microscopy reveals some of these spinels have rims of magnetite.

F18. Resorbed olivine in orthopyroxene oikocryst, p. 62.

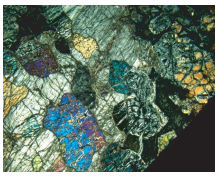

Olivine Gabbro

Only one olivine-bearing gabbro was recovered in Hole 1275B in Section 209-1275B-19R-1. This rock is very fine grained (<0.1 mm) with ~15% fine-grained plagioclase (as large as 3 mm). The larger plagioclase grains in this sample have strong optical zonation and some are dramatically bent (Fig. **F19A**). A later generation of smaller plagioclase crystals have skeletal morphologies and include olivine and clinopyroxene crystals in their core (Fig. **F19B**). We infer that this sample contained a small fraction of plagioclase crystals that were variably deformed during emplacement, after which the remainder of the melt crystallized rapidly.

Some of the olivine-bearing rocks from Hole 1275D are also inferred to have crystallized rapidly and might be described as olivine-plagioclase phyric diabase (Fig. **F20A, F20B**). This is intimately associated with granophyric material with boundaries that are suggestive of liquid-liquid interaction. However, other olivine-bearing rocks probably crystallized more slowly, have uniform granular textures (Fig. **F20C, F20D**), and are appropriately described as olivine gabbro and olivine gabbronorite. The olivine gabbro is present at the top of Unit V (Section 209-1275D-33R-1). It contains ~20% olivine, 15% clinopyroxene, and 65% plagioclase. Contacts between olivine and clinopyroxene and cli-

F19. Bent and skeletal plagioclase in olivine gabbro, p. 63.

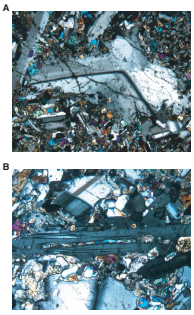

F20. Textures of olivine gabbros, p. 64.

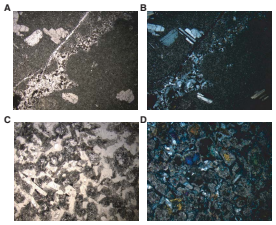

nopyroxene and plagioclase are preserved, but no olivine/plagioclase contacts are present. Instead, olivine and plagioclase are always separated by radiating amphibole crystals that may be interpreted as evidence of an earlier igneous reaction (Fig. F20C, F20D). Small subhedral oxides and brown amphibole that may be magmatic are also present in this sample, but not between olivine and plagioclase. The olivine-bearing rocks deeper in the hole (Section 209-1275D-35R-4) contain subophitic orthopyroxene in addition to clinopyroxene, making them olivine gabbronorites, but are otherwise similar to those in Section 209-1275D-33R-1.

Oxide Gabbro(norite)

The gabbroic rocks that make up the bulk of Holes 1275B and 1275D share a variety of similar features. In both holes, these rocks are mixtures of gabbros and gabbronorites and oxide gabbros and oxide gabbronorites that are mixed at scales ranging from a few grain diameters to tens of centimeters. The mineralogical variation in these samples is primarily in the proportions of orthopyroxene and oxides. Whereas the proportion of orthopyroxene is difficult to estimate in hand sample, the proportion of oxides can be readily estimated visually or by using the bulk magnetic susceptibility.

The oxide distribution is especially heterogeneous in these gabbros and provides a good proxy for other types of variation. This heterogeneity can be observed in thin section, where the oxide is often segregated into bands and associated with fine-grained pyroxenes (Fig. F21). The proportions of the oxides were estimated visually and compared to bulk magnetic susceptibility on selected large core pieces. In general the magnetic susceptibility correlates with the visual estimated modal proportion of oxides, although with significant scatter (Fig. F22). The correlation is not strongly dependent on the grain size of the rocks (Fig. F23), and this, coupled with thin section observations of significant amounts of ilmenite, indicates that the bulk magnetic susceptibility provides only a crude proxy for the total oxide content. Comparing the oxide proportions and mineralogy in large thin sections would ameliorate some of the ambiguity of the bulk susceptibility interpretations. In any case, the susceptibility provides a good measure of the amount of magnetite present and so provides a measure of heterogeneity when plotted against depth (Figs. F24, F25). More detailed examination of the estimates of magnetite contents reveals that the scale of variation is <6 cm in the oxide gabbros (Fig. F26A, F26B, F26C, F26D). The variation documented by changes in the estimated magnetite content is smoothed compared to that seen in grain-size variations because of the inherent averaging done by the susceptibility loop (effectively over at least 3 cm) (see "Igneous and Mantle Petrology," p. 3, in the "Site 1270" chapter).

Although extremely variable in hand sample, the gabbros share many features in thin section. Almost all of the gabbros have an igneous foliation defined by tabular plagioclase and in places by elongate clinopyroxene as well. These fabrics generally parallel grain-size contacts but locally can be nearly orthogonal to such contacts. The foliations also typically define a uniform direction in a single sample, but in several thin sections the foliations can be seen to change orientation over the length of the section. Deformation of individual crystals is common. Examples include kinked and broken crystals (Fig. F27A) and development of neoblasts at the ends of crystals oriented orthogonal to

F21. Clinopyroxene and oxides in oxide gabbro, p. 65.

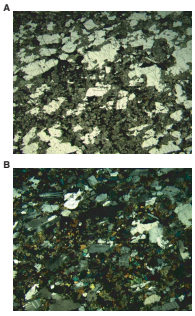

F22. Visual oxide estimates vs. magnetic susceptibility, p. 66.

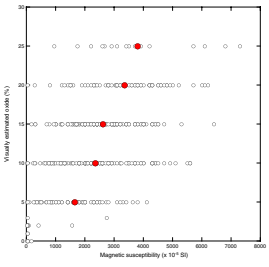

F23. Oxide vs. magnetic susceptibility by grain size, p. 67.

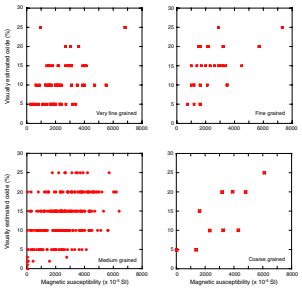

F24. Modal magnetite vs. magnetic susceptibility, p. 68.

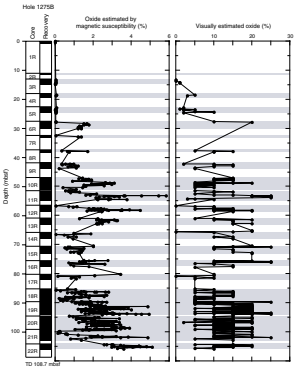

the main foliation (Fig. F27B). This deformation is interpreted to have occurred in the presence of interstitial liquid, perhaps during igneous compaction, because it is localized, the neoblasts are completely recovered, and nearby grains are completely strain free.

Another common feature of these gabbros is the presence of a few conspicuously large plagioclase crystals in many sections. These plagioclase crystals have strong optical zonation and irregular grain boundaries, may be optically discontinuous, and lack polysynthetic twinning (Fig. F28). These characteristics suggest that these plagioclase grains reacted with the crystallizing liquid and were partially resorbed. Other evidence for reaction is found in the relation of the oxide minerals to the silicates. In the majority of the thin sections, the oxides have textures that suggest that they are replacing pyroxenes and plagioclase (Fig. F29). Chemically this does not seem plausible, but the textural features are quite compelling.

Coarsely exsolved orthopyroxene is present in some clinopyroxene (Fig. F30). In detail it can be seen that many of the exsolved orthopyroxenes also contain exsolved clinopyroxenes. This texture may result from breakdown of original igneous pigeonite. Another relatively common but curious feature is the distribution of accessory apatite in these gabbros. In most, apatite is not conspicuous, but when present it is found as relatively large grains that occur in clusters (Fig. F31).

Diabase

Diabase is found throughout Holes 1275B and 1275D. It is invariably aphanitic, and phenocrysts are mostly absent. Chemical analyses suggest that the diabases rapidly crystallized and preserve liquid compositions (see "Geochemistry," p. 22). Diabase crosscuts all other lithologies and is interpreted to reflect a late magmatic event.

Granophyre

Granophyre is common in Site 1275 gabbros. When present as small irregular veins, the granophyre appears to be replacive rather than crosscutting. Where the granophyre traverses plagioclase, the plagioclase is modified to a more albitic composition and clinopyroxene is pseudomorphed by amphibole that is in optical continuity with the original clinopyroxene (Fig. F32). The granophyre illustrated in Figure F32 also contains zircon and apatite, and the vein formation process appears to have completely dissolved an oxide grain. Wider granophyres have sharper boundaries, are composed predominantly of plagioclase and quartz, and contain accessory titanite and apatite. In Hole 1275D there are examples of granophyre that is mixed with olivine-plagioclase phyric diabase. The boundaries between the diabase and granophyre are crenulate and suggestive of liquid-liquid interaction. This granophyre is distinct in that it contains more abundant amphibole, apatite, and titanite than the granophyre associated with the gabbros (Fig. F33).

Discussion

Drilling at Site 1275 sampled a complex assemblage of gabbroic rocks. We discuss their genesis by first considering the crystallization history of the troctolite, the oxide gabbros, and the granophyre. The relationship of the diabase to these lithologies is discussed where appro-

F25. Modal magnetite estimated from susceptibility, Hole 1275D, p. 69.

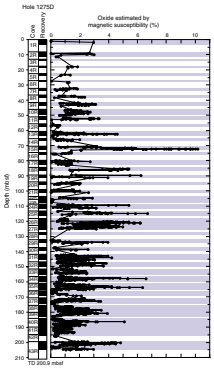

F26. Detail of modal magnetite variation, p. 70.

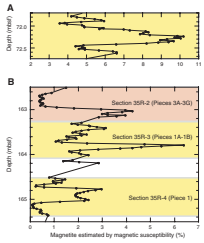

F27. Broken plagioclase crystals and plagioclase neoblasts, p. 72.

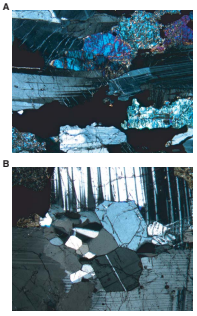

F28. Optically discontinuous resorbed plagioclase grain, p. 73.

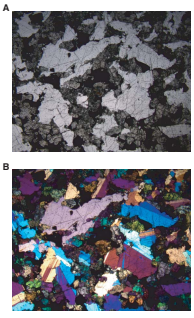

priate. We then consider the larger question of the assembly of these rocks as constrained within Holes 1275B and 1275D and by comparisons between them.

The crosscutting relations indicate that the troctolite and its associated gabbroic material formed the host rock into which the liquid parental to the oxide gabbros was intruded. Based on analogy with other olivine-rich rocks associated with abundant gabbro, we infer that these troctolites were generated by the addition of interstitial plagioclase and pyroxenes to a peridotite via crystallization from a liquid migrating along olivine grain boundaries. This process resulted in isolated olivine grains surrounded by a gabbroic matrix. Where olivine grains are in contact it can be seen that the gabbroic material extends as thinning tendrils between the grains (Fig. F18). In these samples, the olivine grains are rounded and embayed. Optically continuous patches of olivine are separated by interstitial pyroxene or plagioclase. The contemporaneous crystallization of the gabbroic material between the olivine crystals and in the crosscutting gabbros is suggested by the growth of poikilitic pyroxenes across the gabbro/troctolite contact.

The oxide gabbros have complex internal relations and clearly did not crystallize from a single pulse of magma. The presence of regions with discrete grain sizes and irregular crenulate boundaries suggests that multiple injections, magma mingling, and, perhaps, magma mixing were important processes. The variably deformed plagioclase crystals and changes in the orientation of the magmatic foliations suggest that partially solidified gabbro was disrupted on numerous occasions. The combination of periodic intrusion, magma mixing, and disruption of partially solidified gabbros produced the complex textural relations observed. The apparent reaction relationship between the oxides and silicate grains indicates a complex crystallization history, whereas the exsolution features in the pyroxenes imply protracted and possibly nonmonotonic cooling.

The granophyre is closely associated with the oxide gabbros and may represent the product of extreme fractional crystallization. That the granophyre replaces and reacts with the gabbro clearly indicates that the two were not in equilibrium at some times and places. However, this is an expected consequence of fractional crystallization and should not be taken as evidence that the granophyres are exotic to the system.

Simple correlations between Holes 1275B and 1275D are not possible. It is clear that the troctolite in both holes is similar and probably represents the "country rock" into which the oxide gabbros were intruded. Grain size in Hole 1275B consistently increases downhole (Fig. F10), whereas in Hole 1275D the grain size increases to the base of Unit IV and then decreases below (Fig. F15). If the intervening troctolite was removed, the sequence of gabbroic material in Hole 1275B might correspond to that seen in Units II, III, and the upper part of IV in Hole 1275D. The correspondence is somewhat crude and the gabbros in Hole 1275D are on average coarser grained than those in Hole 1275B. If the gabbros in these two holes represent a single pluton, then it may be that Hole 1275B sampled closer to the margin of the intrusion and cooled more rapidly.

METAMORPHIC PETROLOGY

Four holes were drilled at Site 1275 (15°44.47′N, 46°54.21′W; mean water depth = 1567.4 mbsl). Hole 1275A (15°44.489′N, 46°54.211′W;

F29. Resorbed plagioclase cemented by oxide, p. 74.

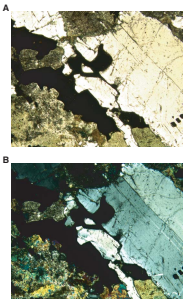

F30. Clinopyroxene exsolved orthopyroxene, p. 75.

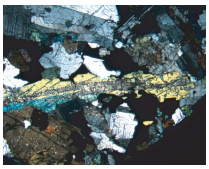

F31. Cluster of apatite crystals, p. 76.

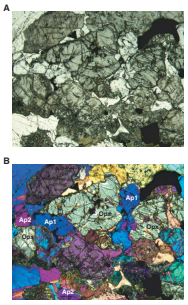

F32. Plagioclase and clinopyroxene alteration, p. 77.

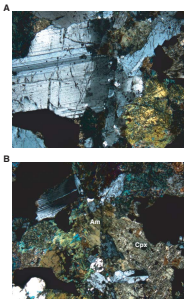

F33. Coarse-grained granophyric patch in diabase, p. 78.

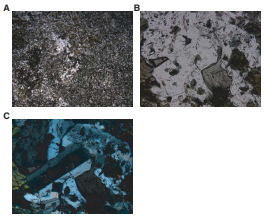

1562.3 mbsl) is 5 m deep and recovered 10 cm of slightly altered diabase with minor chlorite and amphibole replacing mesostasis and a piece of matrix-supported, carbonate-cemented breccia with slightly altered angular diabase clasts. Hole 1275B (15°44.486′N, 46°54.208′W; 1561.7 mbsl) is 108.7 m deep and recovered 46.9 m of core (recovery = 43.1%). Lithologies from Hole 1275B include slightly to highly altered diabase, gabbro, microgabbro, and troctolite cut by variably altered gabbroic and felsic dikes and veins. Metamorphic veining is dominated by amphibole and chlorite-amphibole veinlets. Alteration is static, and macroscopic amphibole and amphibole-chlorite veins, as well as abundant amphibole-filled microcracks, acted as conduits for seawater-derived hydrothermal fluids. Replacive formation of chlorite after clinopyroxene and plagioclase is limited mostly to the uppermost 35 m of Hole 1275B. Coronitic replacement of olivine and plagioclase by talc, chlorite, and tremolite characterizes the alteration of troctolitic rocks in the interval from 28.2 to 34.1 mbsf. Below 34 mbsf, alteration is uniformly dominated by partial replacement of clinopyroxene by green and minor brown amphibole. Plagioclase is <5% altered to secondary plagioclase and green amphibole along cracks. Oxides are partly replaced by titanite and hematite. Felsic dikes and veins in Hole 1275B are variably altered to secondary plagioclase, amphibole, and, locally, carbonate. Talc replacing pyroxene is present in the host gabbro adjacent to some of these veins. Felsic veins have noticeable amounts of quartz, titanite, apatite, and zircon, and patches of titanite, quartz, and apatite are present in some gabbro in proximity to these felsic veins. Metamorphic veins are dominated by amphibole, amphibole-chlorite, and clay-oxide veins and make up 0.43% of the core volume.

Hole 1275C (15°44.440′N, 46°54.218′W; 1552.8 mbsl) recovered <1% of the 20.8 m of basement drilled. Rocks from Hole 1275C comprise highly to completely altered gabbro, microgabbro, and troctolite. Alteration assemblages in gabbroic rocks are dominated by amphibole with minor chlorite and secondary plagioclase. Troctolites are variably serpentinized and talc-altered. Given the low core recovery, alteration of rocks from Holes 1275A and 1275C will not be further discussed in this chapter.

Hole 1275D is 209 m deep, and 104.6 m of core was recovered (recovery = 50.1%). Similar to Hole 1275B, the lithologies encountered in Hole 1275D comprise gabbro, microgabbro, diabase, mafic and felsic magmatic veins, and troctolitic rocks with variable amounts of orthopyroxene and clinopyroxene. The alteration style in Hole 1275D is also similar to that in Hole 1275B. Green amphibole is the most abundant secondary mineral, replacing clinopyroxene (20%–100% alteration) and plagioclase (<1%–15% alteration) in the gabbroic rocks. Alteration of the troctolitic rocks is characterized by serpentine and magnetite replacing olivine (50%–100% alteration) and chlorite, clay, and carbonate replacing plagioclase (50%–90% alteration). Pyroxenes in troctolitic rocks are altered to talc, serpentine, and amphibole. The major difference in alteration between Holes 1275B and 1275D is the higher abundance of lower greenschist facies minerals (chlorite/smectite after plagioclase and clinopyroxene) and low-temperature oxidative alteration (red clay/Fe oxyhydroxide and carbonate after olivine; clay and carbonate after plagioclase) in Hole 1275D. In comparison with Hole 1275B, amphibole, picrolite, and carbonate are more abundant and clay-oxide veins are less abundant in Hole 1275D. In both holes, late-stage metamorphic veins commonly follow preexisting magmatic veins and amphibole veins.

Hydrothermal alteration at Site 1275 started under amphibolite facies conditions (500°–700°C) with the formation of brown amphibole and continued under greenschist, zeolite, and brownstone facies conditions, as indicated by the development of green amphibole, chlorite, chlorite/smectite, clay, Fe oxyhydroxide, and carbonate. Hydrothermal alteration is almost exclusively static, and greenschist facies assemblages with green amphibole and chlorite or chlorite/smectite (in Hole 1275D) are the most abundant secondary minerals. Small veins and microcracks provided the main fluid pathways. These fractures and cracks are either related to cooling or to unroofing of the footwall of a normal fault.

Hole 1275B

Hydrothermal Alteration

Alteration of Gabbro, Microgabbro, and Diabase

Alteration intensities in Hole 1275B range from 10% to 100% (Fig. F34). We distinguish between an upper sequence of gabbro and diabase dikes (0–28 mbsf; Sections 209-1275B-1R-1 to 6R-1) and a lower sequence (34–105 mbsf; Sections 7R-1 to 22R-2) of gabbro and felsic magmatic dikes. In the upper sequence, diabase is 10%–40% altered, manifest in the replacement of mesostasis and clinopyroxene microphenocrysts by fibrous amphibole and chlorite. Gabbro and microgabbro (Fig. F35A) are 20%–50% altered. Clinopyroxene is highly to completely altered, mostly to green amphibole, although noticeable amounts of chlorite are generally present. Plagioclase is slightly altered (5%–10%) to secondary plagioclase and minor chlorite. Alteration of plagioclase is generally limited to narrow zones along grain boundaries and internal cracks. Pre- to synmetamorphically deformed contacts between dikes and gabbro consist of very fine grained felty chlorite and amphibole with minor quartz (e.g., Sample 209-1275B-3R-1 [Piece 9, 57–59 cm]). Fe-Ti oxides show breakdown to titanite and hematite (e.g., intervals 209-1275B-3R-1, 57–59 cm, 84–87 cm, and 105–107 cm). Titanite accounts for as much as 2%–3% by volume in these rocks and is detectable by X-ray diffraction (XRD) (Fig. F35C; Table T2). Titanite usually surrounds hematite grains and is intergrown with amphibole needles (Fig. F35B). In some instances, patches of quartz ± titanite intergrown with acicular amphibole are developed in pockets. These patches are particularly abundant in proximity to, and within, felsic veins.

The lower gabbroic unit (34–108.7 mbsf) is uniform in terms of alteration style and intensity. The extent of alteration varies between 10% and 40% and is dominated by replacement of clinopyroxene by amphibole. Coarse, prismatic brown amphibole can be as abundant as green amphibole in individual thin sections. In most samples, however, green amphibole is more abundant than brown amphibole. Commonly, felty green amphibole is developed along the margins of clinopyroxene veins (Fig. F36). Green amphibole also replaces plagioclase, although this replacement is usually limited to narrow, feathery areas that follow internal cracks in plagioclase (Fig. F37). Also along cracks and grain margins, plagioclase is altered to secondary plagioclase. Overall, plagioclase alteration is <4% throughout the lower gabbro unit. Fe-Ti oxides are mostly fresh, except for subsolidus exsolution/oxidation to trellislike ilmenite lamellae in magnetite (Fig. F38). In contrast to the upper gabbro/diabase sequence, titanite is rare in the lower gabbro unit

F34. Alteration intensities, Hole 1275B, p. 79.

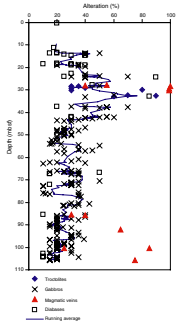

F35. Moderately altered gabbro, p. 80.

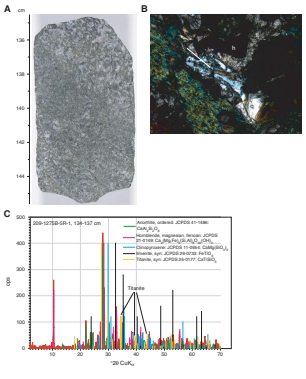

T2. XRD results, p. 156.

F36. Moderately altered gabbro, p. 81.

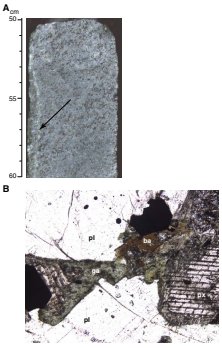

F37. Plagioclase replacement by green amphibole, p. 82.

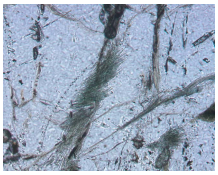

and is present only in felsic veins and in the host gabbro directly adjacent to felsic veins. Felsic dikes and veins (granophyres) make up a significant proportion of the core (0.8 vol%), in particular in Cores 209-1275B-18R and 19R (Fig. F39A). They are variably altered to amphibole and secondary plagioclase. Locally, the felsic veins are rich in carbonate that appears to replace plagioclase and has needlelike inclusions of green amphibole or zeolite (Fig. F39B, F39C).

Alteration of Troctolitic Rocks

Troctolitic rocks with variable amounts of orthopyroxene and clinopyroxene are present in the interval from 209-1275B-6R-1, 56 cm, to 7R-1, 81 cm (28.2–33.1 mbsf). Olivine in the troctolite is moderately to completely altered (20%–98%) to talc, serpentine, and magnetite. Alteration of olivine starts along irregular internal cracks with the formation of magnetite and serpentine networks. In an advanced stage of alteration, these networks form a characteristic mesh texture. Near magmatic veins, which are particularly abundant in Section 209-1275B-7R-1, olivine is dominantly replaced by talc and magnetite. The textural development of this talc alteration is similar to that of serpentinization. Commonly, both serpentinization and talc alteration are developed in a single sample. In these cases, talc surrounds partially serpentinized olivine grains. Along former olivine/plagioclase grain boundaries, coronitic replacement of olivine and plagioclase imposes a characteristic texture to the core (Fig. F40A). These reaction coronas are banded and consist of talc and/or tremolite (after olivine) and chlorite (after plagioclase) (Fig. F40B, F40C). Plagioclase in troctolitic rocks is usually more altered than olivine. Replacement of plagioclase is primarily by fibrous chlorite, although minor amounts of secondary plagioclase, talc, and green amphibole are also present. Orthopyroxene oikocrysts in Section 209-1275B-6R-2 are variably altered (10%–70%) to talc and chlorite. Clinopyroxene, where present, is moderately to highly altered (30%–70%) to chlorite and minor amphibole. Low-temperature oxidative alteration of olivine to Fe oxyhydroxide, red clay, and carbonate (iddingsite) is developed locally, in particular along clay-oxide veinlets. Mafic and felsic magmatic veins in troctolite are abundant in Sections 209-1275B-6R-2 and 7R-1. They are completely altered to amphibole, chlorite, talc, and titanite. The presence of zircon suggests that these veins represent late-stage magmatic products.

Metamorphic Veins

Metamorphic veins in Hole 1275B make up 0.43% of the core volume (Table T3). Amphibole, amphibole-chlorite, and clay-oxide veins are the most common vein types (Fig. F41), along with rare quartz, zeolite, and carbonate veins. The abundance of veins and the vein mineralogy show no systematic correlation with depth (Fig. F42). However, picrolite and minor chrysotile veins are restricted to the troctolitic unit between 28.2 and 33.1 mbsf. These veins account for ~6% of the total vein volume (Figs. F41, F42). Amphibole and amphibole-chlorite veins are the most common vein type in Hole 1275B (52.7%). They are usually <2 mm wide and appear to be predominantly dipping at moderate to steep angles (Fig. F43). In thin section, sets of subparallel, en echelon microscopic amphibole veinlets are apparent (Fig. F44). Veins that consist exclusively of chlorite are rare but tend to be thicker than amphibole and mixed amphibole-chlorite veins. These chlorite veins are particularly prominent between 89 and 97 mbsf. Apart from this interval

F38. Breakdown products of a primary Fe-Ti oxide, p. 83.

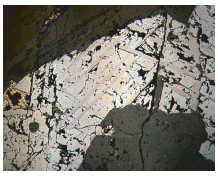

F39. Felsic dikes and veins, p. 84.

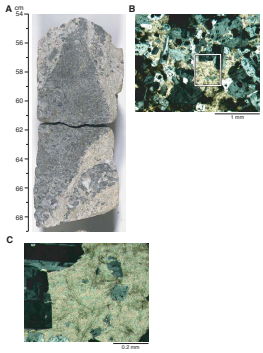

F40. Typical features of troctolite, p. 85.

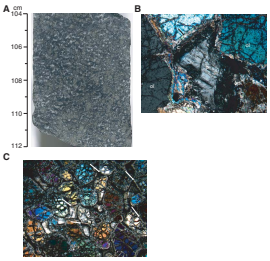

T3. Metamorphic vein statistics, p. 157.

F41. Vein mineral composition, Hole 1275B, p. 86.

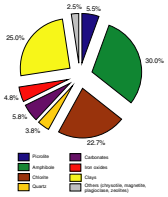

and rare chlorite veins in the diabase of the uppermost 30 m, chlorite in Hole 1275B is associated with green amphibole. Clay-oxide veins make up ~25% of the vein volume. They are usually <1 mm wide and form irregular networks with pronounced orange-brown alteration halos. In thin section they appear dark brown to opaque. Associated alteration halos have minor staining of plagioclase by oxides and replacement of clinopyroxene and plagioclase by brown clay.

Hole 1275D

The style of alteration in Hole 1275D is broadly similar to that in Hole 1275B. However, some particular lithologies and alteration styles are exclusive to Hole 1275D (Fig. F45). The following sections provide a brief overview of alteration features in Hole 1275D with particular emphasis on the differences in alteration style and intensity between Holes 1275B and 1275D.

Hydrothermal Alteration

Alteration of Gabbro, Microgabbro, Olivine Gabbro, and Diabase

Intervals with predominantly gabbroic rocks in Hole 1275D comprise oxide gabbro (53–81 mbsf; Unit II), oxide gabbronorite (91–151 mbsf; Unit IV), and a succession of olivine gabbro and oxide gabbronorite (151–209 mbsf; Unit V). The oxide gabbro is very similar in alteration style and intensity to the oxide gabbro in Hole 1275B (see above). Except for rare intervals of high alteration intensities, alteration of the oxide gabbros and gabbronorites is usually moderate. The most common alteration mineral is green amphibole replacing clinopyroxene (20%–100%) and, to a lesser extent, plagioclase (<10%). Brown amphibole is common as rims around clinopyroxene that is partly to completely replaced by green amphibole in the center. Locally, brown amphibole completely replaces clinopyroxene and is variably overprinted by fibrous green amphibole. Secondary plagioclase appears to be a minor component and generally composes <5% of the rock. Unlike clinopyroxene, alteration of plagioclase is limited to areas along cracks and grain boundaries. Titanite is a breakdown product of Fe-Ti oxides, but the abundance of secondary titanite is somewhat lower than that in Hole 1275B. However, there is abundant titanite in vein networks in the brecciated diabase in Section 209-1275D-1R-1.

A marked difference between Holes 1275B and 1275D is the common development of chlorite and chlorite/smectite after plagioclase and clinopyroxene in Hole 1275D. Locally, these phases can make up 5%–10% of the rock volume. Their presence imposes a greenish to brownish color to the rock in hand specimen (Fig. F45C). In thin section, replacement of primary minerals by chlorite/smectite is patchy and affects clinopyroxene more intensely than plagioclase (Fig. F46).

Olivine-bearing gabbros and gabbronorites of Unit V are moderately to highly altered. Alteration of olivine is characterized by the development of fibrous talc, acicular green amphibole, and subhedral magnetite along the grain margins (Fig. F47). Alteration of olivine starts along cracks with the formation of talc and magnetite. Plagioclase adjacent to olivine is partly replaced by chlorite and talc (Fig. F47). Pyroxene in olivine-bearing gabbros is variably altered to felty green amphibole and minor talc. Locally, oxidative alteration leads to partial alteration of olivine relics to clay, Fe oxyhydroxide, and carbonate (Fig. F45D).

F42. Vein mineralogy, Hole 1275B, p. 87.

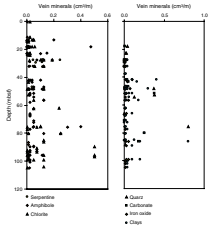

F43. Amphibole vein in moderately altered gabbro, p. 88.

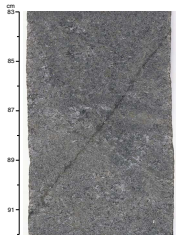

F44. Amphibole veinlets and amphibole-filled microcracks, p. 89.

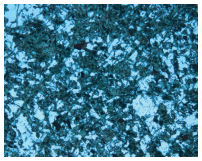

F45. Alteration of troctolites and gabbroic lithologies, p. 90.

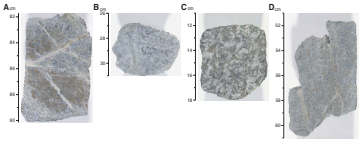

F46. Chlorite/smectite and amphibole replacing clinopyroxene and plagioclase, p. 91.

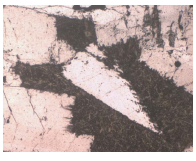

F47. Green amphibole, talc, and magnetite replacing olivine, p. 92.

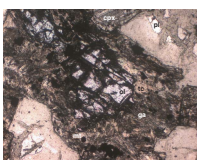

Alteration of Troctolitic Rocks

Troctolitic rocks are highly to completely altered to serpentine, magnetite, clay, talc, carbonate, and Fe oxyhydroxide (after olivine) and chlorite, clay, and carbonate (after plagioclase). Troctolitic units in Hole 1275D are cut by a large number of magmatic veins (both felsic and mafic) that are variably altered to amphibole, chlorite, and talc (mafic veins) or secondary plagioclase, amphibole, and carbonate (felsic veins) (Fig. **F48**). Away from these magmatic veins and dikes, olivine is completely altered to serpentine and trails of magnetite forming mesh textures. Pyroxenes are variably altered to serpentine (bastite after orthopyroxene), talc, and green amphibole. Locally, troctolitic rocks are heavily talc-altered (Fig. **F45A, F45B**). Talc alteration is limited to millimeter-thick halos near magmatic veins and larger-scale contacts with gabbroic rocks (Fig. **F48**), where talc appears to postdate serpentinization. However, talc alteration at boundaries between troctolite and gabbro is by no means universal. Where talc alteration is weak, noticeable amounts of fresh plagioclase and olivine are preserved in the former grain centers. Plagioclase relics are variably affected by a late-stage low-temperature overprint, resulting in the formation of clay and carbonate (Fig. **F49**). Olivine, in particular, is commonly well preserved in proximity to magmatic veins, although it is variably affected by low-temperature alteration to carbonate, clay, and Fe oxyhydroxide (Fig. **F50**). This type of oxidative alteration is most pronounced along irregular networks of carbonate and carbonate-clay veinlets that cut serpentinized olivine grains and follow former plagioclase-olivine grain boundaries (Figs. **F49, F50**). XRD analyses of these domains indicate that the carbonate phase is calcite (Fig. **F50;** Table **T2**). Calcite can make up 3–10 vol% of individual pieces of core in the troctolites of Unit I (0–53 mbsf).

Alteration intensity in Hole 1275D varies considerably within given intervals (Fig. **F51**). This is in part due to differences in the primary lithology. For instance, diabase is usually less altered than gabbros, fine-grained gabbros and microgabbros are less altered than coarse-grained gabbros, and troctolitic rocks are the most altered. In general, the intensity of troctolite and gabbro alteration decreases with depth (Fig. **F51**).

Metamorphic Veins

Metamorphic veins account for 0.65 vol% of the core in Hole 1275D. The most abundant vein types are amphibole, amphibole-chlorite, carbonate, and picrolite (Table **T3;** Fig. **F52**). Minor minerals in metamorphic veins are talc, iron oxides, quartz, and clay. The distribution of vein types is partially controlled by the host lithology. Picrolite and talc veins are restricted to troctolite in Units I and III, whereas amphibole ± chlorite veins are usually present in gabbro. The downhole distribution of metamorphic vein minerals (Fig. **F53**) indicates that carbonate, chlorite, and serpentine veins are particularly abundant in the upper 50 m of the hole. Below 50 mbsf carbonate veins are only locally developed. Amphibole ± chlorite veins are common in gabbro below 50 mbsf but relatively scarce above this level and absent in the troctolite of Units I and III. Compared to Hole 1275B, veining is more intense in Hole 1275D. In particular, carbonate veins are substantially more common in Hole 1275D. Overall, metamorphic veining at Site 1275 is weak. Amphibole ± chlorite veins are 0.2–1 mm thick and make up 0.1–0.2 vol% of the core. The average amphibole vein density at Site 1275 is 1–10 veins/m of core, similar to the amphibole vein densities at Sites 921 and 923 in the Kane Fracture Zone (MARK) area (Dilek et al., 1997).

F48. Mafic vein and host troctolite cut by felsic magmatic vein, p. 93.

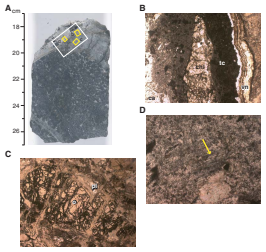

F49. Plagioclase alteration in a troctolite, p. 94.

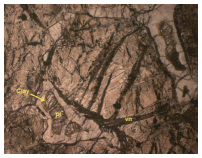

F50. Highly altered troctolite, p. 95.

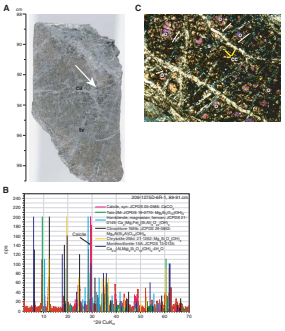

F51. Alteration intensities, Hole 1275D, p. 96.

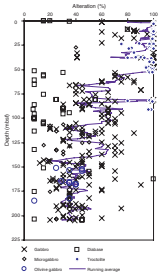

F52. Vein minerals, Hole 1275D, p. 97.

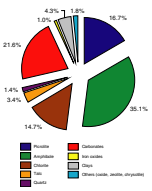

Discussion

Gabbros from Site 1275 show little evidence for crystal-plastic deformation and granulite facies metamorphism. Plagioclase-amphibole veins that splay off felsic dikes are probably transitional magmatic–hydrothermal veins that initially form during late-stage magmatic activity. However, they include hydrothermal amphibole, secondary plagioclase, chlorite, and carbonate, indicating that hydrothermal reactions continued over a range of temperature conditions from amphibolite to zeolite facies.

High-temperature, static background alteration by hydrothermal fluids is pervasive throughout the core. This alteration is generally manifest in coronitic replacement of clinopyroxene by brown amphibole. In gabbronorites, magnesium-amphibole ± talc typically replaces orthopyroxene. The intensity of this amphibolite facies (500°–700°C) alteration is usually low (<5%–10%) and does not appear to correlate with the grain size of the rock. Pervasive background alteration continued at lower temperatures facilitated by the ingress of seawater-derived hydrothermal fluids along fractures (now green pleochroic amphibole veins) that are probably related to cooling and cracking of the rocks in the axial environment at temperatures of ~400°–500°C (e.g., Kelley, 1997). At a smaller scale, microcracks (<100 µm), representing smaller-scale fracturing and fluid penetration, are abundant throughout the core in Holes 1275B and 1275D. These microcracks are filled with serpentine, talc, and magnetite (in troctolites) and secondary plagioclase and amphibole ± chlorite in gabbroic rocks. Troctolitic rocks reacted more rapidly with the hydrothermal fluids than gabbros, as suggested by the intense coronitic replacement of olivine and plagioclase along former grain boundaries. Fracturing and fluid percolation continued under lower greenschist facies and zeolite facies conditions as indicated by the development of chlorite/smectite ± fibrous actinolite, clay-oxide, and carbonate veins and by replacement of olivine and plagioclase by clay and carbonate, particularly in Hole 1275D.

The following section provides a brief comparison of the alteration of plutonic rocks from Site 1275 with those from other locations, namely Hess Deep, MARK, and Atlantis Bank. It is commonly suggested that at slow-spreading ridges alteration of lower ocean crust is facilitated by fluid penetrating the lower crust along shear zones (Ito and Clayton, 1983; Mével and Cannat, 1991; Stakes et al., 1991), whereas static cracking provides pathways for fluids at fast-spreading ridges (Manning et al., 1996; Nehlig, 1994). In Hole 735B (Atlantis Bank, Southwest Indian Ridge) deformation intensity is strongly correlated with the extent of high-temperature alteration and amphibole veining (Dick et al., 2000; Cannat et al., 1991). In the uppermost 200 m of Hole 735B, alteration intensities are generally high to complete and amphibole veins make up ~2% of the core volume (Dick et al., 2000). Gabbros recovered from Sites 921–924 (MARK area, Mid-Atlantic Ridge 23°N) also show a systematic relationship between the intensity of crystal-plastic deformation and alteration intensity (Dilek et al., 1997; Kelley, 1997). At Sites 921–924, static alteration is also abundant (average = ~50%) (Fletcher et al., 1997) away from zones of crystal-plastic deformation, unlike in Hole 735B, where alteration intensity is usually very low in undeformed zones (Dick et al., 2000). Average amphibole vein density at Sites 921 and 923 is 1–10 veins/m of core (Dilek et al., 1997), significantly less than that in the highly deformed uppermost 200 m of Hole 735B and similar to that in the deeper, less deformed section of that hole (Dick et

F53. Vein mineralogy, Hole 1275D, p. 98.

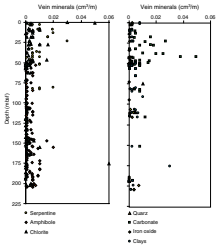

al., 2000). In Hess Deep gabbros, alteration is exclusively static and controlled by a downward-propagating cracking front that developed as the lower crust cooled to 700°–800°C (Gillis, 1995; Manning et al., 1996).

These examples clearly demonstrate that deformation and hydrothermal alteration are strongly related. In areas of pronounced crystal-plastic deformation, alteration intensities and amphibole vein densities tend to be higher than in undeformed zones. Brittle and semibrittle deformation also results in increased alteration intensities, although alteration is controlled by brittle veins rather than by cooling fractures that tend to form at higher temperatures (Magde et al., 1995). The relationship between crystal-plastic deformation and alteration is best illustrated in rocks from Hole 735B that are primarily altered under granulite to amphibolite facies conditions (550°–800°C) with alteration intensities correlated with the extent of crystal-plastic deformation. The amount of amphibolite and greenschist facies alteration in undeformed rocks is <5%–10%, except for more intense alteration related to a few brittle faults (Dick et al., 2000). In the gabbros from the MARK area, a much larger proportion of the total alteration can be related to brittle features, although alteration intensities and amphibole vein densities increase markedly in rare crystal-plastic shear zones (Dilek et al., 1997; Kelley, 1997). Consistent with the notion that alteration started in the ductile region in Hole 735B and mainly in the semibrittle region at MARK, amphibole-plagioclase geothermometry indicates that temperatures of the earliest metamorphic assemblages at MARK were 560°–680°C, whereas amphibolitization in Hole 735B took place at 770°–820°C (Gillis and Meyer, 2001). Crystal-plastic deformation at Site 1275 is very rare, even compared to the MARK area, and hence fluid ingress was largely facilitated by brittle deformation and cracking. The presence of secondary brown amphibole indicates that fluid ingress occurred at temperatures >500°C. Brittle fractures in the Hess Deep gabbros form at temperatures of ~770°C (Manning et al., 1996), which may also be the upper temperature limit (at pressures <4 kbar) for the amphibole veins at Site 1275. The brittle fracturing and high-temperature alteration at Site 1275 might be a result of cooling in an axial or near-axial environment or it could be related to unroofing in the footwall of a normal fault. The variability in metamorphic mineral assemblages, ranging from brown amphibole to green, fibrous amphibole and chlorite/smectite to carbonate and clay, suggests that fluid circulation and water-rock interactions continued throughout a period of progressive cooling and uplift. The abundance of low-temperature alteration is similar to that in a zone between 500 and 600 mbsf in Hole 735B (Bach et al., 2001) and provides further evidence for significant low-temperature exchange between seawater and tectonically exposed gabbroic crust.

STRUCTURAL GEOLOGY

We present the results of a detailed structural study of the core recovered from Site 1275 followed by a discussion of preliminary interpretations of the structural history. Holes 1275A and 1275C recovered minimal quantities of core so it was not possible to make significant structural observations and therefore these holes are not discussed here. Holes 1275B and 1275D show similar lithologic and structural features and are discussed together. Four categories of observations were recorded including magmatic foliation, crystal-plastic deformation, brittle deformation, and alteration vein intensity (see the **"Supplementary**

Material" contents list). These were supplemented by microstructural observations from 120 thin sections. Details of the structural classification scheme for each feature are given in "Structural Geology," p. 9, in the "Explanatory Notes" chapter.

Crystal-Plastic Deformation

Holes 1275B and 1275D show evidence of limited crystal-plastic deformation at irregular intervals throughout both cores. The crystal-plastic deformation intensity does not exceed grade 2 (well foliated) in either hole (Fig. F54). Core from Hole 1275B (average crystal-plastic foliation grade = 0.02) (Fig. F55) has less crystal-plastic deformation than core from Hole 1275D (average grade = 0.07). No measurable crystal-plastic fabric orientations were found in Hole 1275B, but in Hole 1275D 14 foliations were measured in shear zones typically no more than a centimeter wide. Dips of foliations average 50° ± 18° with no systematic variation with depth.

Most of the 120 thin sections from this site show the effects of a pervasive, very weak, high-temperature, crystal-plastic deformation. Plagioclase displays undulose extinction, deformation twins, and subgrain formation. Some olivine displays undulose extinction. A few gabbros have local patches of plagioclase neoblasts on the margins of larger grains, particularly where the larger grains impinge on each other. Samples with minor localized dynamic recrystallization textures and common bent plagioclase grains were graded 0.5 on the crystal-plastic deformation intensity scale.

A small minority of the gabbros from Hole 1275D include more pronounced dynamic recrystallization near boundaries of large plagioclase grains and completely recrystallized small plagioclase grains. This deformation may have enhanced the magmatic foliation present in several samples. These samples are graded 1 or 2 on the crystal-plastic intensity scale depending on the intensity of foliation produced. Plagioclase neoblasts are polygonal, coarse grained, have near 120° grain boundaries, and show nearly complete strain recovery. These are features of very high temperature recrystallization or crystal-plastic deformation in the presence of melt. Several of the most highly deformed samples contain plagioclase porphyroclasts with asymmetric tails of polygonal neoblasts.

Brittle Features

Two different styles of brittle deformation are recognized. The first is gabbro and diabase cataclasites where the dominant strain accommodation process was fracturing and cataclastic flow. The second is semibrittlely deformed schistose rocks where strain was accommodated by schistose growth of chlorite and other alteration minerals.

Gabbro and Diabase Cataclasites

Holes 1275B and 1275D contain several intervals of cataclastically deformed gabbro and diabase. Cataclastic zones rich in green amphibole form branching bands across many brittlely deformed gabbros (Fig. F56). Cataclasites typically contain magmatic fabrics, alteration veins, and minor crystal-plastic fabrics that are overprinted by brittle deformation including fracturing of plagioclase and amphibole. Cataclasites and protocataclasites typically comprise clasts of gabbro, micro-

F54. Crystal-plastic intensity with depth, p. 99.

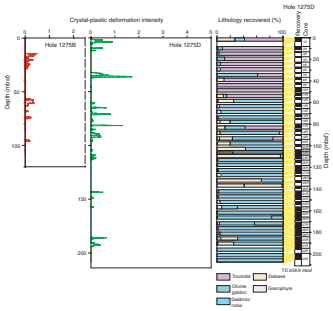

F55. Crystal-plastic deformation by intensity, p. 100.

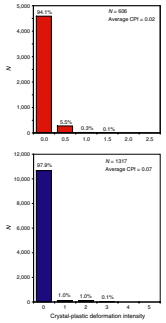

F56. Cataclasite containing clasts of gabbro and diabase, p. 101.

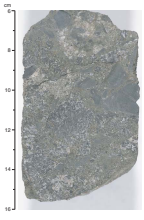

gabbro, diabase, and amphibole schist within a matrix of fractured plagioclase and amphibole (Fig. F57). The clasts are subangular to subrounded and generally range from 1 to 10 mm in size. The matrix has grain sizes ranging from 0.01 to 0.5 mm. Amphibole within the matrix is generally finer grained than fractured plagioclase and sometimes has a slightly schistose fabric indicating growth during deformation. Discrete fractures cutting plagioclase porphyroclasts are typically filled with green amphibole.

Cataclastic deformation in gabbros appears to have occurred after minor crystal-plastic deformation and/or magmatic deformation. Fractured plagioclase in most cataclastically deformed gabbros contains patchy subgrain boundaries and in some cases minor dynamic recrystallization textures. In some grains, brittle fractures appear to be localized on subgrain boundaries. The presence of pleochroic green amphibole that appears to have partially crystallized in cataclasites suggests that brittle deformation occurred within lower amphibolite facies to upper greenschist facies

Several cataclasite samples contain subrounded to subangular diabase clasts that are either undeformed or weakly deformed (e.g., Sample 209-1275B-6R-1[Piece 2, 6–16 cm]) (Figs. F56, F58). Several of these shear zones also contain elongate diabase clasts parallel to the shear foliation (Fig. F59). In some locations, diabase clasts in cataclastic shear zones contain possible preserved remnants of chilled zones parallel to current margins of the clasts (Figs. F56, F58) indicating that diabase may have intruded the cataclasite during active deformation. It is also possible that these features are alteration rinds and not related to magmatic processes.

In Sample 209-1275B-3R-1, 57–60 cm, gabbro and diabase are in fault contact, separated by a shear zone. The shear zone consists of a ~0.5-cm-wide zone of chlorite schist that borders the diabase across a sharp, planar contact. Plagioclase microlites near the margin of the diabase are aligned parallel to the margin but are randomly oriented away from it. The chlorite schist grades into gabbro on the opposite shear zone margin across a zone of cataclastically deformed gabbro. These textures suggest a complex structural relationship between gabbro and diabase that included both magmatic intrusion and faulting.

Semibrittle Shear Zones

Several samples from Holes 1275B and 1275D contain schistose shear zones composed of fine- to medium-grained chlorite, amphibole, and talc. These are discrete zones cutting gabbro and diabase (e.g., Sample 209-1275D-1R-1, 9–14 cm) (Fig. F59) commonly within alteration veins that follow the path of gabbroic veins in troctolite. Fibrous chlorite, talc, and amphibole form an anastomosing foliation that is cut by anastomosing shear fractures (Fig. F60). This type of deformation appears to postdate and partially overprint the cataclastic deformation in Sample 209-1257D-1R-1, 9–14 cm, and may represent a later, lower-temperature phase of strain localization. Amphibole cataclasites are more common in core than semibrittle schists in Holes 1275B and 1275D. This may be because fewer are present or because recovery of semibrittle schists was relatively poor.

F57. Amphibole cataclasite, p. 102.

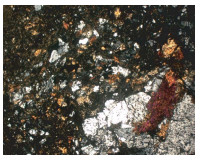

F58. Diabase porphyroclast in gabbro cataclasite, p. 103.

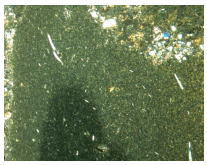

F59. Talc-chlorite-amphibole schist bordering undeformed diabase, p. 104.

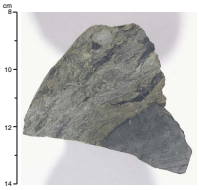

F60. Fine-grained talc-amphibole schist, p. 105.

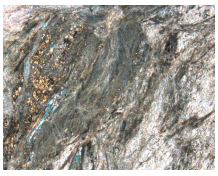

Distribution and Orientation of Brittle Deformation

Brittle deformation is concentrated in the upper portions of Holes 1275B and 1275D. The upper 15 m of Hole 1275B is composed dominantly of undeformed diabase. Gabbro beneath the diabase has been strongly deformed by cataclasis that formed the amphibole and plagioclase matrix cataclasites and lesser semibrittle talc-chlorite schists (Fig. F61). Brittle deformation decreases below 30 mbsf in the troctolites and lower gabbros. The upper 50 m of Hole 1275D shows extensive brittle deformation. This portion of the hole is composed dominantly of troctolite with lesser gabbro. Nearly all gabbros in the upper 55 m of Hole 1275D contain significant amphibole and plagioclase matrix cataclasites and/or talc-chlorite-amphibole schists. The troctolite is strongly fractured and veined. Serpentine veins in troctolite appear to have accommodated some shear deformation and have schistose textures. Some show offsets. The significant decrease in brittle deformation below ~55 mbsf corresponds to the base of the primary troctolite unit. This depth may represent the thickness of a detachment fault system. It is possible that the troctolite is weaker than gabbro, and strain from a detachment fault occurs over a wider interval where troctolite is present. This might explain why strong brittle deformation textures are present at greater depths in Hole 1275D than in Hole 1275B. Peaks in brittle deformation intensity in the lower sections of Holes 1275B and 1275D represent minor localized fracturing, faulting, and weak brecciation. These include narrow (<0.3 cm) normal, reversed, and oblique slip faults with <4 cm total offset found within each hole.

Orientations of brittle deformation features were measured in the core reference frame. Faults, brittle shear zones, and fractures have a wide range of dips, but the magnitude of the dips show no systematic trends with depth (Fig. F62).

Alteration Veins

The distribution and intensity of metamorphic veins in Hole 1275D are strongly correlated with the lithology. The troctolites are more intensely veined than any of the other lithologies (Figs. F61, F63). They are traversed by altered magmatic veins and contain several generations of alteration veins. The earliest generation of veins is white and green picrolite veins, which either form discrete veins (Fig. F64B) or fill sigmoidal expansion cracks orthogonal to the magmatic veins (Fig. F64A). Later carbonate-clay-Fe oxyhydroxide veins (Fig. F64A, F64D) cut these veins and are often located within or parallel to the early magmatic veins (Fig. F64B, F64C). The magmatic veins themselves occasionally contain green amphibole-chlorite veins. Rare chlorite veins are also present within the troctolites.

The gabbros show three distinct generations of veins. The first generation is a set of relatively rare planar black amphibole veins. These are cut by planar green amphibole and green amphibole-chlorite veins that are uniformly developed throughout the gabbros (Fig. F65C). These veins are up to 2 mm thick, are also planar, and occur every 10–20 cm in the core. Later carbonate-clay-Fe oxyhydroxide veins (Fig. F65A, F65B) crosscut these green veins. This last generation of veins are larger (up to 1 cm wide) brittle fractures that acted as conduits for low-temperature seawater circulation.

The diabases contain sparse green amphibole-chlorite veins. The cataclastic rocks are cut by amphibole and serpentine veins, at least some

F61. Brittle deformation and alteration vein intensities, Hole 1275B, p. 106.

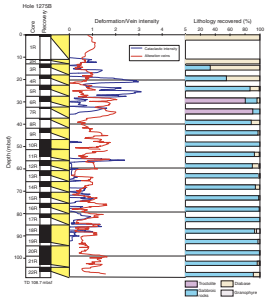

F62. Dips of faults, fractures, and brittle shear zones with depth, p. 107.

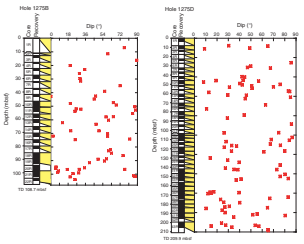

F63. Brittle deformation and alteration vein intensities, Hole 1275D, p. 108.

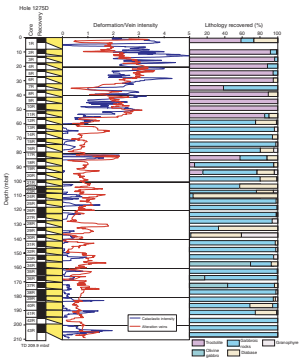

F64. Alteration veins and crosscutting relationships in troctolites, p. 109.

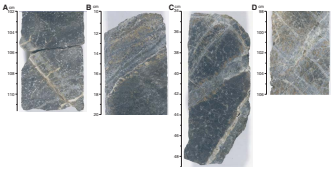

of which are deformed, indicating that these veins were pre- and syndeformational (e.g., interval 209-1275B-1R-2, 20–26 cm).

The intensity and orientation of veins were measured using the intensity scale outlined in "Structural Geology," p. 9, in the "Explanatory Notes" chapter. The intensity of these veins is a measure of their average frequency in a 10-cm piece of core. The variation in total intensity of alteration veining with depth for Holes 1275B and 1275D is shown in Figures F61 and F63. Metamorphic vein intensity is generally low in the gabbros and diabases (vein intensity = ~1) but higher in the troctolites (vein intensity = 2–3). Hole 1275D has a higher intensity of veining in the troctolites than Hole 1275B. This is consistent with the higher degree of alteration in Hole 1275D compared to Hole 1275B, as discussed in "Metamorphic Petrology," p. 10. The correlation of increased cataclastic deformation in the uppermost 55 m of Hole 1275D with increased metamorphic veining and alteration suggests a causal relationship. The high-frequency variation in the lower parts of the holes, shown by the alteration vein intensity curves (Figs. F61, F63), is a function of lithologic variation and grain size. For example, diabases and finer-grained gabbros are less veined than coarser-grained gabbros.

Figure F66 shows that there is no systematic variation in dip with either depth or vein type for both Holes 1275B and 1275D. This figure illustrates the correlation of vein types with lithology and, hence, with depth. Serpentine veins are only found in the troctolite units. Carbonate-clay veins are also predominant in the troctolites. Conversely, amphibole veins are largely absent from the troctolite units, except where they are associated with the magmatic veins cutting the troctolites. The veins in all the lithologies are undeformed except in cataclasites. They are interpreted to be a consequence of brittle fracturing as a result of cooling and unroofing of the footwall of a detachment fault and are thus interpreted to be syndeformational.

Magmatic Fabrics

The gabbros from Holes 1275B and 1275D have a distinctive magmatic layering/foliation defined by variations in plagioclase and pyroxene crystal size and their shape-preferred orientation. The boundaries between the layers can be sharp or diffuse, vary from planar to irregular, and define layers that are between 10 and 30 cm thick. Figures F67 and F68 show poles to the layer boundaries measured in Holes 1275B and 1275D. The measurements are corrected to a common orientation using paleomagnetic azimuth measurements (as described in "Structures in Peridotite and Gabbroic Intrusions," p. 8, in "Mantle Upwelling, Melt Transport, and Igneous Crustal Accretion" in the "Leg 209 Summary" chapter). The dip of these layers is similar in both holes and varies from 0° to 50°, with a mean dip of 17°–22°. Figures F67 and F68 also show the orientations of granophyric veins/segregations. Their dips range from horizontal to vertical; however, they do define a girdle that trends approximately northeast–southwest in the reference frame we used to orient the data. In both holes, there is a population of granophyric veins that have orientations approximately perpendicular to the mean orientation of the magmatic layering. The orientation of fourteen diabase/gabbro contacts is also shown in these figures. Eleven are subhorizontal and only three are steep, suggesting that the recovered diabase might be sills rather than dikes, unless there has been considerable tectonic rotation. Figure F68 also shows that the magmatic veins in the troctolite are randomly oriented.

F65. Alteration veins and crosscutting relationships in gabbros, p. 110.

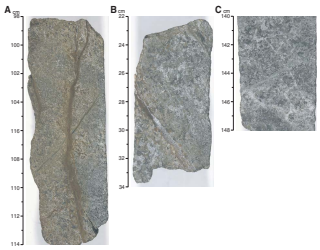

F66. Dips of different vein types, p. 111.

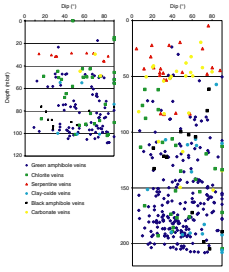

F67. Foliation, granophyric vein, and diabase contact orientations, p. 112.

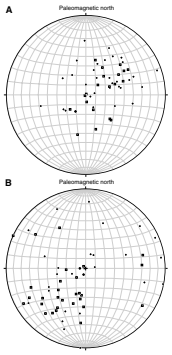

F68. Poles to magmatic foliations and granophyric and magmatic veins, p. 113.

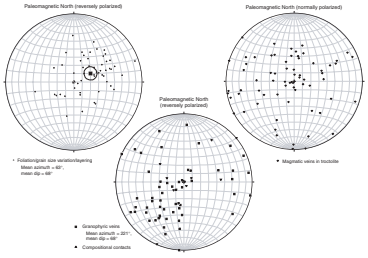

Discussion

The first deformation event took place under hypersolidus to possibly high-temperature subsolidus conditions and produced a weak crystal-plastic deformation. Samples in which limited polygonal neoblasts and porphyroclasts show very minor internal stain and complete recovery probably underwent hypersolidus deformation. Plagioclase grains that show moderate internal strain textures including undulose extinction, deformation twins, and subgrain boundaries were likely deformed at temperatures near the solidus. Lack of significant grain size reduction by dynamic recrystallization in all samples suggests that only a small degree of shear strain was accommodated by crystal-plastic flow.

Samples from the upper portions of both holes are highly deformed by brittle and semibrittle processes. Formation of amphibole and plagioclase matrix cataclasites began at the end of crystal-plastic deformation and continued during down-temperature deformation into upper greenschist facies conditions. The last deformation event formed greenschist-grade talc-chlorite-amphibole schists found in both holes. This extremely localized deformation occurred together with alteration and veining.

Site 1275 was drilled on the surface of a large domal massif core complex or "megamullion" that has been hypothesized to have formed by low-angle normal faulting (Escartin and Cannat, 1999; Fujiwara et al., 2003; McLeod et al., 2002; Escartin et al., 2003). In this hypothesis, the upper surface of the massif is an exposed normal fault. Brittle deformation localized in the upper portion of Holes 1275B and 1275D would therefore represent the thickness of a detachment fault system at this site. If this is the case, strain began to localize on the fault at lower amphibolite or upper greenschist facies conditions over a thickness of 30–50 m.

GEOCHEMISTRY

We performed chemical analyses on 8 troctolites, 5 diabases, and 20 gabbros from Site 1275 selected by the shipboard scientific party, using inductively coupled plasma–atomic emission spectrometry (ICP-AES) for determining major and trace element concentrations and gas chromatography for H_2O, CO_2, and sulfur. These 33 samples are representative of the rocks recovered from Holes 1275B and 1275D (see **"Igneous and Mantle Petrology,"** p. 3, and **"Metamorphic Petrology,"** p. 10, for the characterization of the lithologic units).

We sampled 4 diabases and 14 gabbros (see **"Igneous and Mantle Petrology,"** p. 3) from Units I and III in Hole 1275B. We also sampled 3 troctolites from Unit II. From Hole 1275D, we sampled 4 troctolites and 1 gabbro from Unit I, 3 gabbros from Unit II, 1 troctolite and 1 gabbro from Unit III, and 1 diabase and 1 granophyre from Unit IV. The lower part of Hole 1275D was not sampled because of time constraints for sample preparation and analyses. The results for the major and trace elements, for both ultramafic and mafic rocks, are reported on a volatile-free basis in Table **T4.**

T4. Major and trace element composition, p. 158.

Troctolites

Bulk rock analyses of troctolites from Site 1275 show that the composition of all of these rocks was modified to different extents by alter-

ation, leading to the addition of variable amounts of volatile constituents. Site 1275 troctolites are characterized by high loss on ignition (LOI) values (9.7–15.9 wt%) and high H_2O concentrations (6.8–12.5 wt%). These high LOI values and H_2O concentrations are consistent with the visual core descriptions and X-ray diffraction results (see **"Metamorphic Petrology,"** p. 10), which show that Site 1275 troctolites are altered predominantly to serpentine, a mineral that has a high water content (Fig. **F69**). We note that the highest LOI values (>12 wt%) are found in samples characterized by high CO_2 concentrations (1.1–9 wt%). In Site 1275 troctolites, variations in CO_2 are correlated with variations in CaO (Fig. **F70**). Hence, Sample 209-1275D-6R-1, 89–91 cm, displays the highest CO_2 content (9 wt%) and the highest CaO content (13.30 wt%) among the troctolites. This is consistent with core and thin section descriptions and XRD results that indicate variable but generally high proportions of calcite veins in these samples (see **"Metamorphic Petrology,"** p. 10). The two other samples with CO_2 of ~3 wt% (Samples 209-1275B-6R-1, 61–64 cm, and 209-1275D-10R-2, 104–106 cm) also contain trace amounts of calcite (see XRD results in **"Metamorphic Petrology,"** p. 10; Table **T2**). It is notable that the high CaO contents in these samples are consistent with high Al_2O_3 and with the high modal proportion of plagioclase in the troctolites. Thus, addition of CO_2 to the troctolites was probably not accompanied by metasomatic enrichment in CaO. In this way, carbonate metasomatism of Site 1275 troctolites probably differed from $CaCO_3$ addition inferred for many peridotites at other sites.

Site 1275 troctolites are characterized major element oxides SiO_2 (40.4–45.1 wt%), Fe_2O_3 (9.3–12.5 wt%), Al_2O_3 (1.3–5.1 wt%), TiO_2 (<1 wt%), and MgO (31.2–40.7 wt%) (Fig. **F69**). Site 1275 troctolites have Mg# (molar Mg/[Mg + Fe]) of 87%–89%. These values are high compared to those of cumulate rocks observed previously during Leg 209 (Fig. **F71**). Although they are lower in Mg# than average Leg 209 harzburgites (90%–92%), they are similar to Mg#s in dunite and peridotite with gabbroic impregnation from Site 1271 (85%–89%). However, compared to Site 1271 peridotites, Site 1275 troctolites have a lower MgO content, similar to fertile lherzolite values. They also have FeO contents that are higher than those commonly observed in mantle peridotites (Fig. **F71**). Such compositions may indicate that the Site 1275 troctolites are cumulate rocks. However, they also could have formed as a product of reaction between peridotite and a basaltic melt, as proposed for Site 1271 dunites.

Site 1275 troctolites contain high concentrations of compatible trace elements such as Cr (3390–4440 ppm) and Ni (1596–2048 ppm) and low concentrations of incompatible trace elements such as V (<70 ppm), Y (<6 ppm), Zr (<21 ppm), and Sc (<12 ppm) compared to Site 1275 gabbros. The troctolites have higher incompatible elements than most other Leg 209 peridotites (Figs. **F72, F73**), with the exception of the impregnated peridotite from Site 1271. The high Ni concentrations of the troctolites are consistent with their high olivine content, Ni being preferentially partitioned into olivine. The V and Sc concentrations in some of the troctolites can be attributed to the minor amounts of clinopyroxene. Troctolites show 1%–2% spinel in thin sections (see **"Igneous and Mantle Petrology,"** p. 3, and **"Metamorphic Petrology,"** p. 10), which likely accounts for their high Cr concentrations. For additional discussion of troctolite compositions, please see Figure **F54,** p. 133, and accompanying text in the "Leg 209 Summary" chapter.

F69. H_2O, Al_2O_3 and Mg# vs. SiO_2, p. 114.

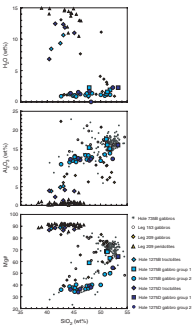

F70. CO_2 vs. CaO, p. 115.

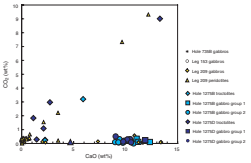

F71. FeO vs. MgO for troctolites, p. 116.

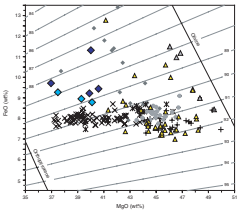

F72. Ni and Cr vs. Mg#, p. 117.

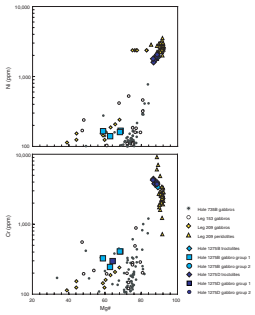

F73. TiO_2, Zr, Cr, and V vs. Al_2O_3, p. 118.

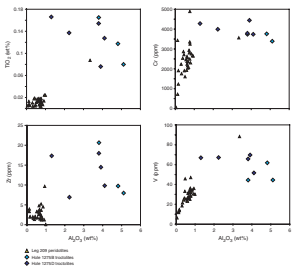

Gabbroic Rocks

We analyzed 18 gabbroic rocks from Hole 1275B and 8 from Hole 1275D. The selected samples include diabase, gabbro, gabbronorite, oxide gabbro, and granophyre. The samples can be divided into two textural groups (diabase/microgabbro and gabbro) based on the visual core and thin section descriptions (see "Igneous and Mantle Petrology," p. 3, "Metamorphic Petrology," p. 10, "Site 1275 Visual Core Descriptions," and "Site 1275 Thin Sections"). This division also groups the rocks in terms of their major and trace element chemistry, defining two groups of gabbroic rocks at Site 1275 with little or no overlap in the concentration of elements such as Mg, Ti, Al, Fe, Sc, V, Cr, and Ni. These chemical groups are found throughout Holes 1275B and 1275D with no apparent systematic spatial distribution.

The Site 1275 gabbroic rocks are similar to the diabase and gabbroic rocks from Sites 1270 and 1272, but they range to slightly more evolved compositions, with higher Fe_2O_3 and lower MgO (Fig. F74). The fine-grained diabase/microgabbro at Site 1275 (Group 1) contain MgO (8.3–9.5 wt%), TiO_2 (0.8–1.3 wt%), Al_2O_3 (15.0–17.6 wt%), and Fe_2O_3 (7.9–12.8 wt%). In contrast, the coarse-grained gabbroic rocks (Group 2) contain MgO (4.7–6.9 wt%), TiO_2 (2.0–8.9 wt%), Al_2O_3 (10.9–13.8 wt%), and Fe_2O_3 (11.2–22.0 wt%) (Fig. F74). The single granophyre analyzed (Sample 209-1275D-31R-2, 69–71 cm) clearly stands out in comparison to the gabbroic groups, having lower MgO (3.2 wt%) and TiO_2 (0.6 wt%) and much higher SiO_2 (69.5 wt%). In Group 2 there are two samples that were initially considered to be an intermediate group on the basis of their texture (Samples 209-1275B-3R-1, 103–107 cm, and 20R-2, 105–107 cm). These two samples are finer grained than the rest of the Group 2 rocks and also have the lowest TiO_2 and Fe_2O_3 and highest Al_2O_3. However, we include them in Group 2 because their concentrations for the other elements are similar to the Group 2 rocks. Nevertheless, their intermediate concentrations of Ti, Fe, and Al, along with their intermediate texture, suggest that grain size may be useful proxy for composition in Site 1275 gabbroic rocks.

The correlation between Fe_2O_3 and TiO_2 (Fig. F75) suggests that their concentrations are governed by the oxide abundance, with Group 1 having only a minor oxide content and therefore low concentrations of Fe_2O_3 and TiO_2. Overall, TiO_2 increases with increasing Fe_2O_3 in the gabbroic rocks from Site 1275. However, with the exception of the most iron-enriched sample (Sample 209-1275B-21R-1, 90–92 cm; Fe_2O_3 = 21.2 wt%) and the intermediate samples, the coarser-grained Group 2 rocks (those with TiO_2 > 4 wt%) show a trend of decreasing TiO_2 with increasing Fe_2O_3 (Fig. F75).

All the gabbroic rocks from Site 1275 have relatively low CO_2 (0.05–0.50 wt%) (Fig. F70; Table T4). The Group 1 rocks have slightly higher H_2O (1.3–2.3 wt%) compared to the Group 2 rocks (0.85–1.7 wt%) except for Sample 209-1275D-1R-1, 113–115 cm, which contains 2.3 wt% H_2O. Site 1275 gabbroic rocks typically contain 10%–40% secondary amphibole (see "Site 1275 Thin Sections"). Overall, there appears to be no systematic relationship between volatile species and other elements in gabbroic rocks from Site 1275.

The compatible trace elements of the gabbroic rocks show the same groupings defined by the major elements. Most Group 1 rocks have Ni and Cr concentrations of ≤170 ppm and 240–410 ppm, respectively. In contrast, most of the Group 2 rocks have Ni and Cr below the detection

F74. Fe_2O_3 and Al_2O_3 vs. MgO for gabbros, p. 119.

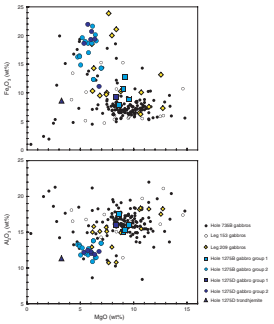

F75. Fe_2O_3 vs. TiO_2 in gabbros, p. 120.

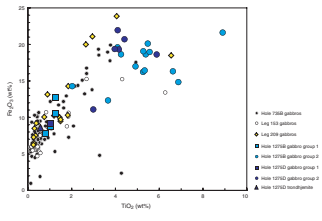

limit (Ni < 165 ppm and Cr < 41 ppm) (Table T4; Fig. F72). The moderately incompatible elements V and Sc show more complex relationships in the gabbroic rocks from Site 1275 related to the proportion of oxides and clinopyroxene. Collectively, the gabbroic rocks from Site 1275 show an increase in V content with increasing TiO_2, although there is considerable scatter (Fig. F76). In the coarsest-grained Group 2 gabbroic rocks (those having TiO_2 > 4 wt%), there is a rough negative correlation between Fe_2O_3 and V with TiO_2 (Figs. F75, F76). The Group 2 gabbroic rocks from Site 1275 have higher Ti/V ratios (20–80) compared to Group 1 rocks (25–35). Collectively, the oxide gabbros recovered from Hole 1270B plus the coarse-grained gabbroic rocks from Site 1275 delineate a broad anticorrelation between V and Ti. This anticorrelation leads to an increase in Ti/V ratio from ~10 to ~80 as TiO_2 increases from ~2.5 to ~7.0 wt% in these rock suites (Fig. F76).

Sc shows a good anticorrelation with Al_2O_3 in the Site 1275 gabbroic rocks (Fig. F77). There is no overlap in Sc and Al_2O_3 contents in Group 1 and Group 2 gabbroic rocks from Site 1275, and Sc and Al_2O_3 form a similar negative trend within each of these groups. Sc also shows a rough positive covariation with TiO_2 (Fig. F78). In the Group 1 gabbroic rocks, Sc and Ti are positively correlated, varying between 32 and 38 ppm (variation = 20%), whereas TiO_2 varies between 0.8 and 1.3 wt% (variation = 60%). The narrow range and lower concentration of Sc in the Group 1 gabbros from Site 1275 also overlaps with the Sc concentrations measured for microbgabbro and diabase from Sites 1270 and 1272 (Fig. F78). In the Group 2 gabbros, Sc shows a restricted range of variation (44–65 ppm), whereas TiO_2 shows a wide range of concentrations (2–9 wt%). There also appears to be an upper limit of ~65–70 ppm for Sc concentration that is common to both the Group 2 gabbroic rocks from Site 1275 and the oxide gabbros from Hole 1270B.

Group 1 and 2 gabbroic rocks from Site 1275 overlap in their Ba, Sr, Zr, and Y contents (Ba = 20–60 ppm and Sr = 125–200 ppm). There is a covariation of Zr with Y, but with considerable scatter, and the Site 1275 gabbroic rocks form a wedge-shaped field on a diagram of Zr vs. Y (Fig. F79). The range of Zr and Y concentrations are 30–105 ppm and 15–85 ppm, respectively. Except for the covariation of Zr with Y, the Site 1275 gabbroic rocks do not show obvious systematic trends or groupings of Ba, Sr, Zr, and Y. We note that the granophyre, Sample 209-1275D-39-R-2, 69–71 cm, has an extremely high Zr concentration of ~1400 ppm.

Discussion

Four types of rocks were distinguished at Site 1275 on the basis of petrographic and textural observations (see **"Igneous and Mantle Petrology,"** p. 3) and chemical composition: troctolites, two groups of gabbroic rocks, and granophyre. All groups are found in both Holes 1275B and 1275D.

The troctolites have high Mg# (87%–89%) and their composition plots close to that of peridotites, although they are slightly MgO depleted and FeO enriched in comparison. They may be cumulates or products of melt/rock reaction in the mantle. The chemical compositions of Group 1 gabbroic rocks are similar to ocean ridge basalts. In contrast, Group 2 gabbroic rock compositions from Site 1275 do not resemble liquid compositions. Their major and trace element composi-

F76. V vs. TiO_2 in gabbros, p. 121.

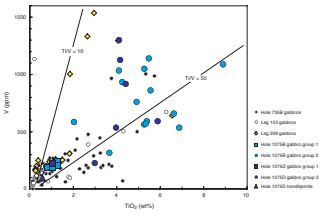

F77. Sc vs. Al_2O_3 in gabbros, p. 122.

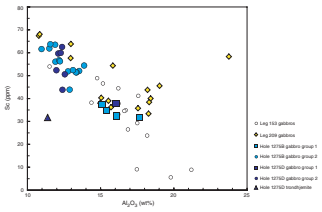

F78. Sc vs. TiO_2 in gabbros, p. 123.

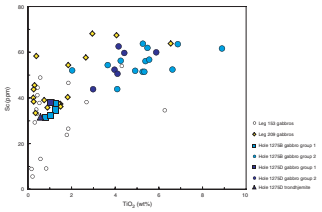

F79. Zr vs. Y in gabbros, p. 124.

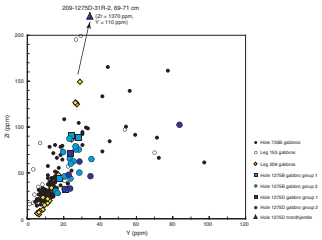

tions dominantly reflect their varying proportions of plagioclase, clinopyroxene, and oxides (magnetite and ilmenite).

Compatible elements such as Ni and Cr define the three mafic groups of Site 1275 rocks quite well. The olivine-rich troctolites are characterized by very high Ni and Cr contents. The Group 1 gabbroic rocks appear to have higher Ni contents than Group 2, although Ni was just above the detection limit when it was measurable in any of the gabbros. Cr contents in Group 1 gabbroic rocks range 250–410 ppm, whereas in Group 2 they are below the detection limit.

Oxide abundance controls much of the chemical systematics in the Site 1275 gabbroic rocks, evidenced by the broad overall covariations of Fe_2O_3 and V with TiO_2 (Figs. **F75, F76**). The Group 1 gabbroic rocks contain only a minor oxide component, and within this group both Fe and V increase with increasing TiO_2. The Group 2 gabbroic rocks show a more complicated behavior related to the presence of Ti-bearing phases. The Group 2 rocks contain some ilmenite ($FeTiO_3$) based on the XRD analyses (see **"Metamorphic Petrology,"** p. 10). A few percent titanite ($CaTiSiO_5$) also replaces the oxide phases in some thin sections (e.g., in Sample 209-1275D-13R2, 49–51 cm, analyzed here) [**N1**].

Correlated increases in Fe_2O_3 and TiO_2 in cumulate rocks result from varying proportions of ilmenite and magnetite. At Site 1275, estimates of magnetite abundance based on the magnetic susceptibility measurements underestimate the amount of oxide observed in these rocks, consistent with the presence of a significant proportion of ilmenite in the more Ti-enriched rocks. The observation that most of the Group 2 gabbros lie along a Fe/Ti trend having a slope of approximately –1 on the Fe_2O_3–TiO_2 diagram (Fig. **F75**) may be accounted for by an increasing proportion of ilmenite (and/or titanite) at higher TiO_2 in these rocks.

The Ti/V ratio in Group 2 gabbros at Site 1275 shows a large range (10–80), in comparison, the Group 1 gabbroic rocks (25–35), somewhat higher than but close to values typically measured in mid-ocean-ridge basalt (MORB) (Shervais, 1982). As briefly discussed previously (see **"Geochemistry,"** p. 34, in the "Site 1270" chapter), the igneous behavior of V depends upon its oxidation state (+3, +4, or +5), which affects its partitioning during fractional crystallization. The crystal/liquid distribution coefficient (bulk *D*) for V in ocean-ridge-basaltic systems is usually greater than the bulk *D* for Ti, so extensive silicate fractionation can drive magma to higher Ti/V ratios (Shervais, 1982). Once magnetite becomes a crystallizing phase, Ti and V concentrations will begin to decrease rapidly and there may be a dramatic increase in Ti/V ratio because V is highly compatible in magnetite (K_D for magnetite in MORB systems ranges between ~5 and 70, depending on oxygen fugacity) (Shervais, 1982). The high Ti/V ratios at higher TiO_2 in the Site 1275 gabbroic rocks (Fig. **F76**) are consistent with a history of crystal fractionation that includes magnetite. The trend of decreasing V with increasing TiO_2 in Group 2 gabbroic rocks from Site 1275 may also be accounted for by an increasing proportion of ilmenite at higher TiO_2 in these rocks.

The Sc budget in the Site 1275 gabbroic rocks is primarily controlled by the abundance of clinopyroxene. Sc is negatively correlated with Al_2O_3 in both the Group 1 and Group 2 gabbroic rocks from Site 1275 (Fig. **F77**). The Al_2O_3 budget of the Site 1275 gabbroic rocks is primarily related to the modal abundance of plagioclase. The negative correlation between Sc and Al_2O_3 is therefore an indicator of changes in the clinopyroxene/plagioclase ratio of these rocks. When the plagioclase/pyrox-

N1. Titanite can also be abundant (~15%), along with other accessory phases such as zircon, in some of the crosscutting dikes (e.g., see **"Site 1275 Thin Sections"** [Sample 209-1275D-1R-1, 60–62 cm]).

ene ratio is low, the bulk rock Sc content is higher and the Al_2O_3 content is lower. Together with the positive Sc–Ti covariation (Fig. F78), these relations are consistent with a simple mass balance involving corresponding increases in the proportion of clinopyroxene plus oxides as plagioclase proportion decreases. The apparent maximum Sc content of ~70 ppm in the Site 1275 gabbroic rocks corresponds to a ~45% modal abundance of clinopyroxene.

The elements Ba, Sr, Zr, and Y do not appear to correlate well with other geochemical indicators in the Site 1275 gabbroic rocks. There is a Zr–Y correlation, but it shows significant scatter (Fig. F79). The scattered diverging trends indicate that there are (at least) two controls on the Zr + Y concentrations. One control may simply be a ~1:1 enrichment in each of these incompatible elements due to increasing concentration of both elements in melts undergoing fractional crystallization. Samples lying along the lower edge of the Zr–Y trend have ~1:1 variation in Zr/Y. The gabbroic rocks lying along the upper edge of the scattered trend are enriched in Zr relative to Y. This suggests that either Zr behaves more incompatibly than Y during late-stage evolution of these rocks or that some trace amount of zircon may control the Zr concentration in some samples. Zircon is present as a trace constituent in some of the Group 2 gabbroic rocks (see "Site 1275 Thin Sections"). It is also notable that the granophyre from Hole 1275D has an extremely high Zr content of 1400 ppm, and high Zr contents were observed in many plutonic rocks during Leg 153 (Agar et al., 1997), indicating that rocks with such enriched compositions are indeed present in the oceanic crust.

The incompatible trace element concentrations measured in the Site 1275 gabbros indicate that small amounts of evolved magma, highly enriched in some trace elements, could be present within the crust along the Mid-Atlantic Ridge near 15°20′N (see similar discussion based on the Site 1270 oxide gabbros in "Geochemistry," p. 34, in the "Site 1270" chapter). For example, taking bulk rock Y and Zr contents of 20 and 50 ppm, respectively (averages for the Site 1275 gabbroic rocks), assuming all the Y and Zr in the rock resides in clinopyroxene with a modal abundance of 40% and assuming appropriate K_D values for clinopyroxene (Y = 0.47 and Zr = 0.12) (Hart and Dunn, 1993), the equilibrium liquid contains Y = 106 ppm and Zr = 1040 ppm. These concentrations are similar to those measured in the granophyre from Hole 1275D and are much higher than Y and Zr concentrations observed for MORB magmas that have average values of 24 and 78 ppm, respectively (Sun and McDonough, 1989). For additional discussion of highly evolved plutonic rocks sampled along the mid-ocean ridges, see Figure F58, p. 137, and accompanying text in the "Leg 209 Summary" chapter.

PHYSICAL PROPERTIES

The physical properties of the gabbros, troctolites, and diabases cored in Holes 1275B and 1275D were characterized through a series of measurements on whole-core sections, split-core pieces, and discrete samples as described in "Physical Properties," p. 18, in the "Explanatory Notes" chapter. We measured natural gamma ray (NGR) activity and magnetic susceptibility on the multisensor track (MST) system and thermal conductivity, compressional wave velocity, density, and porosity. The rock names reported in data tables correspond to the primary lithologies assigned by the igneous group. The data are summarized as a function of depth in Figures F80 and F81.

F80. Physical properties, Hole 1275B, p. 125.

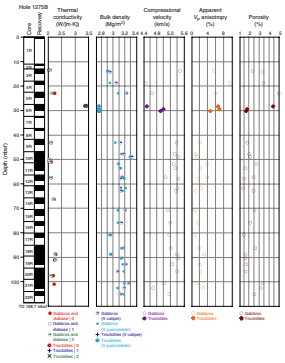

F81. Physical properties, Hole 1275D, p. 126.

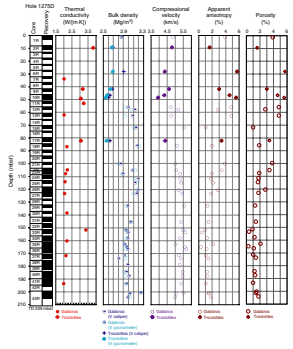

Natural Gamma Radiation

All cores recovered during Leg 209 were measured using the NGR logger on the MST at intervals of 10 cm for a period of 30 s. Results are output in counts per second. The cores from Hole 1275B do not show natural radioactivity significantly higher than background (mean = 2.02 cps); the two highest peaks (~10 cps) (Fig. F82) correspond to gabbro pieces that, macroscopically, do not differ significantly from the surrounding rocks. NGR values for cores from Hole 1275D are in the same range as those in Hole 1275B (mean = 2.07 cps) and counts in the range 8–16 cps from six veined gabbros and troctolites (Fig. F82).

Magnetic Susceptibility

Magnetic susceptibility values were acquired on the MST at 2.5-cm intervals for all recovered cores. The variation of magnetic susceptibility with depth in Holes 1275B and 1275D is shown in Figure F83. Magnetic susceptibility is comparatively low at the top of Hole 1275B and increases gradually to ~0.05 SI in Section 209-1275B-6R-1 (~28.5 mbsf). From that depth, magnetic susceptibility then remains high (0.01–0.1 SI) from 28.5 mbsf to the bottom of the hole. These high magnetic susceptibility values reflect the high oxide content of the gabbros. The gabbros from the upper part of Hole 1275B display lower magnetic susceptibility than those recovered from Hole 735B during Leg 176 (Dick, Natland, Miller, et al., 1999) and Leg 179 (Pettigrew, Casey, Miller, et al., 1999) (Fig. F84). The oxide-rich gabbros of the lower part of Holes 1275B and 1275D are similar to the oxide-rich gabbros from Hole 735B (Dick, Natland, Miller, et al., 1999; Pettigrew, Casey, Miller, et al., 1999), with magnetic susceptibility ranging 0.01–0.1 SI (Fig. F83) (Natland, 2002) or higher, as shown by the discrete sample measurements (see "Paleomagnetism," p. 31). On the Bartington MS2C sensor, all readings >0.1 SI are clipped such that higher values are recorded without the first digit. Thus, the highest magnetic susceptibilities of oxide-rich gabbros recorded are ~0.1 SI. The magnetic susceptibilities of oxide-rich gabbros in Holes 1275B and 1275D are similar to those of the oxide-rich gabbros recovered from Hole 1270B (Fig. F105, p. 159, in the "Site 1270" chapter).

Thermal Conductivity

Thermal conductivities were measured in gabbro, troctolite, and diabase samples taken at irregularly spaced intervals along Holes 1275B and 1275D. The data are summarized in Table T5. The thermal conductivities of the gabbro and diabase samples range 1.97–3.35 W/(m·K) (mean = 2.15 W/[m·K]). These values are similar to those measured at previous Leg 209 sites. The thermal conductivities of the troctolite samples from Holes 1275B and 1275D range 3.06–3.83 W/(m·K) (mean = 3.32 W/[m·K]). All of the thermal conductivity values measured during Leg 209 are shown in Figure F85 and are compared to samples from ODP sites at Atlantis Bank (Robinson, Von Herzen, et al., 1989; Dick, Natland, Miller, et al., 1999), Hess Deep (Gillis, Mével, Allan, et al., 1993), and the MARK area (Cannat, Karson, Miller, et al., 1995).

As described in "Thermal Conductivity," p. 19, in "Physical Properties" in the "Explanatory Notes" chapter, wherever possible, measurements were taken in three directions on the cut face of the archive half of the core. The purpose of these measurements was to determine the

F82. MST NGR, p. 127.

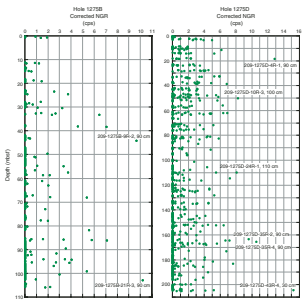

F83. MST magnetic susceptibility, p. 128.

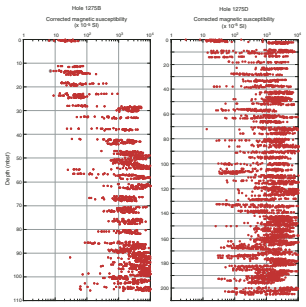

F84. MST magnetic susceptibility in gabbros, p. 129.

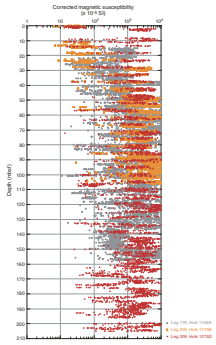

T5. Thermal conductivity, p. 160.

F85. Thermal conductivity, p. 130.

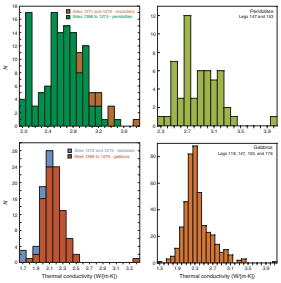

degree of apparent anisotropy. The apparent thermal conductivity anisotropy of the diabases, gabbros, and one troctolite sample measured in cores from Hole 1275B is not very strong (0.3%–5.8%) (Fig. F80; Table T5). (Anisotropy measurements were not made on samples from Hole 1275D, due to the lack of time at the end of the cruise.) Apparent thermal conductivity anisotropies measured during Leg 209 (including Sites 1268, 1270–1272, 1274, and 1275) are compiled in Figure F86. The apparent thermal conductivity anisotropy ranges 0.1%–12.6% (mean = 3.92%) in diabases, gabbros, troctolites, and peridotites.

Many of the core pieces in which we measured thermal conductivity were also sampled for measurements of porosity, density, velocity, and magnetic susceptibility. Mean values of thermal conductivity are plotted against bulk densities in Figure F87 for Leg 209 sites 1268, 1270–1272, 1274, and 1275, together with reference single crystal and monomineralic rock data (Clark, 1966; Clauser and Huenges, 1995). As expected from their high degree of alteration, the conductivities of the Leg 209 peridotites and troctolites are close to those of serpentine and talc. Thermal conductivities in gabbro and diabase samples are similar to values reported for anorthite and anorthosite.

Porosity, Density, and Seismic Velocity

Bulk density, grain density, and porosity were measured on small sample chips (~3–6 cm³) from Holes 1275B and 1275D. *P*-wave velocity and wet bulk density were measured in cube samples, as described in "*P*-Wave Velocity," p. 20, and "Porosity and Density," p. 20, in "Physical Properties" in the "Explanatory Notes" chapter. These data are summarized in Table T6.

The variations of *P*-wave velocity, seismic anisotropy, bulk density, and porosity in gabbros and troctolites with depth in Holes 1275B and 1275D are shown in Figures F80 and F81. Through Core 209-1275B-6R (~30 mbsf), the physical properties of these rocks are variable. The bulk densities and porosities of the three troctolite samples are lower than those of the gabbros from higher in the hole. Apparent compressional wave velocity anisotropy in the upper part of Hole 1275B is in the range 4%–10%. Below Core 209-1275B-6R, the properties of the gabbros are less variable. Bulk densities are generally in the range 3.1–3.2 Mg/m³, porosities are commonly 1.5%–2.5%, velocities are mostly 4.7–5.4 km/s (mean = 5.2 km/s), and the apparent seismic anisotropy is generally <2.5% (mean = ~2%).

P-wave velocities in troctolite samples from Cores 209-1275D-2R to 10R (10–50 mbsf) from Hole 1275D (Fig. F81) are <4.8 km/s, and the velocity anisotropy is <5%. Densities of these samples are in the range 2.6–2.9 Mg/m³, and porosities range as high as 5%. The transition between the troctolite in Core 209-1275D-10R (47 mbsf) and the gabbros in Core 12R (56 mbsf) is an abrupt increase in bulk density from <2.6 to ~2.9 Mg/m³ and a modest increase in *P*-wave velocity. From 55 mbsf to the bottom of the hole at 209 mbsf, *P*-wave velocities of gabbros remain in the range 5–5.5 km/s (mean = ~5.3 km/s) and the degree of anisotropy is low, generally <2%. Bulk densities reach a maximum of 3.0–3.1 Mg/m³ between 110 and 120 mbsf then decrease to 2.9–3.0 Mg/m³ between 130 and 209 mbsf. Porosities in the lower part of the hole range from near 0% to 2.5% (mean = 1.6%).

The density and velocity data for the gabbros and troctolites recovered from Holes 1275B and 1275D are compared with data from Legs 147 and 153, as well as Leg 209 Sites 1268, 1270–1272, and 1274 (see

F86. Thermal conductivity anisotropy, p. 131.

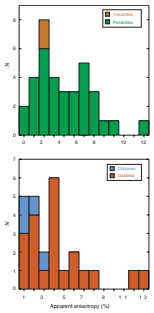

F87. Thermal conductivity vs. bulk density, p. 132.

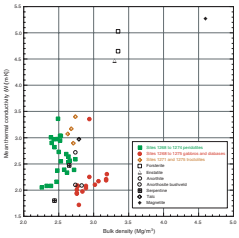

T6. Porosity, density, and velocity, p. 161.

"Physical Properties" sections in the Sites 1268, 1270–1272, and 1274 chapters) in Figure F88. The troctolites have velocities and densities comparable to those of samples from Sites 1268 through 1274 but lower than the densities of gabbroic rocks from Leg 153 Site 923 (Cannat, Karson, Miller, et al., 1995). A few of the gabbros recovered from Holes 1275B and 1275D have densities and velocities comparable to the lowest values reported from Hole 923A, but most have lower velocities and higher densities (>3 Mg/m^3). These properties reflect the relatively high oxide contents of the gabbros from Holes 1275B and 1275D.

F88. *P*-wave velocity vs. wet bulk density, p. 133.

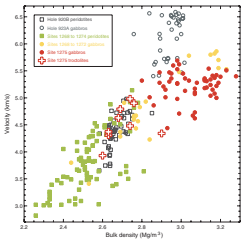

Magnetic Susceptibility and Density

As suggested by Toft et al. (1990), the magnetic susceptibility of serpentinized peridotites should be inversely correlated with their density because of the increasing contents of magnetite and Fe-bearing brucite and serpentinite during multireaction serpentinization. If so, petrophysical data can potentially be used as a proxy for alteration of abyssal peridotites. This working hypothesis can be tested using magnetic susceptibility and density measurements made on cube and minicore samples taken during Leg 209. The results are shown in Figure F89 and compared to data from the Josephine ophiolite (Toft et al., 1990), the Oman ophiolite (B. Ildefonse, unpubl. data), Site 895 (Gillis, Mével, Allan, et al., 1993), and Site 920 (Cannat, Karson, Miller, et al., 1995). Exponential regression lines are plotted through data from each hole (1268A, 1270A, 1270C, and 1270D), except for those holes for which the data points are too scattered. Regression lines fit to the samples from Holes 1271A and 1271B have slopes similar to those fit to data from the Josephine ophiolite and Site 920 (from the MARK area) and close to the fit to samples from the Oman ophiolite. The regression lines for Holes 1272A and 1274A have steeper slopes, similar to the fit to data from Site 895 (Hess Deep). These two families of trends may point to two different types of serpentinization processes.

F89. Magnetic susceptibility vs. density, peridotites and gabbros, p. 134.

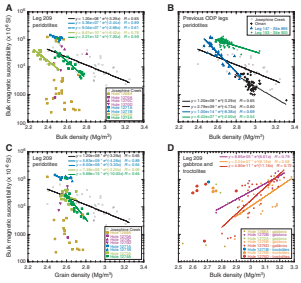

The positions of sample points in Figure F89A and F89B also depend on the porosity of the peridotites as we plot the bulk densities. This problem can be avoided by plotting the magnetic susceptibilities against grain densities (Fig. F89C). The Hole 1272A samples, which are the most altered peridotites recovered during Leg 209, plot close to the Hole 1274A samples. However, the data from Hole 1272A are more scattered in this plot and do not show a good correlation between magnetic susceptibility and density. Although we do not have a clear explanation for this phenomenon, it may be due to a larger imprecision in grain density estimates in these very highly altered peridotites, possibly related to the problems experienced in measuring the volumes of highly serpentinized peridotites in the helium pycnometer (see "Physical Properties," p. 37, in the "Site 1268" chapter).

The peridotite samples from Hole 1268A do not show any inverse correlation between magnetic susceptibility and density (Fig. F89A, F89B). This lack of correlation is probably due to the presence of distinct alteration products in the serpentinized peridotites of this core, with decreasing magnetite and increasing talc contents ("Metamorphic Petrology," p. 10, in the "Site 1268" chapter), leading to a decrease of magnetic susceptibility while the density is little affected. This type of vertical trend in a magnetic susceptibility vs. density diagram may be indicative of the unusual talc-rich alteration encountered in Hole 1268A.

Data for the gabbros sampled during Leg 209 are plotted in Figure F89D. The samples from Holes 1270B, 1275B, and 1275D show positive correlations between magnetic susceptibility and bulk density that probably reflect variable oxide content. Increasing oxide proportions result in increasing magnetic susceptibility and density of the gabbros.

PALEOMAGNETISM

A variety of gabbroic rocks (primarily oxide gabbro/gabbronorite and troctolite; see "Igneous and Mantle Petrology," p. 3) were recovered from Holes 1275B and 1275D. These two holes were drilled within ~100 m of each other, and both had relatively deep penetration (109 and 210 m, respectively) and good recovery. Thus, the site is particularly well suited for continuous measurements of archive halves. Pass-through measurements yielded stable remanence directions for >500 core pieces (~350 from Hole 1275D and ~200 from Hole 1275B). In addition, stable directions were determined from 60 discrete samples (Table T7). Both Holes 1275B and 1275D are characterized by shallow, dominantly negative inclinations (mean inclinations = –10° and –4°, respectively) that presumably represent a reversed polarity remanence. Some intervals in Hole 1275D, particularly from the top 50 m, have positive inclinations and therefore may be of normal polarity. The presence of both polarities is not entirely unexpected, given the location of the site near Anomaly 2 (Fujiwara et al., 2003). The average inclinations in both Holes 1275B and 1275D are significantly shallower than the value expected from a geocentric axial dipole (±28°), apparently requiring significant tectonic rotations since remanence acquisition.

T7. Discrete sample data, p. 162.

Continuous Measurements

Remanence measurements were made on all archive halves longer than ~7 cm. The archive halves were subjected to stepwise alternating-field (AF) demagnetization at 5- to 10-mT steps up to maximum peak fields of 70 mT. The characteristic remanent magnetization (ChRM) directions were calculated by principal component analysis (PCA) (Kirschvink, 1980) at about the midpoint of each piece or at 10-cm intervals for pieces >15 cm. Whole-core (or archive half for Hole 1275D) susceptibility data obtained from the MST (see "Magnetic Susceptibility," p. 28, in "Physical Properties") were filtered to preserve only data corresponding to the intervals where ChRM directions were determined. Thus, the resulting remanence and susceptibility data sets (Figs. F90, F91) are significantly less affected by artifacts resulting from small core pieces than are the original unfiltered data sets.

F90. Archive-half magnetic measurements, Hole 1275B, p. 135.

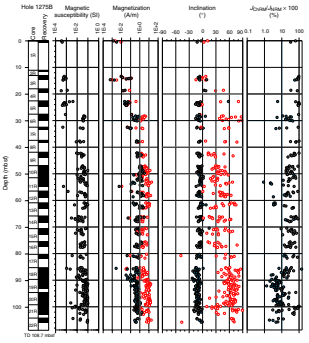

F91. Archive-half magnetic measurements, Hole 1275D, p. 136.

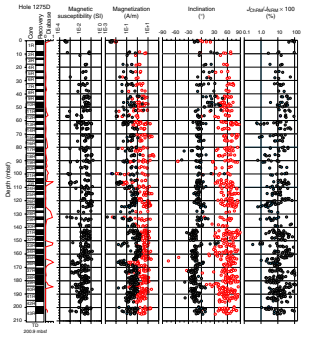

Hole 1275B

The most significant variations in the natural remanent magnetization (NRM) intensity and susceptibility for archive halves from Hole 1275B are well correlated with the lithology (Fig. F90). The diabase and oxide gabbro(norite) samples from lithologic Unit I (see "Igneous and Mantle Petrology," p. 3) are characterized by very low susceptibilities (~10^{-3} SI) and remanent intensities (1–100 mA/m). The lowest susceptibility values in this unit could be attributed almost entirely to a paramagnetic contribution (e.g., 10% FeO corresponds to a susceptibility of ~6×10^{-4} SI) and thus are apparently at odds with the visual estimates of

Fe-Ti oxides (1% to >5%) (see **"Igneous and Mantle Petrology,"** p. 3). Reflected-light observations indicate that the oxide minerals in the oxide gabbros are predominantly hemoilmenites with little or no magnetite (which has a much higher susceptibility of ~3 SI). The dominance of hemoilmenite can account for both the low susceptibility as well as the low NRM intensities and high magnetic stability of this unit (see below).

In contrast to lithologic Unit I, the troctolites and oxide gabbros of lithologic Units II and III are characterized by high susceptibilities (generally 0.01 to >0.1 SI) and NRM intensities (typically 1–10 A/m), indicative of much higher concentrations of magnetite. The maximum magnetic susceptibility and NRM intensity values were observed in Cores 209-1275B-19R to 20R. In this interval, magnetic susceptibility values exceeded the maximum value (0.1 SI) measurable with the MST susceptibility meter. The susceptibility of many individual archive-half pieces was subsequently measured to identify and correct these intervals of clipped data (see **"Igneous and Mantle Petrology,"** p. 3).

The differences in magnetic mineralogy between lithologic Unit I and the lower units is also reflected in the directions of the natural remanence. NRM inclinations for the more magnetite-rich lower units are scattered but include values ranging from +20° to +90°. In particular, Cores 209-1275B-19R to 20R have the most uniformly steep NRM inclinations (+50° to +80°) and this interval is also characterized by uniformly high susceptibility values. This association of steep initial inclinations and high susceptibility may be explained by the presence of coarse-grained magnetite that has low coercivity and thus is most susceptible to acquiring a drilling remanence. Much of the variability in NRM inclination in Units II and III may therefore be plausibly attributed to variations in the amount of such coarse-grained magnetite. The diabase and oxide gabbros from Unit I have shallow NRM inclinations that reflect the paucity of coarse magnetite.

Stepwise demagnetization of the archive halves reveals a variable contribution from a steep, presumably drilling-related, low-stability overprint (Fig. **F92**). This low-stability component is generally removed by AF demagnetization at 15–25 mT. The ChRM directions from Hole 1275B were typically calculated from the remanence remaining after demagnetization at 30–70 mT (Table **T8**). The ChRM directions were classified into two categories; samples showing a linear decay trend toward the origin (e.g., Fig. **F92D**) were labeled as Class A and are considered to be a reliable record of the stable remanence, and samples with a curving demagnetization trajectory (e.g., Fig. **F92F**) were identified as Class C and provide a less reliable record of the paleomagnetic inclination as a result of the significant overlap between the ChRM and the low-stability drilling overprint. Class C directions, however, can provide useful information for reorientation of structural features in the core because the vertical drilling overprint causes no significant variations in declination. Class A components represent on average 40% of the NRM, whereas Class C components represent approximately <10% of the NRM.

As with the remanent intensity and susceptibility, there is a distinct difference in magnetic stability (as measured by the class of the ChRM and the percentage of the NRM represented by the ChRM) between lithologic Unit I and Units II and III. Samples from Unit I have dominantly (90%) Class A remanence directions (Fig. **F92D**) and the ChRM represents a large fraction (average = 80%) of the NRM (Fig. **F90**). In contrast, the ChRM constitutes a smaller fraction (average = 25%) of the NRM for

F92. Vector endpoint diagrams, Hole 1275B, p. 137.

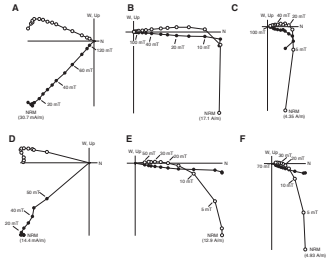

T8. Piece orientations, p. 164.

samples from Units II and III (Fig. F92E, F92F) and these units have a greater proportion of Class C directions.

Hole 1275D

The NRM intensity and susceptibility values of gabbroic rocks from Hole 1275D (Fig. F91) are comparable to those measured on samples from Hole 1275B. NRM intensities are typically 1.0–10 A/m, with maximum intensities as high as 35 A/m. This maximum value essentially corresponds to the highest number of flux counts that can be measured by the 2G magnetometer (10^5 counts). The high magnetic moment of the archive halves frequently resulted in residual counts even at the slowest track speeds (1 cm/s) available with the current version of the LongCore program. Susceptibility values were also high enough to cause clipping of the whole-core data measured by the MST. In order to provide an accurate measure of the susceptibility variations, the archive halves were scanned with the MST (see "Igneous and Mantle Petrology," p. 3). The smaller volume resulted in very few intervals that still exceeded the maximum measurable susceptibility (0.1 SI).

As with Hole 1275B, the downhole variations in NRM intensity and susceptibility for Hole 1275D generally reflect lithologic variations. The most notable lithologic control on magnetic properties is for intervals of diabase (Fig. F91). These finer-grained units are generally associated with lower susceptibilities (10^{-3} to 10^{-2} SI) and NRM intensities that are generally <1 A/m (e.g., near 108 and 167 mbsf). The troctolites of lithologic Unit I (0–52.99 mbsf) have somewhat lower NRM intensities than do units from lower in the section. However, the troctolites in Unit III (81.00–90.94 mbsf) are not obviously distinct from adjacent units in either their susceptibility or NRM intensity. Overall, the variations in the magnetic properties are less closely related to the lithologic units defined for Hole 1275D than was the case for Hole 1275B.

Most NRM inclinations for Hole 1275D are 30°–90° (mean = ~60°) (Fig. F91). The only exceptions are the shallow initial inclinations associated with some diabase units (e.g., the lower portion of Core 209-1275D-39R and the brecciated diabase in Core 1R). Stepwise AF demagnetization of the archive halves from Hole 1275D reveals the presence of a significant low-stability component with steep inclination that is presumably related to the drilling/coring process (Fig. F93). This low-stability drilling remanence is effectively removed by AF treatments of 15–25 mT. The NRM inclinations from Hole 1275D are, in general, steeper than those from Hole 1275B, reflecting the relatively larger contribution of a drilling remanence in cores from Hole 1275D.

ChRM directions were calculated from the archive-half demagnetization data following the same procedure as for Hole 1275B. Class A components could be calculated from nearly all intervals, even in samples with substantial drilling overprints and where the ChRM represents as little as 1% of the initial NRM (Table T8). The intensity of the ChRM varies significantly as a function of lithology. Gabbros yielded ChRM intensities that ranged ~0.1–1 A/m, or even higher (e.g., Cores 209-1275D-31R, 32R, and 34R). In contrast, diabases and microgabbros (e.g., Cores 209-1275D-23R, 29R, 33R, and 36R) have ChRM intensities as much as an order of magnitude lower than the coarser gabbroic rocks.

The stable inclinations from Hole 1275D may be subdivided into three groups (Fig. F91). The troctolite samples from lithologic Unit I have dominantly positive inclinations, although some isolated shallow negative inclinations (e.g., Core 209-1275D-1R) are also present. The

F93. Vector endpoint diagrams for gabbros, p. 138.

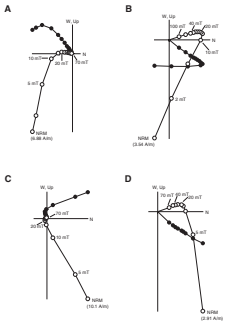

ChRM in this interval generally represents >10% of the initial NRM. Cores 209-1275D-11R to 30R (~50–140 mbsf) constitute a second inclination group. The inclinations in this interval are shallow and negative, with a mean of about –10° that is similar to the mean inclination obtained from Hole 1275B. An abrupt shift in inclination to values near –20° occurs between Cores 209-1275D-30R and 31R. The steeper inclinations below ~140 mbsf constitute a third inclination group. This inclination group broadly corresponds to lithologic Unit V (olivine gabbro and oxide gabbronorite; see **"Igneous and Mantle Petrology,"** p. 3). Within this lower inclination group, intervals of diabase and microgabbro are characterized by inclinations that are distinctly more positive than the surrounding gabbro.

Discrete Samples

Stepwise demagnetization of the NRM and magnetic susceptibility measurements were carried out on 27 discrete samples (9.2-cm^3 cubes) from Hole 1275B and 36 samples from Hole 1275D. When possible, directional data obtained from AF demagnetization were used to approximately restore the magnetic anisotropy data of the samples into a geographic reference frame.

Remanence Data

AF demagnetization of discrete samples from Hole 1275B (Fig. **F92**) yielded variable results depending on the lithology, but stable characteristic components after treatment to 20–30 mT were observed in most of the samples. Diabase samples from the upper Unit I have the lowest NRM intensities but very stable magnetizations (e.g., Fig. **F92A**). The drilling overprint in this sample is insignificant, and the ChRM constitutes nearly 100% of the initial NRM. Oxide gabbro(norite) samples show a variable drilling overprint that is removed by AF treatments of 15–20 mT (Fig. **F92B, F92C**). However, a linear characteristic component trending toward the origin can generally be calculated from the 30- to 100-mT demagnetization intervals.

As observed at previous sites, the characteristic component is more clearly isolated in the discrete sample data than in the long-core measurements. For example, Sample 209-1275B-19R-1, 76–78 cm, shows a linear decay trend from 30 to 100 mT (Fig. **F92C**), from which a PCA direction of Class A can be calculated. The same interval in the long-core data does not show a clear isolation of the higher-coercivity component but yields a smooth curve from the vertical drilling overprint component to the shallow directions of the last demagnetization steps (Class C direction).

As observed for samples from Hole 1275B, the demagnetization of discrete samples of gabbros from Hole 1275D reveals a stable characteristic component after demagnetization to 20- to 30-mT peak fields. This stable component typically represents 10%–100% of the initial NRM (Fig. **F93**), shows a linear decay toward the origin, and has maximum coercivities between 70 and 100 mT (Class A direction). Overall, the discrete sample data agree well with the long-core data, particularly with respect to the remanent declination.

Most gabbros, both from Holes 1275B and 1275D, have remanence inclinations that are either subhorizontal or negative. However, a significant number of troctolite, diabase, and microgabbro samples recovered from Hole 1275D yielded less uniform inclinations and include

clearly positive inclinations (Fig. F94). The characteristic component for some of these samples has lower coercivities (typically <50 mT) than the average of the coarser-grained gabbros. For example, a diabase sample from Core 209-1275D-33R is nearly completely demagnetized by 15 mT (Fig. F94C) but has an apparently stable final component with positive inclination that represents <1% of the NRM (Class C direction). However, some positive inclinations are associated with Class A demagnetization behavior. For example, a troctolite sample from Core 209-1275D-9R (Fig. F94A) yielded a well-isolated characteristic component with an inclination of +12°, representing 23% of the NRM. More rarely, samples with two shallow, nearly antipodal components were recognized (Fig. F94B), with the higher-stability component having a positive inclination. A similar pattern, though less clearly defined, is evident in the demagnetization data from the corresponding archive-half interval (Fig. F94E).

F94. Vector endpoint diagrams for diabase, microgabbros, p. 139.

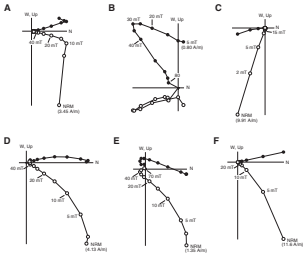

Anisotropy of Magnetic Susceptibility

The anisotropy of magnetic susceptibility (AMS) was determined for all discrete samples from Site 1275 (Table T9). Gabbroic samples from Site 1275 exhibit low to moderate degrees of susceptibility anisotropy, and the AMS fabrics are triaxial to oblate. The degree of anisotropy (P = maximum/minimum eigenvalue) ranges ~1.00–1.23, though typically the degree of anisotropy is <1.10. Although only a small number of diabase samples were measured, these fine-grained lithologies have nearly isotropic susceptibility tensors (Table T9).

T9. AMS data, p. 165.

In order to compare the orientations of magnetic fabrics from different samples, some common reference frame is required. Under the assumption that the stable remanent magnetization approximates the time-averaged reversed polarity direction (see below), the magnetic fabric data have been restored to a common reference frame by a simple vertical axis rotation that restores the remanent declination to the presumed reversed polarity direction (180°). After this reorientation, the minimum eigenvectors of the AMS tensors for gabbros from Hole 1275B form a distinct cluster at steep inclinations (Fig. F95). The corresponding maximum eigenvectors delineate a nearly horizontal girdle, possibly dipping slightly to the northwest. The restored AMS data from Hole 1275D are much more scattered, although the mean orientation of the minimum eigenvectors is also steep.

F95. AMS data, p. 140.

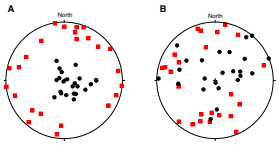

Remanence Directions

Inclinations of Class A components from 186 archive-half pieces agree well with the inclination distribution from the discrete sample data from Hole 1275B (Fig. F96). The discrete sample data yield a mean inclination of –9.5° (+3.9°/–3.7°; κ = 50.3; N = 26; using the inclination-only method of McFadden and Reid, 1982), which is significantly lower than that expected for the geocentric axial dipole at the site (28°). Despite their different magnetic properties, both the gabbros and the diabases from the upper part of Hole 1275B show similar directional results.

F96. Inclination data, p. 141.

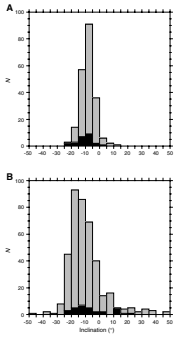

Overall, the inclinations from Hole 1275D are in agreement with the data from Hole 1275B. However, Hole 1275D samples show less uniform results, both with respect to the lithology and as a function of depth. The mean remanence inclination for discrete samples from Hole

1275D is –3.5° (+7.0°/–6.7°; κ = 11.9; *N* = 34), a value that is statistically indistinguishable from the mean inclination for Hole 1275B.

Although both Holes 1275B and 1275D apparently have dominantly reversed polarity magnetizations, some normal polarity magnetizations are apparently also present in Hole 1275D. In particular, the troctolites and diabases of Unit I have scattered but generally positive inclinations that may be interpreted as normal polarity magnetizations. Some of the intervals in Unit I (e.g., from Cores 209-1275D-9R and 10R) (Fig. **F91**) have similar magnetic stability to the presumed reversed polarity samples elsewhere in the hole. In addition, the presence of one sample with two nearly antipodal magnetization components (Fig. **F94B**) suggests that both normal and reversed polarity magnetizations are recorded at this site. At present, the origin of this normal polarity (positive inclination) signal is uncertain. It may reflect either an ancient thermoremanence or a more recent chemical or viscous remanence.

MICROBIOLOGY

Solid Sample 209-1275D-10R-2 (Piece 3, 26–37 cm)

At Site 1275 one rock sample, a completely altered pyroxene-bearing troctolite (Sample 209-1275D-10R-2 [Piece 3, 26–37 cm]), was collected to characterize the microbial community inhabiting this environment. The sample was prepared as described in **"Igneous Rocks,"** p. 24, in "Microbiology" in the "Explanatory Notes" chapter. The type and extent of contamination caused by drill fluids was evaluated as described in **"Contamination Tests,"** p. 26, in "Microbiology" in the "Explanatory Notes" chapter. The sample was rinsed in nanopure water, and the collected water (35 mL) was filtered and examined under a fluorescence microscope. Microsphere concentration was 2.55×10^3 microspheres/mL of wash. A 0.2-g interior piece of the sample was examined under a fluorescence microscope and no microspheres were observed, indicating they did not penetrate to the interior of the sample. The perfluorocarbon tracer was not used in this hole.

Seawater and Water Samples and Atmospheric Data

One liter of surface water was collected and prepared for deoxyribonucleic acid (DNA) analysis and direct counts as described in **"Seawater and Water Samples,"** p. 26, in "Microbiology" in the "Explanatory Notes" chapter.

Table **T10** is a summary of atmospheric and surface water data for the period 20–30 June 2003. For surface water direct count data, 1 mL of water was stained as described in **"Microbiology,"** p. 24, in the "Explanatory Notes" chapter. Funnel rinse water (1 mL) was used as a control. Salinity, temperature, and pH values for all surface water values varied; salinity ranged 36.0–37.0 psu, temperature 25.5°–26.4°C, and pH 7.96–7.99. Surface water samples were collected between 1215 and 1545 hr. Air samples were collected for culture-based studies between 0633 and 1835 hr. Air sample volumes ranged from 89.3 to 12179.9 L per sample. Microbial growth (colony forming units) was for the total volume at 48 and >96 hr of incubation (Table **T10**). Air temperatures, humidity, wind speed, and wind direction ranged 24.8°–29.6°C, 67.4%–81.2%, 3.9–6.7 m/s, and 62°–110°, respectively. Samples for shore-based

T10. Surface water and atmospheric microbiology data, p. 167.

analysis of bacterial community DNA and bacteria and viral direct counts were collected daily and stored according to protocol.

DOWNHOLE MEASUREMENTS

Hole 1275C

Logging-While-Coring Operations

On 24 June the RAB-8 LWC system was deployed for the first time during an ODP hard rock leg. Initial operations were delayed owing to tool construction, as there was a 2-in error in the assembly drawing, specifically with a bearing coupling part. This error prevented coupling of the inner and outer core barrel. Shipboard parts fabrication resolved the misfit with little loss of operations time. Because we had very few spare parts for this system, the rig mechanics fabricated two spacer subs from an extra core barrel in order to build a second lower core barrel assembly. More than 15 hr was required to core to 20.8 mbsf, and the three core barrels recovered returned only a few small pieces of rock (<20 cm curated length). Based on poor recovery, LWC operations were terminated. In comparison, coring with the conventional RCB system a few meters away in Hole 1275D reached >17 m in just over 10 hr, and the three cores recovered from this interval averaged >30% recovery (5.62 m). In a postcruise evaluation, the core technician hypothesized that a design flaw in the one-way core flow valve (core catcher) contributed to poor recovery with the LWC system.

Data Processing

Ship heave during the RAB-8 tool deployment averaged 0.15 m with peaks of ~0.45 m. The first core was drilled using active heave compensation (AHC), whereas the second and third cores were drilled using the passive heave compensation (PHC) system. AHC deviations from heave at surface were consistently ~0.06 m, and PHC deviations from heave at surface were ~0.10 m with peaks up to 0.20 m. Therefore, heave was not a factor in depth control and image quality. The drillers kept between 5 and 15 kft·lb of weight on the bit (measured by AHC cylinder force when using the AHC and by hookload differential when using the PHC), ensuring constant contact between the bit and the bottom of the hole.

The RAB-8 tool records time vs. formation properties, and the Schlumberger surface acquisition system records time vs. depth. The downhole and surface files are merged in order to generate logs of formation properties as a function of depth. Depth is monitored using a monitor on the drawworks (drawworks encoder; DWE) and a hook and sensor.

While drilling Hole 1275C, the DWE measurement did not always correspond with actual bit movement. At times, the driller lowered the block but the weight was taken by pipe compression and flexing, in which case the bit experienced little or no downward-directed force. Similarly, raising the drill string did not necessarily lift the bit off bottom as the pipe unflexed and decompressed. Thus, the time-depth file generated by the surface system is flawed, and logs generated by merging it with the downhole data resulted in smeared resistivity images.

To correctly process the data, the time-depth file was modified to account for what the bit was doing at a given moment. Figure F97 illustrates the improvement of the smoothed image over the original. Our fundamental assumption in smoothing the data was that the bit was always on bottom except during core retrievals and one other brief interval. The assumption is supported by the surface weight on bit and AHC cylinder force data recorded by the TruVu rig instrumentation system.

The time vs. depth data were smoothed (37 vs. >1000 time-depth pairs in the raw data) but adjusted to match the original slope (i.e., rate of penetration) and points of known depth obtained from drillers depth, the only reference. Figure F98 is a graphical representation of the original and smoothed time-depth file. This depth-tracking problem is uncommon in the oil industry, for which the DWE system was designed. However, ODP operations (specifically LWC in Hole 1275C) are significantly different than typical oilfield operations. In Hole 1275C, we did not have a riser and we were coring in a hard rock formation with a light BHA, resulting in a slow penetration rate.

RAB-8 Measurements

Only shallow- and deep-resistivity images were obtained during the RAB-8 deployment in order to conserve tool memory. Static and dynamic processing of deep-resistivity images shows a significant number of structures, and the static images show distinct delineations between resistive and conductive intervals (Fig. F99). Some of the most prominent features are the upper resistive layer and a distinct resistivity contrast interpreted to be a large fracture between 3.5 and 4 mbsf. Three-dimensional presentations of the dynamic RAB images show orientations of structural features that likely represent fractures dipping in various directions (Fig. F100). Electrical resistivity values show deep measurements (BD) of 0.3–24.1 Ωm, intermediate (BM) measurements of 0.3–26.3 Ωm, and shallow measurements (BS) of 0.3–36.6 Ωm (Fig. F101). The BS curve shows the widest range of variability, likely due to changes in fracture intensity.

Hole 1275D

Wireline Logging Operations

Prior to the beginning of wireline operations on 30 June, a 30-bbl sepiolite sweep was done during the last core, the bit was released at the bottom of the hole, 60 bbl of sepiolite mud was pumped after releasing the bit, and the pipe was brought up to a logging depth of 1582 meters below rig floor (mbrf). The first deployment consisted of the triple combo tool string, which contained the Hostile Environment Gamma Ray Sonde (HNGS), the Accelerator Porosity Sonde (APS), the Hostile Environment Litho-Density Sonde (HLDS), the Dual Induction–Phasor Resistivity Tool (DIT-E), and the Lamont Doherty Earth Observatory Temperature/Pressure/Acceleration tool (TAP). The APS was included in this deployment after the previously documented problems at Site 1272 were resolved. After an 11-min temperature equilibration station at seafloor, we began lowering the tool string at 200 m/hr until a hole obstruction was encountered at ~104.1 mbsf. Several attempts to get past the obstruction failed; therefore, we did a 5-min temperature station at the bottom of the hole and then began logging upward at 274 m/hr. The HLDS caliper arm did not open until reaching 67 mbsf. Once the

F97. RAB-8 resistivity images, p. 142.

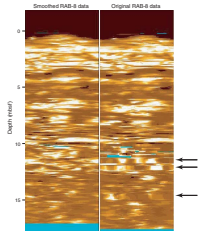

F98. RAB-8 time-depth file, p. 143.

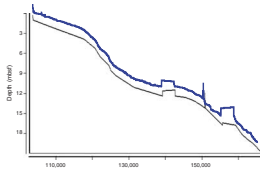

F99. Static and dynamic images of possible fractures, p. 144.

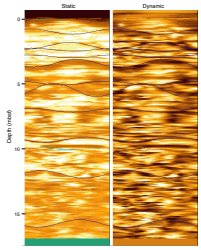

F100. RAB images of geographical orientations, p. 145.

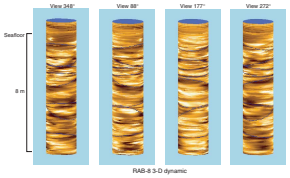

F101. RAB-8 gamma ray and resistivity logs, p. 146.

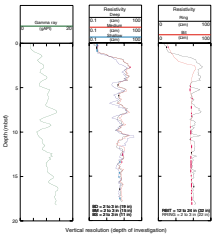

tool string reached the bottom of the pipe, the HLDS caliper would not close; therefore, the tool was slowly brought inside the pipe and a second open hole pass was aborted. The maximum heave during this run was ~0.82 m.

The second tool string deployment consisted of the Scintillation Gamma Ray Tool (SGT), the General Purpose Inclinometry Tool (GPIT), and the FMS. Attempts to pass through the obstruction at 104 mbsf also failed, and two full passes above the obstruction were completed. After the first pass, the tool string was brought completely inside the pipe and the BHA was raised 10 m. The tool string was then lowered to the bottom of the hole and the second pass recorded images up to 21 mbsf. After the second deployment had concluded, the wireline and the sheaves were removed and the pipe was lowered to 104 mbsf in an attempt to break through the obstruction. After circulating and putting >20,000 lb of weight on the BHA, all other attempts to bypass the obstruction were terminated.

The wireline heave compensator (WHC) began to move erratically during the first SGT-GPIT-FMS pass, and it was turned off for both passes. After examining the WHC for ~1 hr, sudden changes in pressure were observed, suggesting that either the linear positioning transducer or air in the lines from a previous oil and filter change could have been contributing to the problem. However, the problem was not solved and all subsequent logging runs were done without the WHC. The heave varied from 0.75 to 0.87 m during the first SGT-GPIT-FMS pass and from 0.95 to 1.06 m during the second pass. The logging speed for both runs was 274 m/hr.

A third tool string deployment consisted of the SGT, GPIT, and Dipole Sonic Imager (DSI). Two passes were made at 540 m/hr with this tool string, although problems with the tool's isolation joint produced intermittent low voltage and hardware failure error messages throughout the deployment. Postcruise waveform processing and assessment of the shipboard time coherence analyses corrected for these problems.

Borehole Conditions

The HLDS and FMS calipers show a relatively good borehole with dimensions ranging 8.6–17.4 in (mean = 10.8 in). There are several intervals with large washouts including sections at 41–42 mbsf, 77–78 mbsf, and 94–98 mbsf. The widest portion of the borehole measured with the HLDS caliper was at 41–42 mbsf, with a maximum dimension of 17.4 in. The maximum aperture of the FMS calipers is 15.5 in, and this was recorded in the bottommost washout interval.

Electrical Resistivity and Porosity Measurements

Deep measurements (IDPH) of electrical resistivity range 8.7–45.4 Ωm, and the shallow resistivity (SFLU) varies between 5.9 and 98.4 Ωm (Fig. F102). The SFLU curve shows the widest range of variability, likely due to changes in fracture intensity and alteration. Several zones with higher resistivity values occur over the same interval as changes in density, photoelectric effect, and porosity (Figs. F102, F103).

Porosity measurements are relatively high, especially for the interval 34–52 mbsf that corresponds to Cores 209-1275D-7R to 11R (Fig. F102). The porosities range 3%–80% (mean = 20.1%). The highest porosity value was recorded in a washout zone located between 41 and 42 mbsf. Four discrete samples from the high-porosity interval (34–52 mbsf) do

F102. Caliper, resistivity, and porosity logs, p. 147.

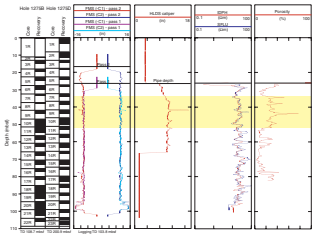

F103. Density, PEF, gamma ray, Th, U, K, and velocity logs, p. 148.

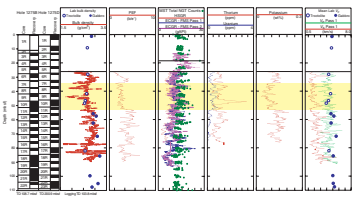

not have high porosity relative to samples from the rest of the core. However, the interval in the core between 25 and 45 mbsf is more intensely altered than the rest of the core (see **"Hydrothermal Alteration,"** p. 14, in "Hole 1275D" in "Metamorphic Petrology").

Density and Photoelectric Effect Measurements

High-resolution density measurements show values of 1.6–3.8 g/cm³ (mean = 2.7 g/cm³ for the logged interval). Densities are lower in the depth interval 34–52 mbsf, where the highest porosities are also encountered (Fig. **F103**). In keeping with the HLDS measurements, which show a washout at 41–42 mbsf, the density values in this interval are low. The photoelectric effect (PEF) values range 1.3–11.0 barns/e⁻ (mean = 4.1 barns/e⁻ for the logged interval) (Fig. **F103**). The relatively high PEF values are consistent with minerals such as amphiboles, pyroxenes, Fe-Ti oxides, and calcite found in these rocks (see Table **T13,** p. 75, in the "Explanatory Notes" chapter).

Natural Radioactivity Measurements

Formation natural radioactivity was measured during each run with two different tools. The SGT measured total gamma counts, whereas the HNGS provided spectral measurements. The different gamma ray tools produced similar response curves. The high-resolution environmentally corrected gamma ray (ECGR) total counts curve from the SGT and spectral data from the HNGS are shown in Figure **F103.** The SGT total count curve ranges 3.5–24.5 gAPI. The spectral gamma ray measured values of Th (≤0.35–3.4 ppm), U (–0.2–0.9 ppm), and K (0.03–0.2 wt%) (Fig. **F103**). In some instances the spectral values fall below the tool detection limits of Th (0.7 ppm), U (0.35 ppm), and K (0.18 wt%). The spectral data for K are low in the same interval (34–52 mbsf) as the low-density, high-porosity, high-alteration interval. PEF in this interval is low as well. A positive Th anomaly occurs between 46 and 48 mbsf (Fig. **F103**). Laboratory NGR total count measurements obtained using the shipboard MST are compared with logging data in Figure **F103.**

Sonic Velocities

All modes of the two passes (monopole and upper and lower dipole) were reprocessed postcruise. Overall, the waveforms were noisy and a slowness/time coherence algorithm was applied in a "multishot" mode instead of the full array mode. Coherence was calculated between all combinations of three adjacent receivers at each depth, and the best coherence result was then used. This provided an improvement over the full array coherence processing, although all the logs are noisy.

Compressional wave velocities obtained from the first pass range 2.2–6.5 km/s (mean = 4.3 km/s). In general, the mean compressional wave velocity is lower than expected for lower oceanic crust or upper mantle lithologies and may reflect the intensity of alteration and/or high fracture density present in the rocks. Compressional wave velocities are generally in good agreement with laboratory measurements made at ambient pressure (Fig. **F103**). Shear wave velocities from the first pass range 1.0–5.7 km/s (mean = 2.2 km/s). These values are generally low, and in some small intervals anomalies such as higher shear wave velocities than compressional wave velocities are present even after reprocessing (Fig. **F103**).

Inclinometry and Magnetic Measurements

The GPIT was run in conjunction with the FMS and DSI to provide information on the intensity and direction of magnetization in the formation (see "Downhole Measurements," p. 29, in the "Explanatory Notes" chapter). The pad 1 azimuth shows different orientations for both FMS passes, increasing the borehole coverage obtained from the microresistivity images (Fig. F104). The magnetic field logs show variations in the horizontal components between both passes, although the total field measurements (FNOR) remain constant (Fig. F104). The magnetic inclination measurements (FINC) show average values of 36.9°, which is steep when compared to the expected value of ~28° for this area (see "Paleomagnetism," p. 31). The FNOR and FINC curves also show a pipe effect that extends for ~15 m and anomalies at 72–75 and 88–92 mbsf (Fig. F104). Maximum hole deviation is 4.5° and hole azimuth is ~230° (Fig. F104).

Temperature Measurements

The TAP tool downgoing temperature profile ranges 5.59°–5.55°C and the temperature gradient is 0.002°C/m (Fig. F105A). The pressure profile shows hydrostatic conditions throughout the entire hole (Fig. F105A). The TAP tool was held stationary for 5.4 min at a depth of 104 mbsf after all attempts to pass the obstruction failed. These measurements show no significant temperature changes during this time interval (Fig. F105B).

Formation MicroScanner Measurements

FMS images show many zones that are interpreted to represent high fracture density and deformation. The interval between 21 and 48.8 mbsf is characterized by mostly conductive features that occur in the same interval as high porosity and low density logging data, PEF, and potassium measurements. An apparent contact at 48.8 mbsf showing a distinct change from a conductive to resistive formation suggests a lithologic change or a transition to a less altered formation (Fig. F106). Below this contact, many conductive features interpreted to be fractures are also present, although the overall resistive nature of the formation is still apparent. We interpret the combination of steep- and shallow-dipping conductive features in the FMS images between 63 and 66.6 mbsf (Fig. F107) to be an intensely fractured interval. A speckled appearance in the FMS image between 69.9 and 71 mbsf (Fig. F108) suggests the presence of disseminated Fe-Ti oxides. Thin subvertical features resemble veins, large steep fractures, and resistivity contrasts, suggesting lithologic contacts are also present throughout the entire logged interval (Fig. F108).

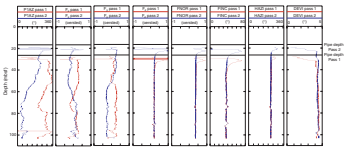

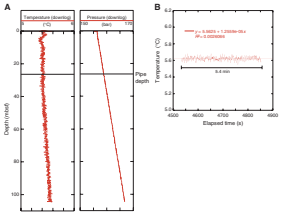

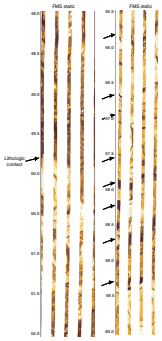

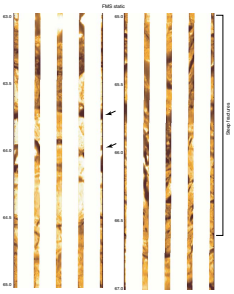

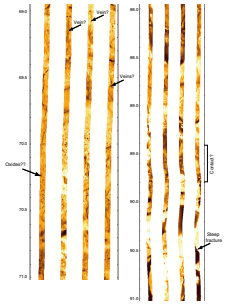

REFERENCES

Agar, S.M., Casey, J.F., and Kempton, P.D., 1997. Textural, geochemical, and isotopic variations in gabbroic shear zones from the MARK area. *In* Karson, J.A., Cannat, M., Miller, D.J., and Elthon, D. (Eds.), *Proc. ODP, Sci. Results,* 153: College Station, TX (Ocean Drilling Program), 99–121.

Bach, W., Alt, J.C., Niu, Y., Humphris, S.E., Erzinger, J., and Dick, H.J.B., 2001. The geochemical consequences of late-stage low-grade alteration of lower ocean crust at the SW Indian Ridge: results from ODP Hole 735B (Leg 176). *Geochim. Cosmochim. Acta,* 65:3267–3287.

Bodinier, J.-L., 1988. Geochemistry and petrogenesis of the Lanzo peridotite body, Western Alps., *Tectonophysics,* 149:67–88.

Cannat, M., Karson, J.A., Miller, D.J., et al., 1995. *Proc. ODP, Init. Repts.,* 153: College Station, TX (Ocean Drilling Program).

Cannat, M., Mével, C., and Stakes, D., 1991. Normal ductile shear zones at an oceanic spreading ridge: tectonic evolution of Site 735 gabbros (southwest Indian Ocean). *In* Von Herzen, R.P., Robinson, P.T., et al., *Proc. ODP, Sci. Results,* 118: College Station, TX (Ocean Drilling Program), 415–429.

Casey, J.F., 1997. Comparison of major- and trace-element geochemistry of abyssal peridotites and mafic plutonic rocks with basalts from the MARK region of the Mid-Atlantic Ridge. *In* Karson, J.A., Cannat, M., Miller, D.J., and Elthon, D. (Eds.), *Proc. ODP, Sci. Results,* 153: College Station, TX (Ocean Drilling Program), 181–241.

Clark, S.P., 1966. Thermal conductivity. *In* Clark, S.P. (Ed.), *Handbook of Physical Constants*. Mem.—Geol. Soc. Am., 97:461–482.

Clauser, C., and Huenges, E., 1995. Thermal conductivity of rocks and minerals. *In* Ahrens, T.J. (Ed.), *A Handbook of Physical Constants: Rock Physics and Phase Relations* (Vol. 3), Am. Geophys. Union, Ref. Shelf Ser., 3:105–126.

Dick, H.J.B., Natland, J.H., Alt, J.C., Bach, W., Bideau, D., Gee, J.S., Haggas, S., Hertogen, J.G.H., Hirth, G., Holm, P.M., Ildefonse, B., Iturrino, G.J., John, B.E., Kelley, D.S., Kikawa, E., Kingdon, A., LeRoux, P.J., Maeda, J., Meyer, P.S., Miller, D.J., Naslund, H.R., Niu, Y., Robinson, P.T., Snow, J., Stephen, R.A., Trimby, P.W., Worm, H.-U., and Yoshinobu, A., 2000. A long in situ section of the lower ocean crust: results of ODP Leg 176 drilling at the Southwest Indian Ridge. *Earth Planet. Sci. Lett.,* 179:31–51.

Dick, H.J.B., Natland, J.H., Miller, D.J., et al., 1999. *Proc. ODP, Init. Repts.,* 176 [CD-ROM]. Available from: Ocean Drilling Program, Texas A&M University, College Station, TX 77845-9547, U.S.A.

Dilek, Y., Kempton, P.D., Thy, P., Hurst, S.D., Whitney, D., and Kelley, D.S., 1997. Structure and petrology of hydrothermal veins in gabbroic rocks from Sites 921 to 924, MARK area (Leg 153): alteration history of slow-spread lower oceanic crust. *In* Karson, J.A., Cannat, M., Miller, D.J., and Elthon, D. (Eds.), *Proc. ODP, Sci. Results,* 153: College Station, TX (Ocean Drilling Program), 155–178.

Escartin, J., and Cannat, M., 1999. Ultramafic exposures and the gravity signature of the lithosphere near the Fifteen-Twenty Fracture Zone (Mid-Atlantic Ridge, 14°16.5°N). *Earth Planet. Sci. Lett.,* 171:411–424.

Escartin, J., Mével, C., MacLeod, C.J., and McCraig, A., 2003. Constraints on deformation conditions and the origin of oceanic detachments, the Mid-Atlantic Ridge core complex at 15°45′N. *Geochem., Geophys., Geosyst.,* 4:10.1029/2002GC000472.

Fletcher, J.M., Stephens, C.J., Petersen, E.U., and Skerl, L., 1997. Greenschist facies hydrothermal alteration of oceanic gabbros: a case study of element mobility and reaction paths. *In* Karson, J.A., Cannat, M., Miller, D.J., and Elthon, D. (Eds.), *Proc. ODP, Sci. Results,* 153: College Station, TX (Ocean Drilling Program), 389–398.

Fujiwara, T., Lin, J., Matsumoto, T., Kelemen, P.B., Tucholke, B.E., and Casey, J., 2003. Crustal evolution of the Mid-Atlantic Ridge near the Fifteen-Twenty Fracture Zone in the last 5 Ma. *Geochem., Geophys., Geosyst.,* 4:10.1029/2002GC000364.

Gillis, K., Mével, C., Allan, J., et al., 1993. *Proc. ODP, Init. Repts.,* 147: College Station, TX (Ocean Drilling Program).

Gillis, K.M., 1995. Controls on hydrothermal alteration in a section of fast spreading oceanic crust. *Earth Planet. Sci. Lett.,* 134:473–489.

Gillis, K.M., and Meyer, P.S., 2001. Metasomatism of oceanic gabbros by late stage melts and hydrothermal fluids: evidence from the rare earth element composition of amphiboles. *Geochem., Geophys., Geosys.,* 2:10.1029/2000GC000087.

Godard, M., Jousselin, D., and Bodinier, J.-L., 2000. Relationships between geochemistry and structure beneath a paleo-spreading centre: a study of the mantle section in the Oman ophiolite. *Earth Planet. Sci. Lett.,* 180:133–148.

Hart, S.R., and Dunn, T., 1993. Experimental cpx/melt partitioning of 24 trace elements. *Contrib. Mineral. Petrol.,* 113:1–8.

Hébert, R., Adamson, A.C., and Komor, S.C., 1990. Metamorphic petrology of ODP Leg 109, Hole 670A serpentinized peridotites: serpentinization processes at a slow spreading ridge environment. *In* Detrick, R., Honnorez, J., Bryan, W.B., Juteau, T., et al., *Proc. ODP, Sci. Results,* 106/109: College Station, TX (Ocean Drilling Program), 103–115.

Ito, E., and Clayton, R.N., 1983. Submarine metamorphism of gabbros from the Mid-Cayman Rise: an oxygen isotopic study. *Geochim. Cosmochim. Acta,* 47:535–546.

Iturrino, G.J., Miller, D.J., and Christensen, N.I., 1996. Velocity behavior of lower crustal and upper mantle rocks from a fast-spreading ridge at Hess Deep. *In* Mével, C., Gillis, K.M., Allan, J.F., and Meyer, P.S. (Eds.), *Proc. ODP, Sci. Results,* 147: College Station, TX (Ocean Drilling Program), 417–440.

Kelley, D.S., 1997. Fluid evolution in slow-spreading environments. *In* Karson, J.A., Cannat, M., Miller, D.J., and Elthon, D. (Eds.), *Proc. ODP, Sci. Results,* 153: College Station, TX (Ocean Drilling Program), 399–415.

Kirschvink, J.L., 1980. The least-squares line and plane and the analysis of palaeomagnetic data. *Geophys. J. R. Astron. Soc.,* 62:699–718.

MacLeod, C.J., Escartin, J., Banerji, D., Banks, G.J., Gleeson, M., Irving, D.H.B., Lilly, R.M., McCaig, A.M., Niu, Y., Allerton, S., and Smith, D.K., 2002. Direct geological evidence for oceanic detachment faulting: the Mid-Atlantic Ridge, 15°45′N. *Geology,* 30:10:879–882.

Magde, L.S., Dick, H.J.B., and Hart, S.R., 1995. Tectonics, alteration and the fractal distribution of hydrothermal veins in the lower ocean crust. *Earth Planet. Sci. Lett.,* 129:103–119.

Manning, C.E., Weston, P.E., and Mahon, K.I., 1996. Rapid high-temperature metamorphism of East Pacific Rise gabbros from Hess Deep. *Earth Planet. Sci. Lett.,* 144:123–132.

McFadden, P.L., and Reid, A.B., 1982. Analysis of paleomagnetic inclination data. *Geophys. J. R. Astron. Soc.,* 69:307–319.

Mével, C., and Cannat, M., 1991. Lithospheric stretching and hydrothermal processes in oceanic gabbros from slow-spreading ridges. *In* Peters, T., Nicolas, A., and Coleman, R.J. (Eds.), *Ophiolite Genesis and Evolution of the Oceanic Lithosphere:* Dordrecht (Kluwer), 293–312.

Miller, D.J., and Christensen, N.I., 1997. Seismic velocities of lower crustal and upper mantle rocks from the slow-spreading Mid-Atlantic Ridge, south of the Kane Fracture Transform Zone (MARK). *In* Karson, J.A., Cannat, M., Miller, D.J., and Elthon, D. (Eds.), *Proc. ODP, Sci. Results,* 153: College Station, TX (Ocean Drilling Program), 437–454.

Natland, J.H., 2002. Magnetic susceptibility as an index of the lithology and composition of gabbros, ODP Leg 176, Hole 735B, Southwest Indian Ridge. *In* Natland, J.H., Dick, H.J.B., Miller, D.J., and Von Herzen, R.P. (Eds.), *Proc. ODP, Sci. Results,* 176 [Online]. Available from World Wide Web: <http://www-odp.tamu.edu/publications/176_SR/chap_11/chap_11.htm>. [Cited 2003-07-06]

Nehlig, P., 1994. Fracture and permeability analysis in magma-hydrothermal transition zones in the Samail ophiolite (Oman). *J. Geophys. Res.,* 99:589–601.

Niu, Y., and Hekinian, R., 1997. Basaltic liquids and harzburgitic residues in the Garrett Transform: a case study at fast-spreading ridges. *Earth Planet. Sci. Lett.,* 146:243–258.

Parkinson, I.J., and Pearce, J.A., 1998. Peridotites from the Izu-Bonin-Mariana forearc (ODP Leg 125); Evidence for partial melting and melt-mantle interactions in a supra-subduction zone setting. *J. Petrol.,* 39:1577–1618.

Pettigrew, T.L., Casey, J.F., Miller, D.J., et al., 1999. *Proc. ODP, Init. Repts.,* 179 [CD-ROM]. Available from: Ocean Drilling Program, Texas A&M University, College Station, TX 77845-9547, U.S.A.

Rampone, E., Hofmann, A.W., Piccardo, G.B., Vannucci, R., Bottazzi, P., and Ottolini, L., 1996. Trace element and isotope geochemistry of depleted peridotites from an N-MORB type ophiolite (Internal Liguride, N. Italy). *Contrib. Mineral. Petrol.,* 123:61–76.

Robinson, P.T., Von Herzen, R., et al., 1989. *Proc. ODP, Init. Repts.,* 118: College Station, TX (Ocean Drilling Program).

Shervais, J.W., 1982. Ti-V plots and the petrogenesis of modern and ophiolitic lavas. *Earth Planet. Sci. Lett.,* 59:101–118.

Snow, J.E., and Dick, H.J.B., 1995. Pervasive magnesium loss by marine weathering of peridotite. *Geochim. Cosmochim. Acta,* 59:4219–4235.

Stakes, D., Mével, C., Cannat, M., and Chaput, T., 1991. Metamorphic stratigraphy of Hole 735B. *In* Von Herzen, R.P., Robinson, P.T., et al., *Proc. ODP, Sci. Results,* 118: College Station, TX (Ocean Drilling Program), 153–180.

Streckeisen, A., 1974. Classification and nomenclature of plutonic rocks. *Geol. Rundsch.,* 63:773–786.

Sun, S.-S., and McDonough, W.F., 1989. Chemical and isotopic systematics of oceanic basalts: implications for mantle composition and processes. *In* Saunders, A.D., and Norry, M.J. (Eds.), *Magmatism in the Ocean Basins.* Geol. Soc. Spec. Publ., 42:313–345.

Toft, P.B., Arkani-Hamed, J., and Haggerty, S.E., 1990. The effects of serpentinization on density and magnetic susceptibility: a petrophysical model. *Phys. Earth Planet. Inter.,* 65:137–157.

Figure F1. Bathymetric map indicating subsea camera survey tracks (purple = Hole 1275A, green = Hole 1275C) and hole locations. Bathymetric data courtesy of T. Fujiwara and T. Matsumoto of JAMSTEC (Fujiwara et al., 2003).

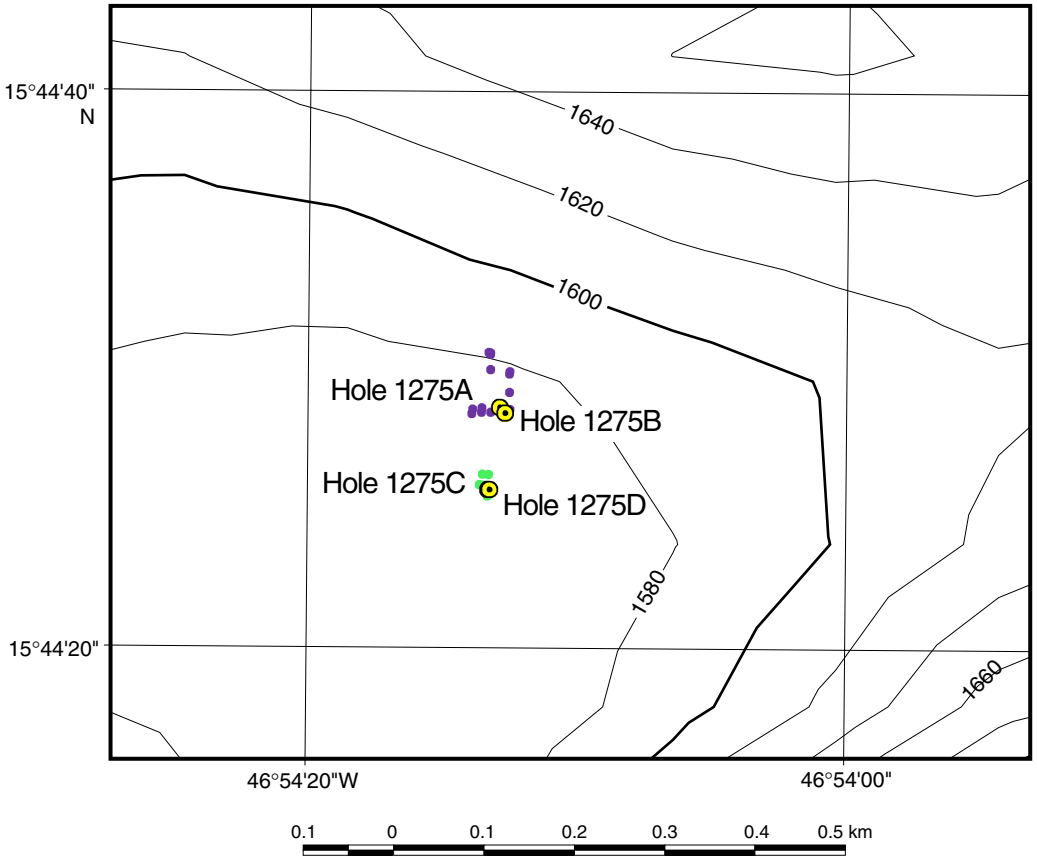

Figure F2. A. Location map with track of the 1998 *Shinkai* 6500 Dive 422 (red line), locations and lithologies of samples from that dive, and the approximate positions of Holes 1275A, 1275B, 1275C, and 1275D. **B.** Bathymetric section based on *Shinkai* 6500 Dive 422, projected along 000° with no vertical exaggeration. Locations and lithologies of samples collected during the dive, as well as the approximate positions of Holes 1275A, 1275B, 1275C, and 1275D are indicated.

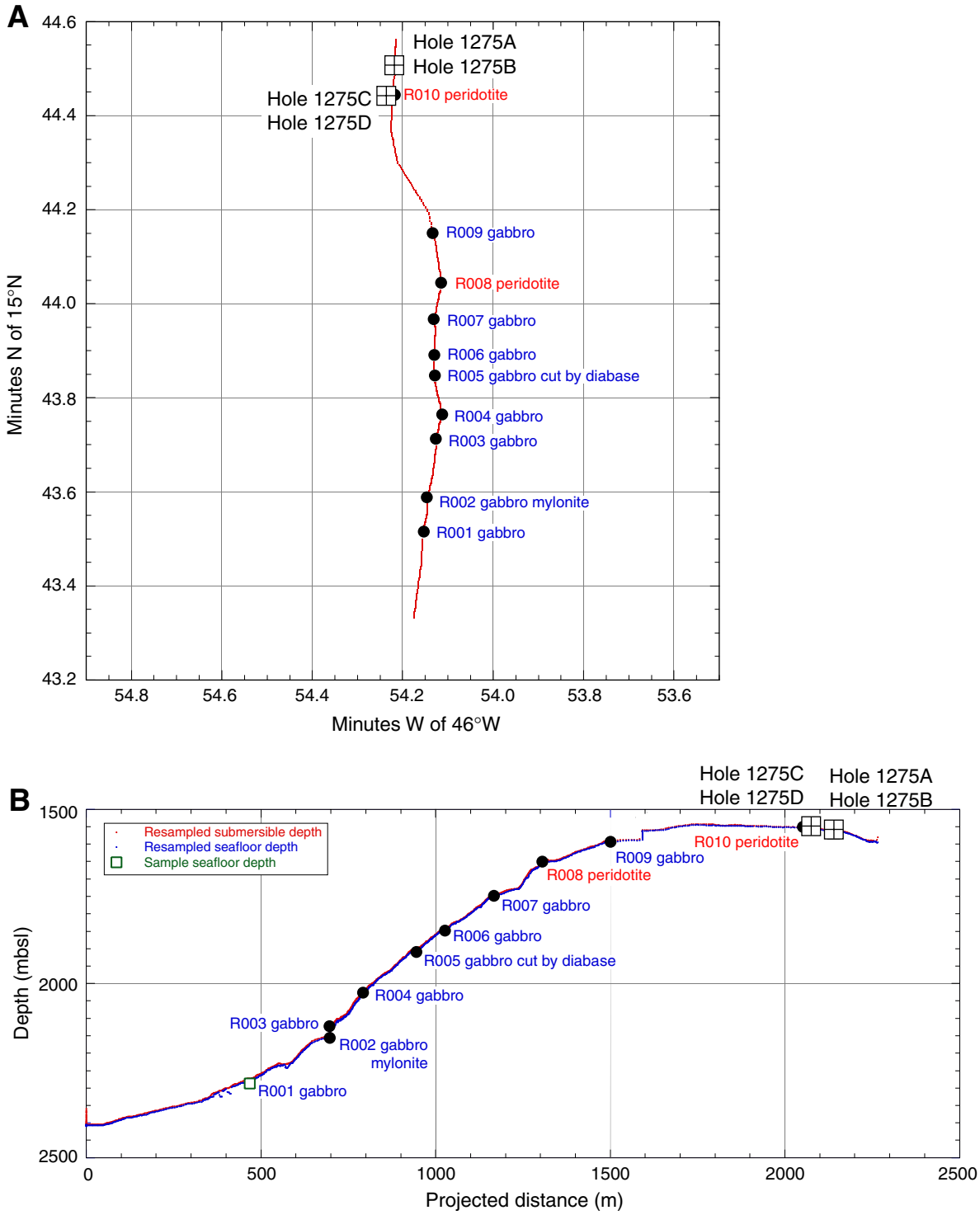

Figure F3. Comparison of recovery in the first three cores between resistivity-at-the-bit while coring (RAB-C) (Hole 1275C) and conventional rotary core barrel (RCB) (all other Leg 209 holes).

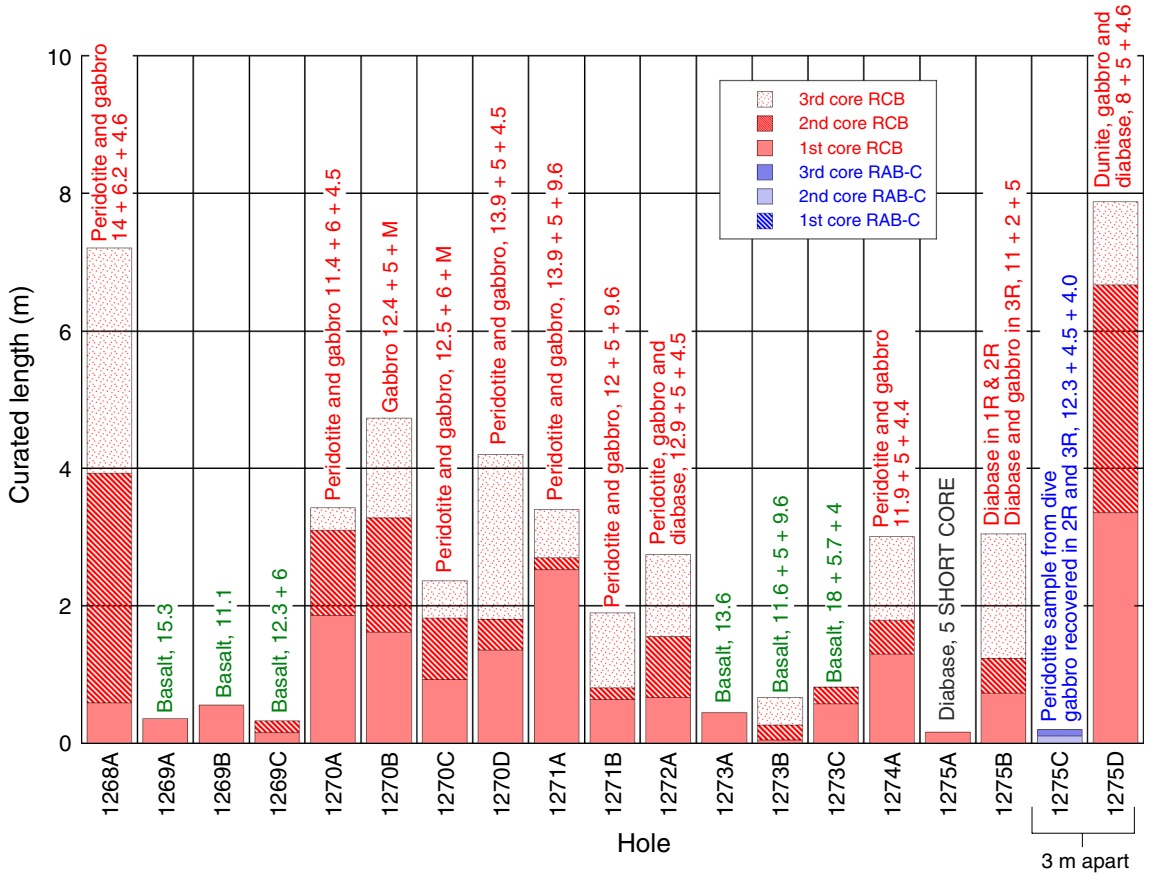

Figure F4. Lithostratigraphic summary for Hole 1275B. TD = total depth.

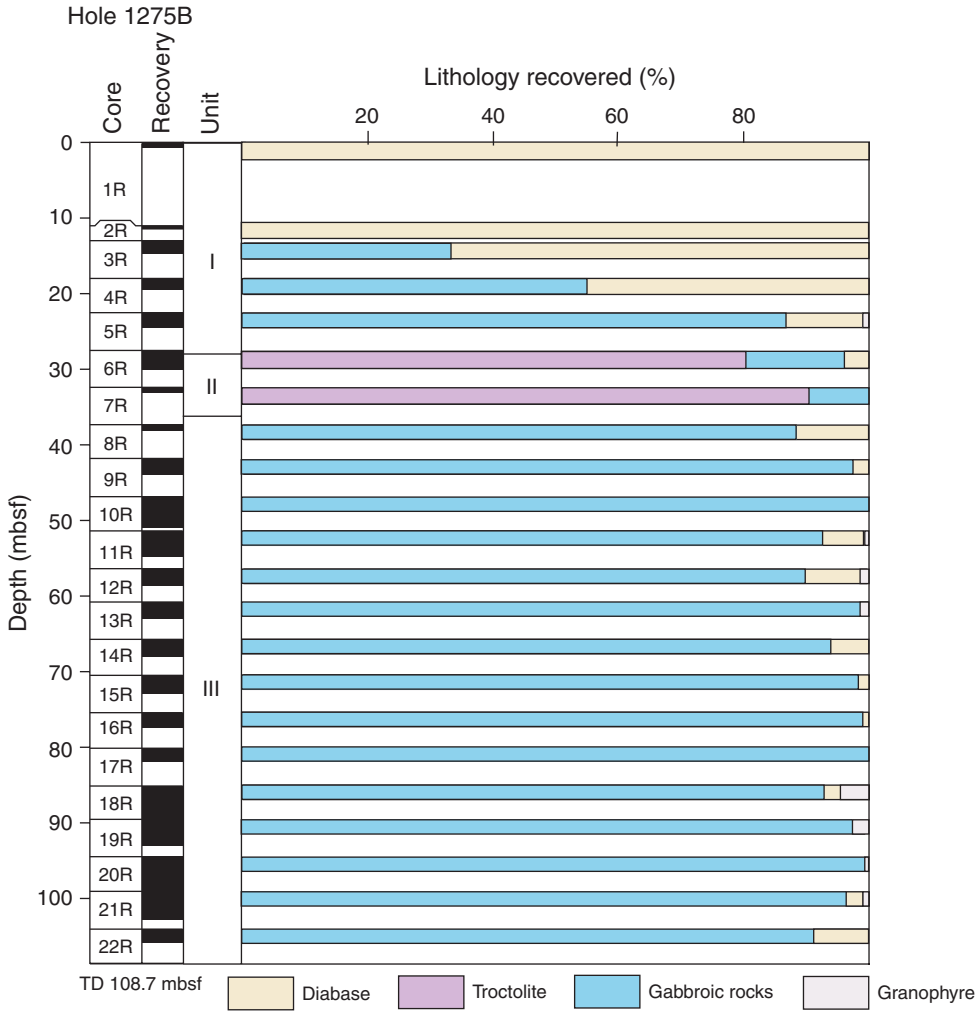

Figure F5. Close-up photograph of gabbro with fine-grained patches in a matrix of medium-grained crystals (interval 209-1275B-5R-1 [Piece 19, 112–119 cm]).

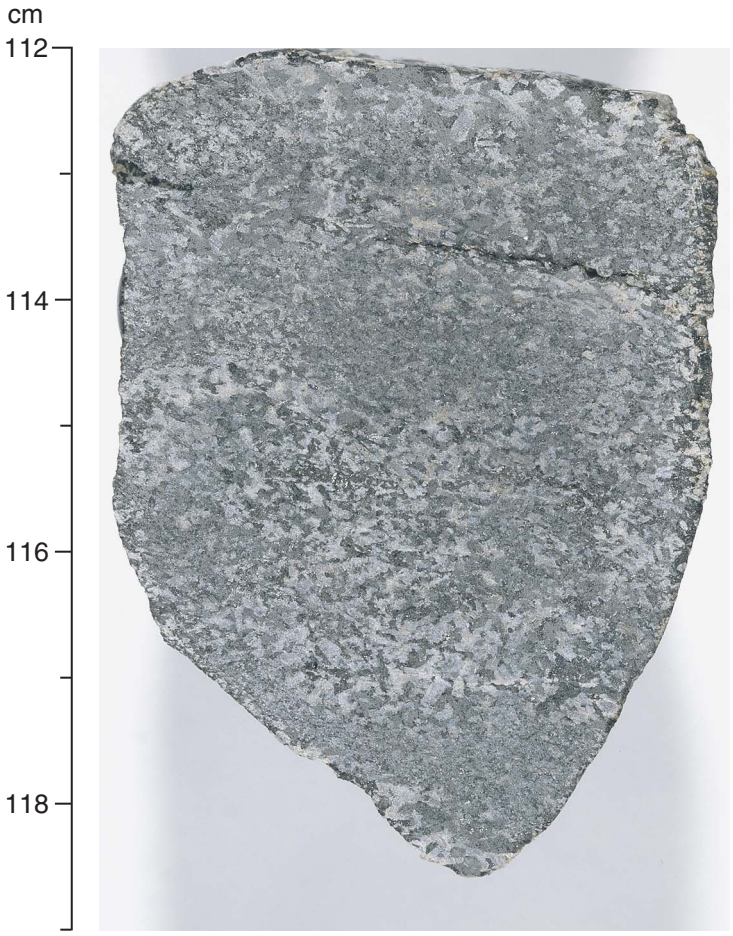

Figure F6. Close-up photograph of typical appearance of troctolite from Site 1275. Note the crosscutting dike with irregular margins that appear to be continuous with the interstitial material between the olivine grains (interval 209-1275B-6R-2 [Piece 4, 24–48 cm]).

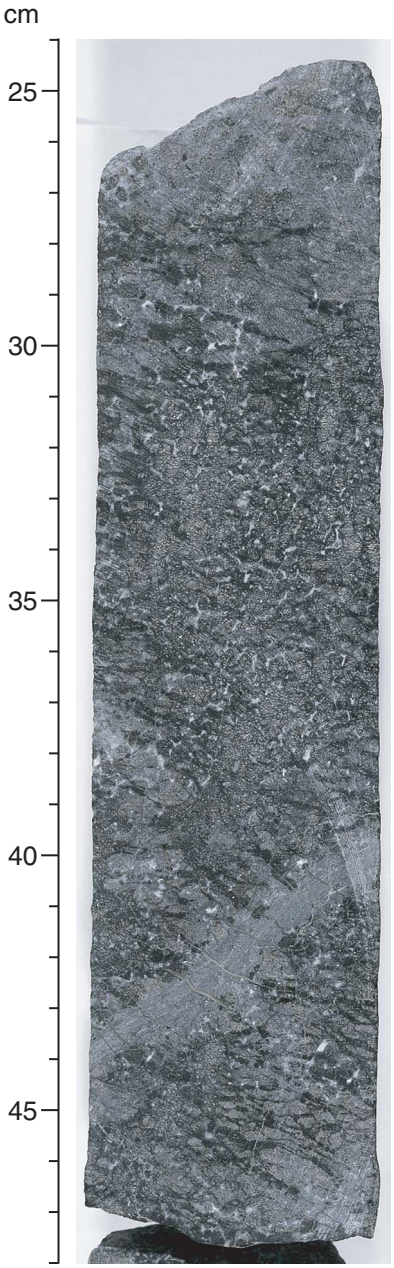

Figure F7. Close-up photograph of coarse-grained oxide gabbro in contact with fine-grained gabbro (interval 209-1275B-18R-3 [Piece 3, 7–18 cm]).

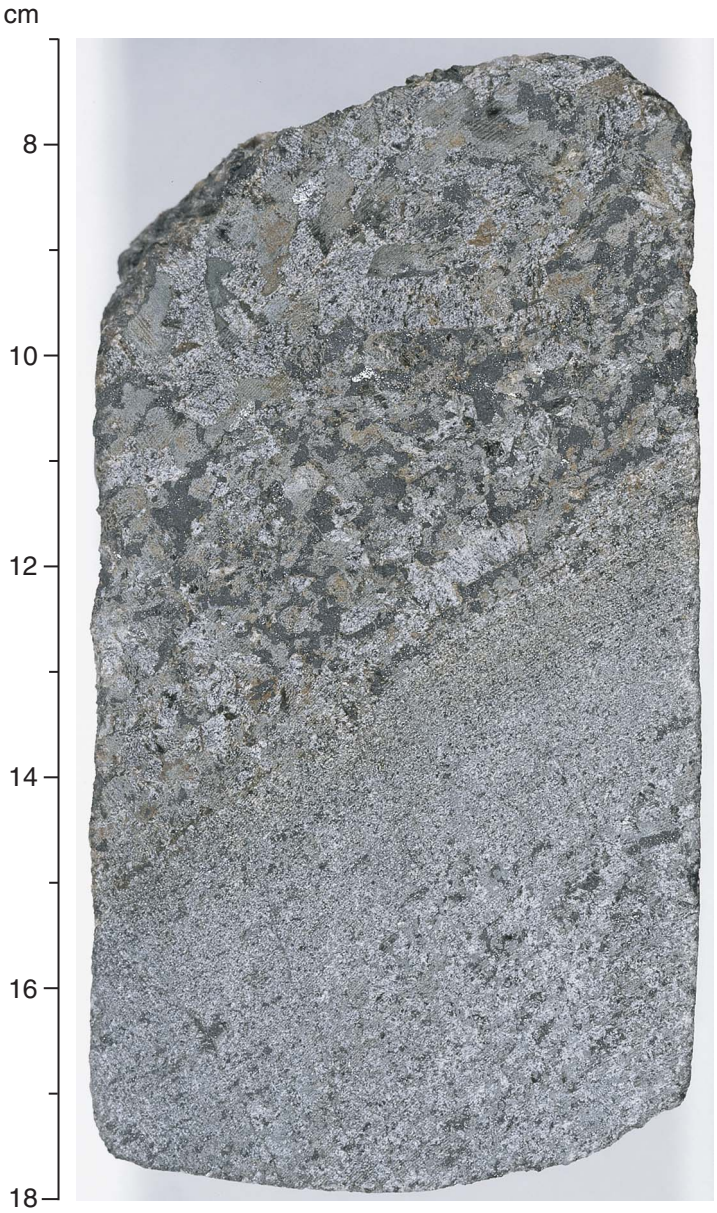

Figure F8. Close-up photograph of medium- to coarse-grained gabbro in flat and sharp contact with very fine grained gabbro (interval 209-1275B-21R-1 [Piece 1A, 6–16 cm]).

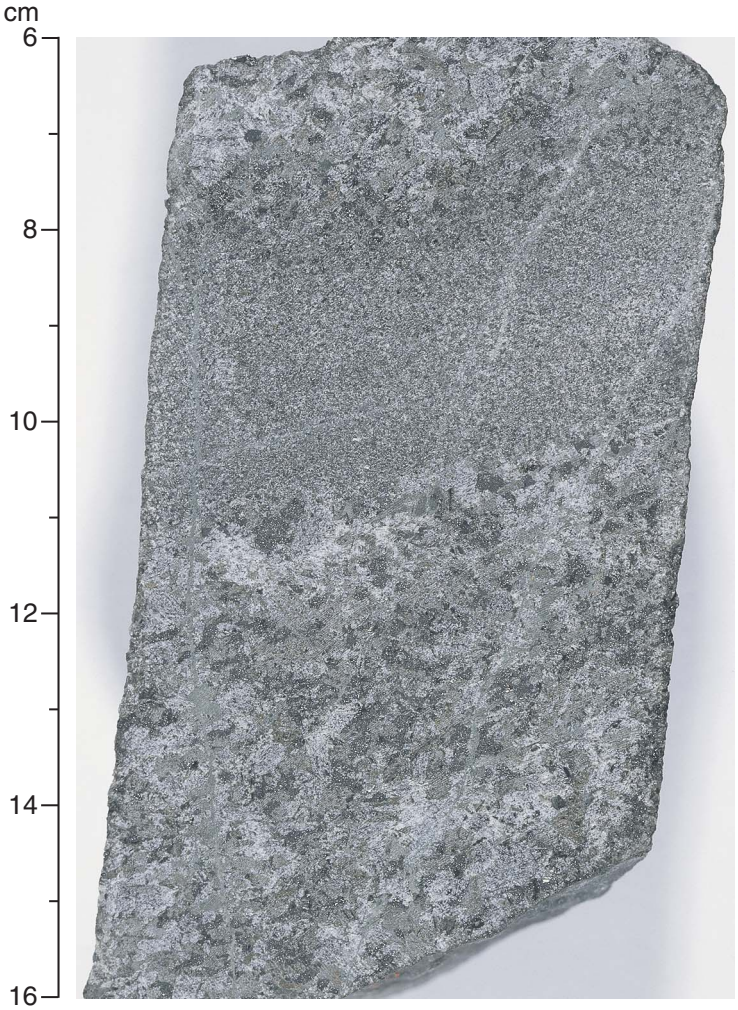

Figure F9. Close-up photographs of gabbroic rocks with different grain sizes mixed in an irregular fashion. The boundaries are crenulate and suggestive of liquid-liquid interaction. **A.** Interval 209-1275B-13R-1 (Piece 6, 75–91 cm). **B.** Interval 209-1275B-18R-1 (Piece 9A, 84–107 cm).

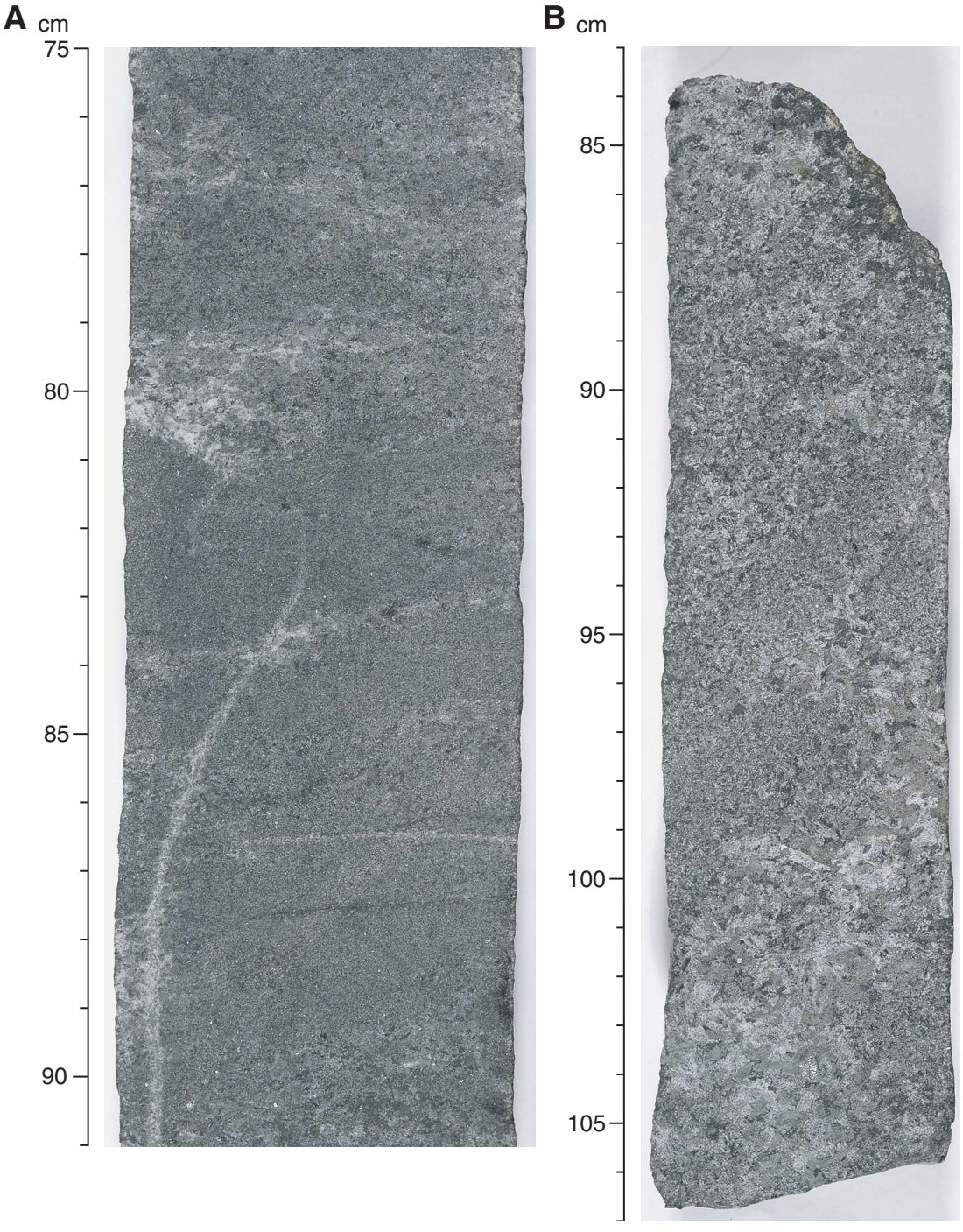

Figure F10. Downhole variation of grain size in Hole 1275B gabbros. Size classifications are very fine (<0.2 mm), fine (0.2–2 mm), medium (2–7 mm), and coarse (≥7 mm). TD = total depth.

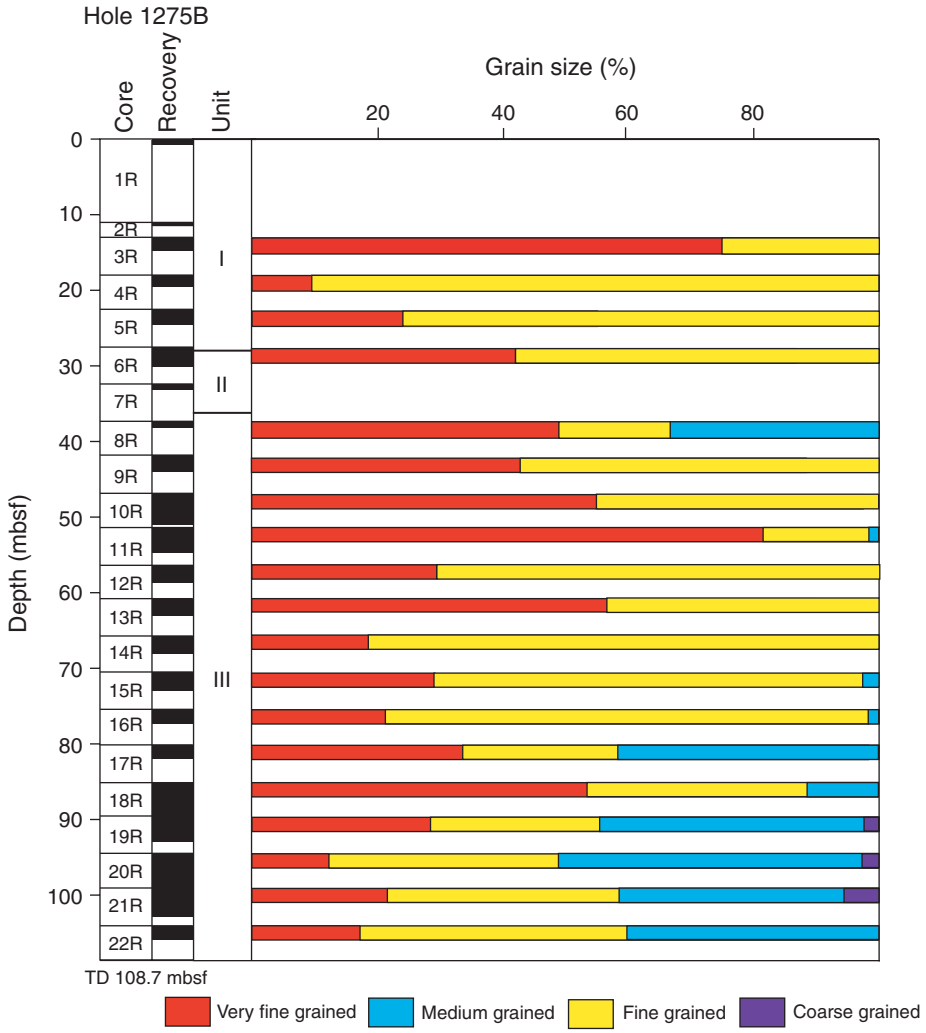

Figure F11. Close-up photographs of typical examples of a dikelet of granophyre cutting gabbro. **A.** Interval 209-1275B-19R-1 (Piece 3, 10–42 cm). **B.** Granophyres are variable in width and many are oriented subparallel to the drilling direction (interval 209-1275B-19R-3 [Piece 1B, 48–81 cm]).

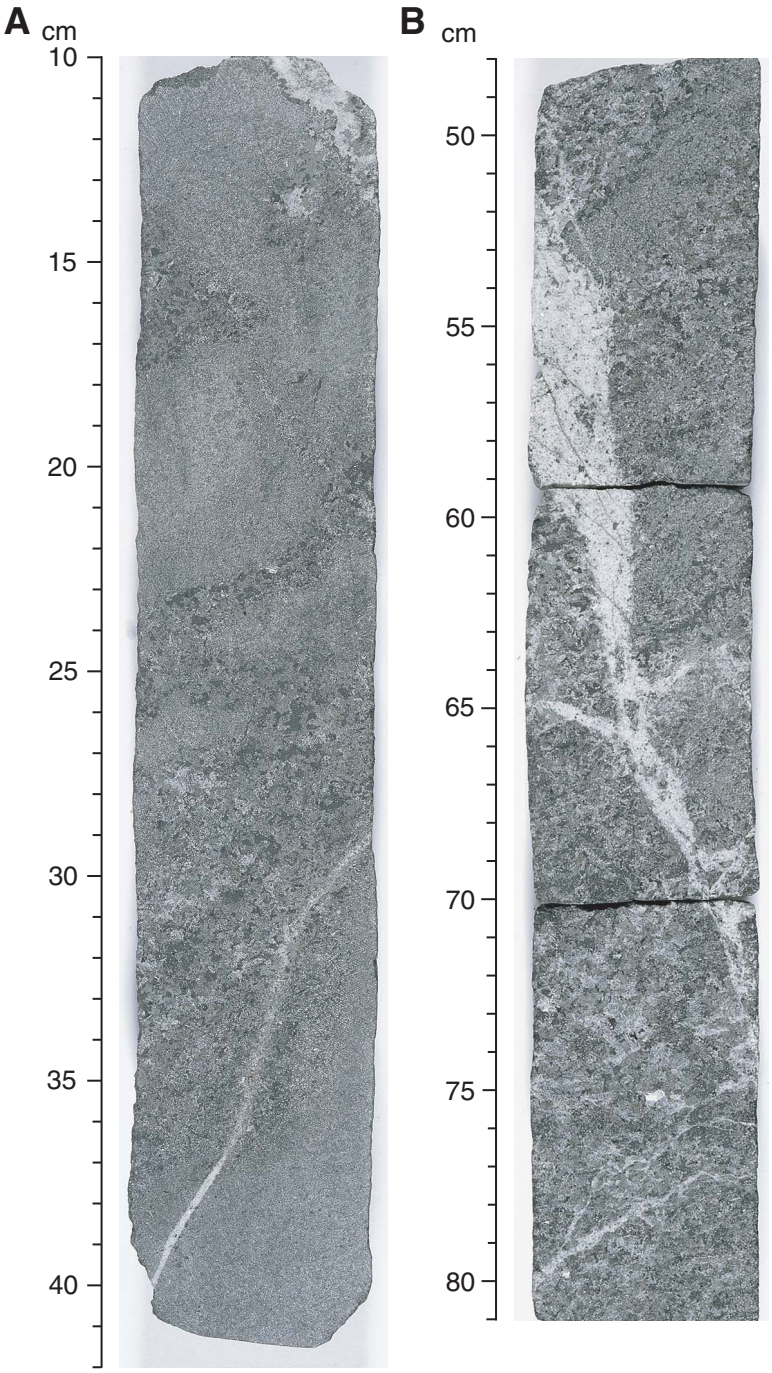

Figure F12. Close-up photograph of large amphibole grains formed by reaction between gabbro and granophyre (interval 209-1275B-18R-1 [Piece 12, 54–77 cm]).

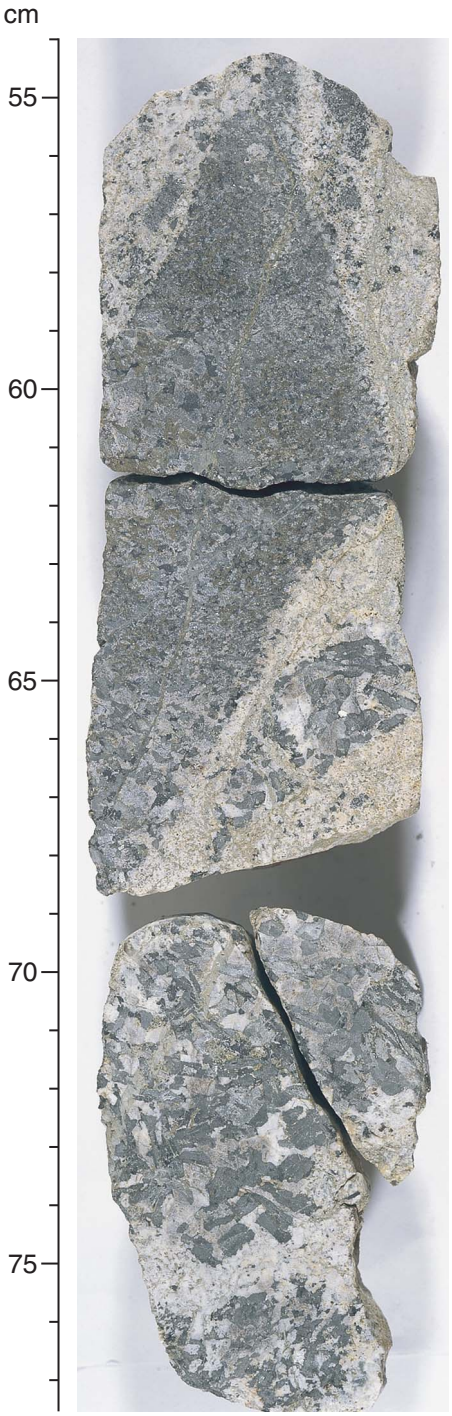

Figure F13. Lithostratigraphic summary for Hole 1275D. TD = total depth.

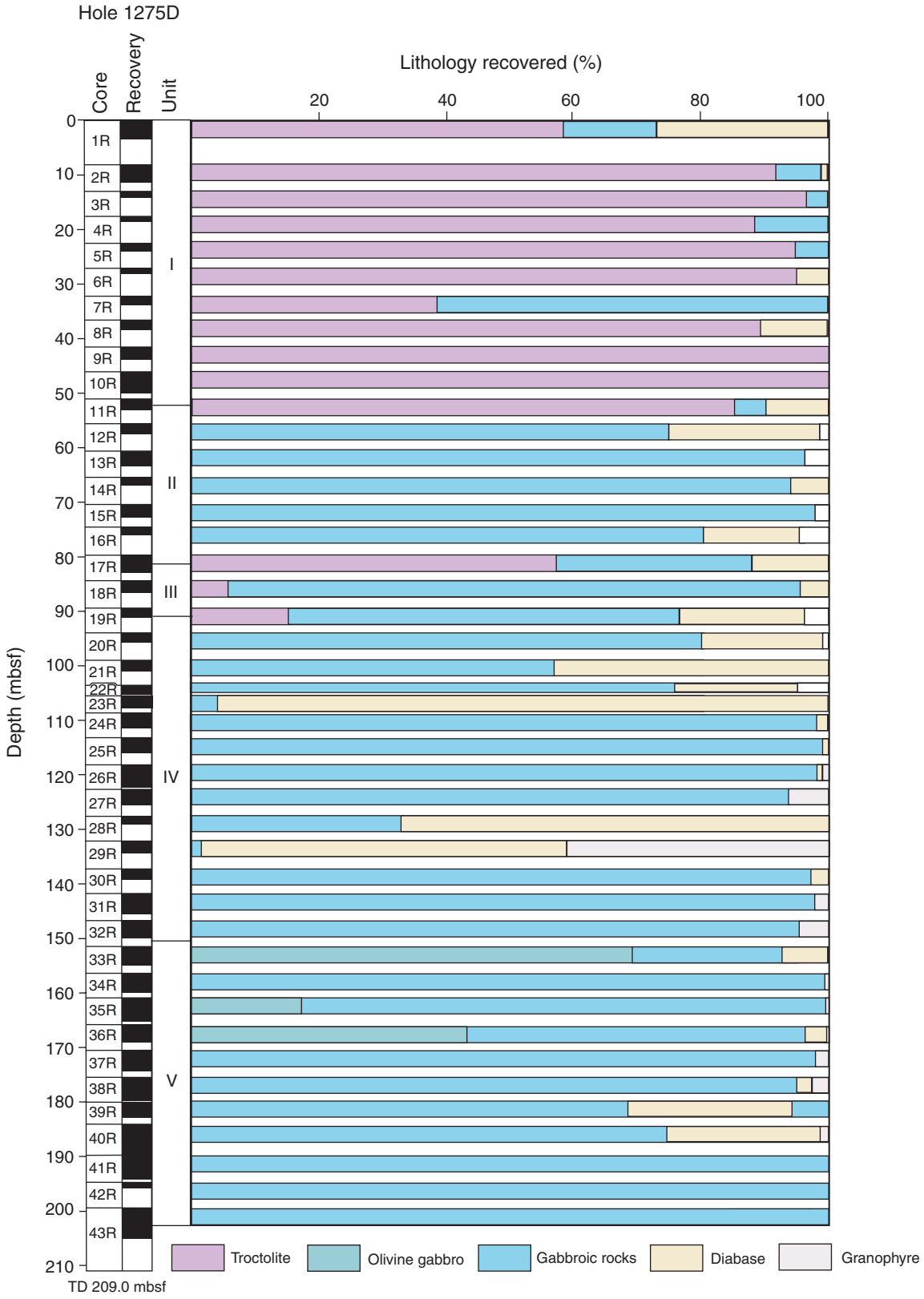

Figure F14. Close-up photograph of an example of a granophyre that has well-defined margins where it cuts the gabbro between 35 and 22 cm, but widens between 24 and 19 cm and becomes less distinct, and finally becomes completely indistinct in the gabbro upsection (interval 209-1275D-13R-2 [Piece 1A, 12–45 cm]).

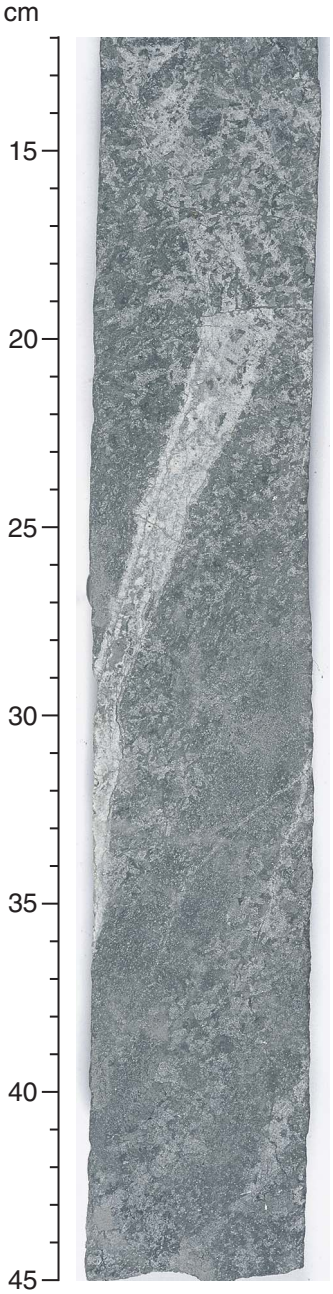

Figure F15. Downhole variations in the grain size in Hole 1275D gabbros. Size classifications are: very fine (<0.2 mm), fine (0.2–2 mm), medium (2–7 mm), and coarse (≥7 mm). TD = total depth.

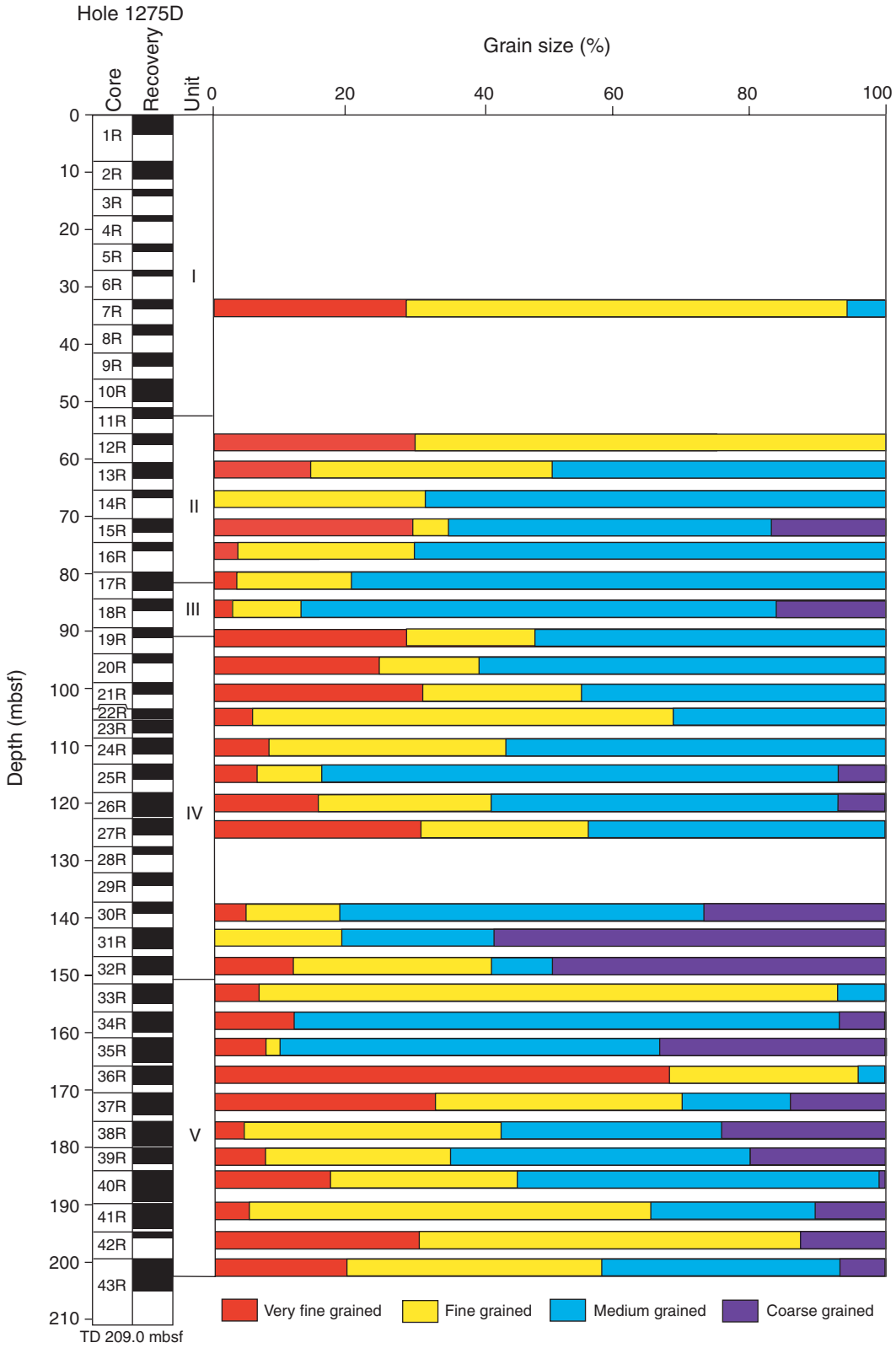

Figure F16. Close-up photograph of olivine gabbro with millimeter-sized olivine grains altered to iddingsite (interval 209-1275D-33R-1 [Piece 5B, 65–80 cm]).

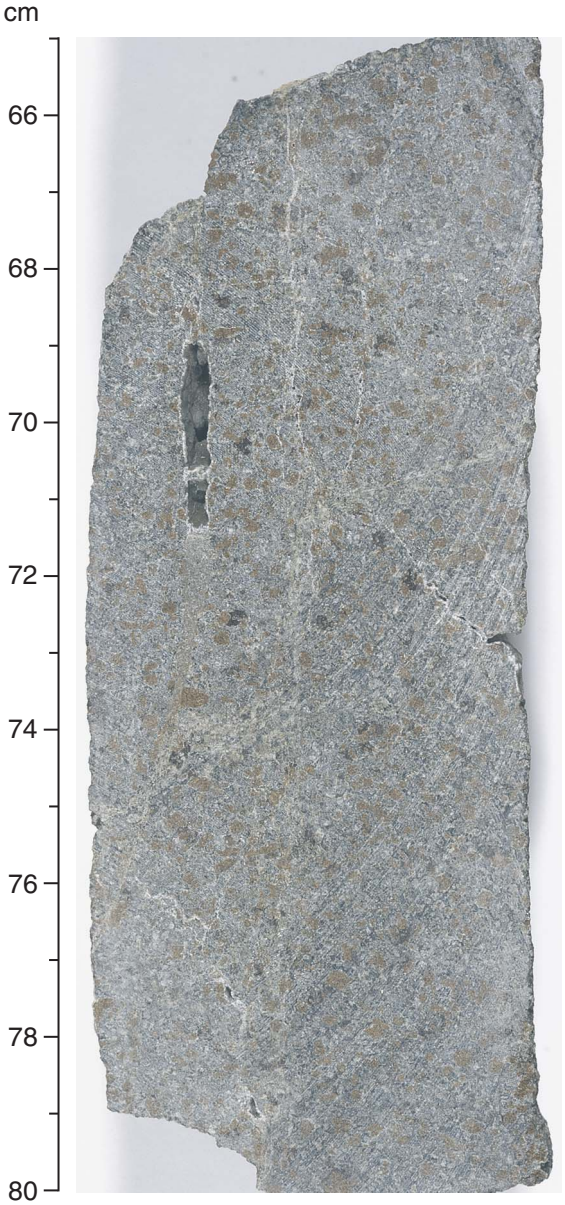

Figure F17. Close-up photographs. **A.** Band of very coarse euhedral orthopyroxene (Opx) crystals in olivine gabbro (interval 209-1275D-35R-4 [Piece 1C, 70–95 cm]). **B.** Olivine and plagioclase phyric diabase mixed with granophyre patches (interval 209-1275D-36R-1 [Piece 10A–10C, 52–74 cm]).

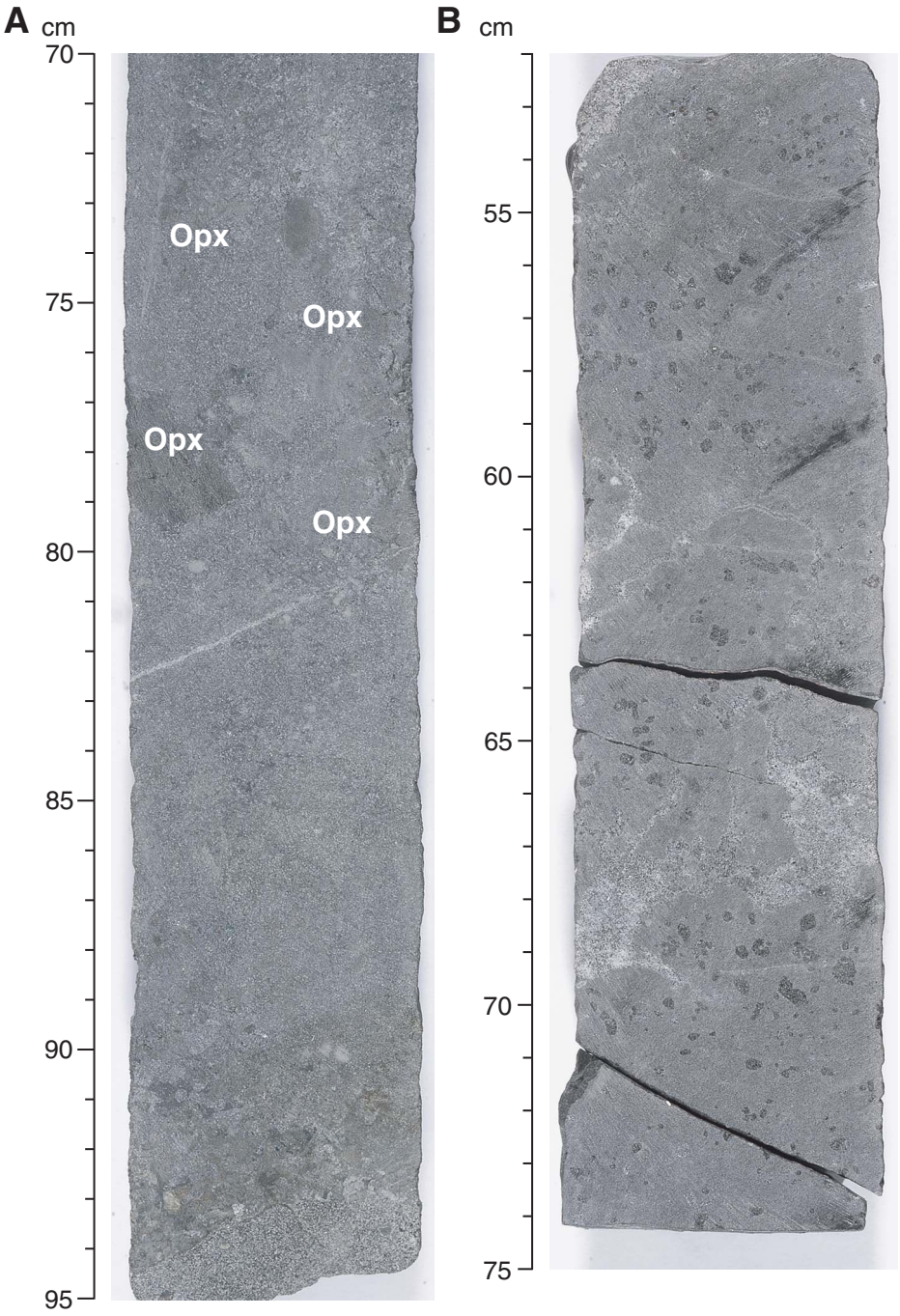

Figure F18. Photomicrograph showing resorbed olivine in orthopyroxene oikocryst. Note how the olivine is isolated by orthopyroxene along the crystal margins (Sample **209-1275B-6R-2, 27–30 cm**) (cross-polarized light: blue + dark gray filters; field of view = 11 mm; image 1275B_046).

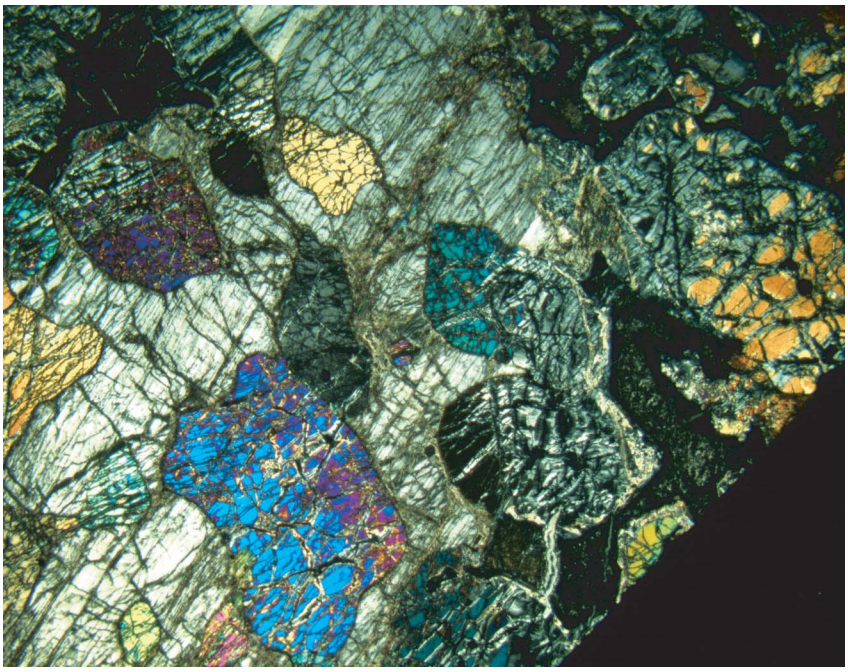

Figure F19. Photomicrographs of Sample **209-1275B-19R-1, 49–51 cm** (cross-polarized light: blue filter). **A.** Example of a bent plagioclase phenocryst that is optically zoned and lacks polysynthetic twinning (field of view = 2.75 mm; image 1275B_037). **B.** Skeletal plagioclase enclosing crystals of clinopyroxene and olivine (field of view = 1.4 mm; image 1275B_036).

A

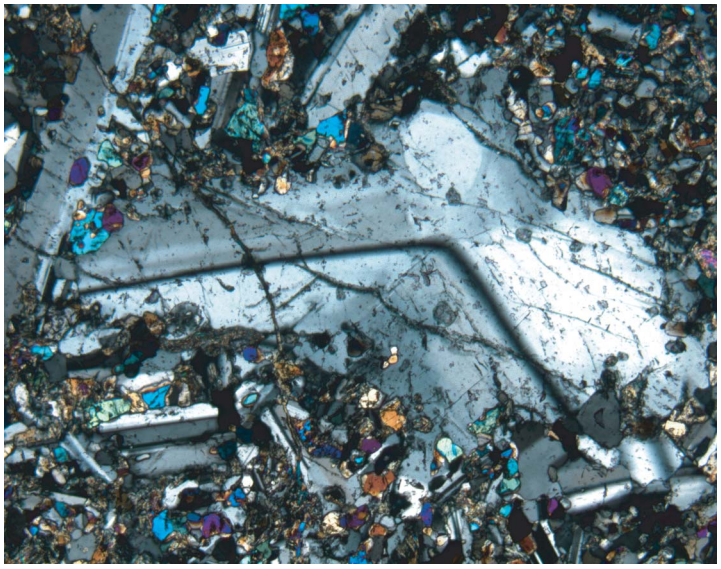

B

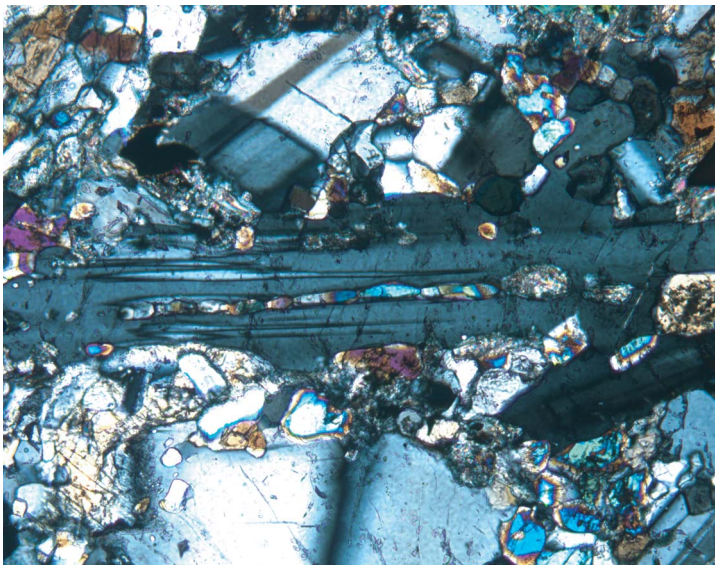

Figure F20. Photomicrographs showing alteration of gabbro. **A, B.** Granophyre in a porphyritic diabase (Sample 209-1275D-36R-1, 70–72 cm) (field of view = 11 mm); (A) plane-polarized light (PPL): blue + light gray filters; image 1275D_025; (B) cross-polarized light (XPL): blue + light gray filters; image 1275D_026. **C, D.** General view of altered olivine gabbro (Sample 209-1275D-33R-1, 22–24 cm) (field of view = 11 mm); (C) PPL: blue + light gray filters; image 1275D_023; (D) XPL: blue + light gray filters; image 1275D_024).

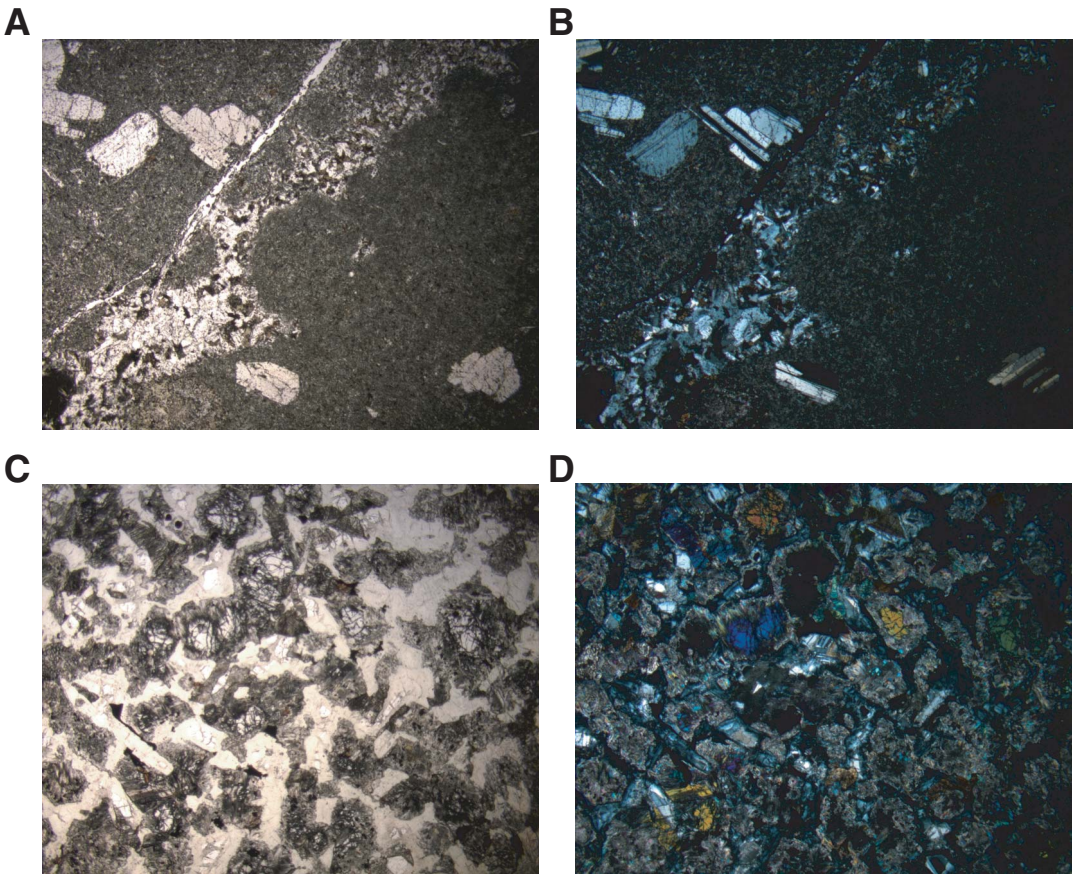

Figure F21. Photomicrographs showing clinopyroxene and oxides in fine-grained oxide gabbro (Sample 209-1275B-10R-2, 41–44 cm) (field of view = 11 mm). **A.** plane-polarized light: blue + dark gray filters; image 1275B_050. **B.** cross-polarized light: blue filter; image 1275B_049.

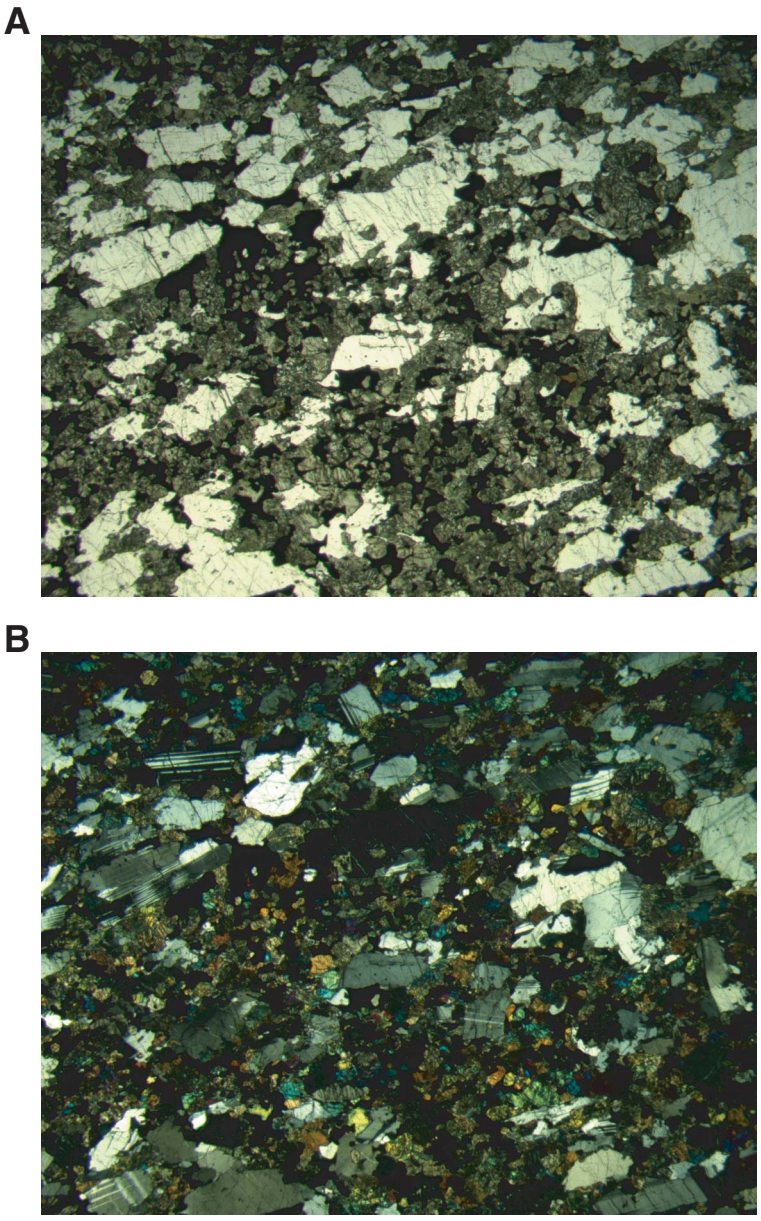

Figure F22. Covariation diagram for visually estimated oxide proportion (vol%) against magnetic susceptibility determined for each piece of oxide gabbro from Hole 1275B. Open circles = individual pieces, large red circles = averages of magnetic susceptibility measurements binned by 5% visual oxide estimates.

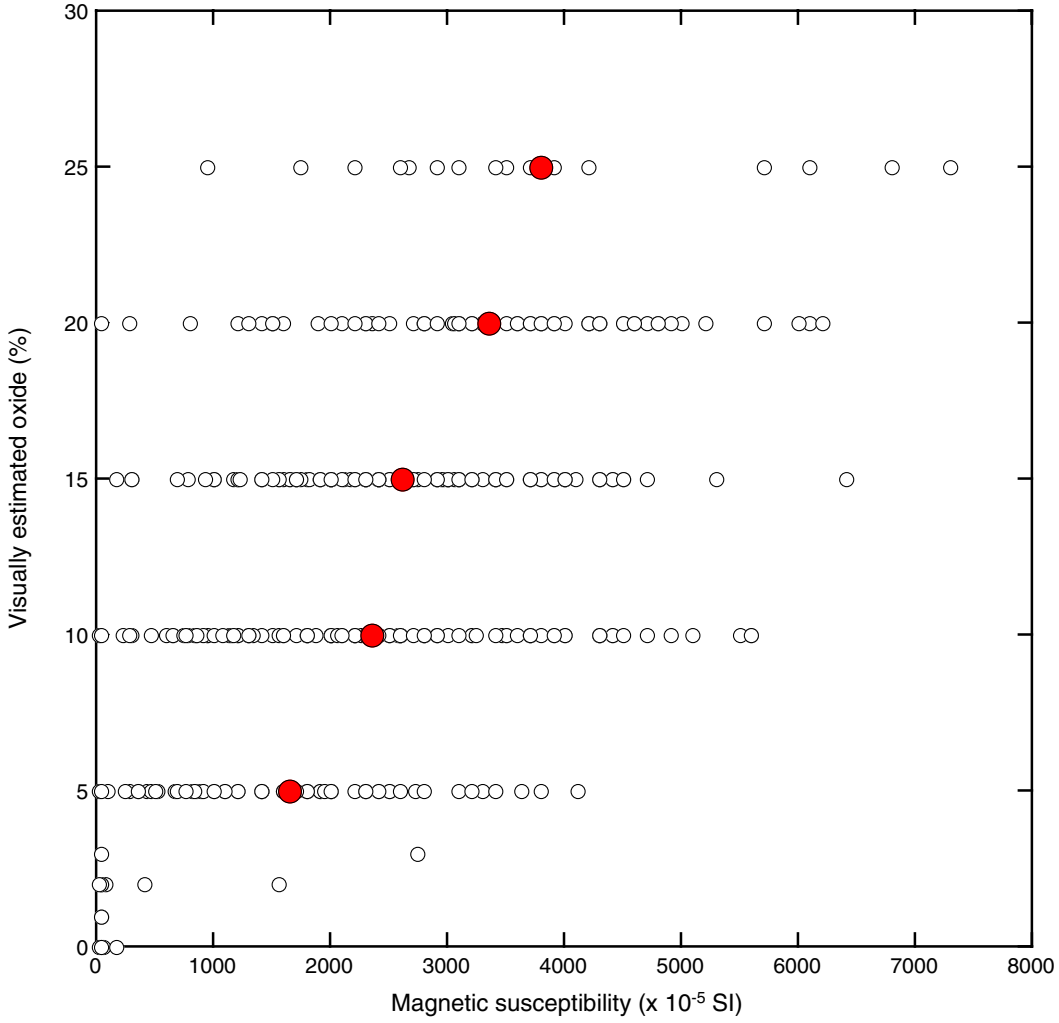

Figure F23. Covariation diagrams for visually estimated oxide proportion (vol%) against magnetic susceptibility determined for each piece of gabbro from Hole 1275B. Each plot summarizes the data for a given range of grain sizes: very fine (<0.2 mm), fine (0.2–2 mm), medium (2–7 mm), and coarse (≥7 mm). All plots show a broad positive correlation. The data for magnetic susceptibility are corrected to the susceptibility for whole-round core with a diameter of 6 cm.

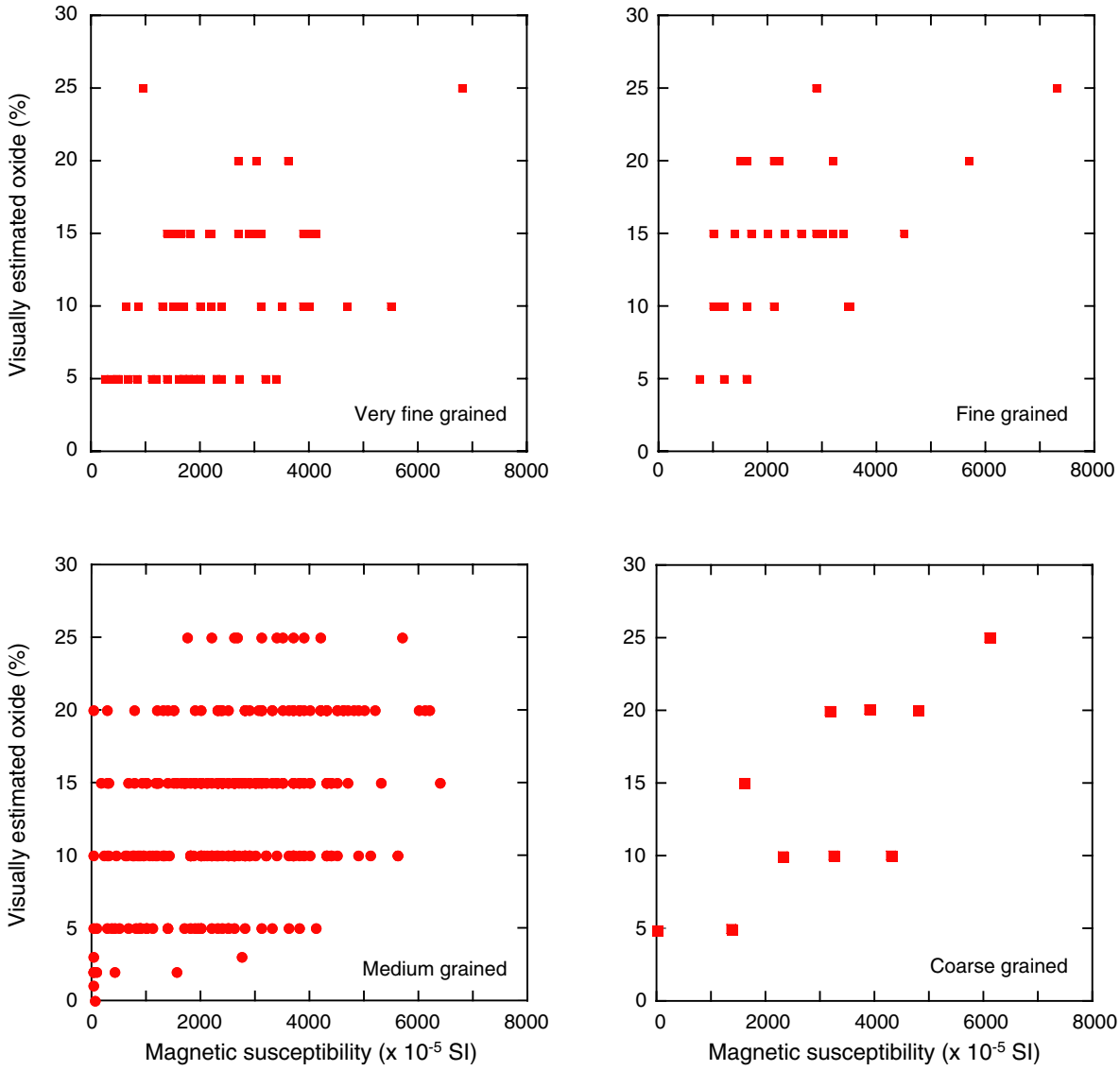

Figure F24. Downhole variation of modal magnetite in Hole 1275B determined on the basis of magnetic susceptibility (left panel) is compared to visual estimates of oxide proportions (right panel). Light blue bars indicate the depth ranges of recovered cores. TD = total depth.

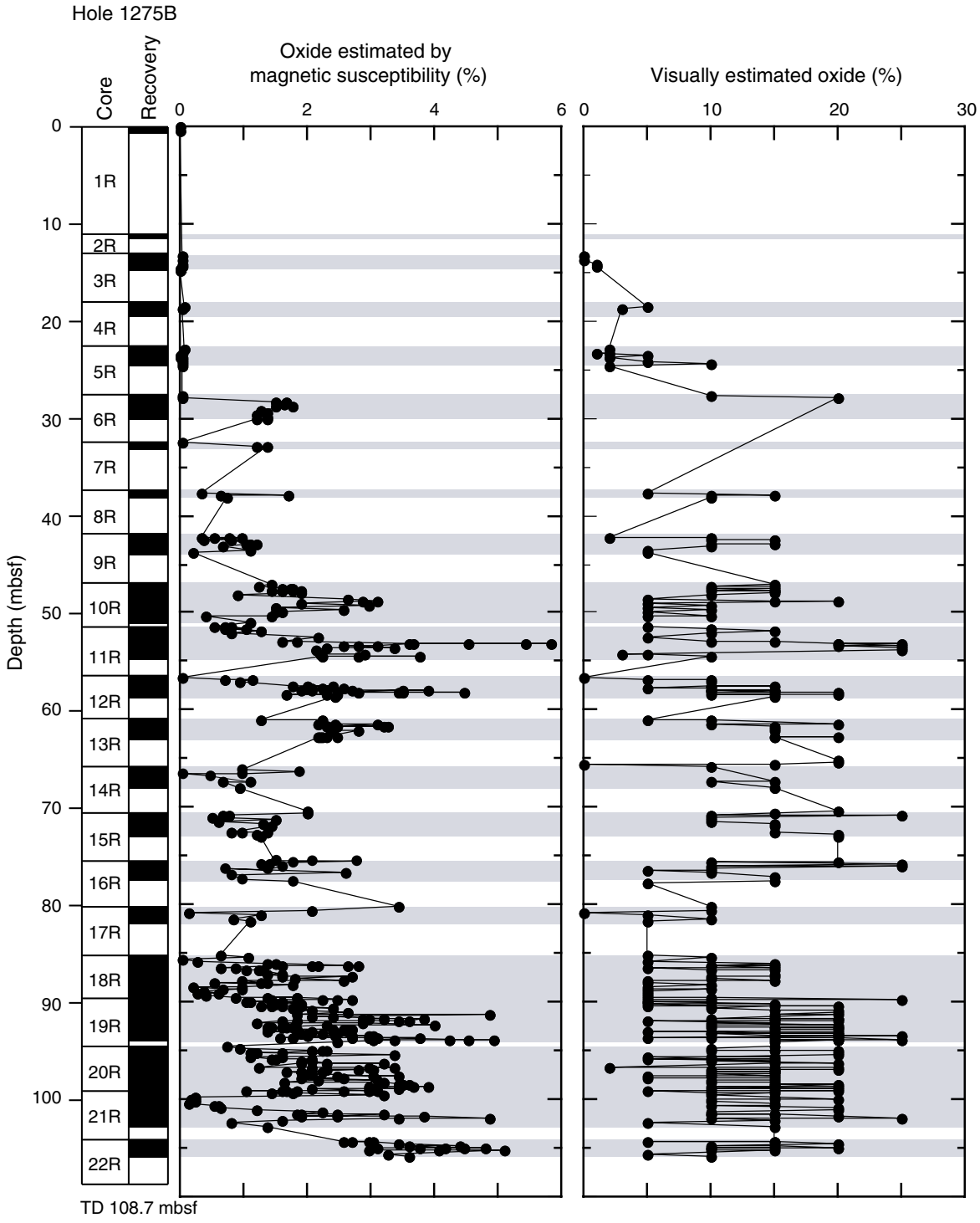

Figure F25. Downhole variation of modal magnetite in Hole 1275D determined on the basis of magnetic susceptibility. Measurements were made every 2 cm and then the data were trimmed such that only data on pieces at least 6 cm in length are presented. TD = total depth.

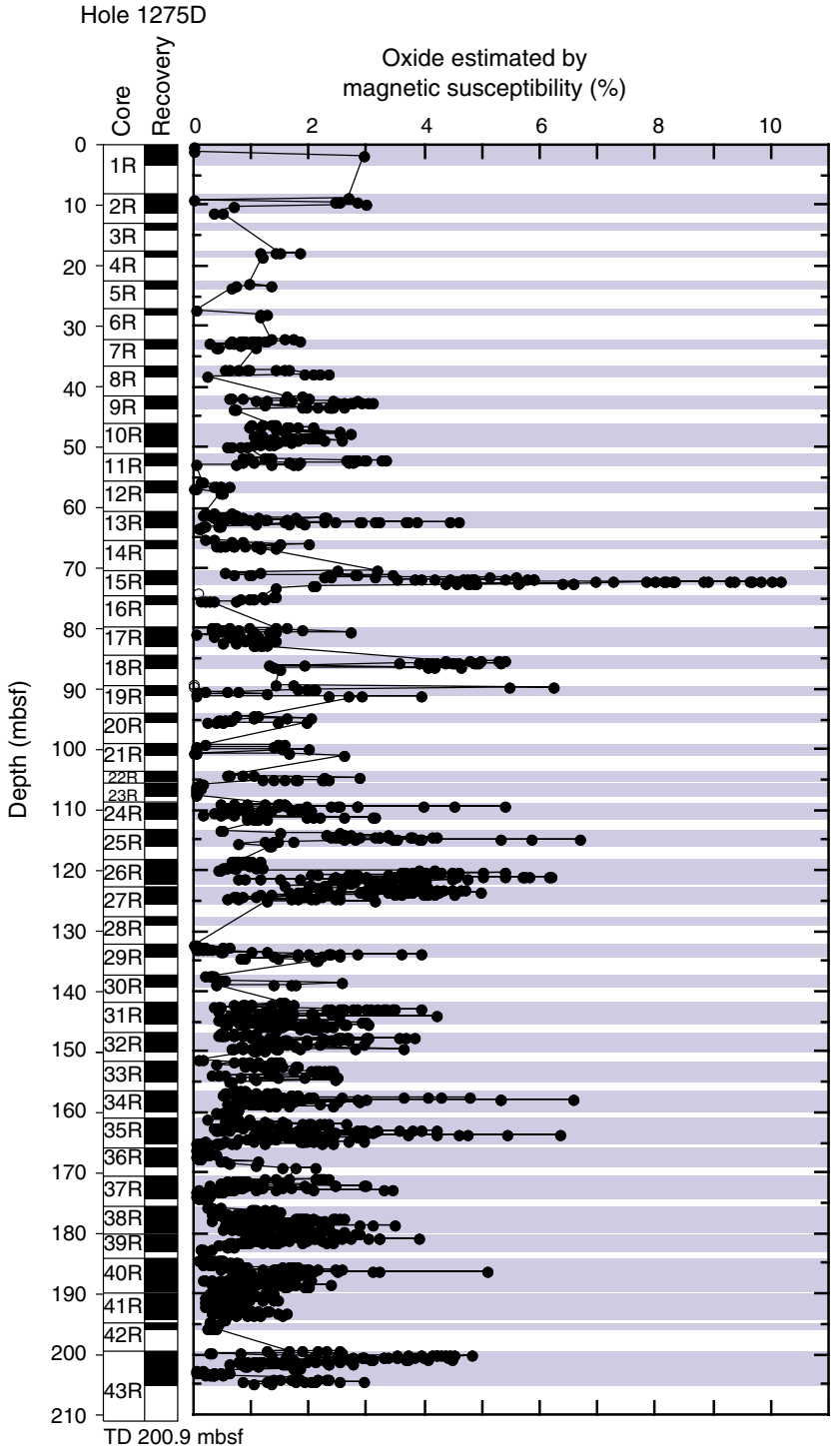

Figure F26. Details of the variation in modal magnetite in sections of Hole 1275D. Note that large variations in magnetite content take place over small spatial scales. The depths for relatively long continuous pieces are highlighted by yellow bands. **A.** Section 209-1275D-15R-2 (Pieces 1A–1D). **B.** Core 209-1275D-35R. (Continued on next page.)

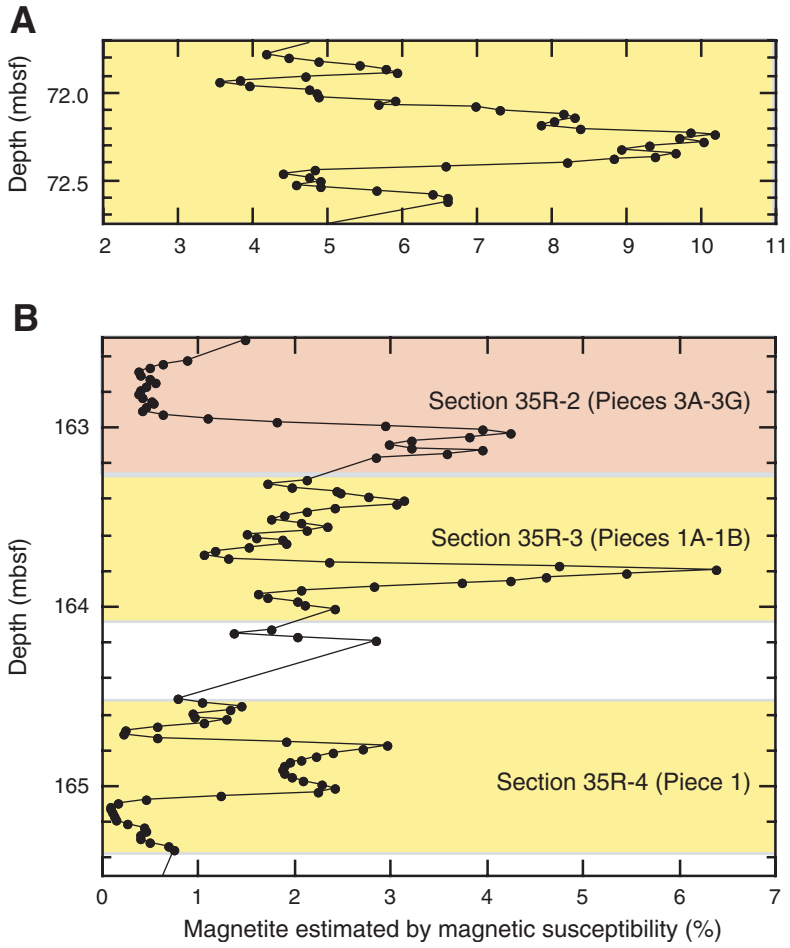

Figure F26 (continued). **C.** Core 209-1275D-40R. **D.** Core 209-1275D-43R.

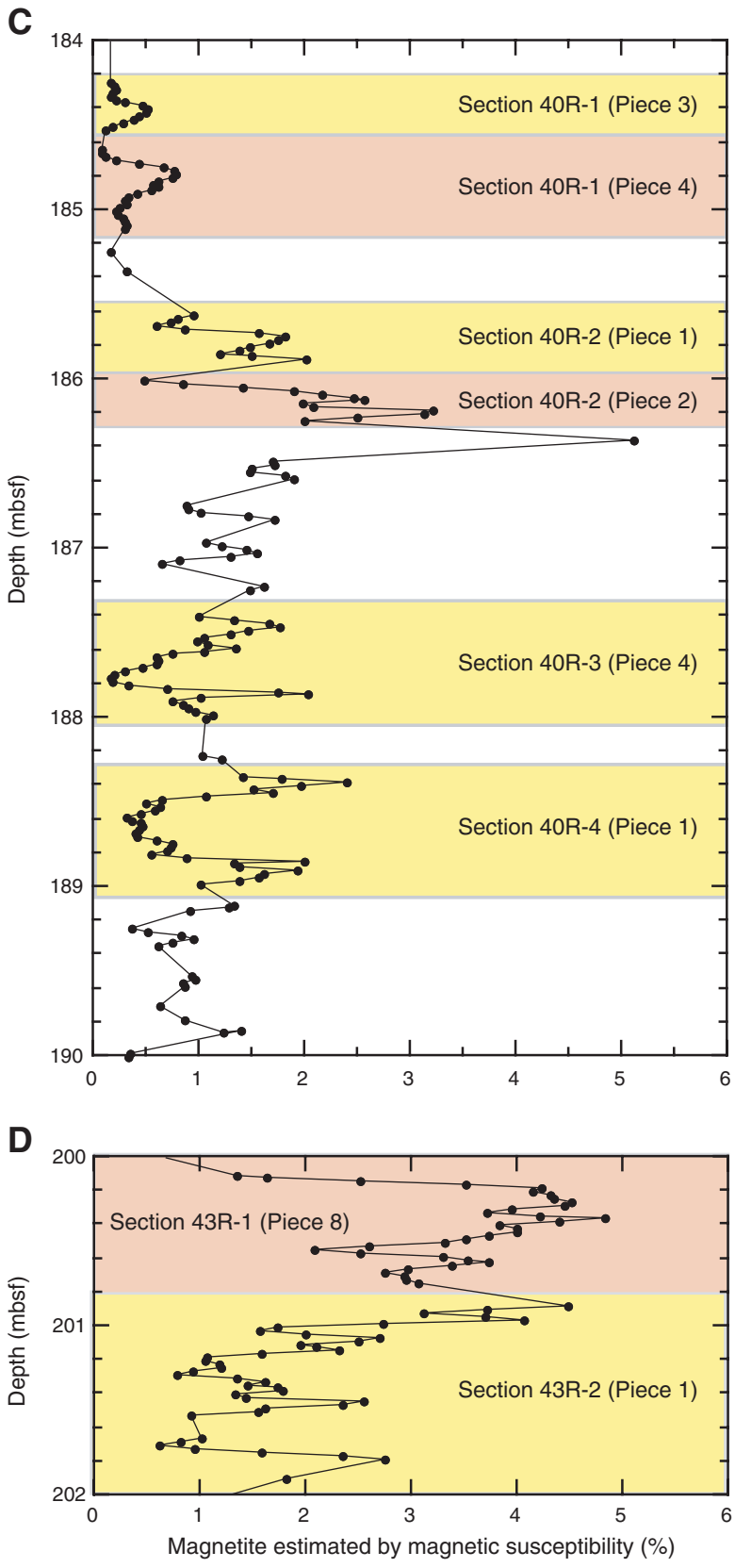

Figure F27. Photomicrographs showing plagioclase (Sample 209-1275B-17R-1, 60–62 cm) (cross-polarized light: blue filter; field of view = 2.75 mm). **A.** Broken plagioclase crystals infilled and partially replaced by oxide (image 1275B_022). **B.** Plagioclase neoblasts developed at the junction of two grains (image 1275B-023).

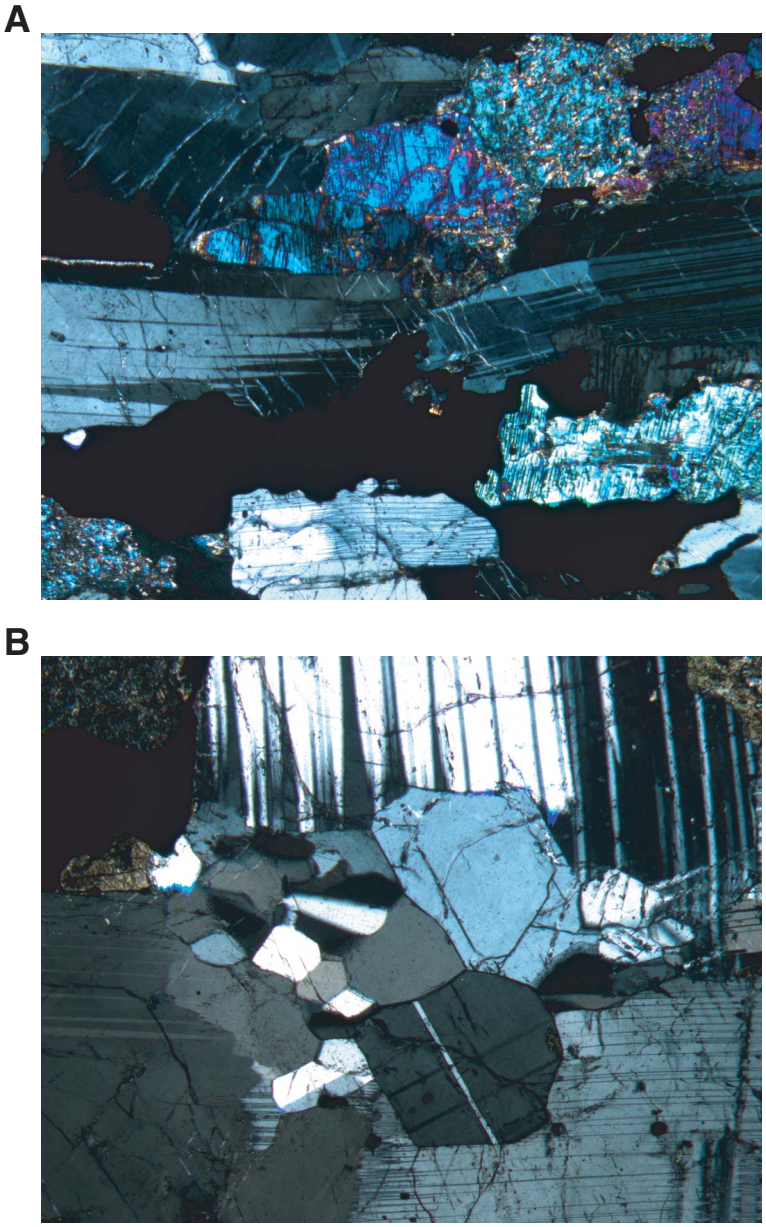

Figure F28. Photomicrograph showing large resorbed plagioclase grain that is optically discontinuous (Sample 209-1275B-21R-3, 28–30 cm) (field of view = 11 mm). **A.** plane-polarized light: blue + dark gray filters; image 1275B_043. **B.** cross-polarized light: blue filter + gypsum plate; image 1275B_041.

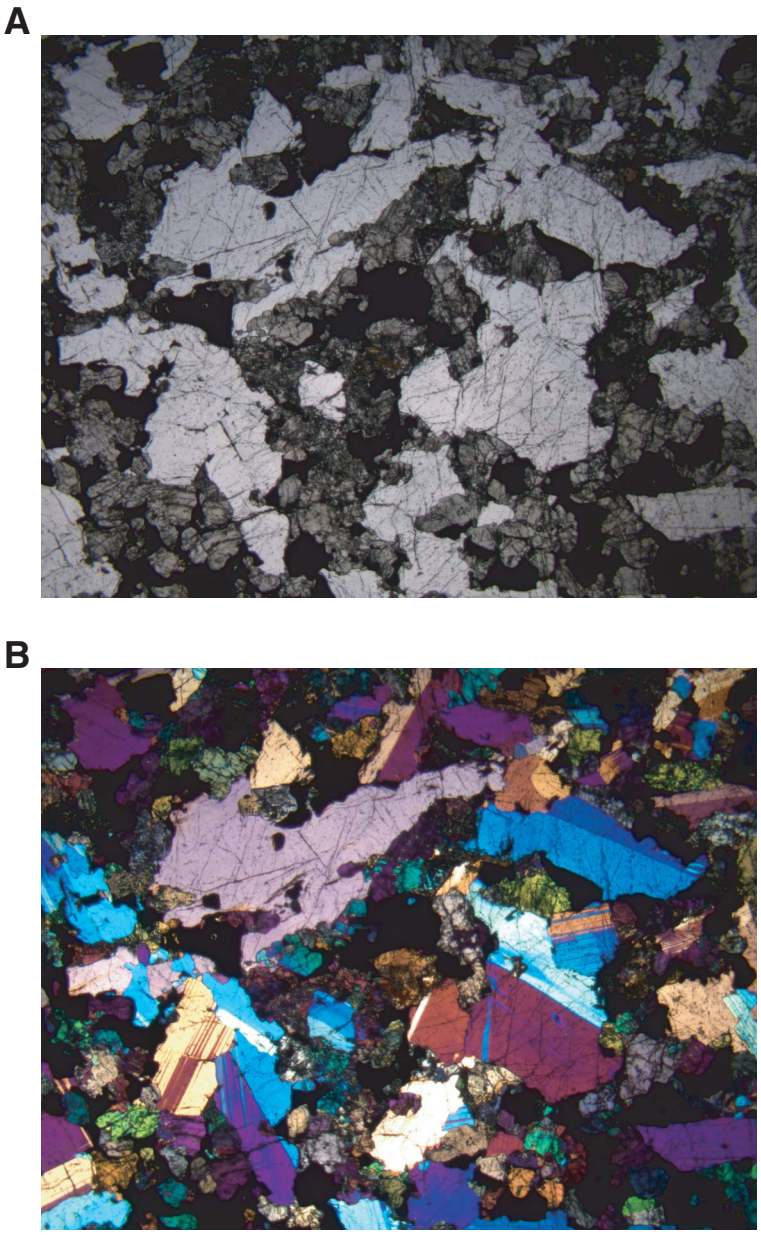

Figure F29. Photomicrographs showing large resorbed plagioclase grain that is optically discontinuous and cemented by oxide (Sample 209-1275B-19R-1, 135–137 cm) (field of view = 2.75 mm). **A.** plane-polarized light: blue + dark gray + light gray filters; image 1275B_045. **B.** cross-polarized light: blue + dark gray filters; image 1275B_044.

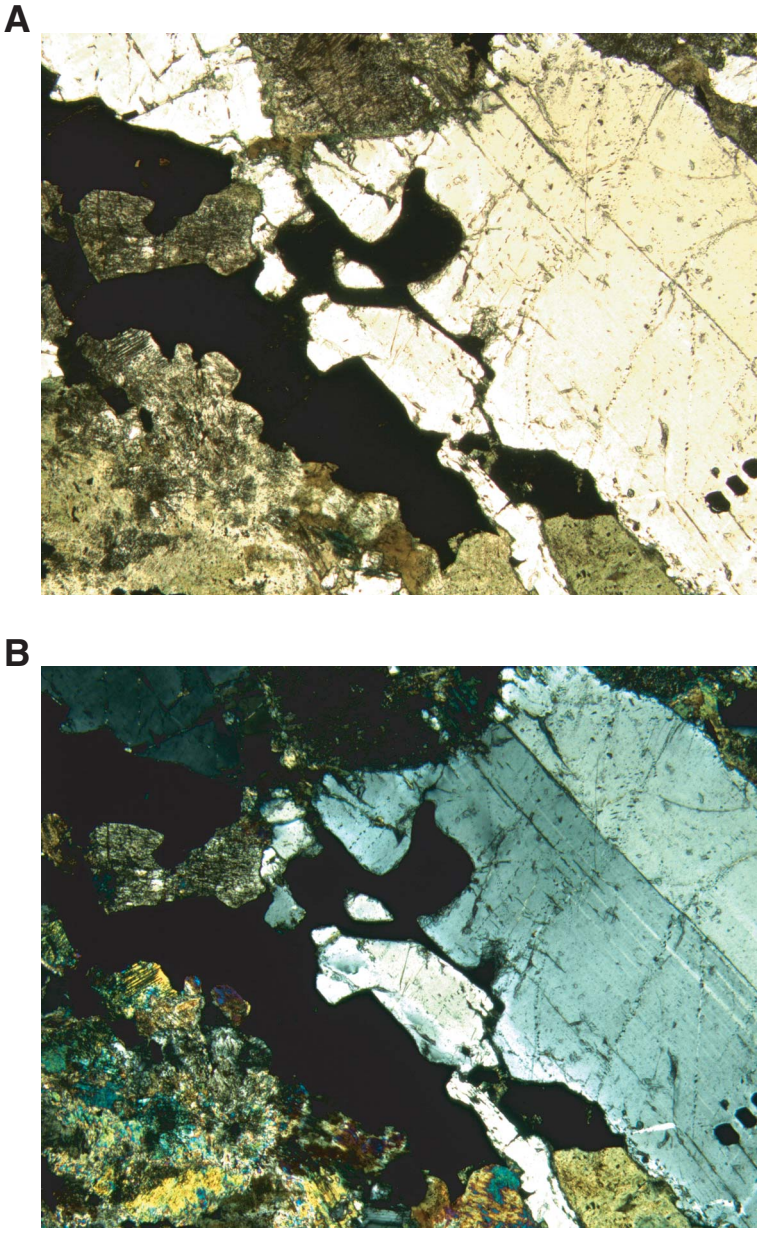

Figure F30. Photomicrograph showing clinopyroxene that exsolved a large amount of orthopyroxene (Sample 209-1275B-20R-2, 4–6 cm) (cross-polarized light: blue filter; field of view = 11 mm; image 1275B_038).

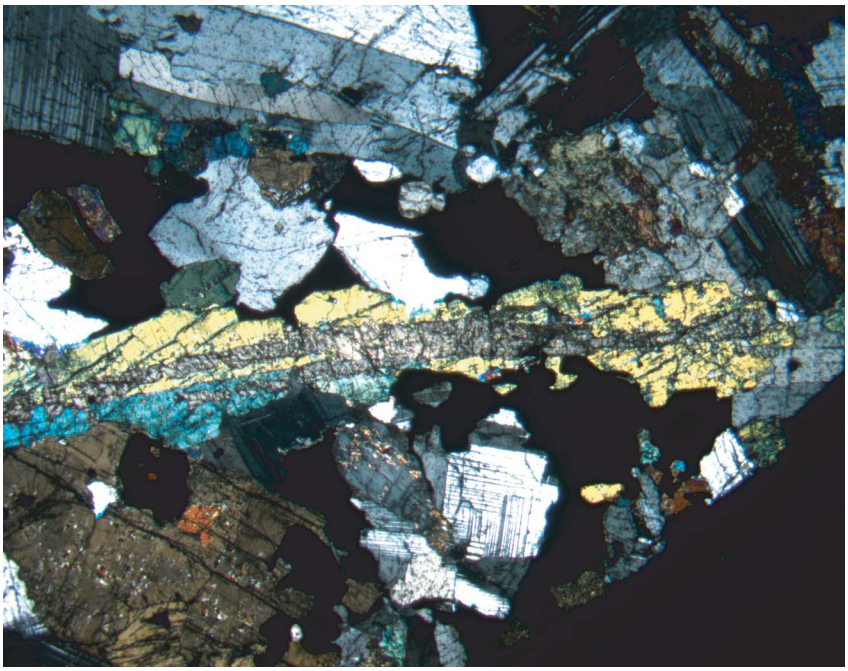

Figure F31. Photomicrographs showing a cluster of apatite crystals, many of which are in optical continuity associated with orthopyroxene, clinopyroxene, plagioclase, and oxide (Sample 209-1275B-12R-2, 57–60 cm) (field of view = 2.75 mm). **A.** plane-polarized light: blue + dark gray filters; image 1275B_053. **B.** Two optically continuous apatite grains are designated as Ap1 and Ap2. cross-polarized light: blue filter + gypsum plate; image 1275B_051.

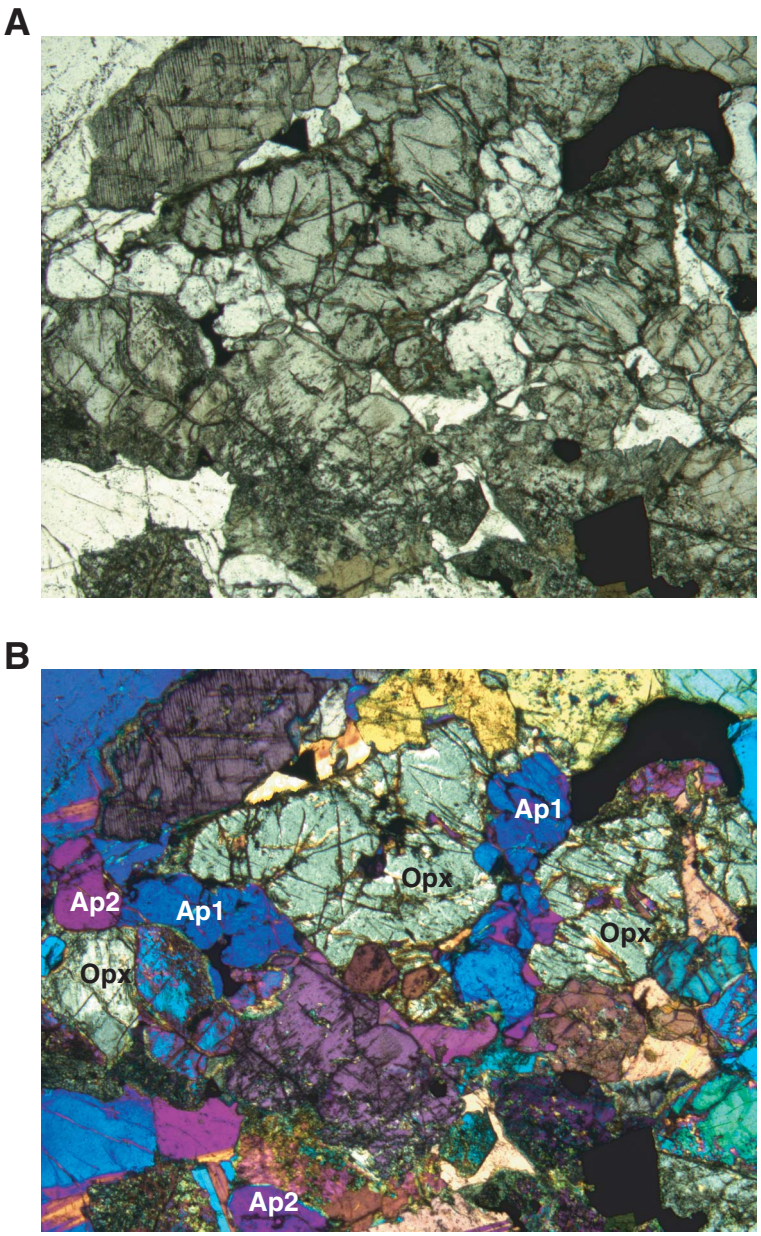

Figure F32. Photomicrographs showing plagioclase and clinopyroxene being pseudomorphed (Sample 209-1275B-19R-1, 135–137 cm) (cross-polarized light: blue filter; field of view = 2.75 mm). **A.** Plagioclase pseudomorphed by more albitic plagioclase along the path of a granophyre vein (image 1275B_024). **B.** Clinopyroxene pseudomorphed by amphibole along the path of a granophyric dikelet (image 1275B_025).

A

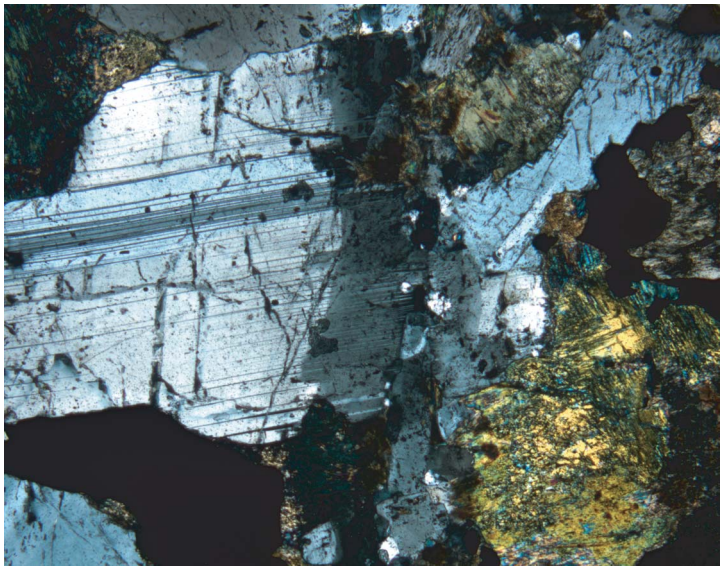

B

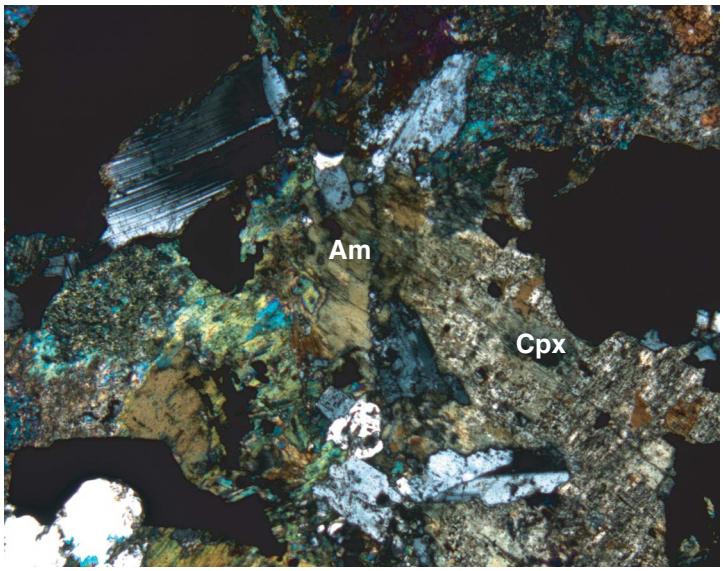

Figure F33. Photomicrographs showing a coarser-grained patch (Sample 209-1275D-40R-1, 126–129 cm). **A.** Textural relations between an olivine-plagioclase phyric diabase and granophyric material enclosed in it (coarser-grained patch) (plane-polarized light [PPL]: blue + light gray filters; field of view [FOV] = 11 mm; image 1275D_20. **B, C.** Close-up images of the coarser-grained patch made of plagioclase, amphibole, and titanite all enclosing acicular apatite; (B) PPL: blue + light gray filters; FOV = 1.4 mm; image 1275D_021; (C) cross-polarized light: blue + light gray filters; FOV = 1.4 mm; image 1275D_022.

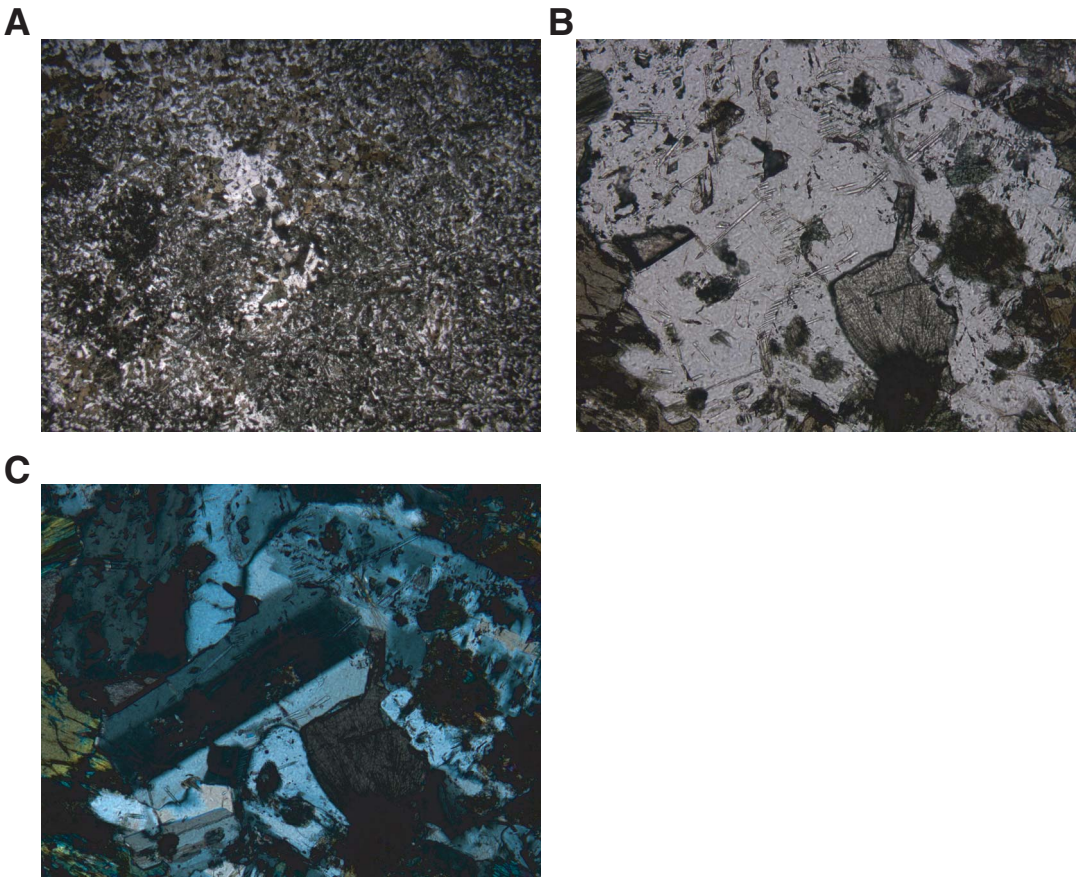

Figure F34. Downhole variation in alteration intensity of Hole 1275B. The running average excludes magmatic veins and diabase.

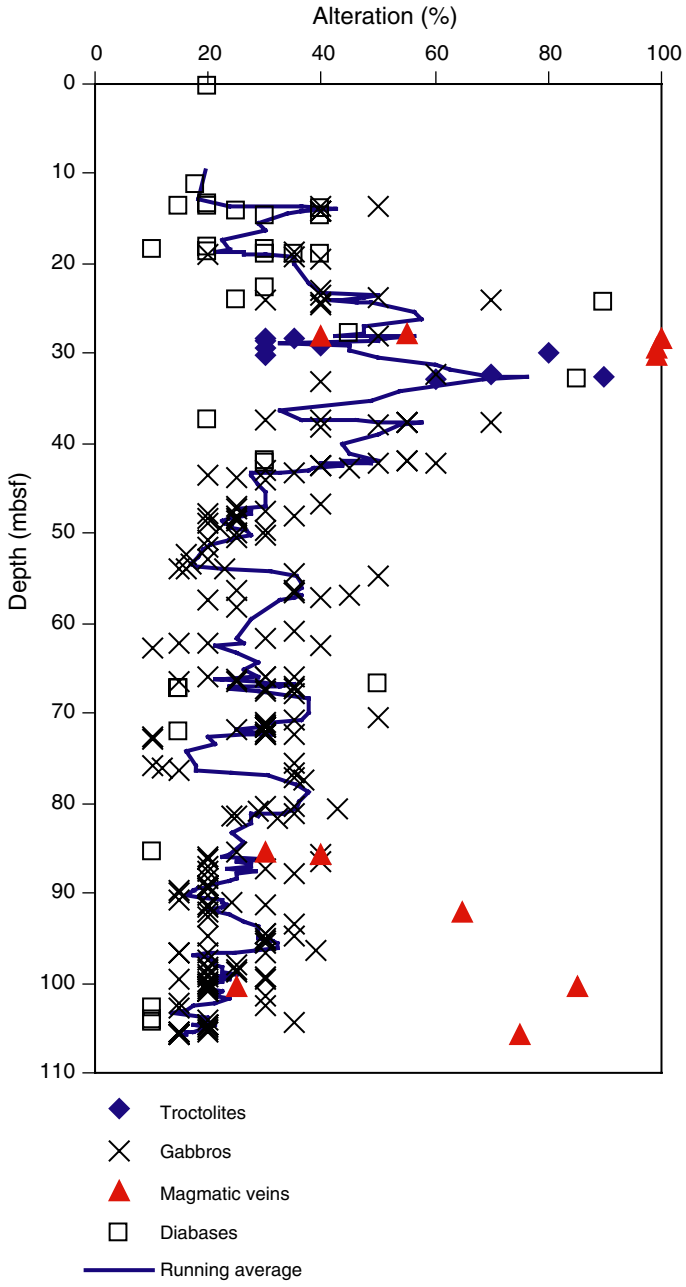

Figure F35. A. Photograph of hand specimen of moderately altered gabbro (interval 209-1275B-5R-1, 135–145 cm). **B.** In this part of Hole 1275B titanite (ti) is a common accessory phase. In thin section a photomicrograph shows that titanite forms rims along the margins of hematite (h) and borders against secondary plagioclase with acicular amphibole (arrow). Quartz (q) with amphibole needles is present in the lower right corner (Sample **209-1275B-5R-1, 134–137 cm**) (cross-polarized light: blue filter; field of view = 1.4 mm; image 1275B_004). **C.** The X-ray diffractogram of Sample 209-1275B-5R-1, 134–137 cm, is dominated by peaks of plagioclase and amphibole. Minor peaks diagnostic of titanite confirm the petrographic observation that it is an abundant phase in the upper gabbro/diabase sequence of Hole 1275B.

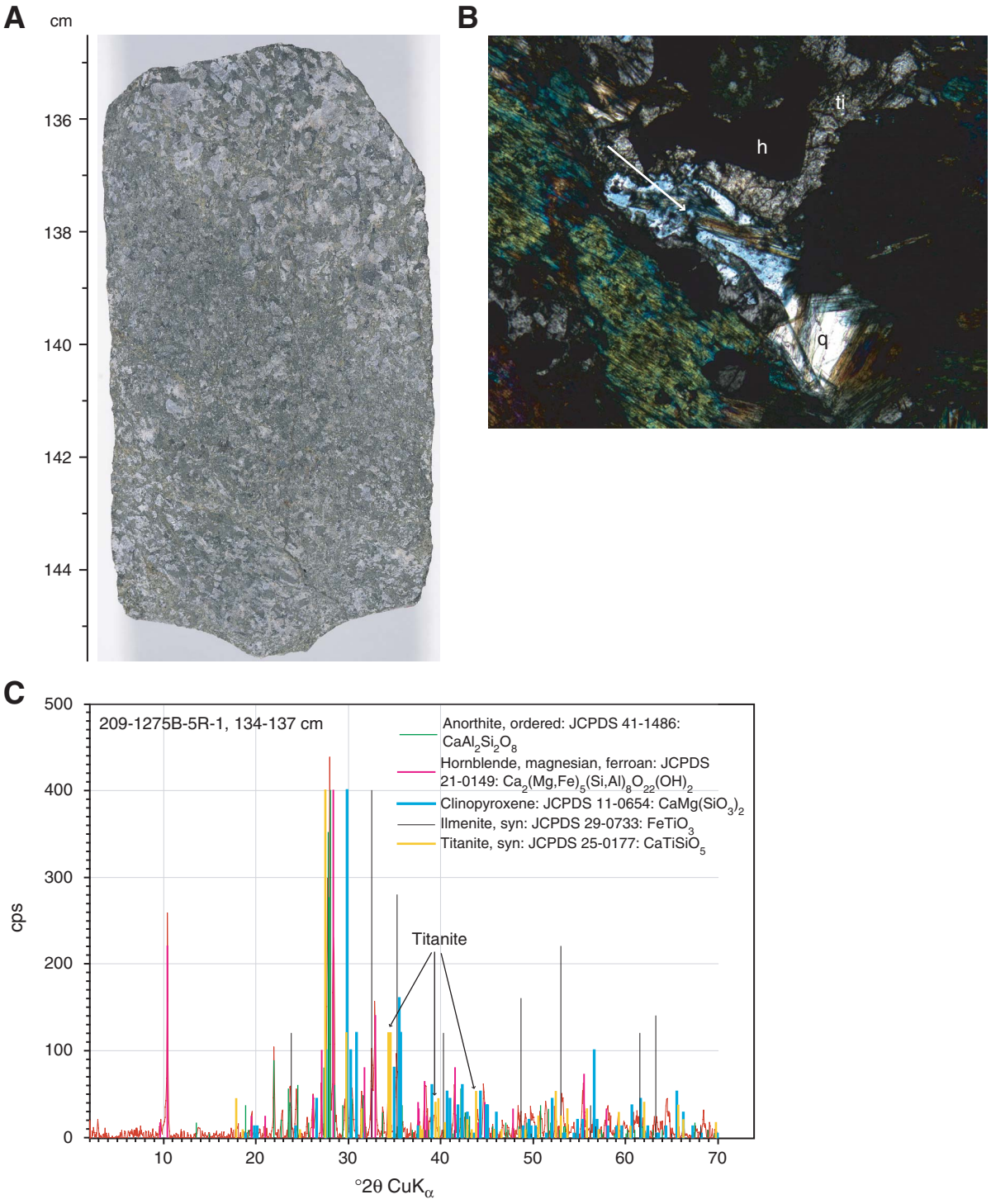

Figure F36. A. Photograph of hand specimen of a typical moderately altered gabbro from the lower gabbro sequence of Hole 1275B. A narrow, completely altered, composite magmatic vein is indicated by the arrow (interval 209-1275B-14R-1, 50–60 cm). **B.** Photomicrograph showing the moderate alteration of the gabbro dominated by replacement of pyroxene (px) by aggregates of fibrous green amphibole (ga). Brown amphibole (ba) of uncertain magmatic or hydrothermal origin is a minor component. The plagioclase (pl) is mostly fresh (Sample **209-1275B-14R-1, 50–53 cm**) (plane-polarized light: blue + light gray filters; field of view = 1.4 mm; image 1275B_015).

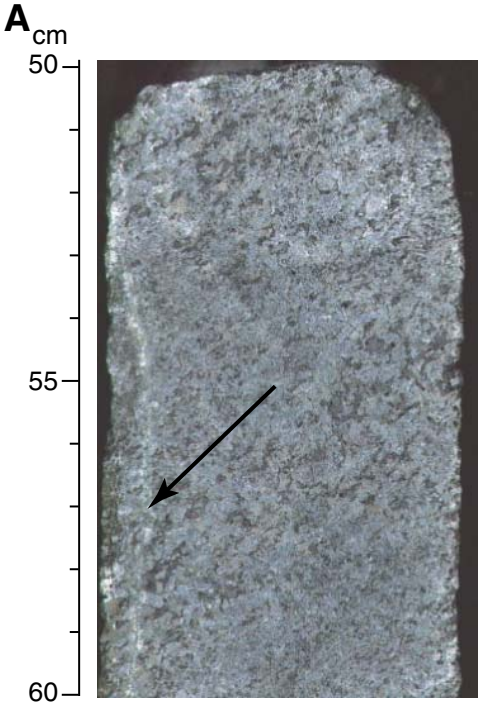

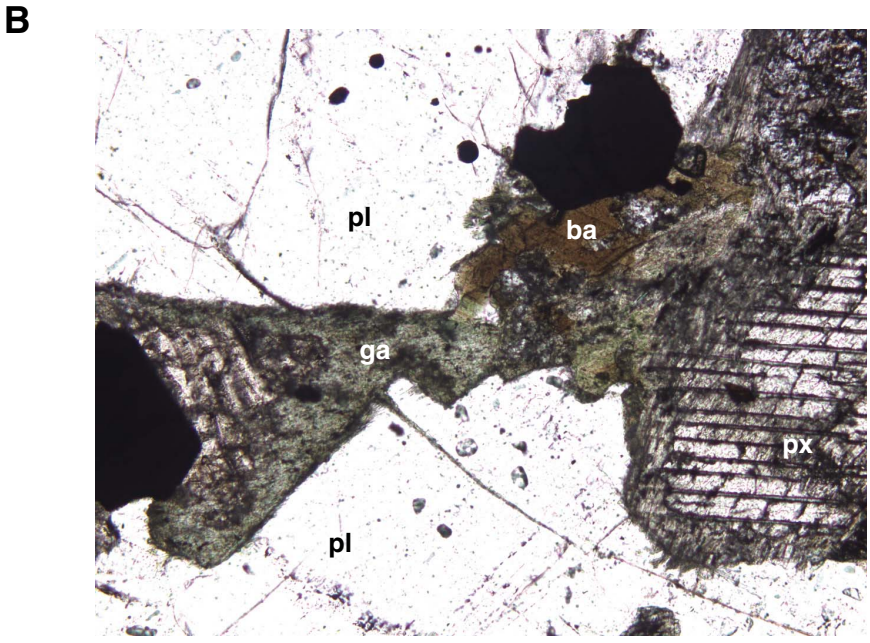

Figure F37. Photomicrograph showing alteration of plagioclase largely restricted to minor replacement by feathery green amphibole along internal cracks (Sample **209-1275B-18R-2, 9–12 cm**) (plane-polarized light: blue + light gray filters; field of view = 0.7 mm; image 1275B_016).

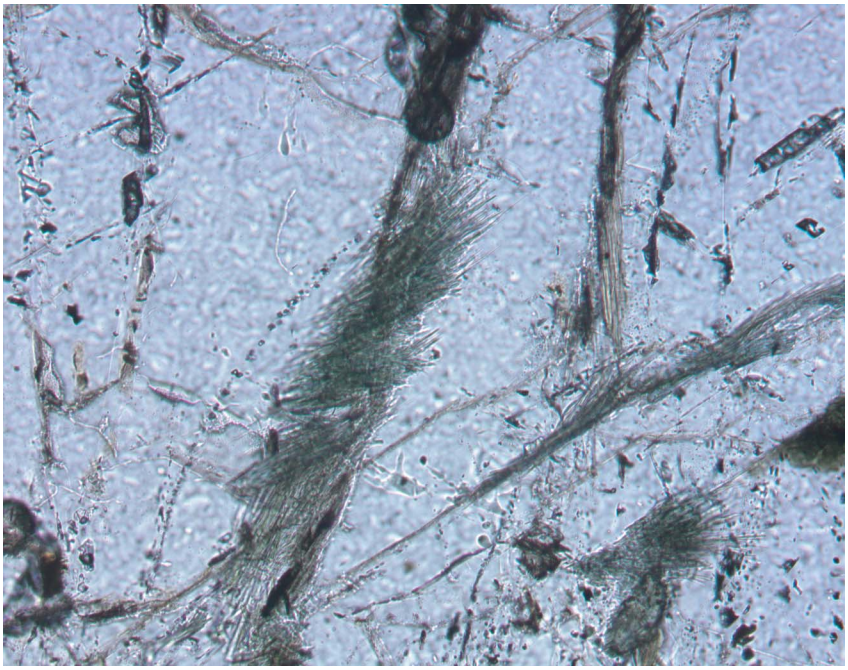

Figure F38. Photomicrograph showing subsolidus exsolution/oxidation of trellislike ilmenite lamellae, together with host magnetite, representing breakdown products of a primary Fe-Ti oxide (Sample **209-1275B-12R-2, 57–60 cm**) (reflected light; field of view = 1.4 mm; image 1275B_012).

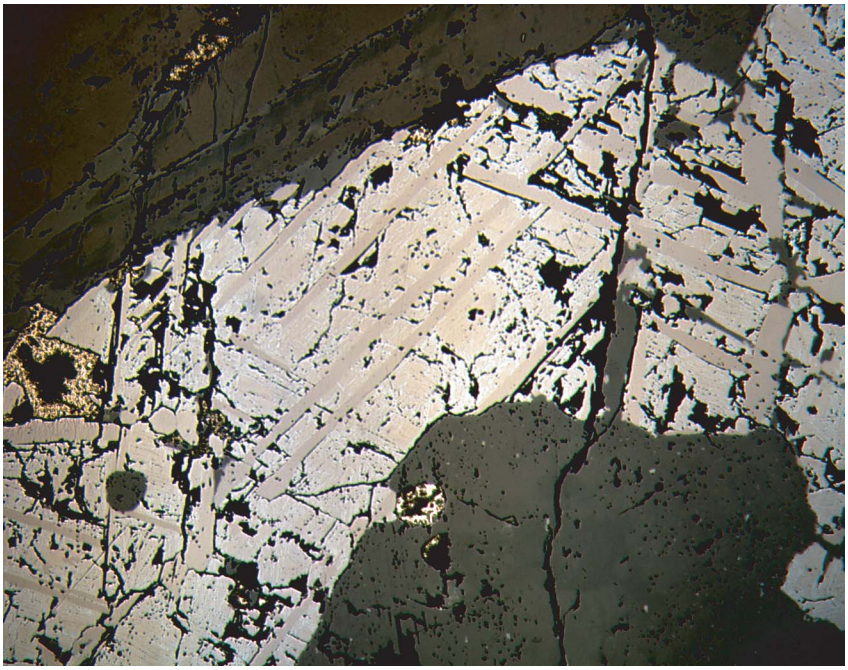

Figure F39. A. Photograph of felsic dikes and veins that are common in Hole 1275B and may be present as well-defined dikelets or irregular, patchy domains (interval 209-1275B-18R-1, 54–69 cm). **B.** Photomicrograph of a felsic vein in which carbonate (ca) encloses numerous plagioclase grains. The rectangle shows the position of enlargement pictured in C (Sample **209-1275B-18R-1, 66–70 cm**) (cross-polarized light: blue + dark gray filters; field of view = 2.75 mm; image 1275B_047). **C.** Enlargement of the area outlined by the rectangle in B. Carbonate appears to replace plagioclase. There are abundant fibrous needlelike crystals within the carbonate which could be apatite, tremolite, or zeolite (Sample **209-1275B-18R-1, 66–70 cm**) (cross-polarized light: blue + light gray filters; field of view = 0.7 mm; image 1275B_048).

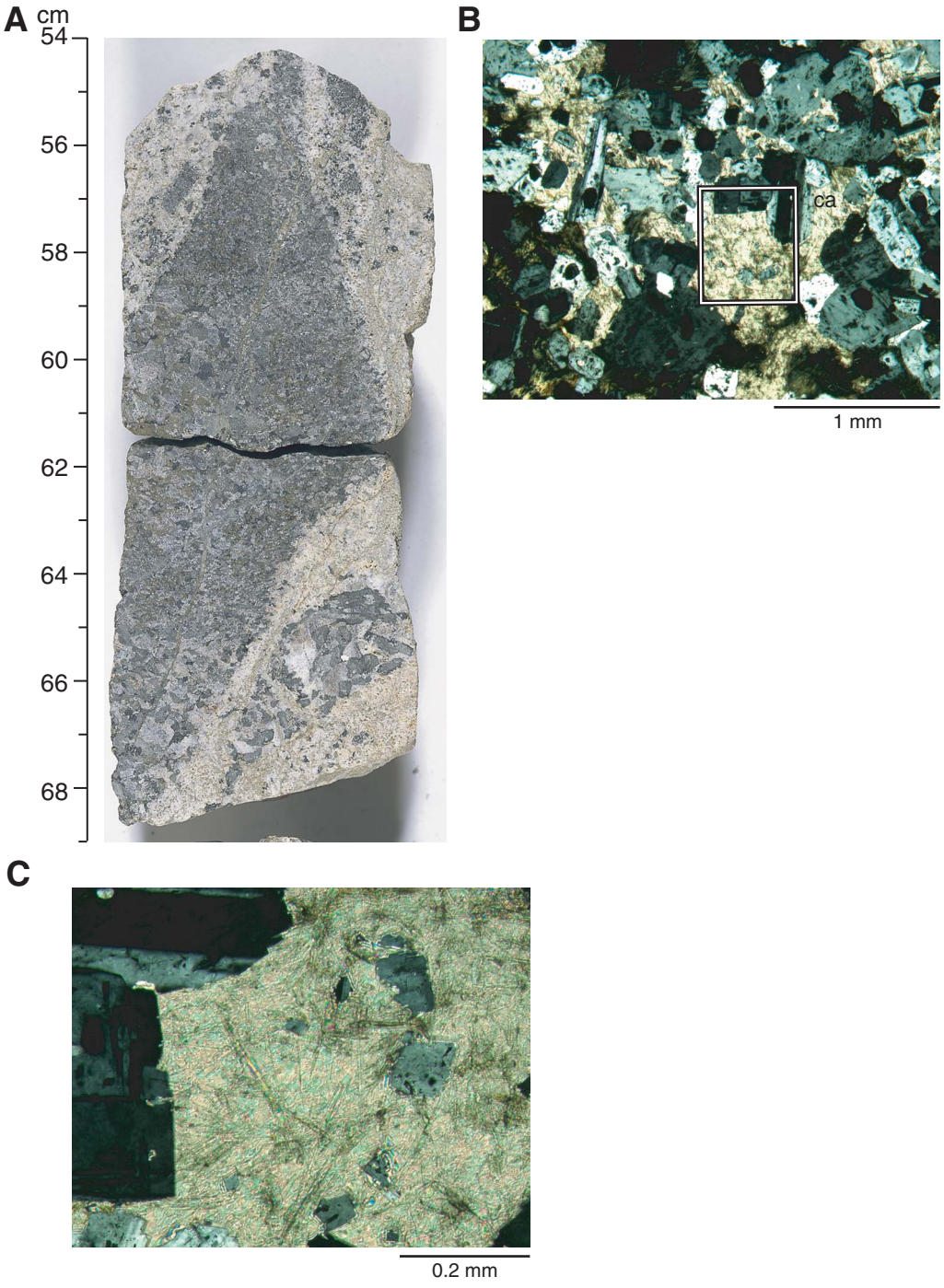

Figure F40. A. Close-up photograph of typical troctolite from the 28.3- to 34.1-mbsf interval in Hole 1275B, showing prominent plagioclase-rich domains that may be interpreted as melt impregnation features (interval 209-1275B-6R-2, 104–112 cm). **B.** Photomicrograph showing the plagioclase (p) in troctolite is typically separated from the surrounding olivine (ol) by a corona of chlorite (c), amphibole (a), and talc + magnetite (arrow). (Sample **209-1275B-6R-2, 57–61 cm**) (cross-polarized light: blue filter; field of view = 2.75 mm; image 1275B_011). **C.** Photomicrograph of coronitic textures in troctolite. Coronas of chlorite and talc (arrows) develop in the contact between plagioclase and olivine (Sample **209-1275B-6R-1, 70–75 cm**) (cross-polarized light: blue filter; field of view = 11 mm; image 1275B_007).

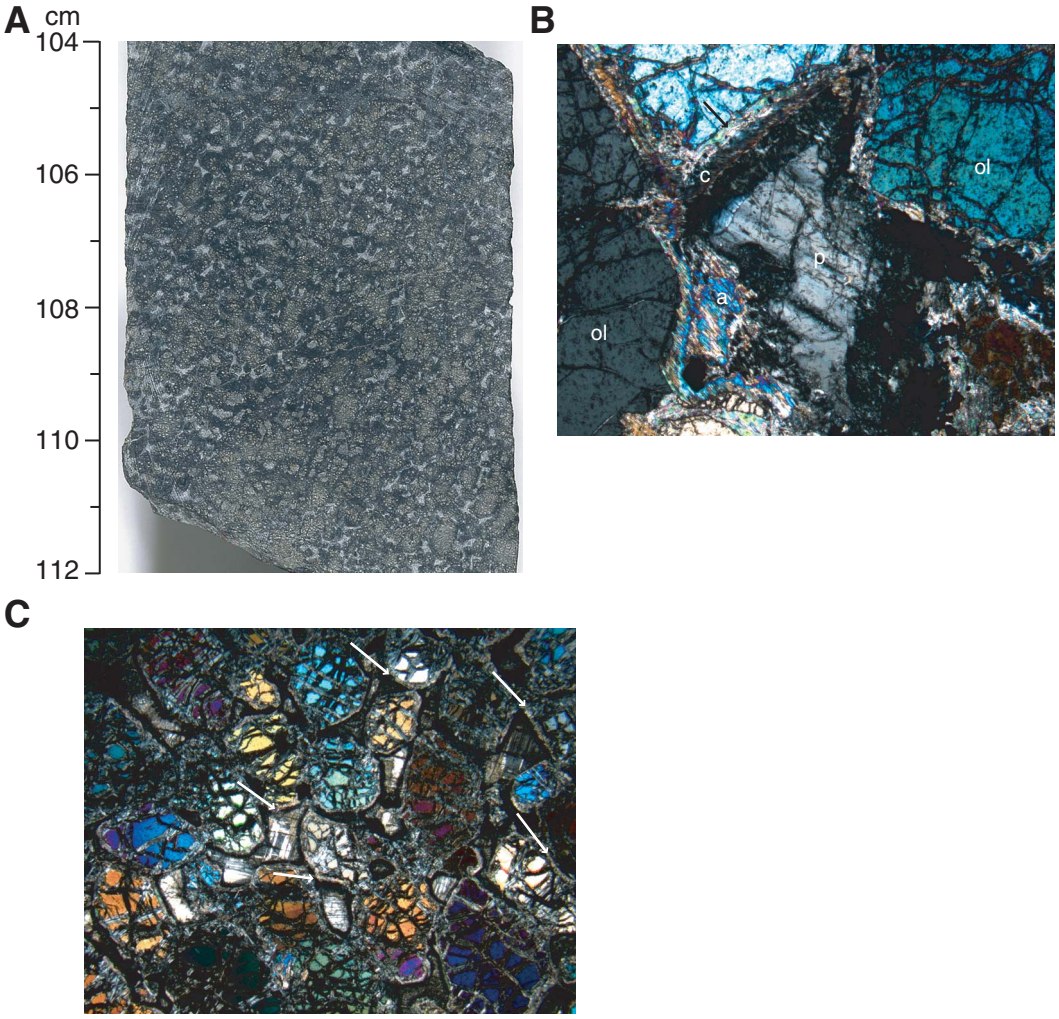

Figure F41. Relative volume percentage of the different vein minerals encountered in Hole 1275B.

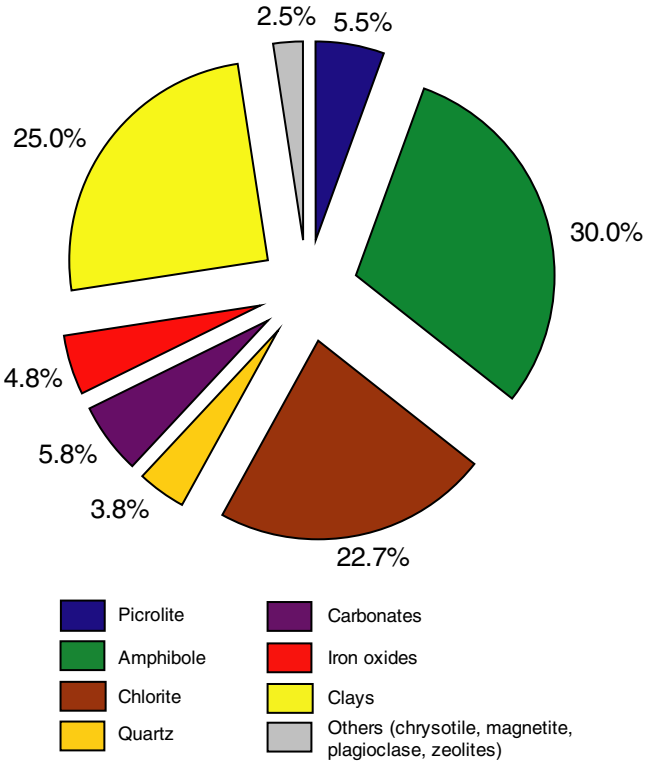

Figure F42. Downhole variation of vein mineralogy in Hole 1275B.

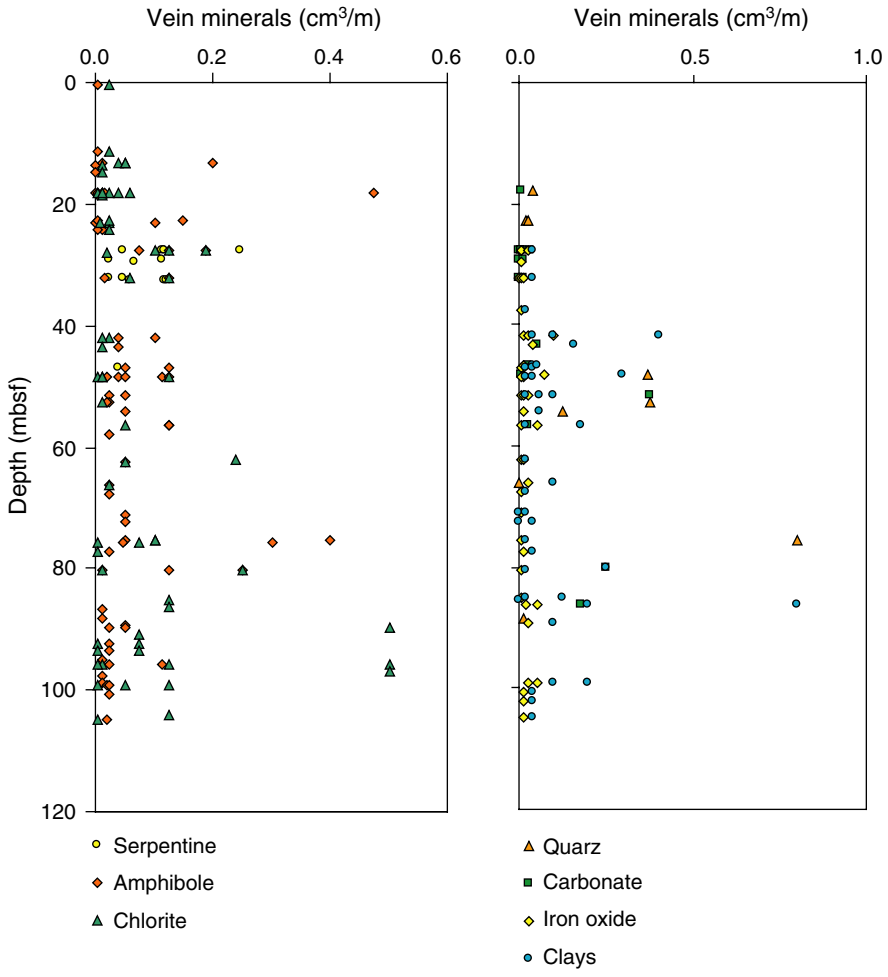

Figure F43. Close-up photograph showing an amphibole vein in moderately altered gabbro (interval 209-1275B-10R-1, 83–92 cm).

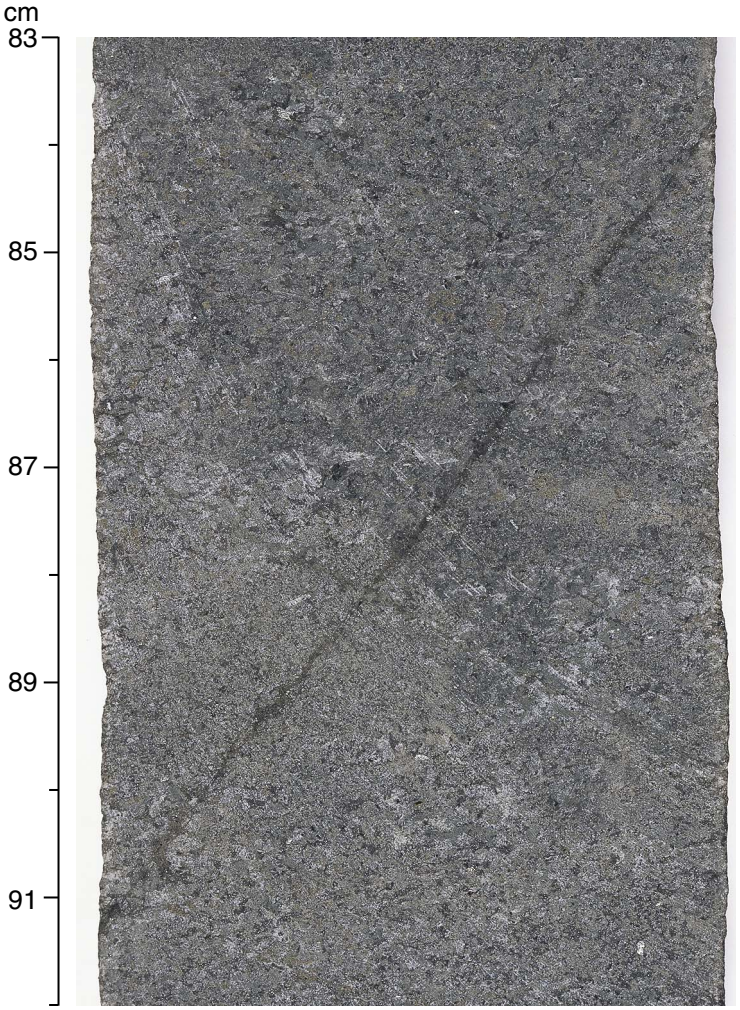

Figure F44. Photomicrograph showing amphibole veinlets and amphibole-filled microcracks (Sample 209-1275B-17R-1, 60–62 cm) (plane-polarized light: blue + gray + dark gray filters; field of view = 2.75 mm; image 1275B-021).

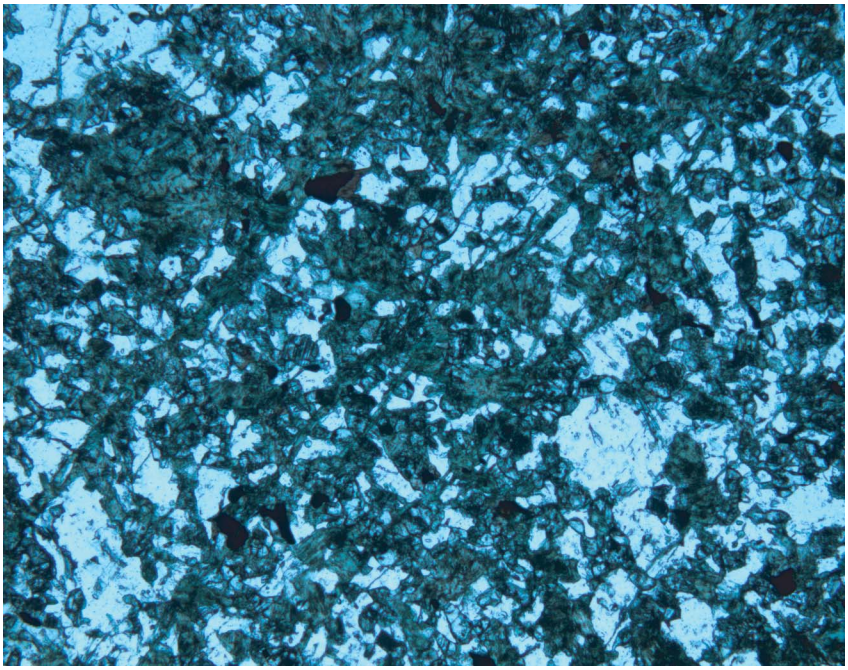

Figure F45. Photographs showing an overview of alteration of troctolites and gabbroic lithologies in Hole 1275D. **A.** Typical alteration of a troctolite showing olivine alteration to serpentine overprinted by iron oxyhydroxides, carbonates (red), and talc (gray). In the areas with iron hydroxides, rare fresh olivine is preserved in the kernels of the serpentine mesh texture. In the areas of talc alteration, serpentine and olivine crystals are replaced by talc (white). Igneous veins crosscutting the troctolite (green) are completely altered to green amphibole (interval 209-1275D-5R-1, 82–90 cm). **B.** Troctolite is altered to talc with olivine completely replaced by pseudomorphic talc (white). Pervasive talc alteration of troctolites is common near diabase dikes and gabbroic intrusions (interval 209-1275D-1R-2, 26–31 cm). **C.** Hand specimen of moderately altered gabbro (interval 209-1275D-20R-1, 11–18 cm). The alteration of the gabbro is dominated by replacement of pyroxene by aggregates of fibrous green amphibole and rare brown amphibole. **D.** Hand specimen of olivine gabbro showing olivine replaced by red iron oxyhydroxide and carbonate. Clinopyroxene is replaced by green amphibole and plagioclase is largely fresh. The sample is crosscut by felsic veins and late, vuggy carbonate veins (interval 209-1275D-33R-1, 52–61 cm).

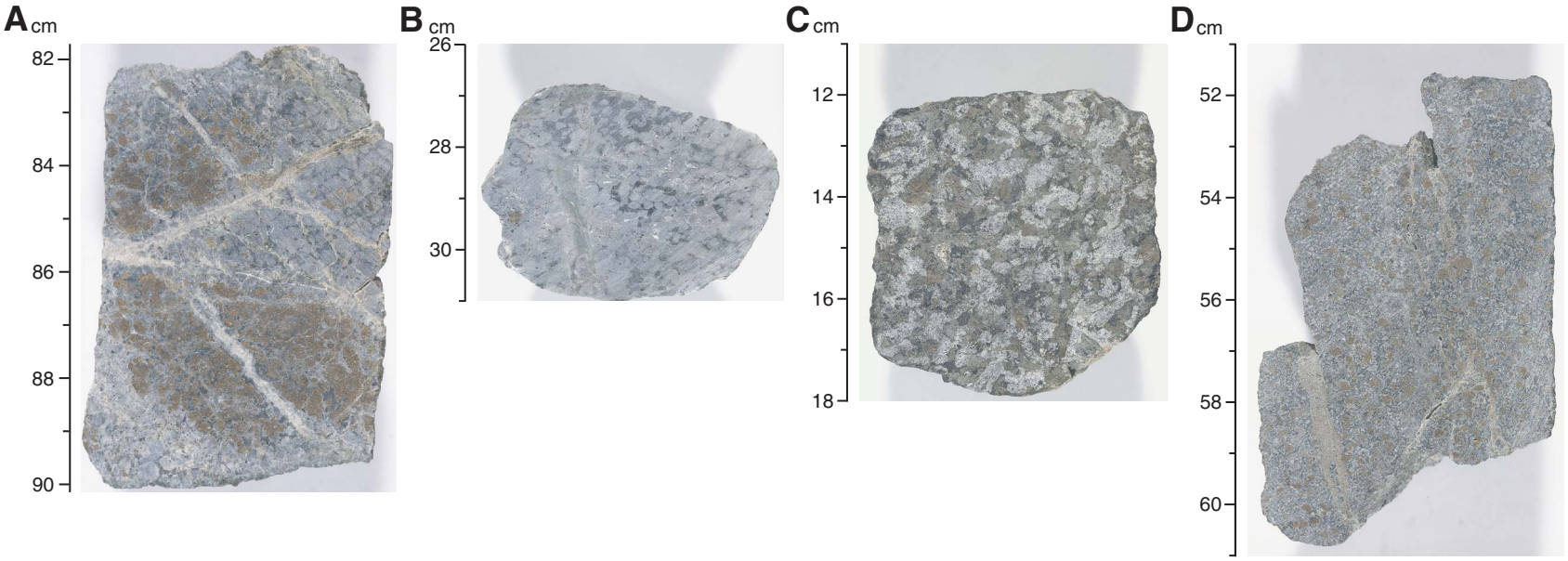

Figure F46. Photomicrograph showing replacement of clinopyroxene and, marginally, plagioclase by chlorite/smectite and green amphibole (Sample **209-1275D-34R-2, 54–57 cm**) (plane-polarized light: blue filter; field of view = 5.5 mm; image 1275D_017.)

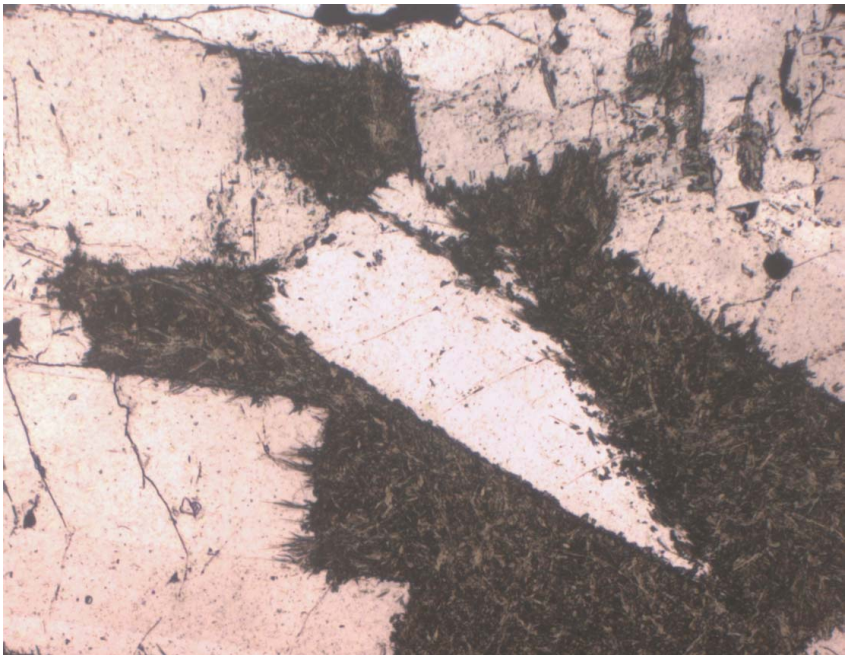

Figure F47. Replacement of olivine (ol) by green amphibole (ga), talc (tc), and magnetite (mt). Adjacent plagioclase (pl) is strongly altered to chlorite and talc. Clinopyroxene (cpx) is only slightly altered to amphibole (Sample **209-1275D-33R-1, 22–24 cm**) (plane-polarized light: blue filter; field of view = 2.75 mm; image 1275D_018).

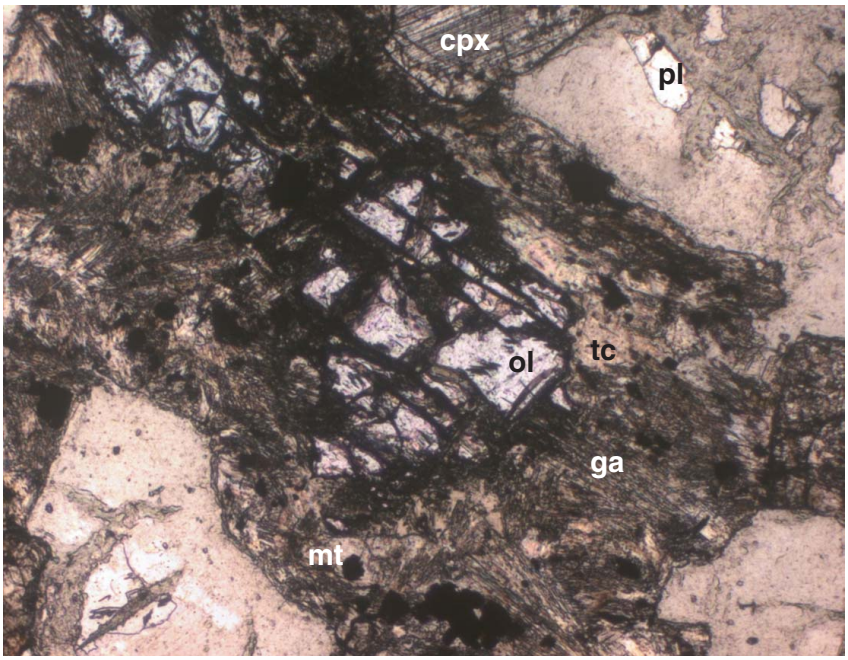

Figure F48. A. Close-up photograph of a mafic vein and host troctolite cut by a felsic magmatic vein. Note that the brownish colors in the troctolite near the contact with the mafic vein are due to the presence of relict olivine (see C). The white box outlines the area of a thin section (interval 209-1275D-9R-2, 17–27 cm). **B–D.** Photomicrographs of areas indicated by small yellow boxes in A (Sample **209-1275D-9R-2, 17–20 cm**) (plane-polarized light: blue filter); (B) contact between a talc-chlorite–altered mafic vein (right) and a carbonate-altered felsic vein (left). Near the contact, the felsic vein is rich in talc (tc; turbid, appears dark). An elongate chlorite-rich clast (chl) and a rhythmically banded serpentine-carbonate vein (vn) are also developed (field of view = 5.5 mm; image 1275D_010); (C) fresh olivine (o) and plagioclase (pl) at the contact between a completely altered gabbroic vein (upper right corner) and very highly altered troctolite (lower left corner) (field of view = 5.5 mm; image 1275D_011); (D) completely altered felsic vein. Alteration is mainly to carbonate and patches of talc. Relict plagioclase cleavage is preserved (arrow) (field of view = 2.75 mm; image 1275D_012).

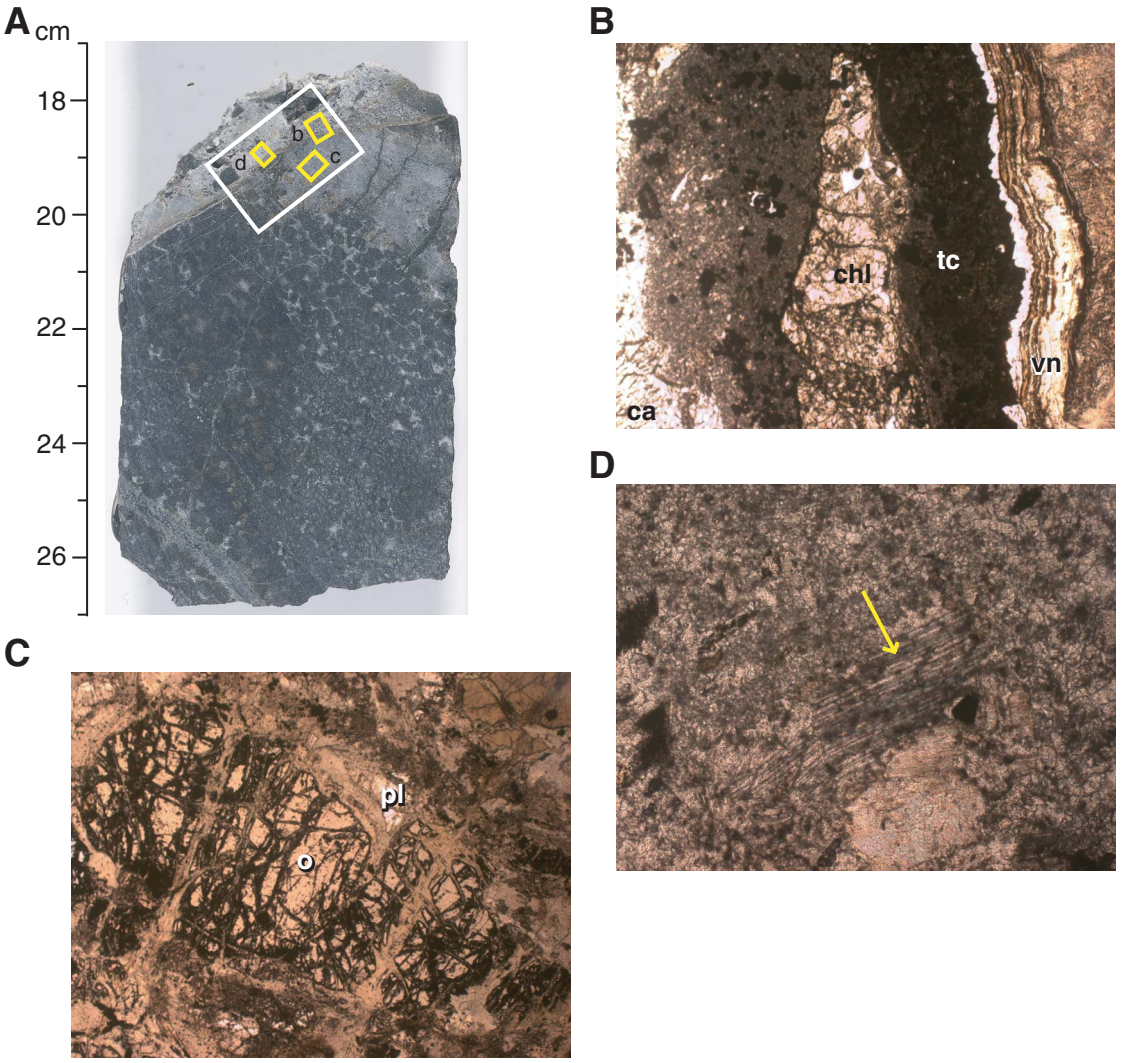

Figure F49. Photomicrograph showing plagioclase alteration in a troctolite. Plagioclase (pl) is preserved in the center. In addition to the typical coronitic replacement by chlorite and talc, plagioclase is altered to greenish brown clay (arrow) along the margins of the relics. Olivine is completely altered to sepentine and trains of magnetite that form mesh textures. Irregular networks of carbonate-clay veinlets (vn, high relief) cut the serpentinized olivine grains and follow former plagioclase/olivine grain boundaries (Sample **209-1275D-6R-1, 89–91 cm**) (plane-polarized light: blue + gray filters; field of view = 2.75 mm; image 1275D_019).

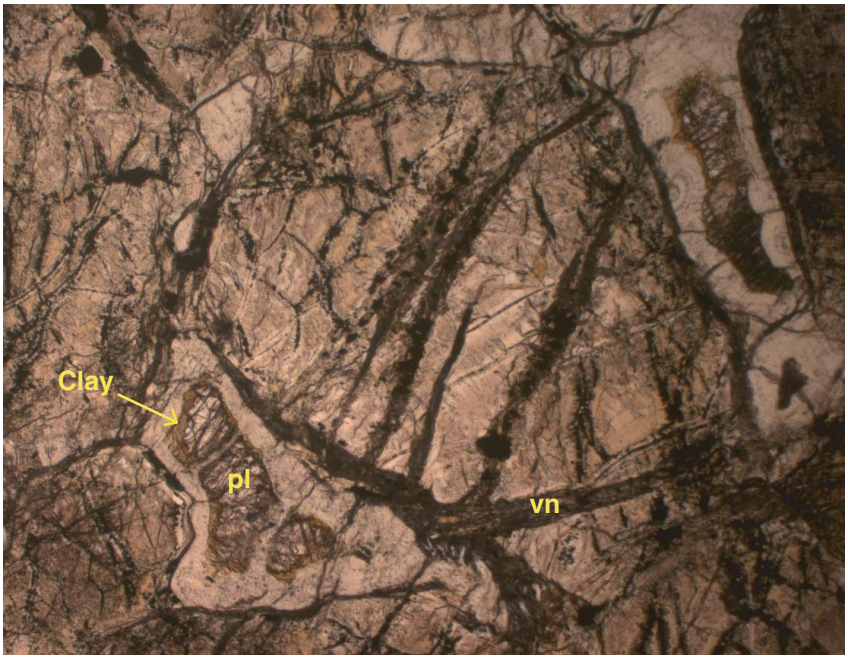

Figure F50. A. Photograph of hand specimen of highly altered troctolite from the upper portion of Hole 1275D. In addition to relatively wide talc-rich veins (tv), there is a fine network of carbonate-rich veinlets (ca) developed in the groundmass. Arrow indicates approximate position of XRD and thin section samples (interval 209-1275D-6R-1, 88–99 cm). **B.** The X-ray diffractogram shows that the altered troctolite has a complex mineralogical composition including calcite. Arrow indicates approximate position of the sample (Sample 209-1275D-6R-1, 89–91 cm). **C.** Photomicrograph showing olivine (o) preserved within the kernels of a fine network of calcite (cc, yellow arrows) and serpentine (s) veins. Along the calcite veins, the margins of the relict olivine are replaced by calcite (cc) and very fine grained aggregates of red clay and iron oxyhydroxide (white arrows) (Sample **209-1275D-6R-1, 89–91 cm**) (cross-polarized light; field of view = 2.75 mm; image 1275D_019).

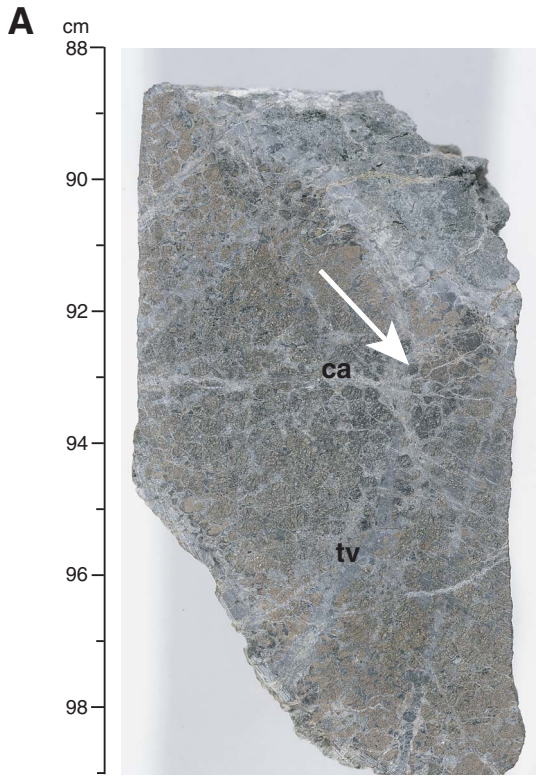

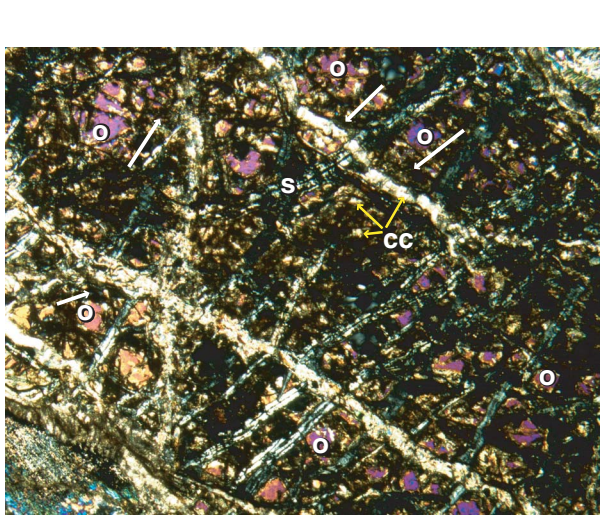

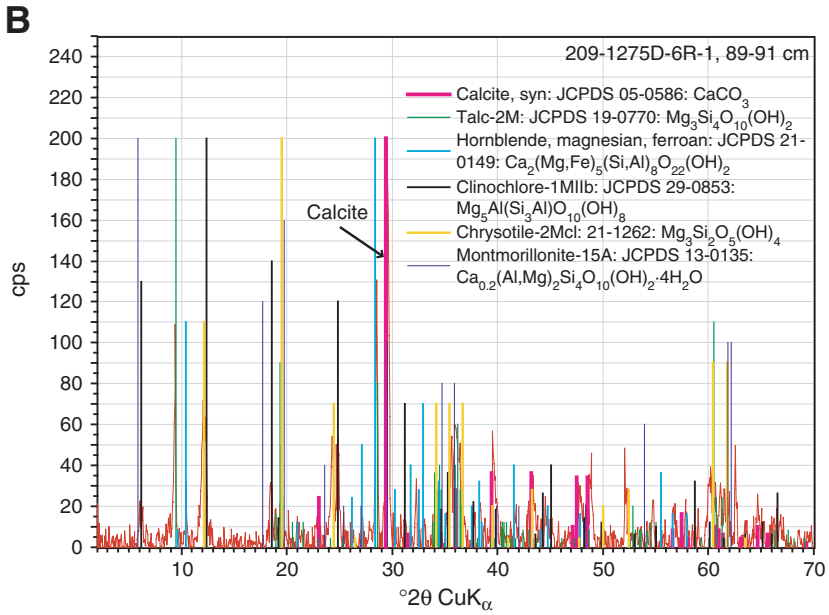

Figure F51. Downhole variation of alteration intensity in Hole 1275D. The running average excludes diabase.

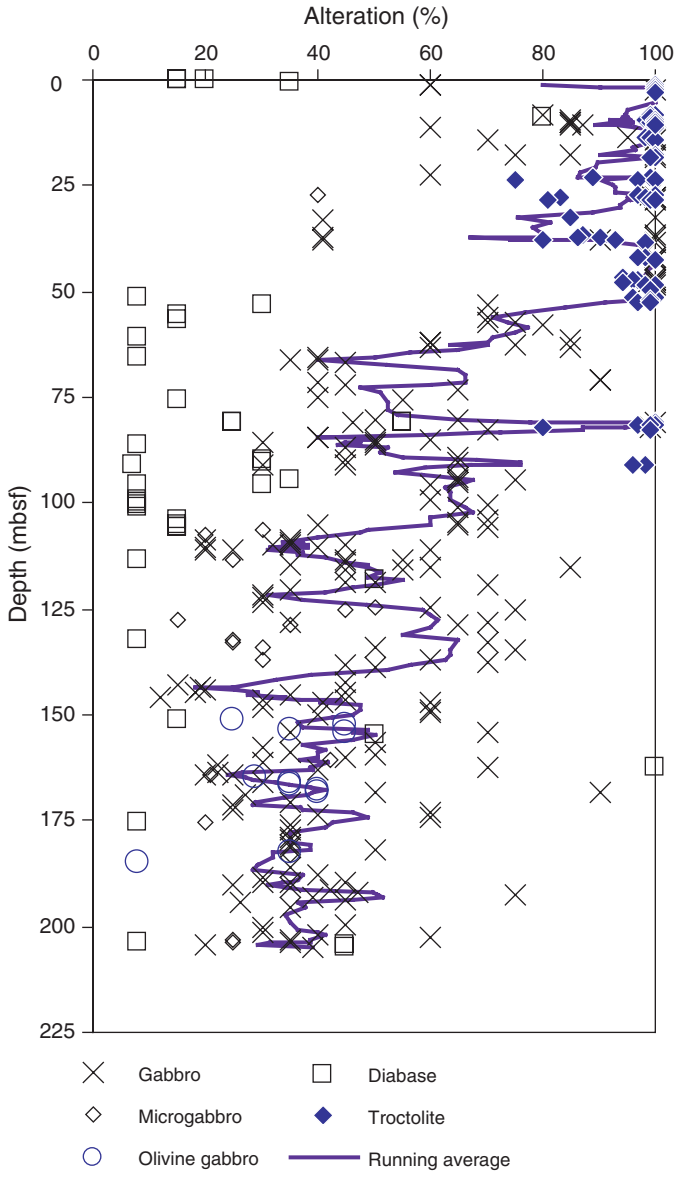

Figure F52. Relative volume percentage of the different vein minerals in Hole 1275D.

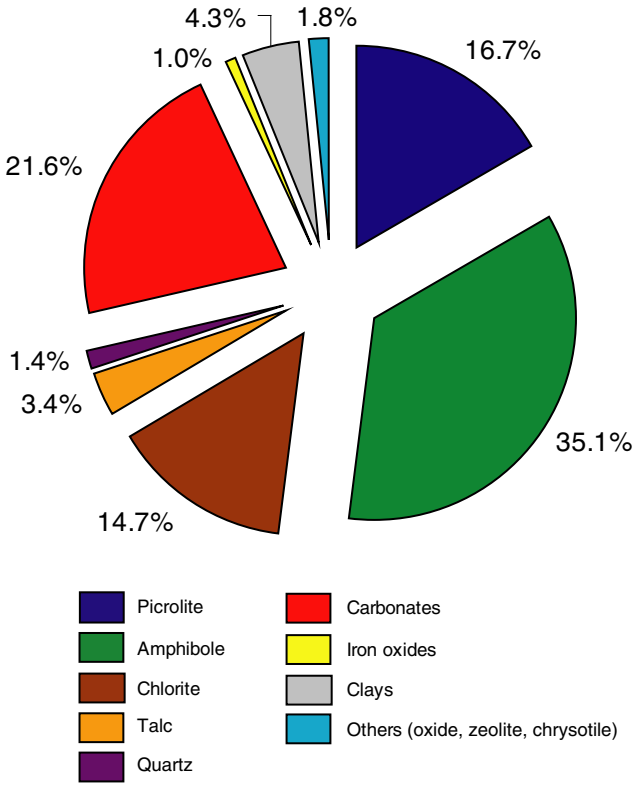

Figure F53. Downhole distribution of vein minerals in Hole 1275D.

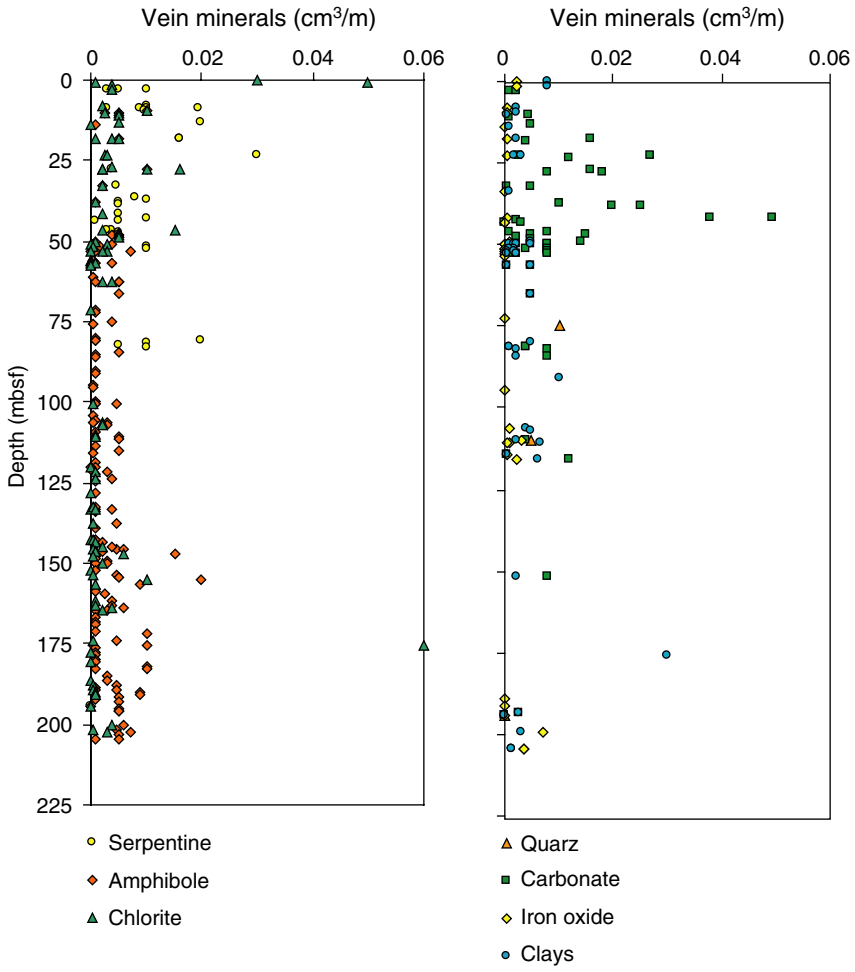

Figure F54. Downhole plot of crystal-plastic intensities in Holes 1275B and 1275D. Expanded depth of cored interval is plotted on the vertical axis. Yellow cones reflect the depth range of expansion for each core. Intensity estimate is based on visual core description of individual core pieces. Intensities are plotted as a running downhole average of 7 pieces, weighted by piece length, at each depth (473 pieces from Hole 1275B and 1320 pieces from Hole 1275D). Horizontal bars reflect the percentage of lithologies recovered from each core. TD = total depth.

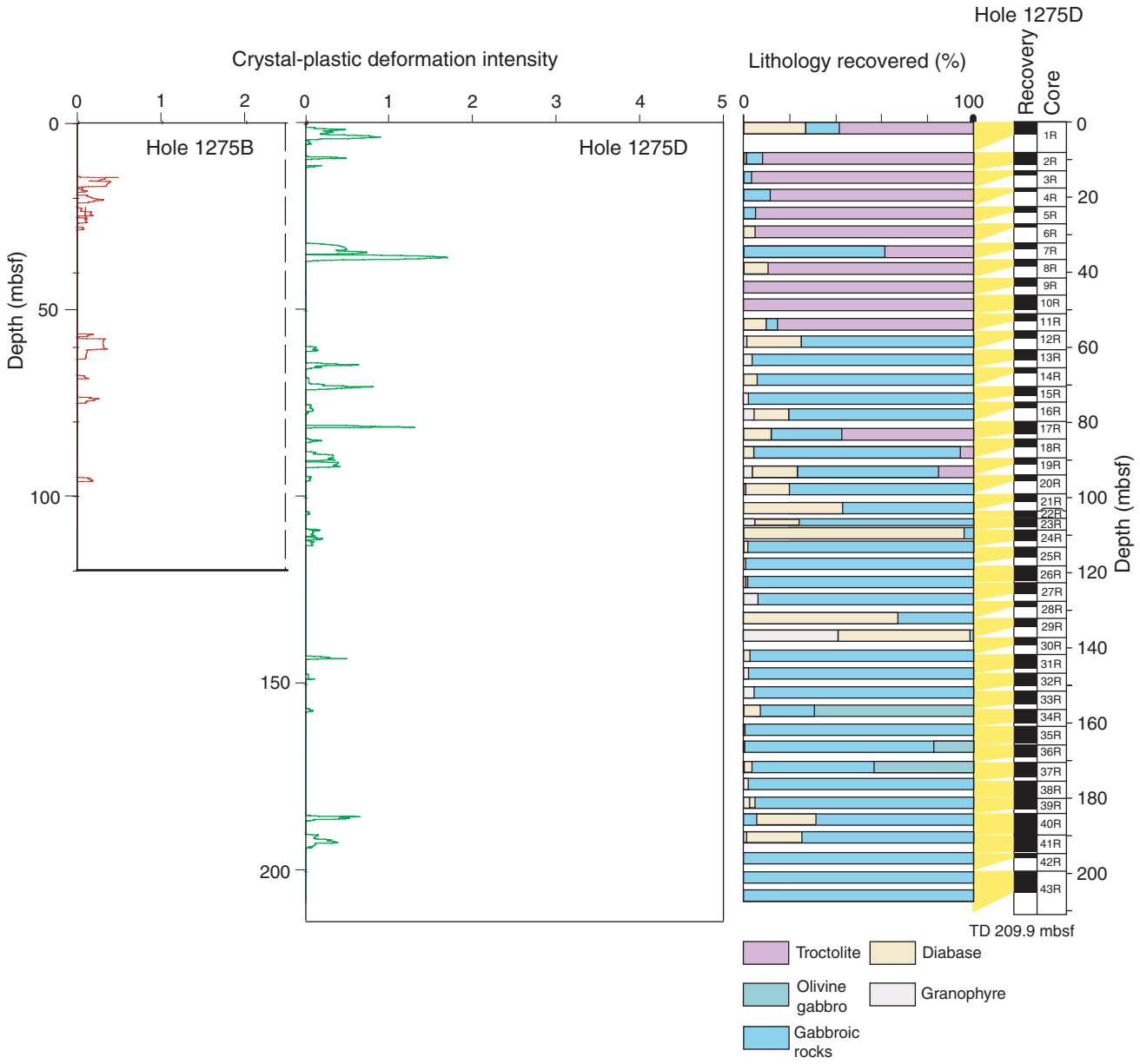

Figure F55. Histograms showing the distribution of crystal-plastic deformation (CPf) by intensity in Holes 1275B and 1275D. Deformation intensity is logged on a scale from 0 (undeformed) to 5 (ultramylonite) as discussed in "Structural Geology," p. 9, in the "Explanatory Notes" chapter.

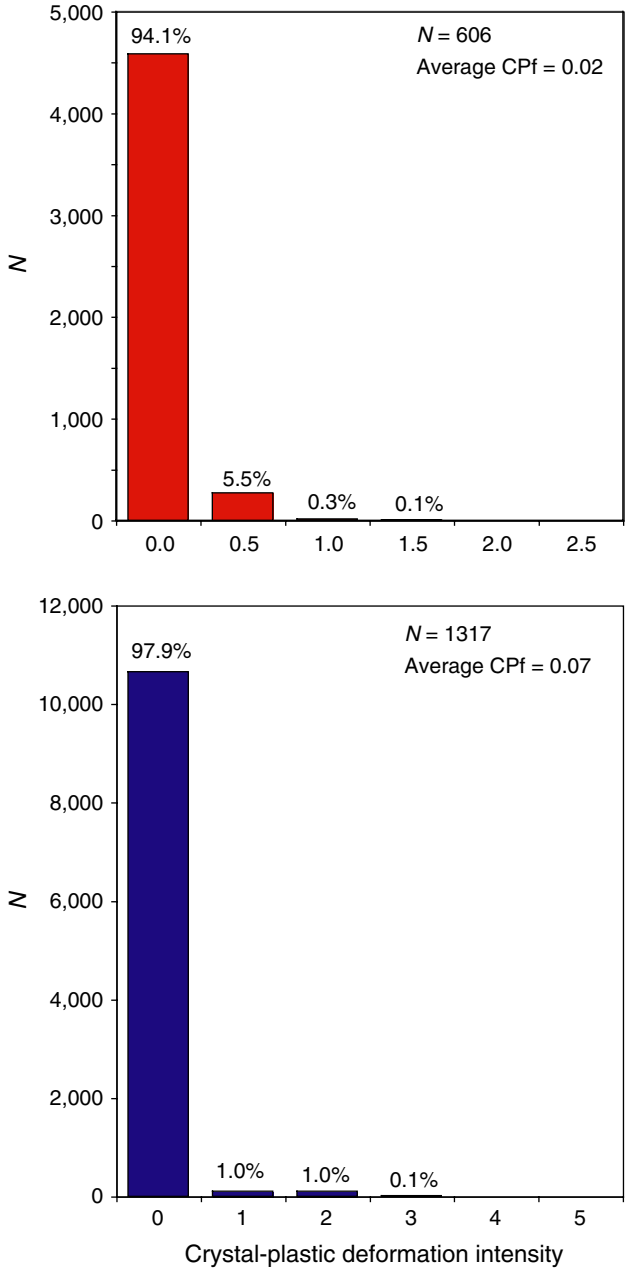

Figure F56. Close-up photograph of green amphibole cataclasite (green bands) containing clasts of gabbro and subrounded diabase. Some of the diabase clasts contain lighter bands around their margins that may be chilled margins or alteration rinds (interval 209-1275B-6R-1, 6–16 cm).

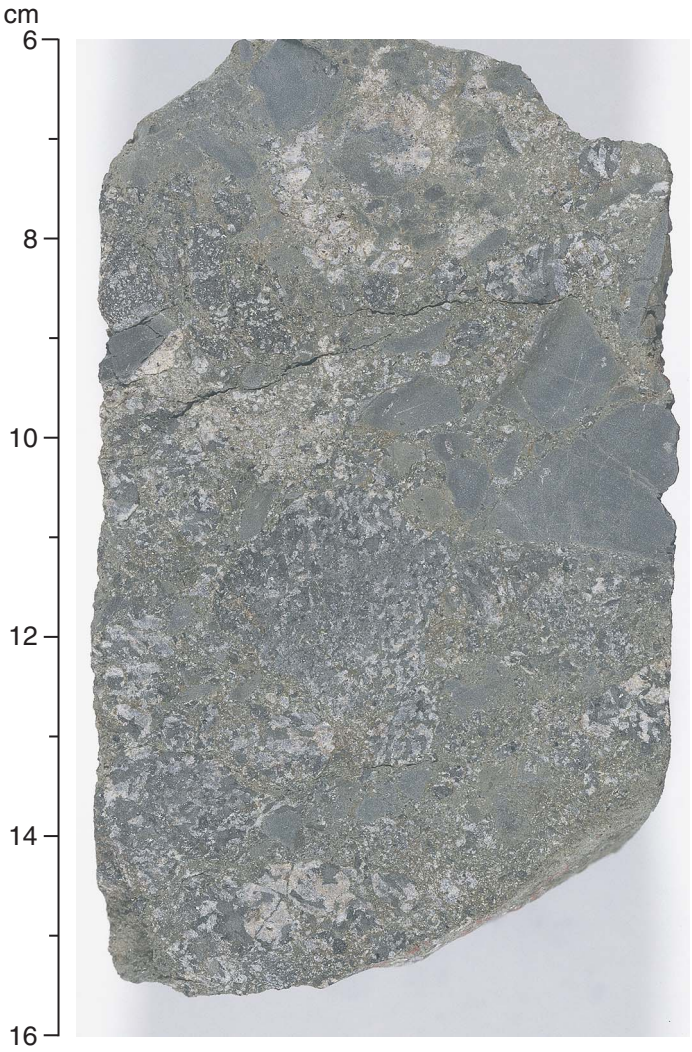

Figure F57. Photomicrograph showing amphibole cataclasite: clasts of fractured amphibole and plagioclase contained within a matrix of very fine grained fractured green amphibole and plagioclase. The cataclasite is dominantly clast supported with limited matrix-supported areas (Sample **209-1275B-3R-1, 57–59 cm**) (cross-polarized light; field of view = 5.5 mm; image 1275B_054).

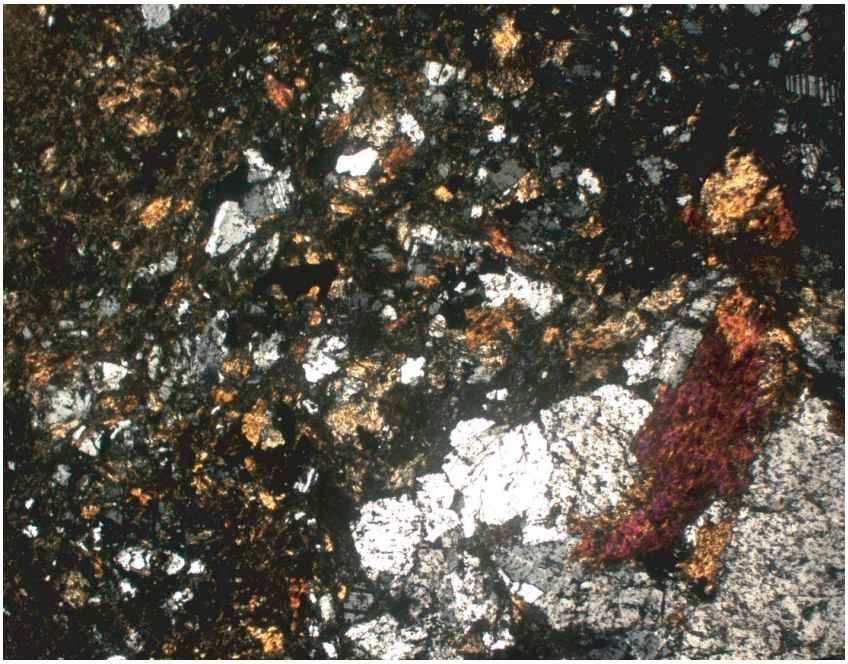

Figure F58. Photomicrograph showing diabase porphyroclast within a gabbro cataclasite. The zone of lighter-colored material parallel to the margin of the porphyroclast may be a chilled margin or an alteration rind (Sample **209-1275D-1R-1, 110–113 cm**) (cross-polarized light: blue filter; field of view = 2.75 mm; image 1275D-028).

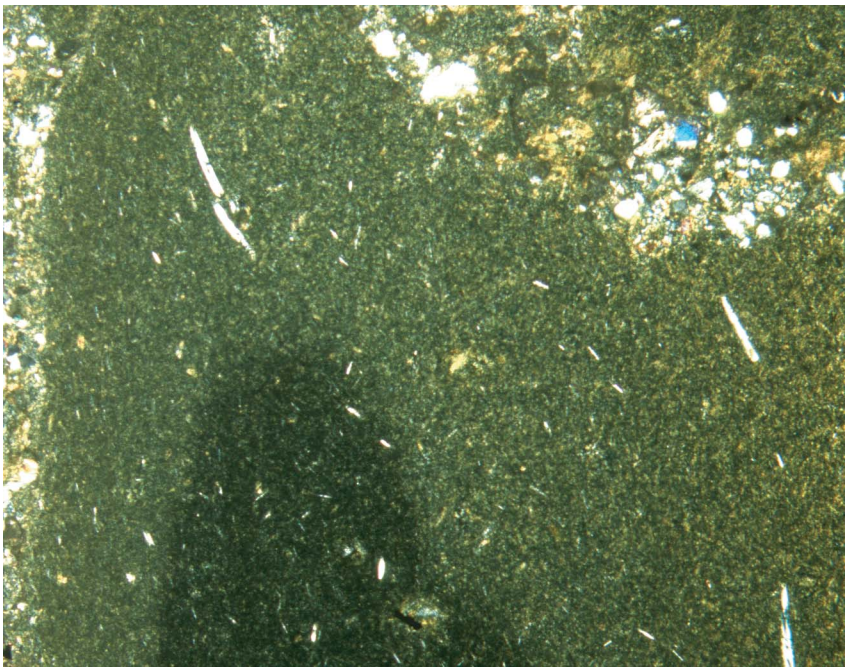

Figure F59. Close-up photograph of talc-chlorite-amphibole schist bordering undeformed diabase. Presumed clasts of diabase within the shear zone have been stretched parallel to the shear foliation (interval 209-1275D-1R-1, 8–14 cm).

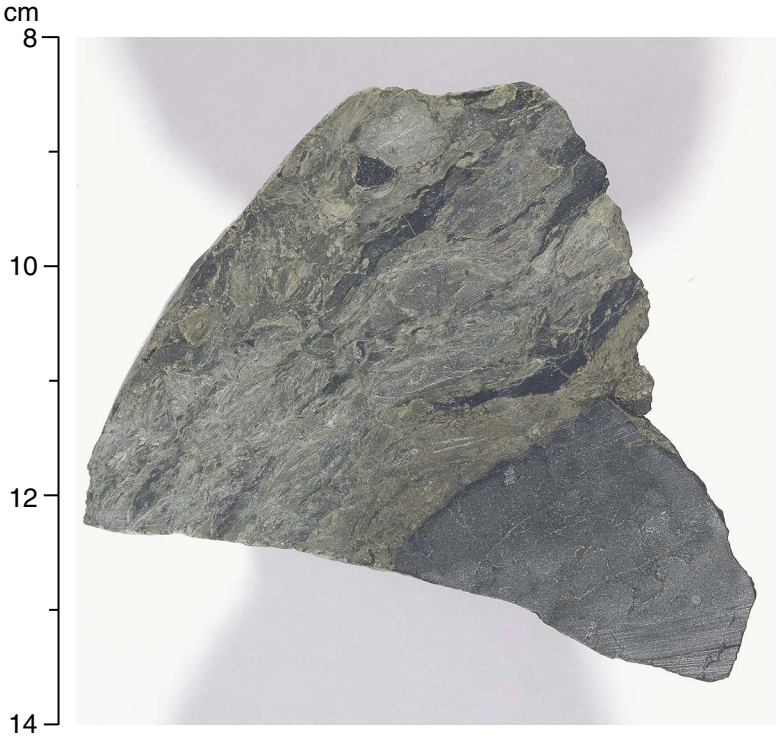

Figure F60. Photomicrograph showing fine-grained talc-amphibole schist. Layered schistose talc defines a strong foliation that is cut by anastomosing shear fractures. Fibrous amphibole may represent an earlier phase of deformation. The original mineralogy of the altered porphyroclast on the left side of the image is unknown (Sample **209-1275D-1R-1, 9–11 cm**) (cross-polarized light; field of view = 2.75 mm; image 1275D_029).

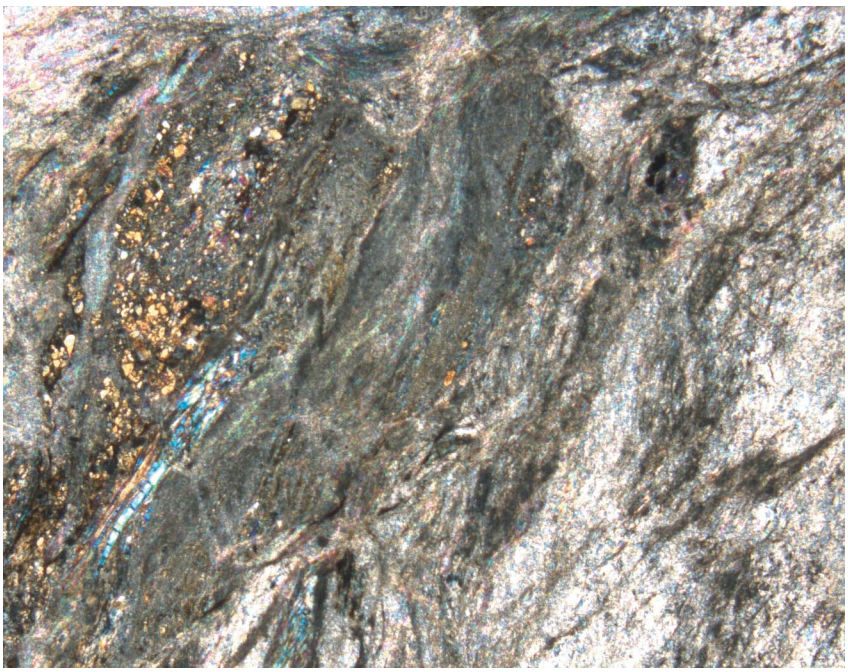

Figure F61. Downhole plot of brittle deformation and alteration vein intensities in Hole 1275B. Expanded depth of cored interval is plotted on the vertical axis. Yellow cones reflect the depth range of expansion for each core. Intensity estimate is based on visual core description of individual core pieces. Intensities are plotted as a running downhole average of 7 pieces, weighted by piece length, at each depth (550 pieces total). Horizontal bars on the right side of the figure reflect the percentage of lithologies recovered from each core. TD = total depth.

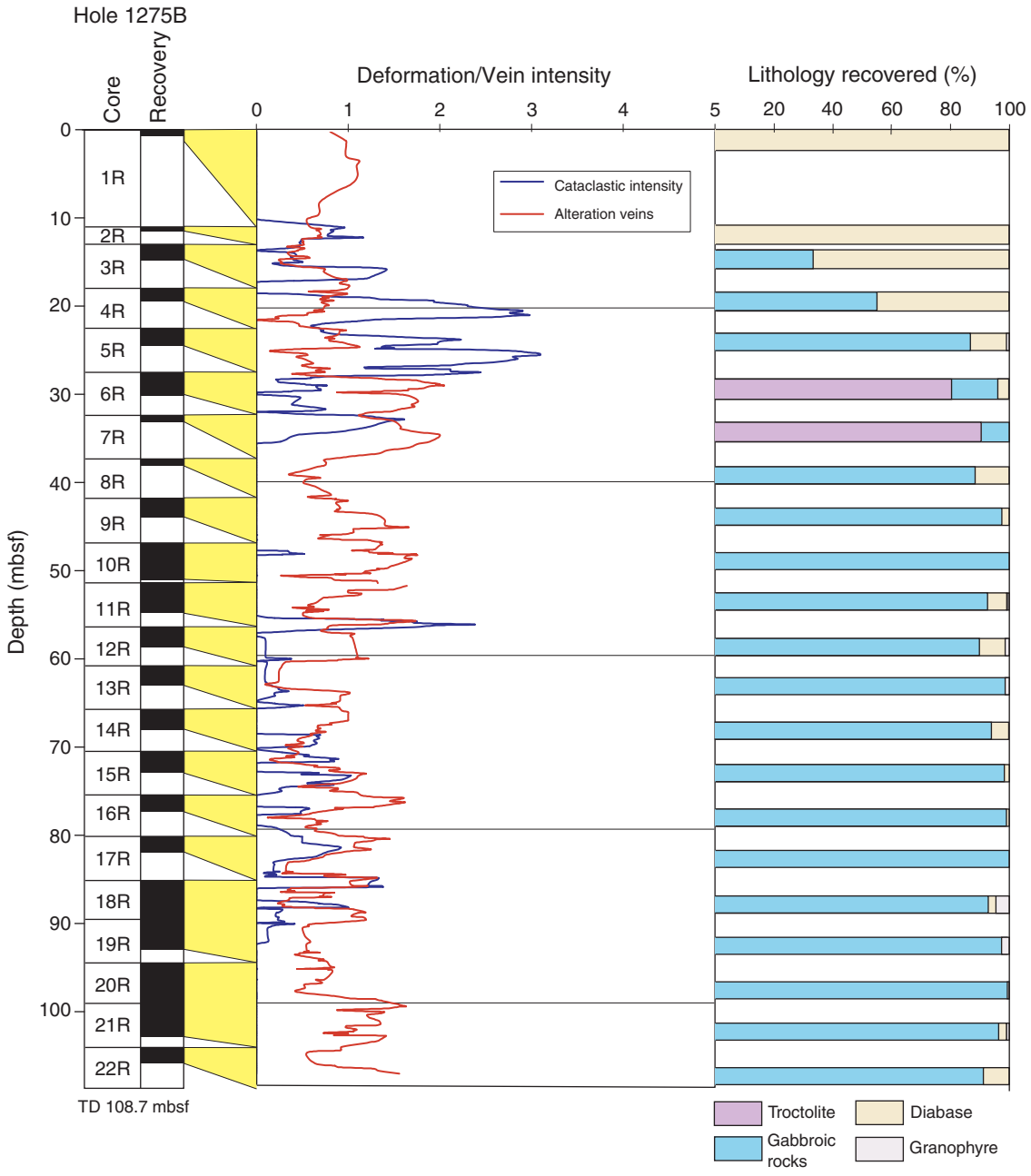

Figure F62. Downhole plot of the measured dips of faults, fractures, and brittle shear zones in Holes 1275B and 1275D. Expanded depth of cored interval is plotted on the vertical axis. Yellow cones reflect the depth range of expansion for each core. TD = total depth.

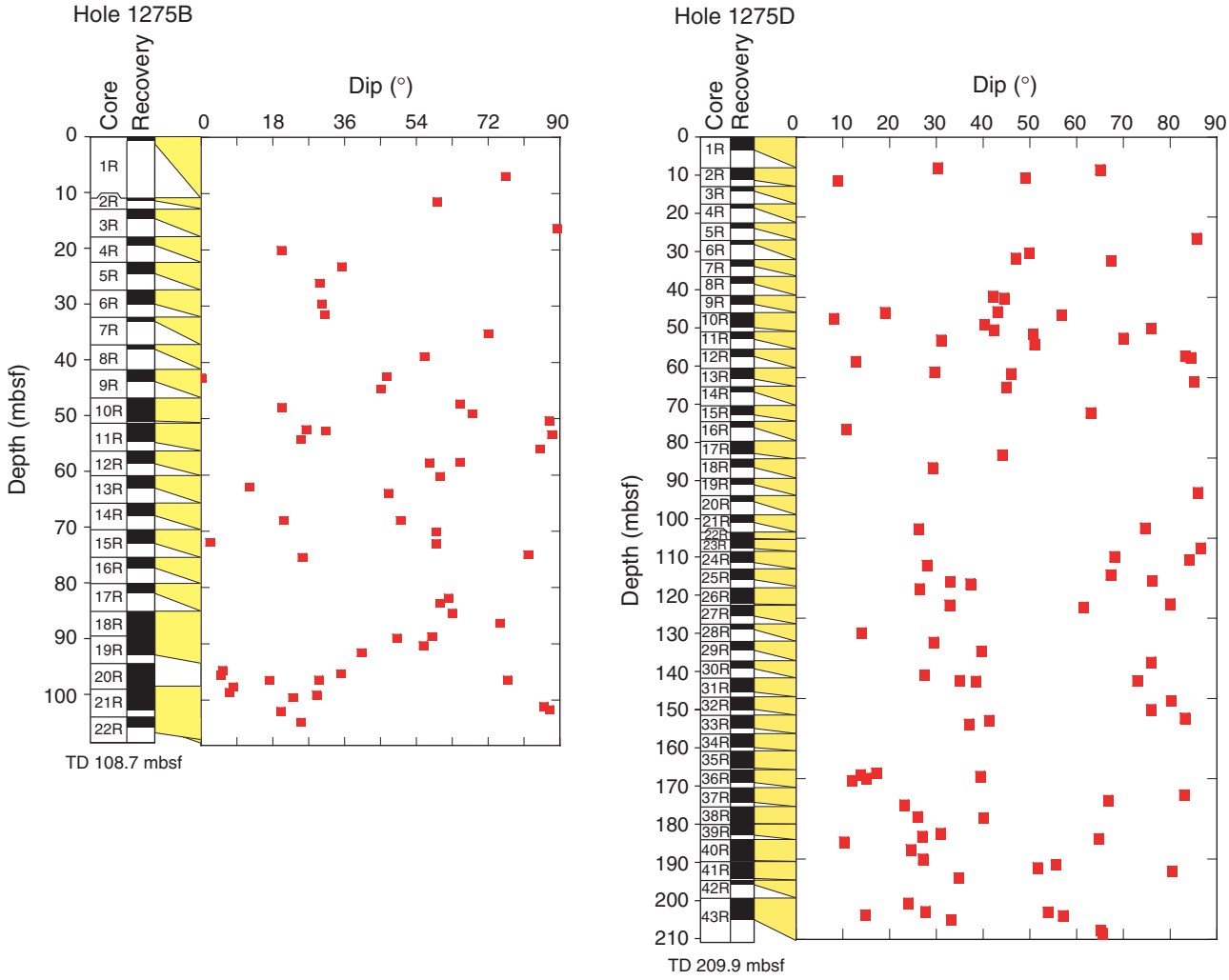

Figure F63. Downhole plot of brittle deformation and alteration vein intensities in Hole 1275D. Expanded depth of cored interval is plotted on the vertical axis. Yellow cones reflect the depth range of expansion for each core. Intensity estimate is based on visual core description of individual core pieces. Intensities are plotted as a running downhole average of 9 pieces, weighted by piece length, at each depth (1194 pieces total). Horizontal bars on the right side of the figure reflect the percentage of lithologies recovered from each core. TD = total depth.

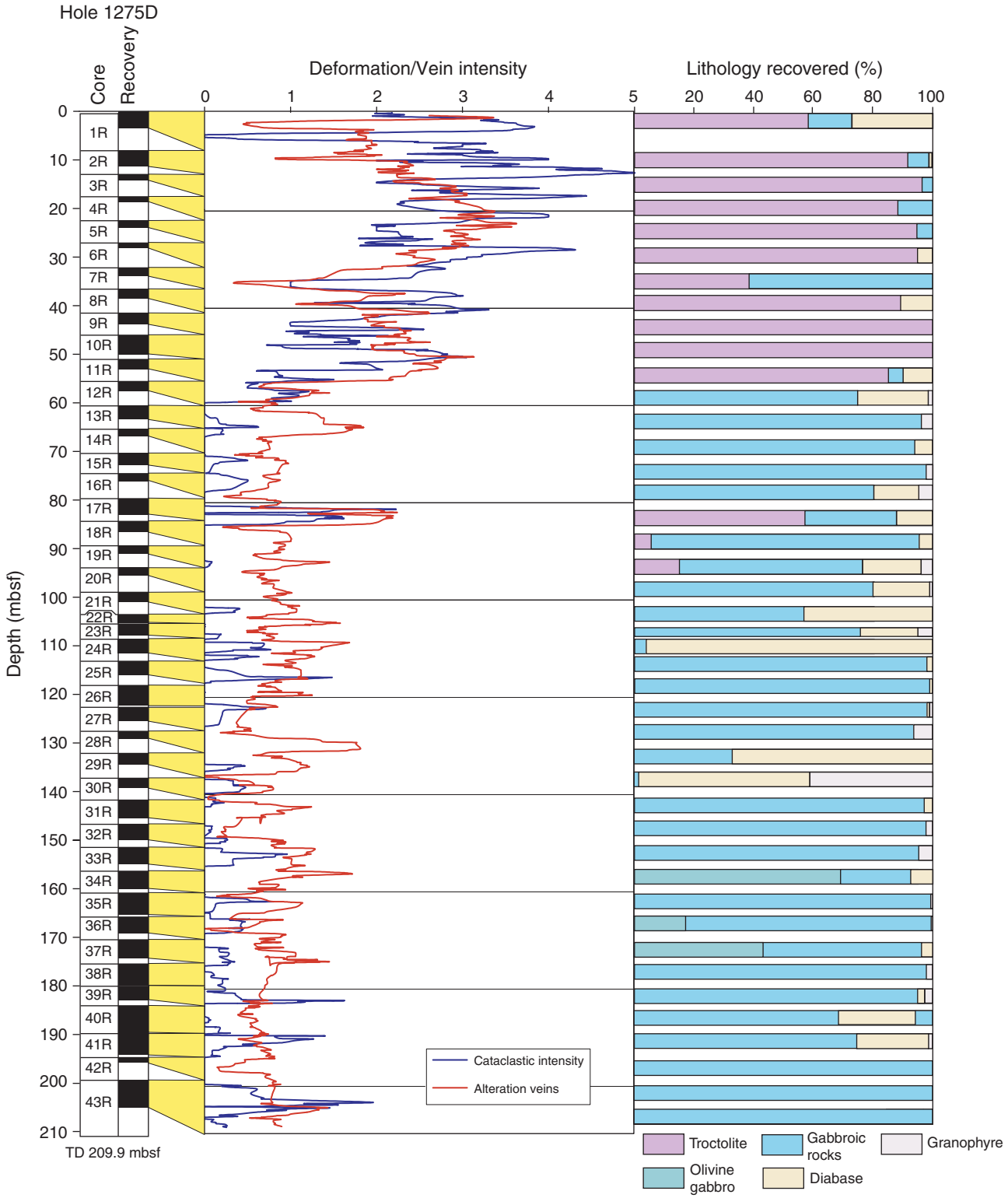

Figure F64. Close-up photographs of examples of alteration veins and their crosscutting relationships in troctolites from Hole 1275D. **A.** Light gray, altered, magmatic vein crosscutting troctolite. The vein exhibits orthogonal extension fractures filled with cream-colored picrolite serpentine that are in turn crosscut by a white carbonate-Fe oxyhydroxide vein that is parallel to the magmatic vein (interval 209-1275D-17R-2, 102–111 cm). **B.** Discrete green picrolite vein and a parallel-trending carbonate vein traversing a troctolite (interval 209-1275D-11R-2, 11–20 cm). **C.** Troctolite cut by gray, altered magmatic veins, showing crosscutting carbonate veins. Note that the carbonate vein in the bottom left-hand corner follows the trace of the magmatic vein (interval 209-1275D-10R-1, 34–49 cm). **D.** Altered, gray magmatic veins cutting a troctolite. The magmatic veins have been subsequently exploited by a later green picrolite vein and by an even later crosscutting carbonate vein (interval 209-1275D-10R-3, 98–106 cm).

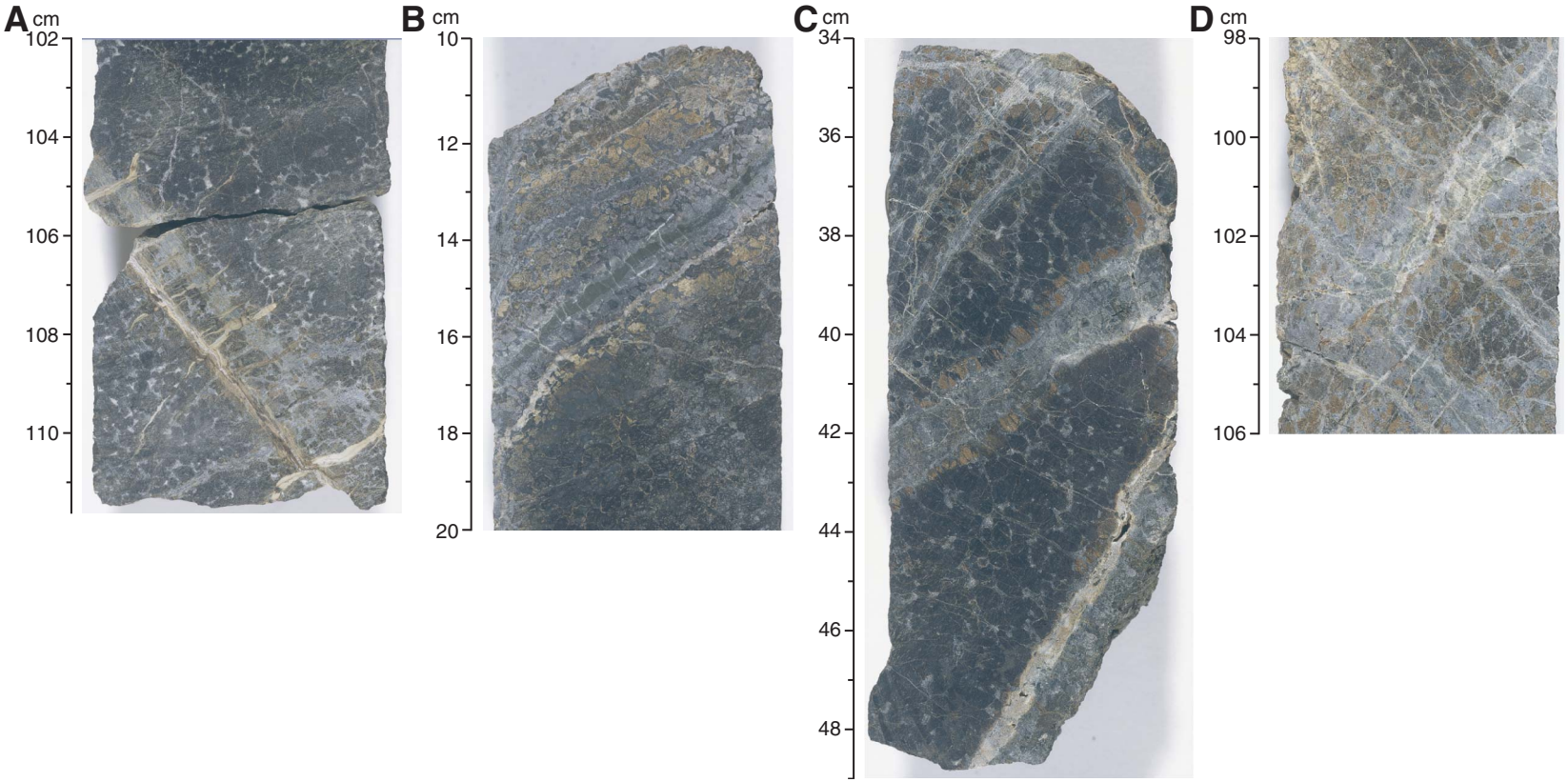

Figure F65. Close-up photographs of examples of alteration veins and their crosscutting relationships in gabbros from Hole 1275D. **A.** Green amphibole-chlorite vein crosscut by a brown clay-carbonate vein (interval 209-1275D-24R-1, 98–114 cm). **B.** Brown clay, Fe oxyhydroxide-carbonate vein cutting a gabbro (interval 209-1275D-25R-3, 22–33 cm). **C.** Green amphibole-chlorite vein crosscutting earlier felsic veins in a gabbro (interval 209-1275D-27R-1, 140–148 cm).

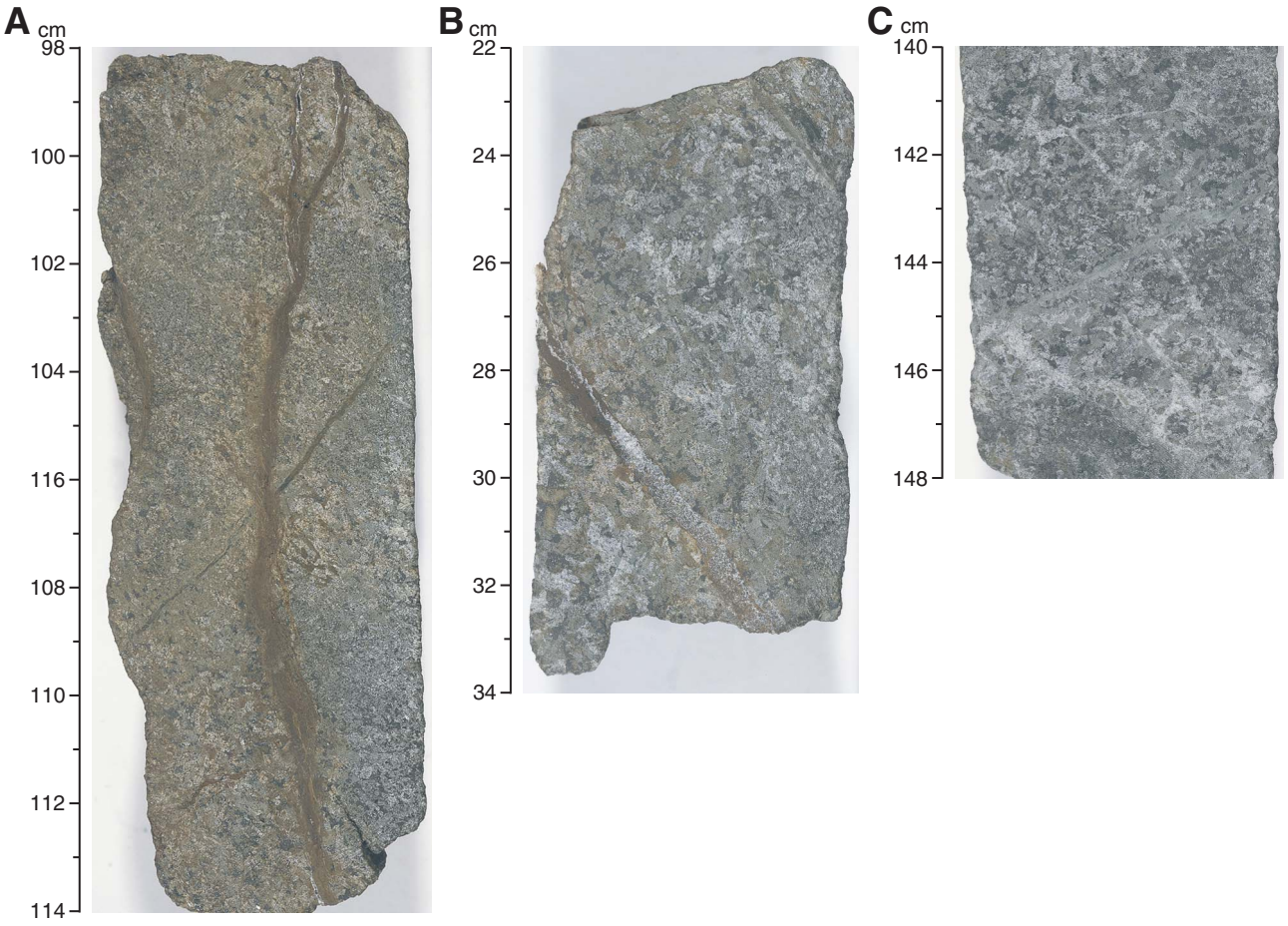

Figure F66. Downhole plot of dips of different alteration vein types in Holes 1275B and 1275D. Expanded depth of cored interval is plotted on the vertical axis.

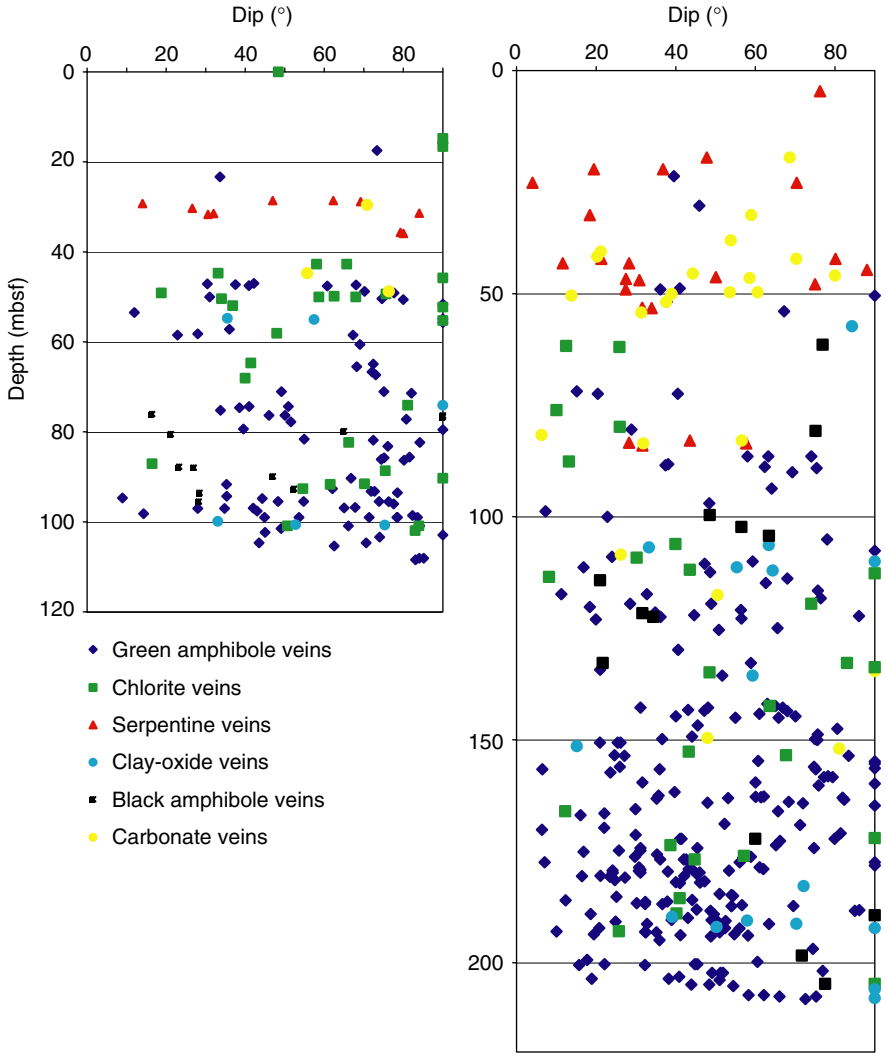

Figure F67. Lower hemisphere stereoplots showing the orientation of poles to magmatic foliations, granophyric veins, and diabase contacts in Hole 1275B. **A.** Depth-sorted foliations. Circles = 50–140 mbsf, squares = 140–210 mbsf. **B.** Depth-sorted granophyre veins. Circles = 50–140 mbsf, squares = 140–210 mbsf. Measurements were rotated into a common orientation using the measured paleomagnetic azimuth as described in "Structures in Peridotite and Gabbroic Intrusions," p. 8, in "Mantle Upwelling, Melt Transport, and Igneous Crustal Accretion" in the "Leg 209 Summary" chapter. It was assumed that samples from this hole record reversed polarity magnetization.

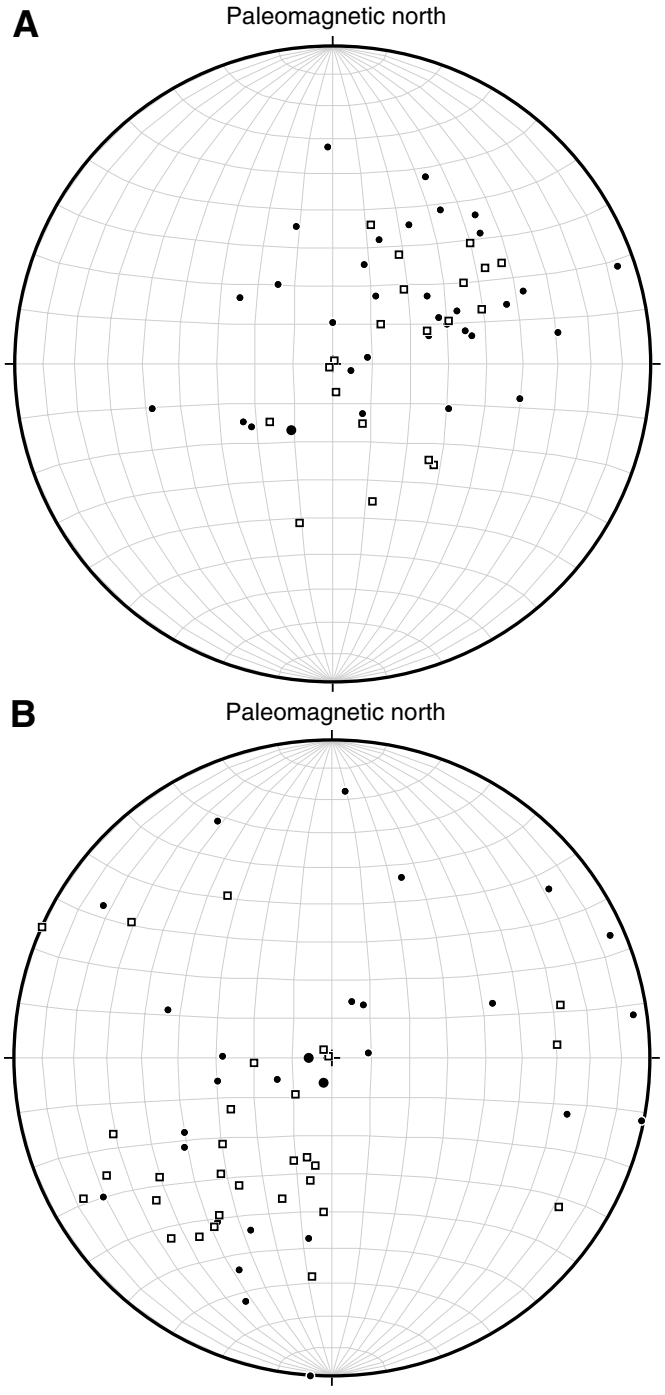

Figure F68. Lower hemisphere stereoplots showing the orientation of poles to magmatic foliations, granophyric veins, magmatic veins in troctolites, and compositional contacts in Hole 1275D. Measurements were rotated into a common orientation using the measured paleomagnetic azimuth as described in **"Structures in Peridotite and Gabbroic Intrusions,"** p. 8, in "Mantle Upwelling, Melt Transport, and Igneous Crustal Accretion" in the "Leg 209 Summary" chapter. It was assumed that samples from this hole record reversed polarity magnetization.

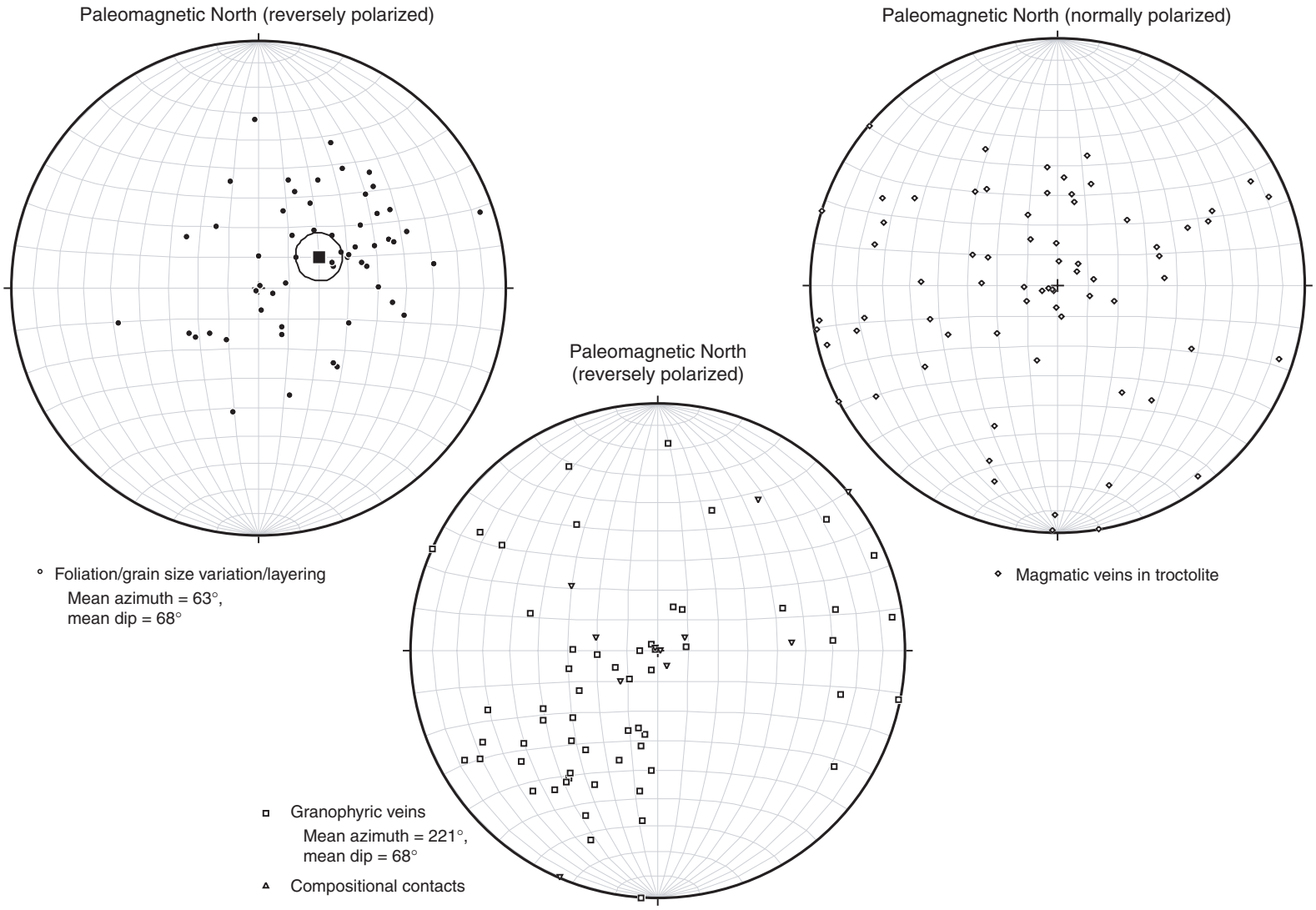

Figure F69. H_2O, Al_2O_3 and Mg# vs. SiO_2 for rocks from Site 1275. Shown for comparison are peridotites and gabbros from Sites 1270, 1271, 1272, and 1274. Published data for Leg 153 gabbros (Agar et al., 1997) and Hole 735B (Dick, Natland, Miller, et al., 1999) are shown for comparison.

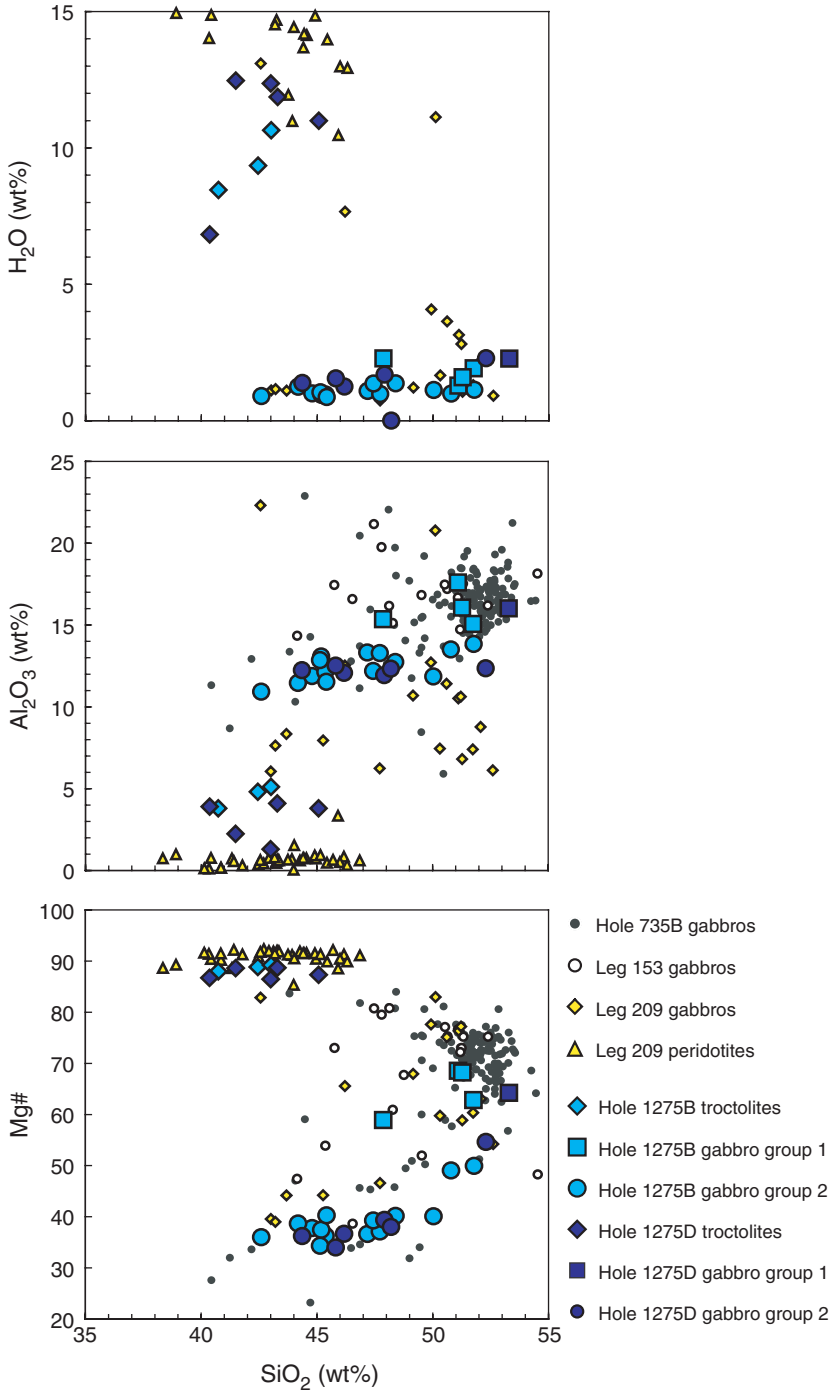

Figure F70. CO_2 vs. CaO for rocks from Site 1275. Shown for comparison are peridotites and gabbros from Sites 1270, 1271, 1272, and 1274.

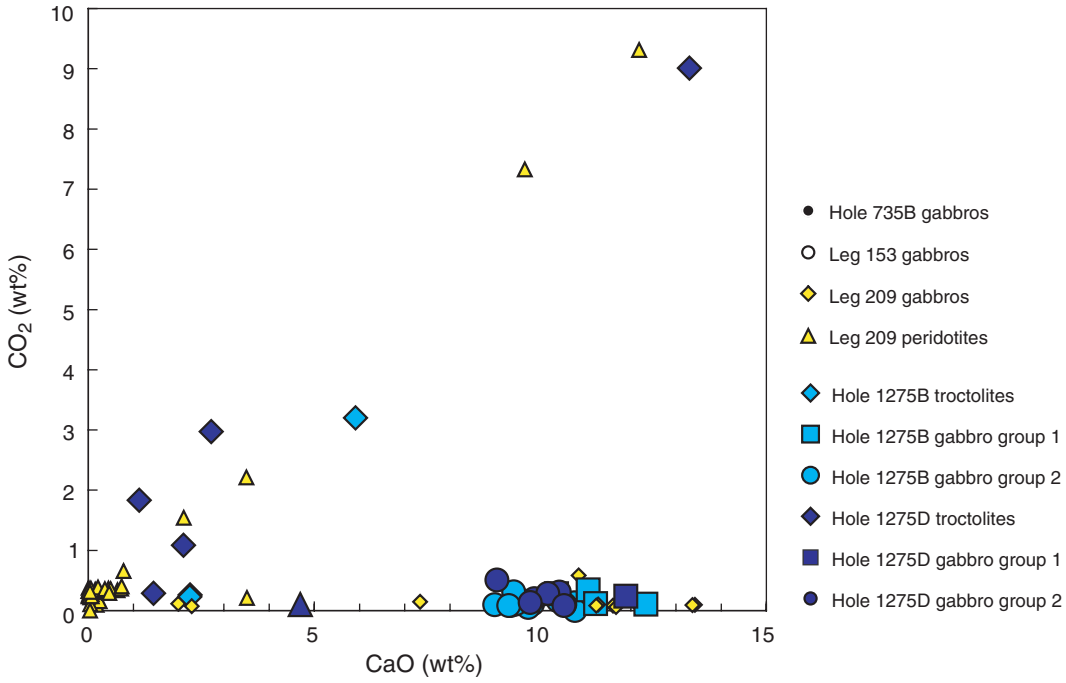

Figure F71. FeO vs. MgO for troctolites from Site 1275 (blue diamonds). Yellow triangles = Site 1270, 1271, 1272, and 1274 peridotites, open dots = Mid-Atlantic Ridge peridotites from Leg 109 Site 670 and Leg 153 Site 920. Published data are also shown for comparison: open diamonds = Mid-Atlantic Ridge peridotites from Leg 109 Site 670 (Hébert at al., 1990) and Leg 153 Site 920 (Casey, 1997). Other symbols: * = Southwest Indian Ridge (Snow and Dick, 1995), + = Izu-Bonin-Mariana forearc (Parkinson and Pearce, 1998), diamond = East Pacific Rise peridotites (Niu and Hekinian, 1997); X = Western Alps orogenic lherzolites and ophiolites (Bodinier, 1988; Rampone et al., 1996), circle = Oman ophiolite harzburgites (Godard et al., 2000), triangle = Oman ophiolite mantle transition zone dunites (Godard et al., 2000). Whole-rock compositions are presented on a volatile-free basis assuming all Fe is FeO. The solid black lines show olivine and orthopyroxene composition as a function of Fe/Mg. Fine gray lines show constant values of Mg# (Mg# = 100 × molar Mg/[Mg + Fe_{total}]). Fe_{total} = total Fe as FeO.

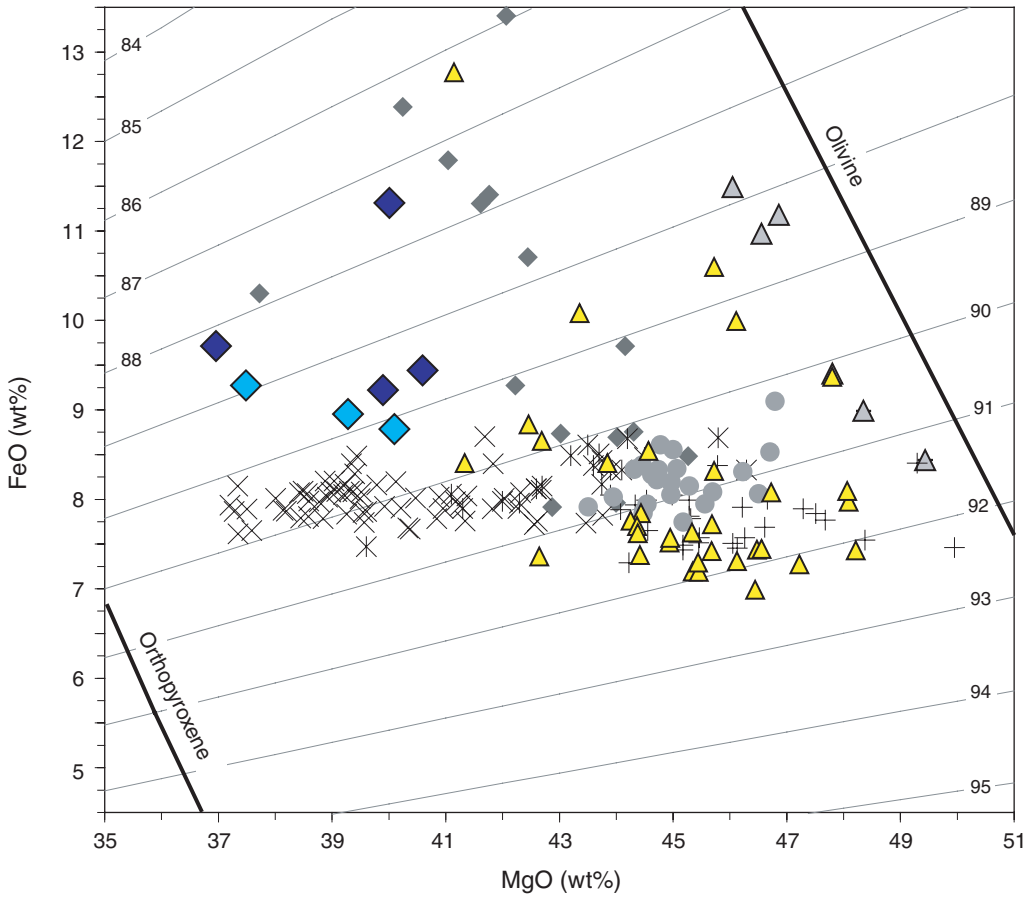

Figure F72. Ni and Cr vs. Mg# for rocks from Site 1275. Shown for comparison are compositions of peridotites and gabbros from Sites 1270, 1271, 1272, and 1274. Data for Leg 153 gabbros (Agar et al. 1997) and Hole 735B (Dick, Natland, Miller, et al., 1999) are also shown for comparison.

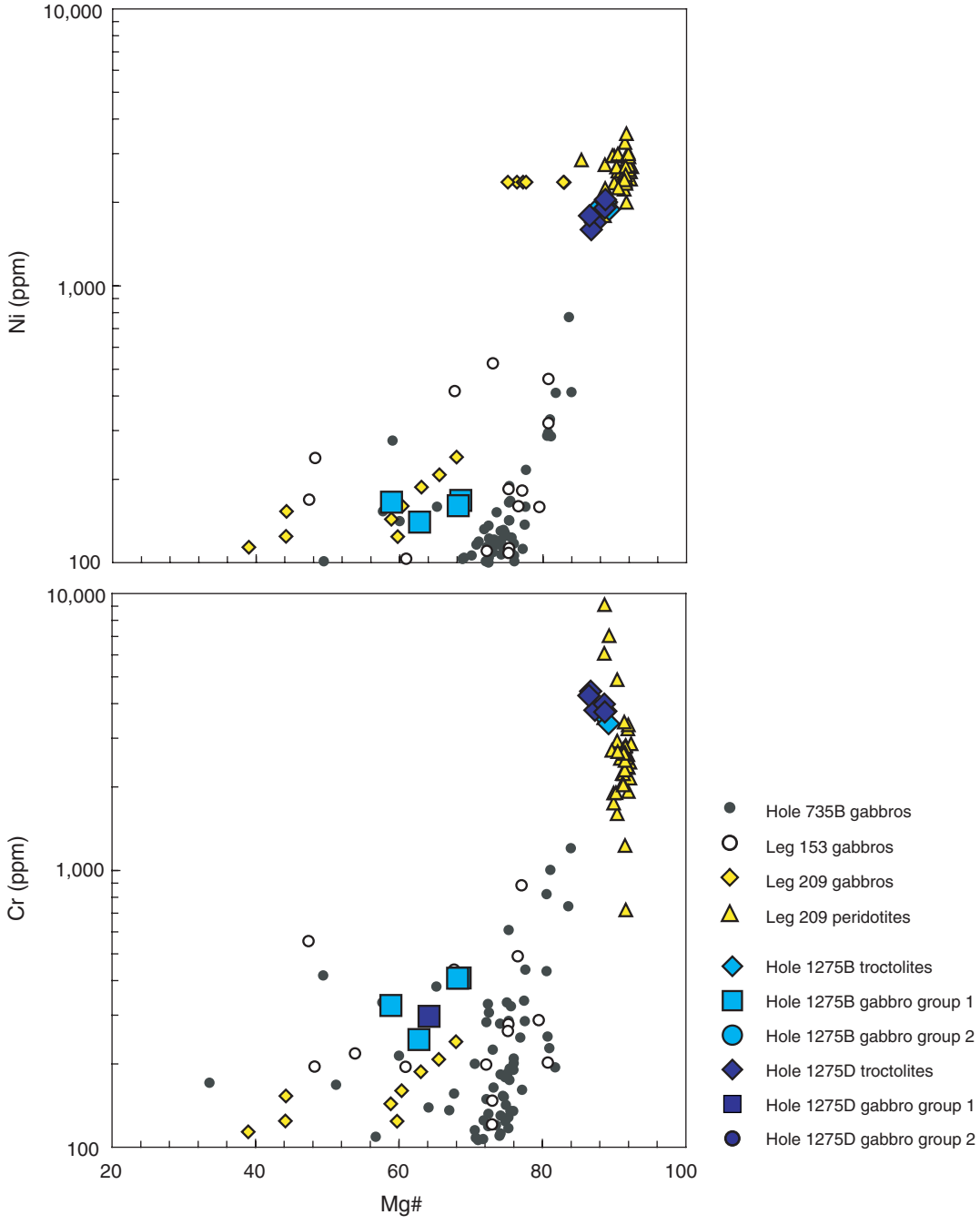

Figure F73. TiO_2, Zr, Cr, and V vs. Al_2O_3 for rocks from Site 1275. Shown for comparison are compositions of peridotites and gabbros from Sites 1270, 1271, 1272, and 1274.

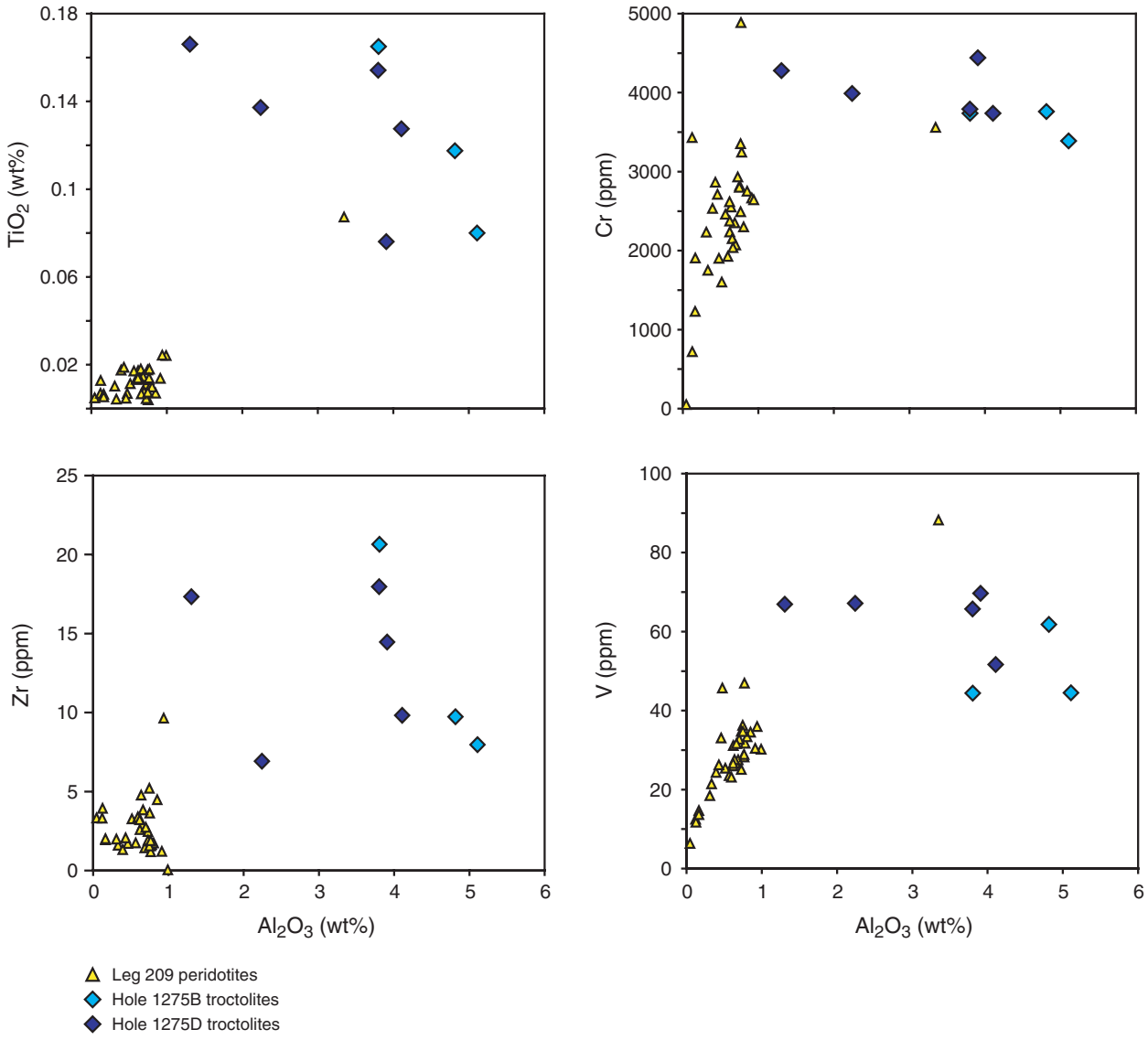

Figure F74. Fe_2O_3 and Al_2O_3 vs. MgO for gabbroic rocks from Site 1275. Shown for comparison are compositions of gabbroic rocks from Leg 153 (Agar et al., 1997) and Hole 735B (Dick, Natland, Miller, et al., 1999).

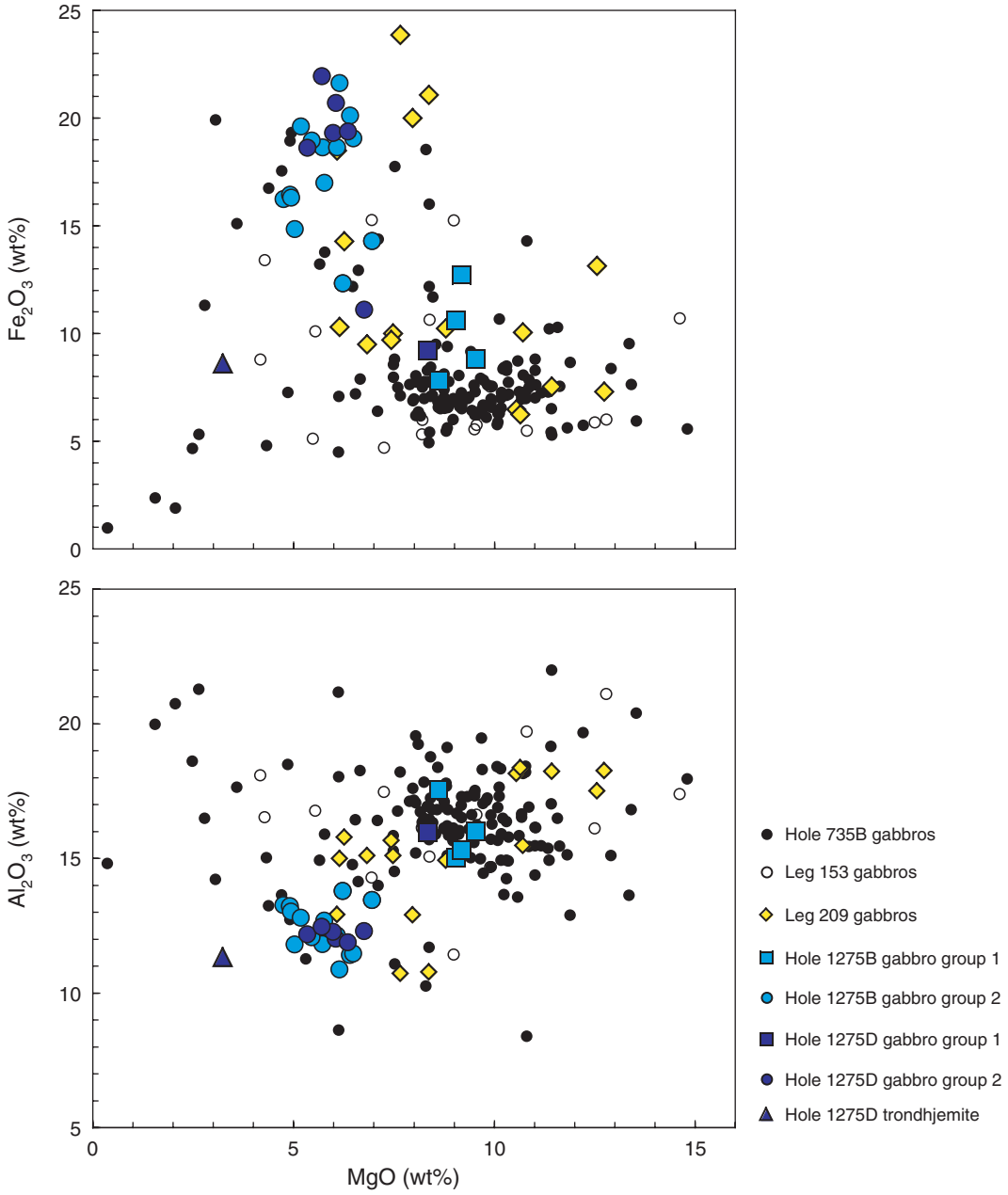

Figure F75. Fe_2O_3 vs. TiO_2 in gabbroic rocks from Site 1275. Shown for comparison are compositions of gabbroic rocks from Leg 153 (Agar et al., 1997) and Hole 735B (Dick, Natland, Miller, et al., 1999).

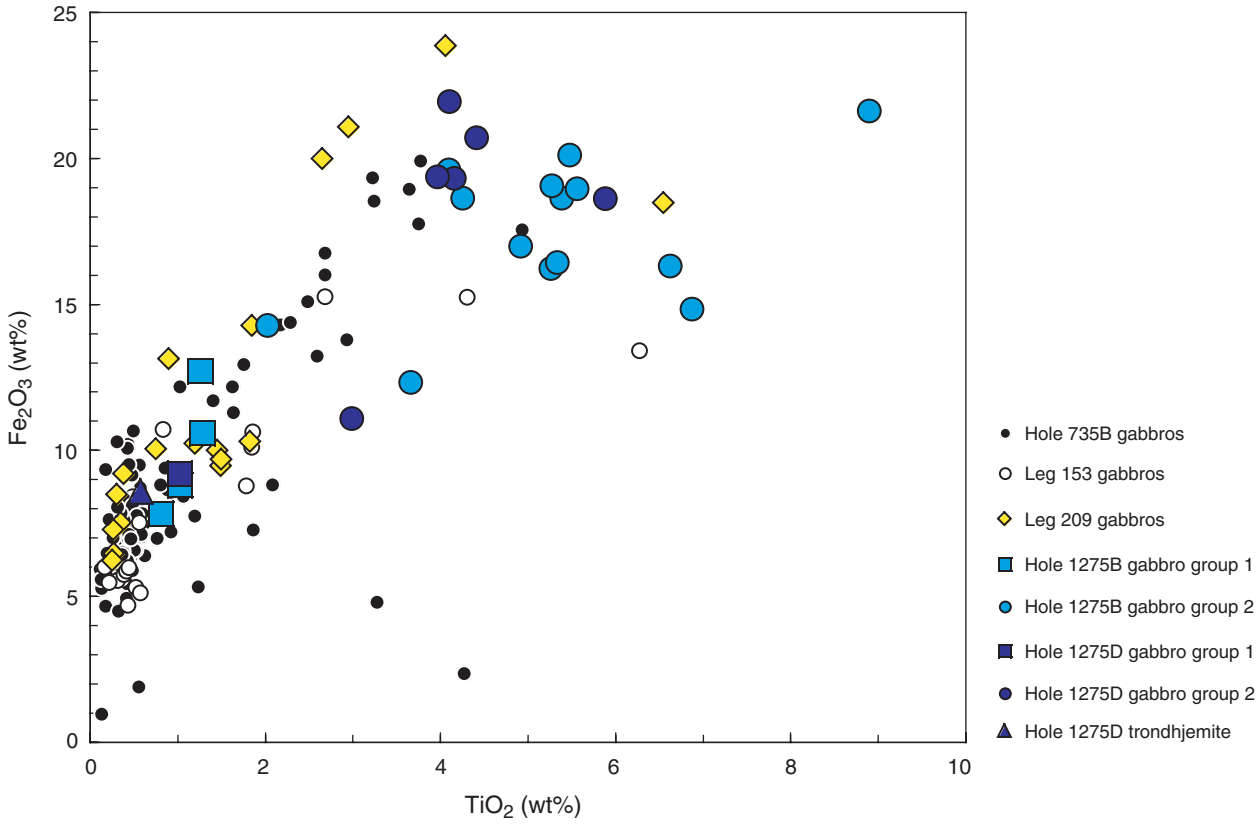

Figure F76. V vs. TiO_2 in gabbroic rocks from Site 1275. Shown for comparison are compositions of gabbroic rocks from Leg 153 (Agar et al., 1997) and Hole 735B (Dick, Natland, Miller, et al., 1999).

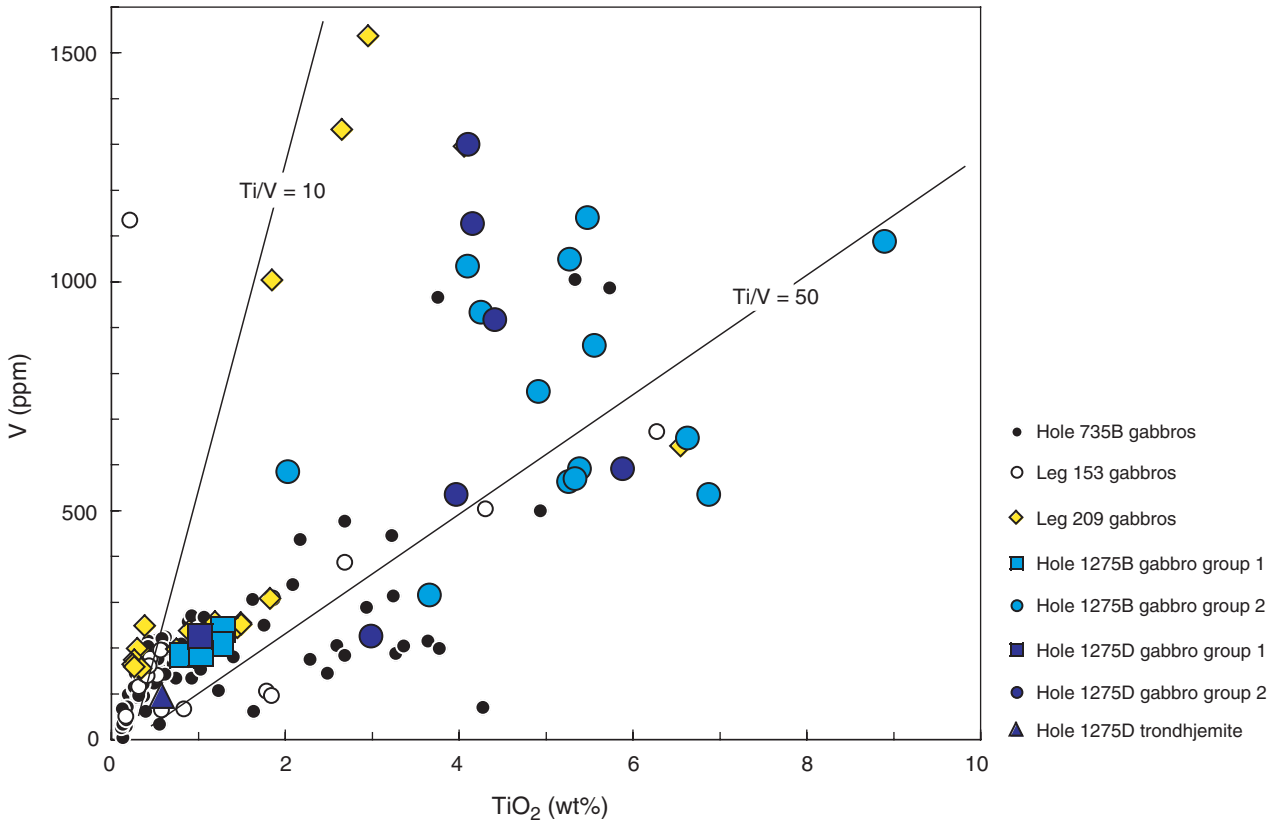

Figure F77. Sc vs. Al_2O_3 in gabbroic rocks from Site 1275. Shown for comparison are compositions of gabbroic rocks from Leg 153 (Agar et al., 1997).

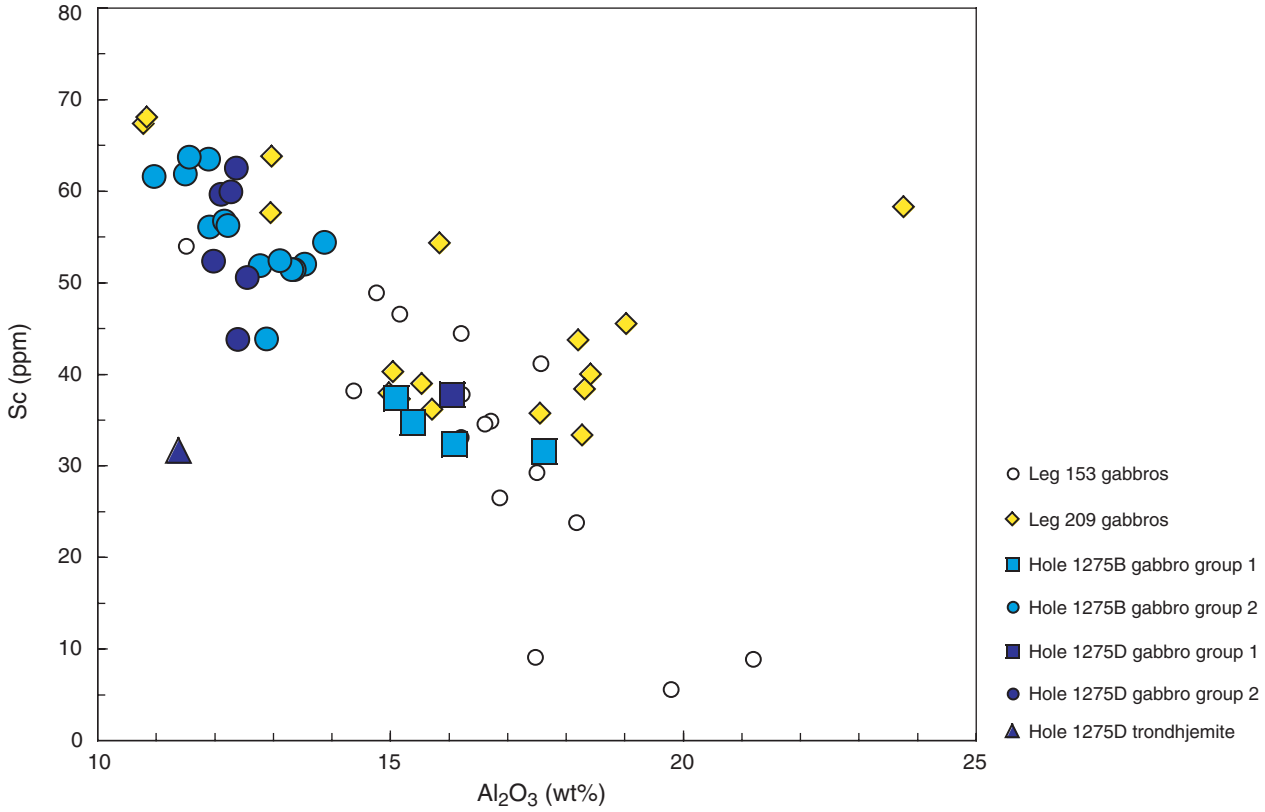

Figure F78. Sc vs. TiO_2 in gabbroic rocks from Site 1275. Shown for comparison are compositions of gabbroic rocks from Leg 153 (Agar et al., 1997).

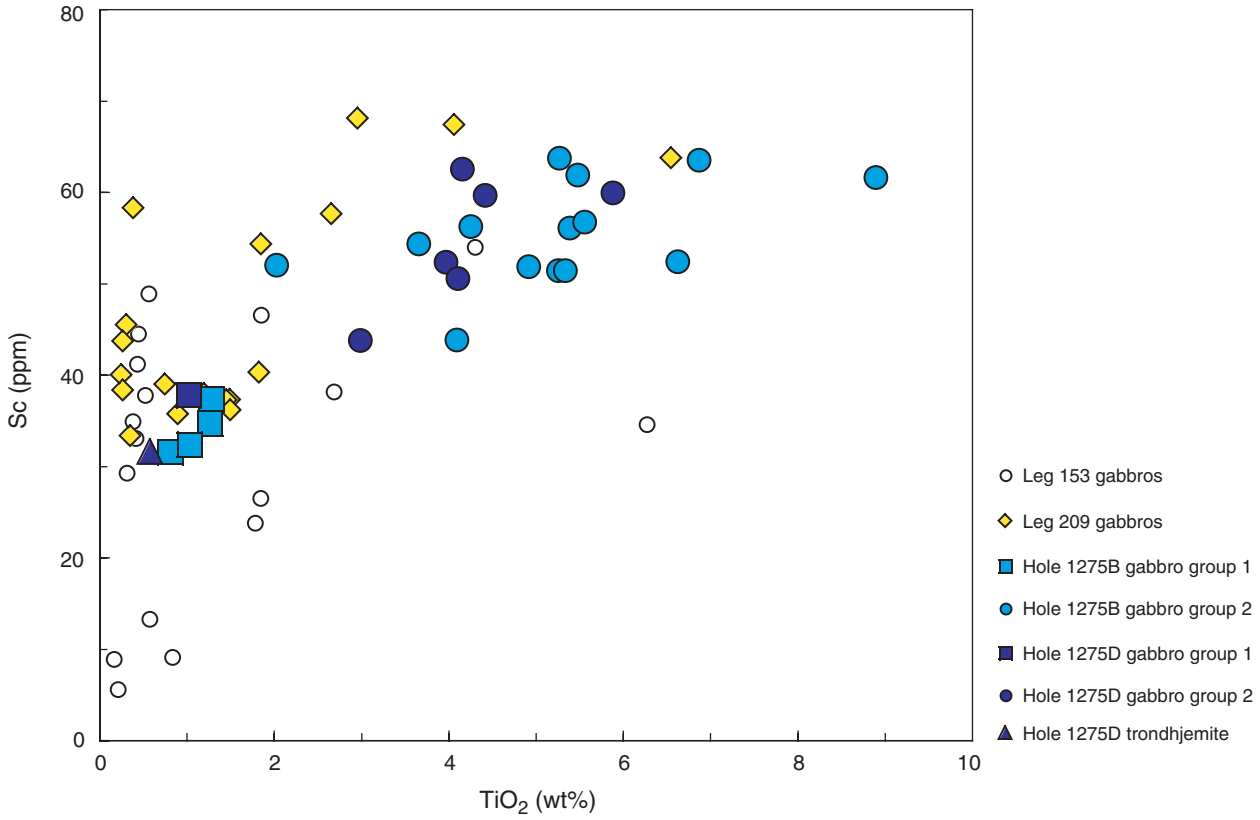

Figure F79. Zr vs. Y for gabbroic rocks from Site 1275. Shown for comparison are gabbroic rocks from Leg 153 (Agar et al., 1997) and from Hole 735B (Dick, Natland, Miller, et al., 1999). The arrow indicates the trajectory toward the trondhjemite sample with extremely high Zr content.

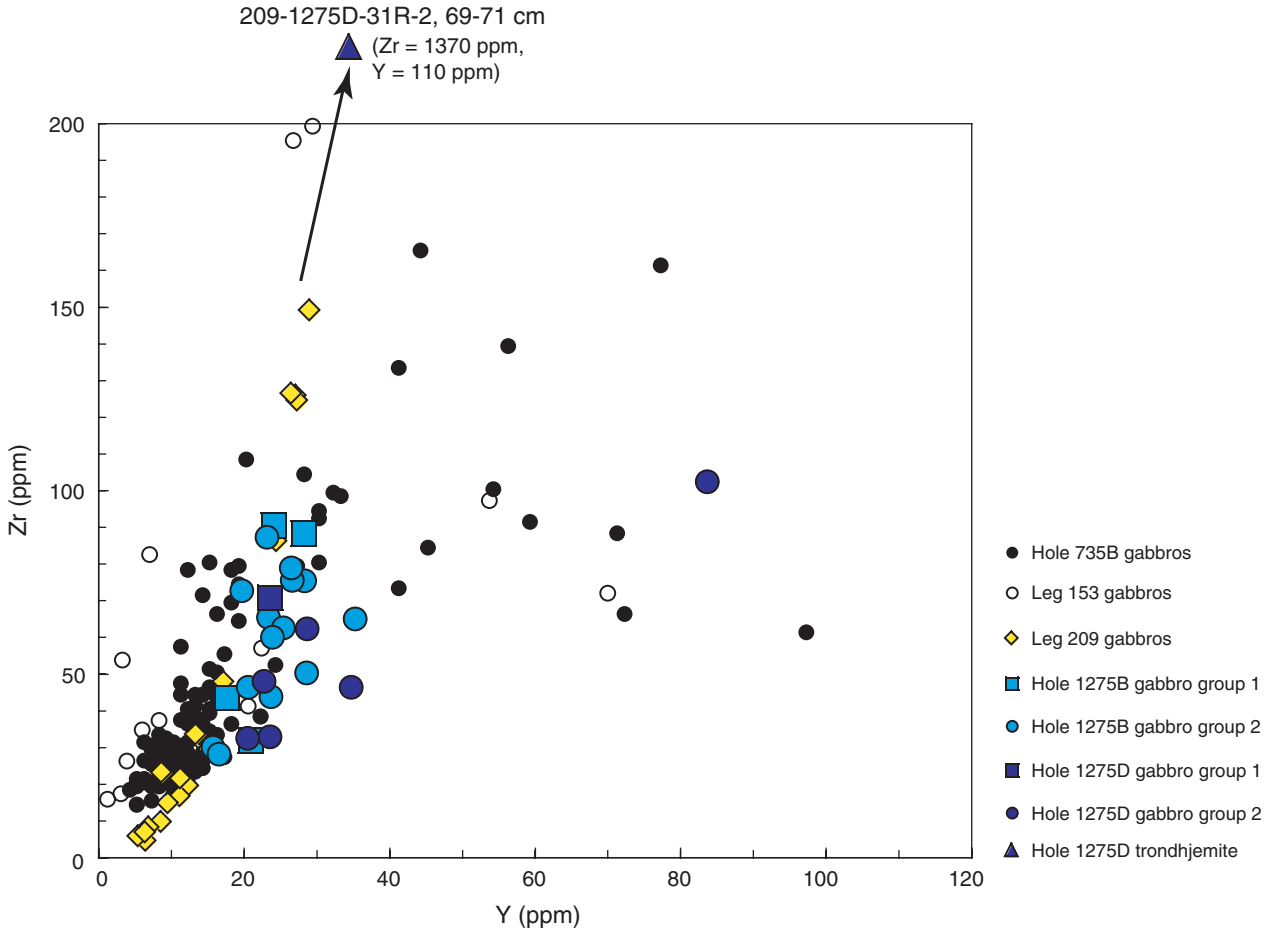

Figure F80. Thermal conductivity, *P*-wave velocity, apparent P-wave anisotropy, bulk density, and porosity in diabases, gabbros, and one troctolite recovered from Hole 1275B. The numbers 0, 1, and 2 in the legend of the thermal conductivity graph refer to the probe needle orientation with respect to the core axis (0 = parallel to the core axis, 1 and 2 = oblique to the core axis), as shown in Figure F11, p. 53, in the "Explanatory Notes" chapter. TD = total depth.

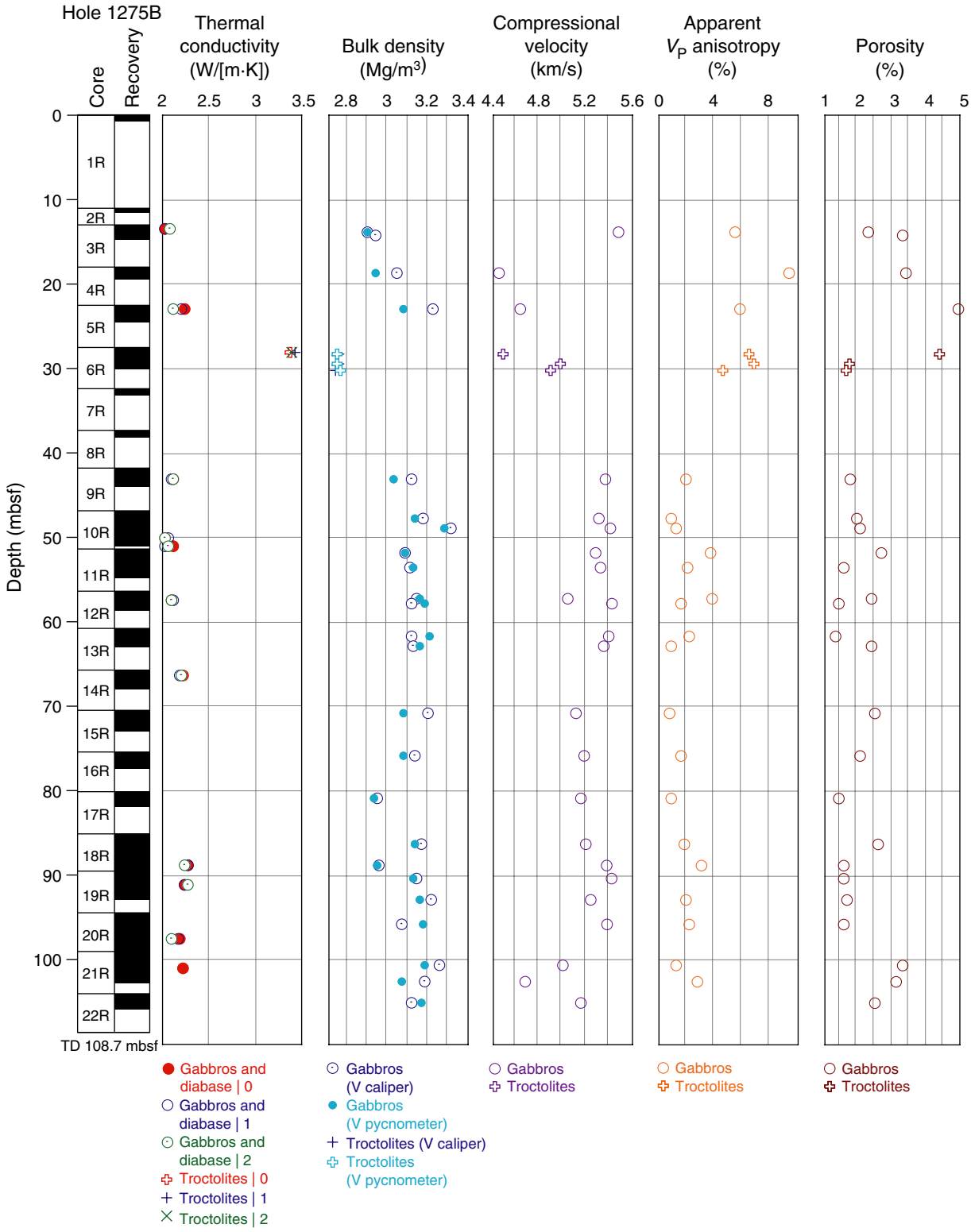

Figure F81. Thermal conductivity, *P*-wave velocity, apparent P-wave anisotropy, bulk density, and porosity in gabbros and troctolites recovered from Hole 1275D. All thermal conductivity measurements were done with the needle probe parallel to the core axis. TD = total depth.

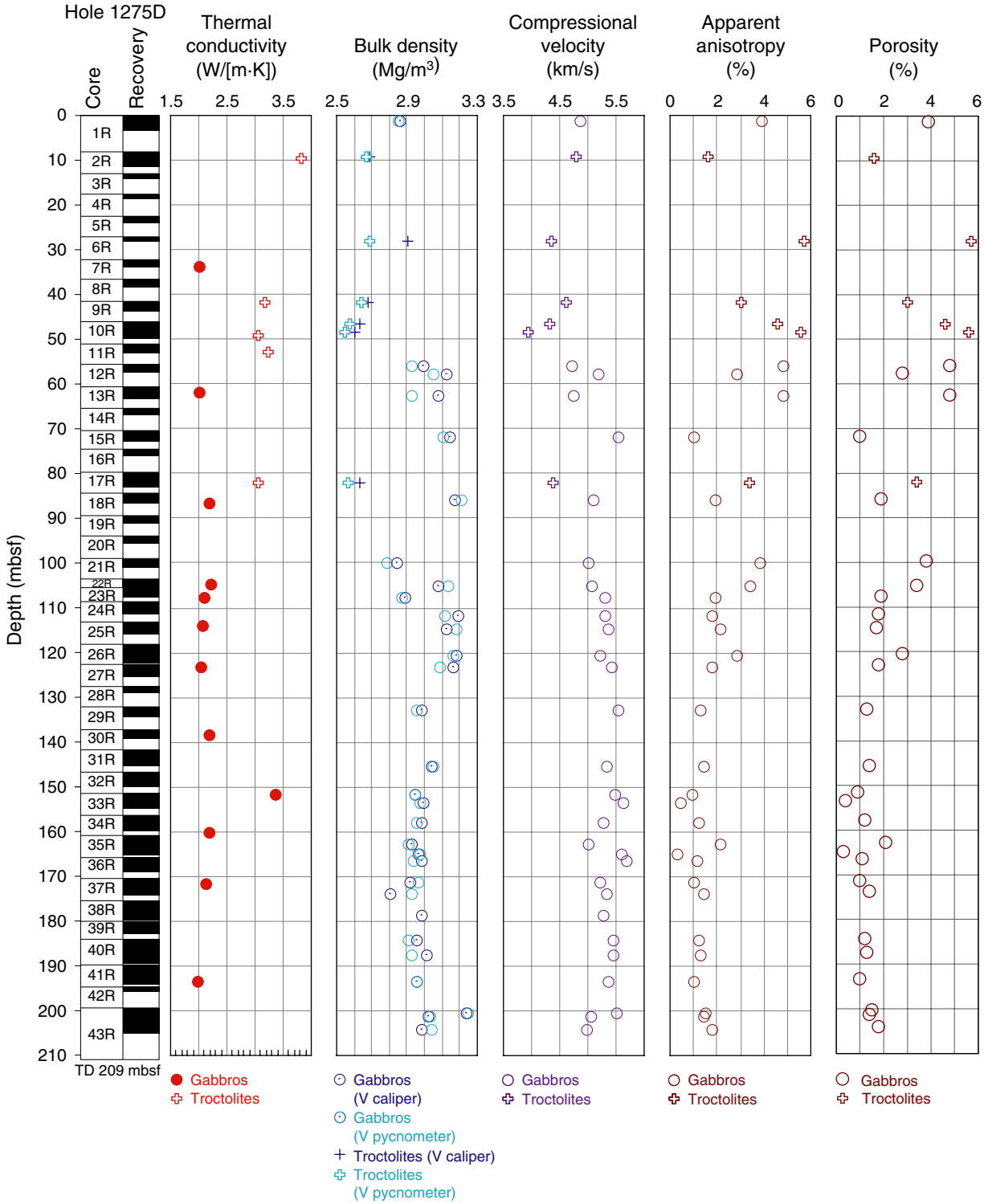

Figure F82. Natural gamma ray (NGR) emission of cores from Holes 1275B and 1275D, measured on the MST.

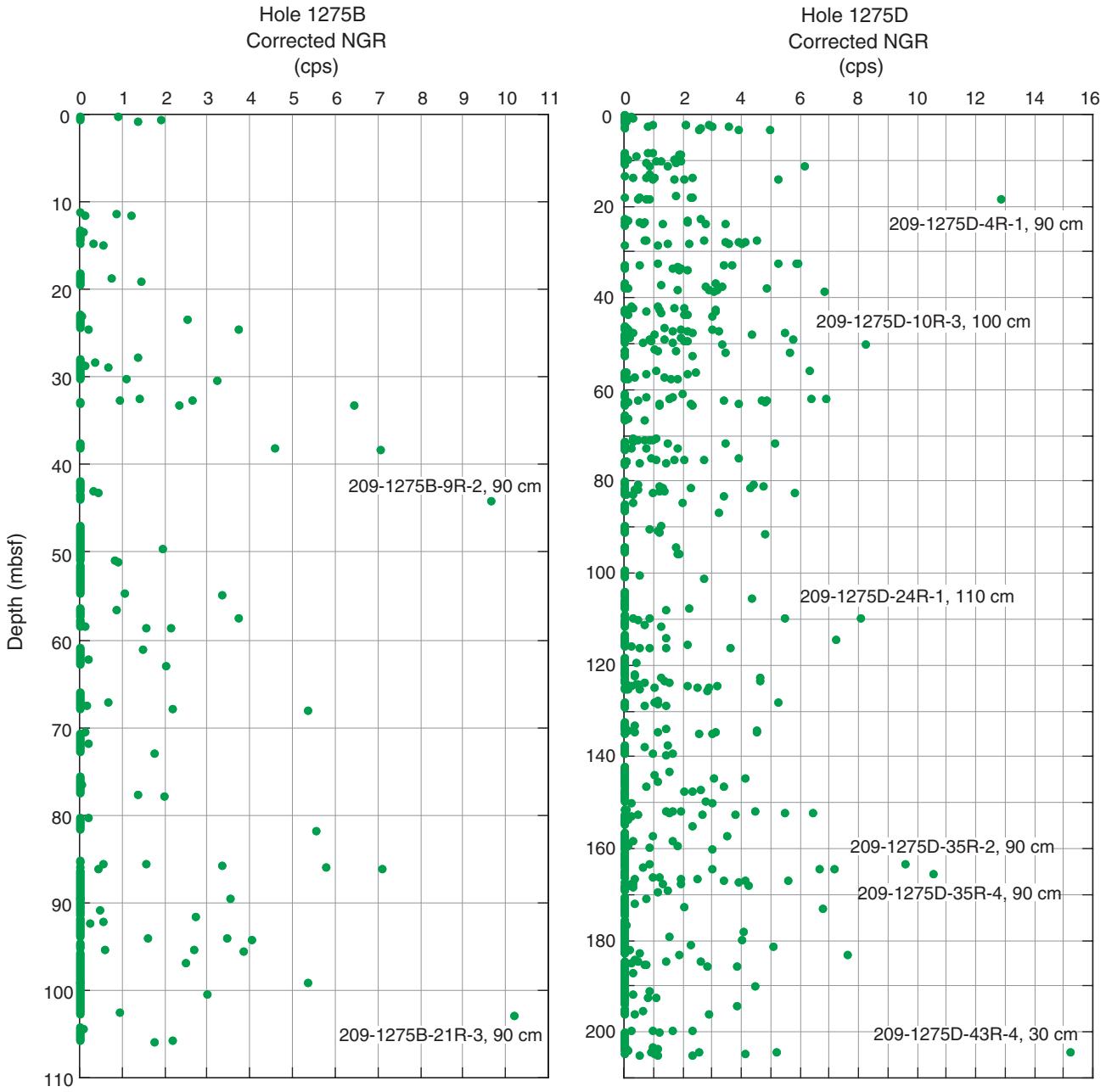

Figure F83. Magnetic susceptibility of cores from Holes 1275B and 1275D, measured on the MST.

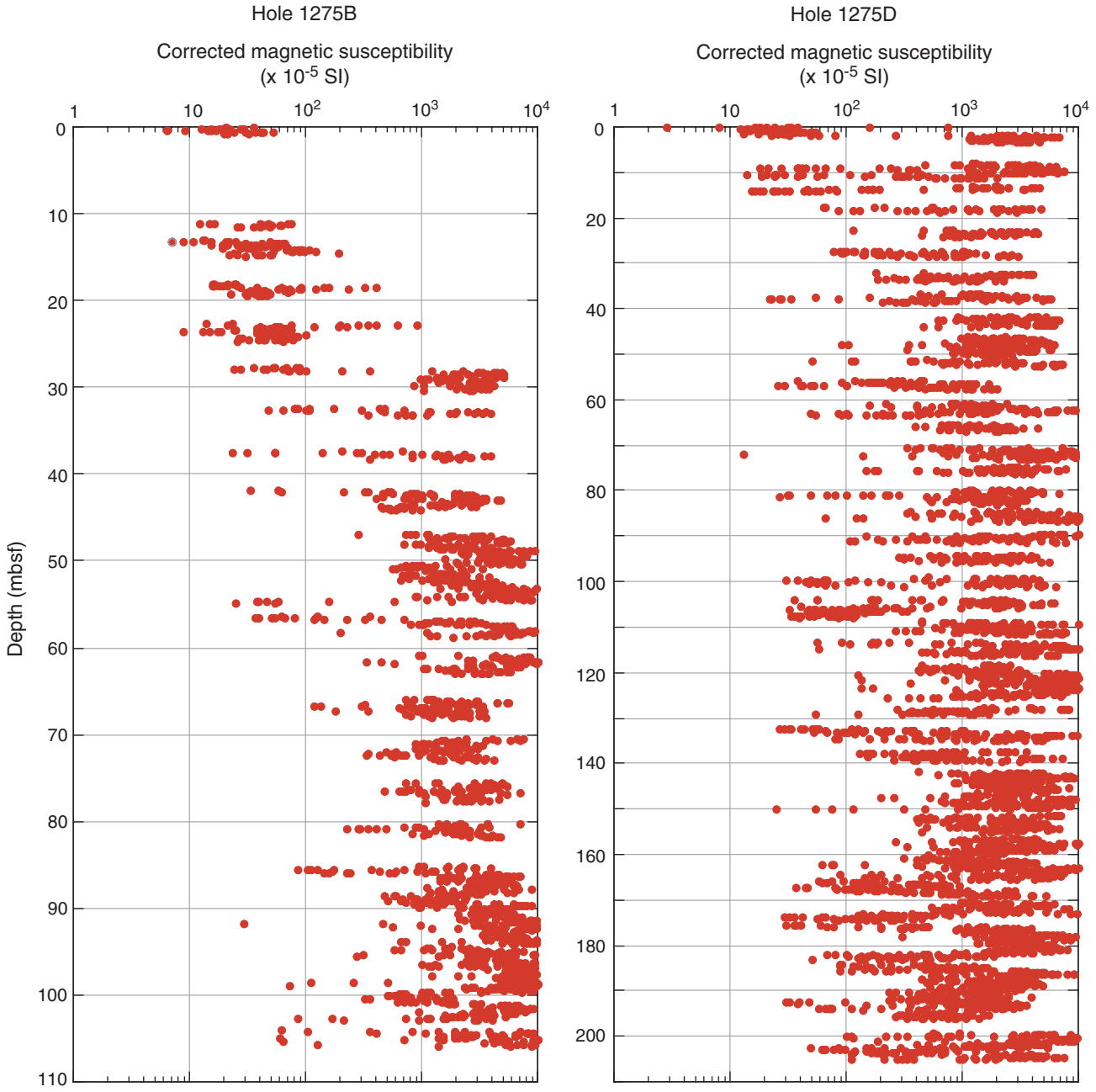

Figure F84. Magnetic susceptibility vs. depth in cores from Holes 1275B and 1275D, compared with data from Leg 179 Hole 1105A (Casey, Pettigrew, Miller, et al., 1999).

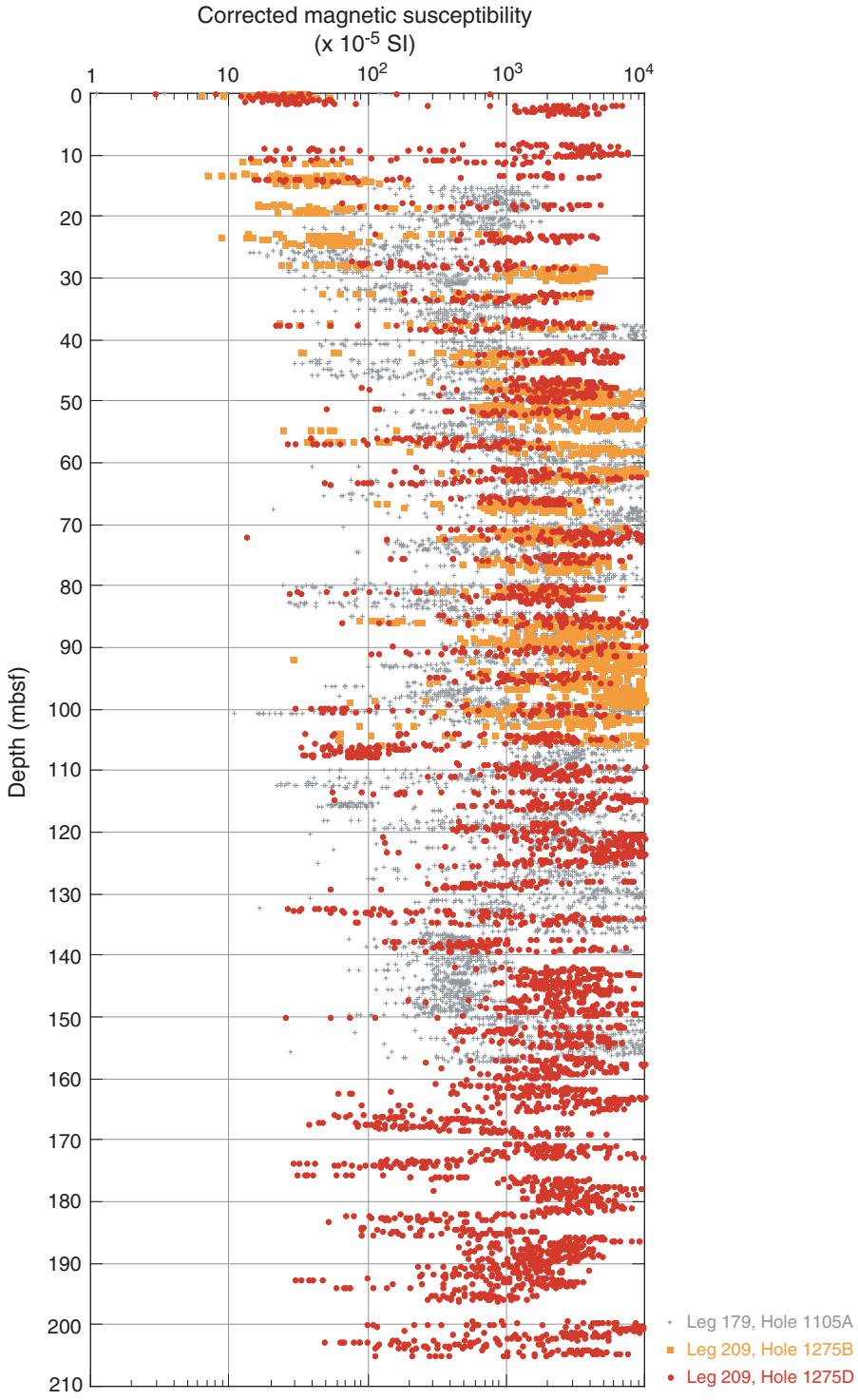

Figure F85. Thermal conductivity of peridotite, troctolite, gabbro, and diabase samples from Sites 1268, 1270, 1271, 1272, 1274, and 1275, compared with values from Legs 118 (Robinson, Von Herzen, et al., 1989), 176 (Dick, Natland, Miller, et al., 1999), 147 (Gillis, Mével, Allan, et al., 1993), and 153 (Cannat, Karson, Miller, et al., 1995). The highest gabbro value was measured in an olivine-gabbro.

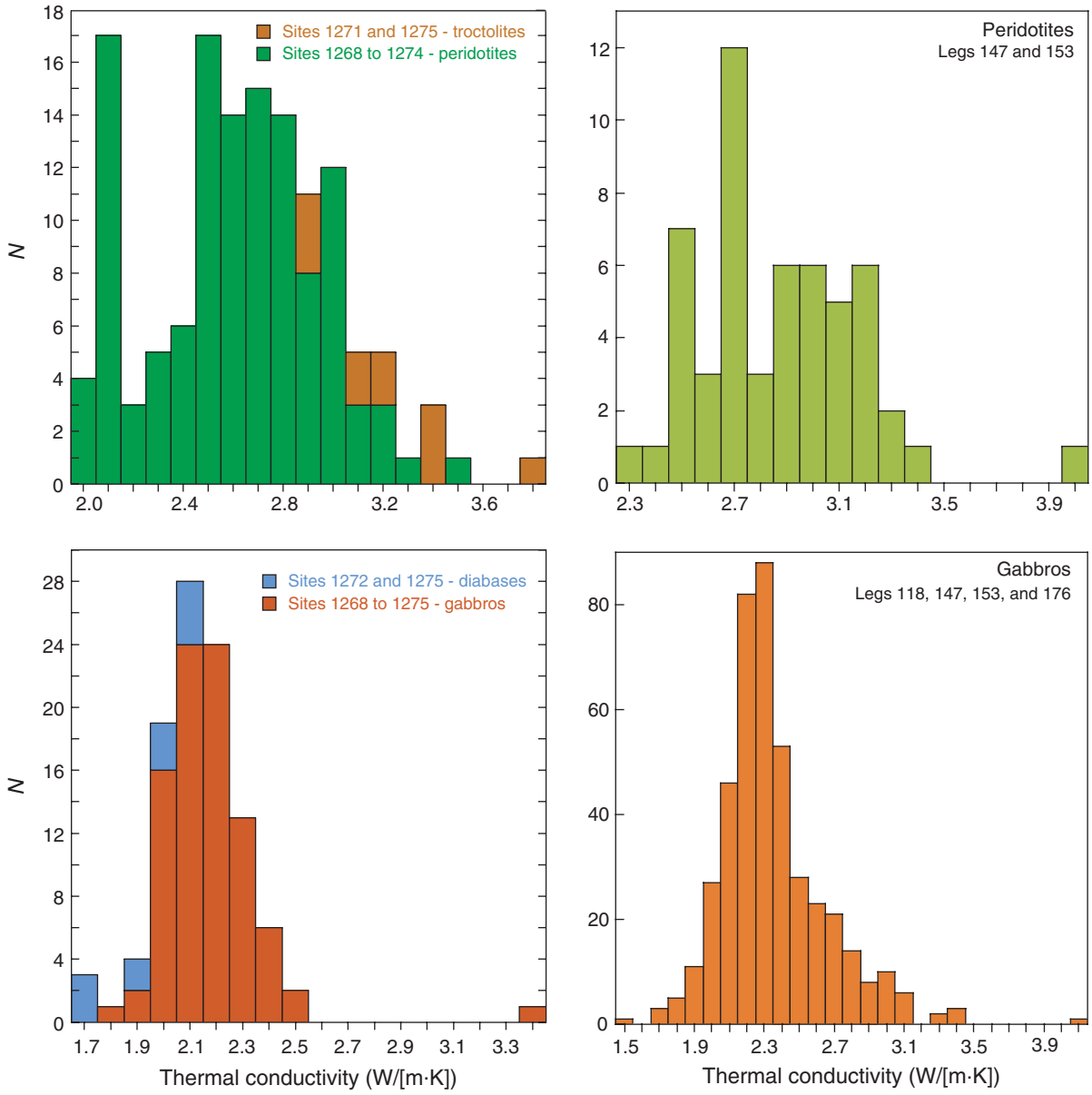

Figure F86. Thermal conductivity anisotropy in peridotite (green), troctolite (brown), gabbro (red), and diabase (blue) samples from Sites 1268, 1270, 1271, 1272, 1274 and 1275.

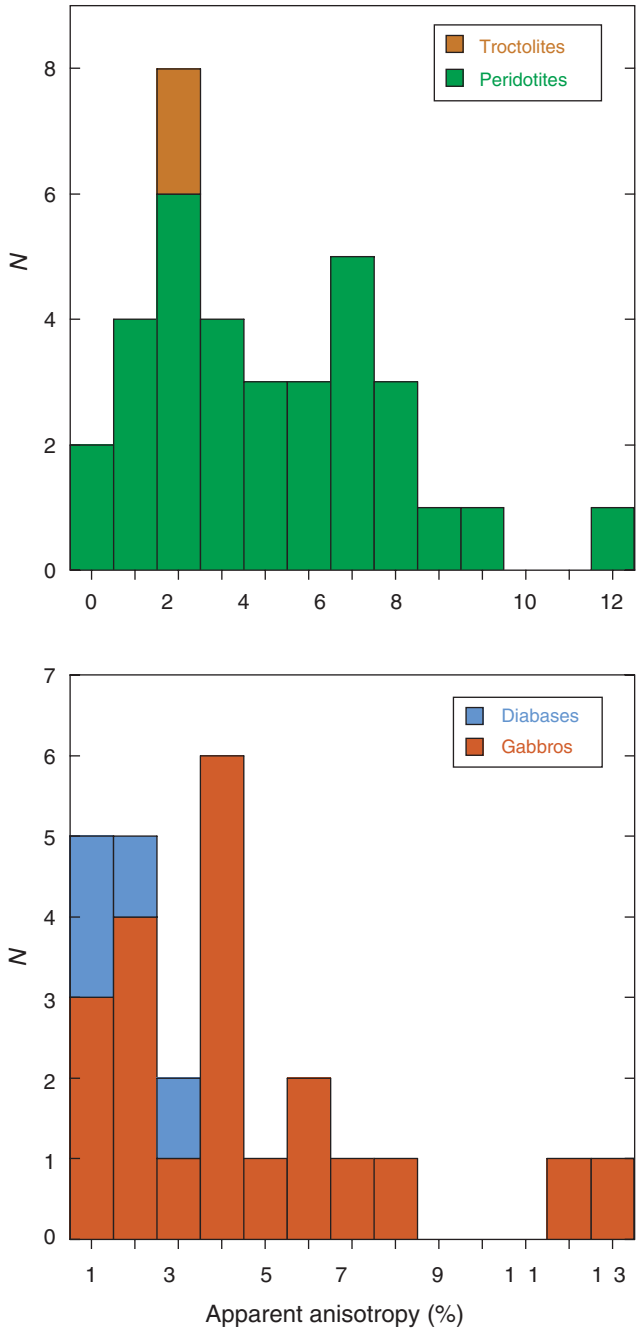

Figure F87. Thermal conductivity (mean of the three measured values for each sample) vs. bulk density in samples from Sites 1268, 1270, 1271,1272, 1274, and 1275. The reference data are from Clark (1966) and Clauser and Huenges (1995).

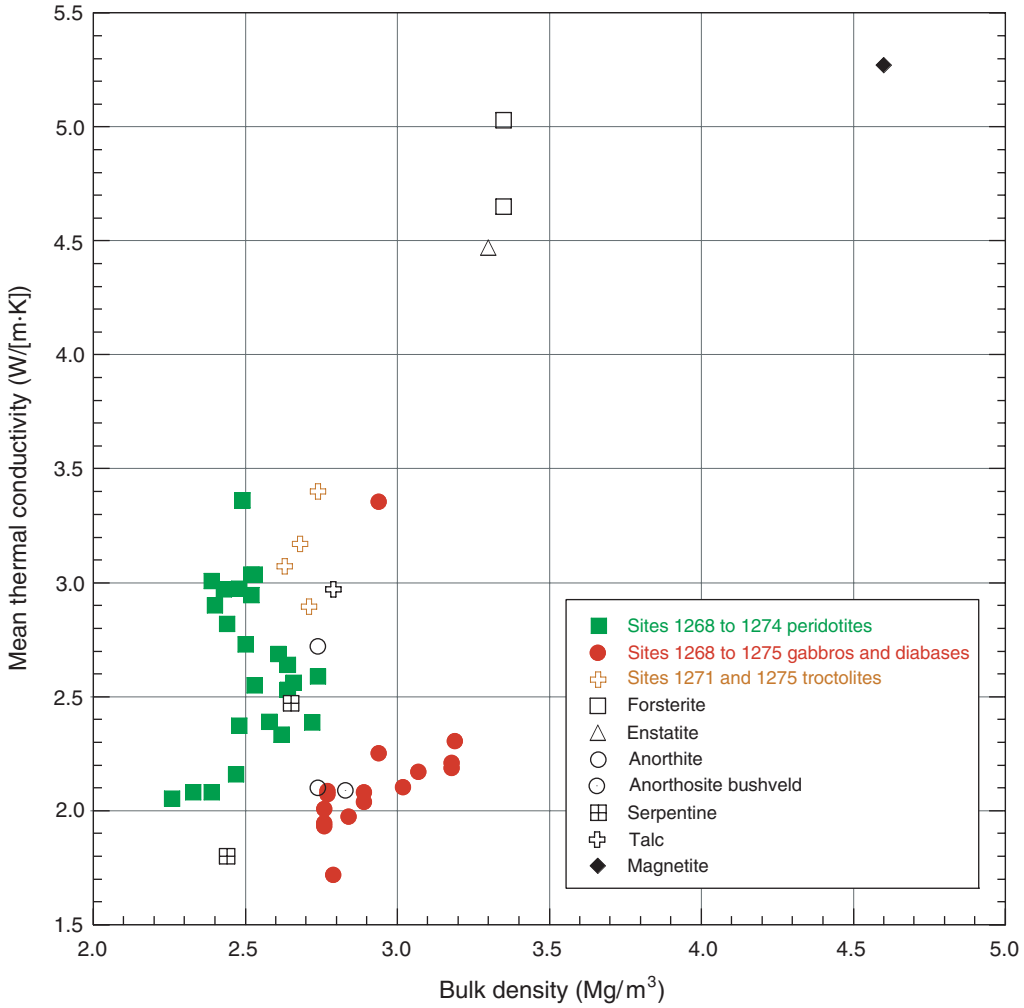

Figure F88. *P*-wave velocity vs. wet bulk density in samples from Site 1275, compared with data from Legs 147 (Gillis, Mével, Allan, et al., 1993; Iturrino et al., 1996) and 153 (Cannat, Karson, Miller, et al., 1995; Miller and Christensen, 1997), as well as Sites 1268, 1270, 1271, 1272, and 1274.

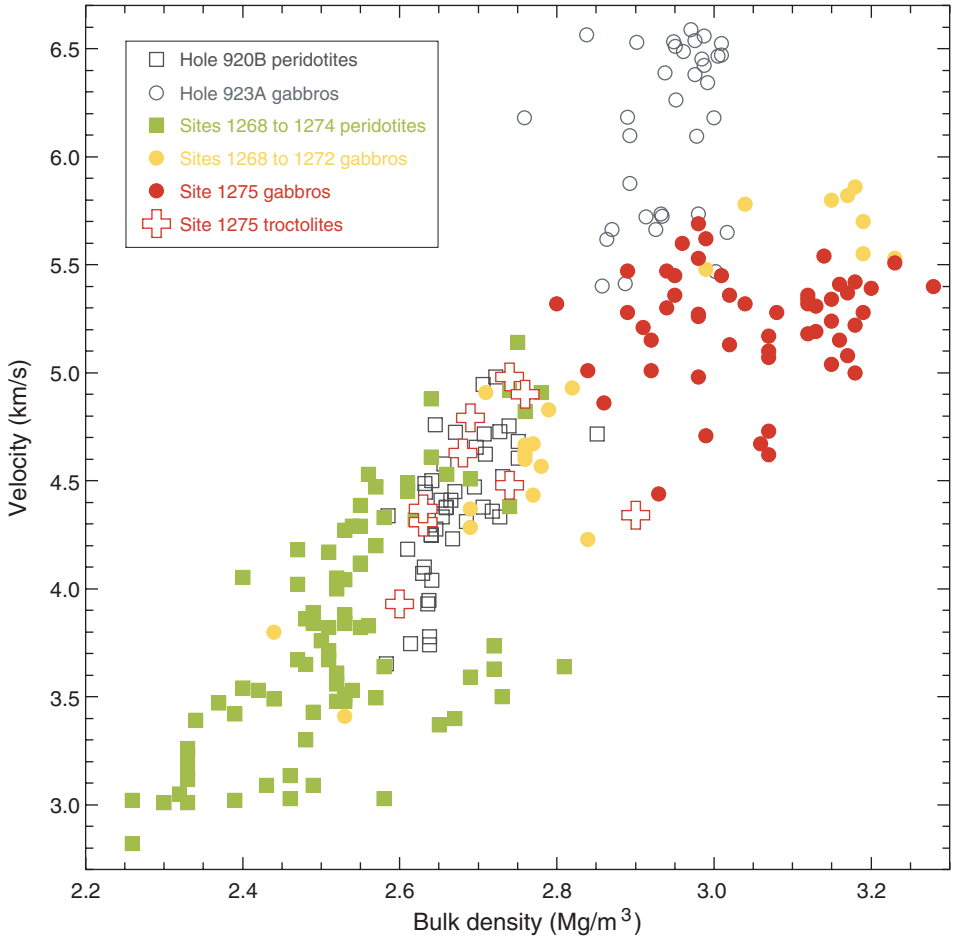

Figure F89. A–D. Magnetic susceptibility vs. bulk or grain density in peridotite and gabbro samples recovered at Sites 1268, 1270, 1271, 1274, and 1275. Shown for comparison are data from Legs 147 (Gillis, Mével, Allan, et al., 1993) and 153 (Cannat, Karson, Miller, et al., 1995) and data from the Josephine ophiolite (Toft et al., 1990) and the Oman ophiolite (B. Ildefonse, unpubl. data).

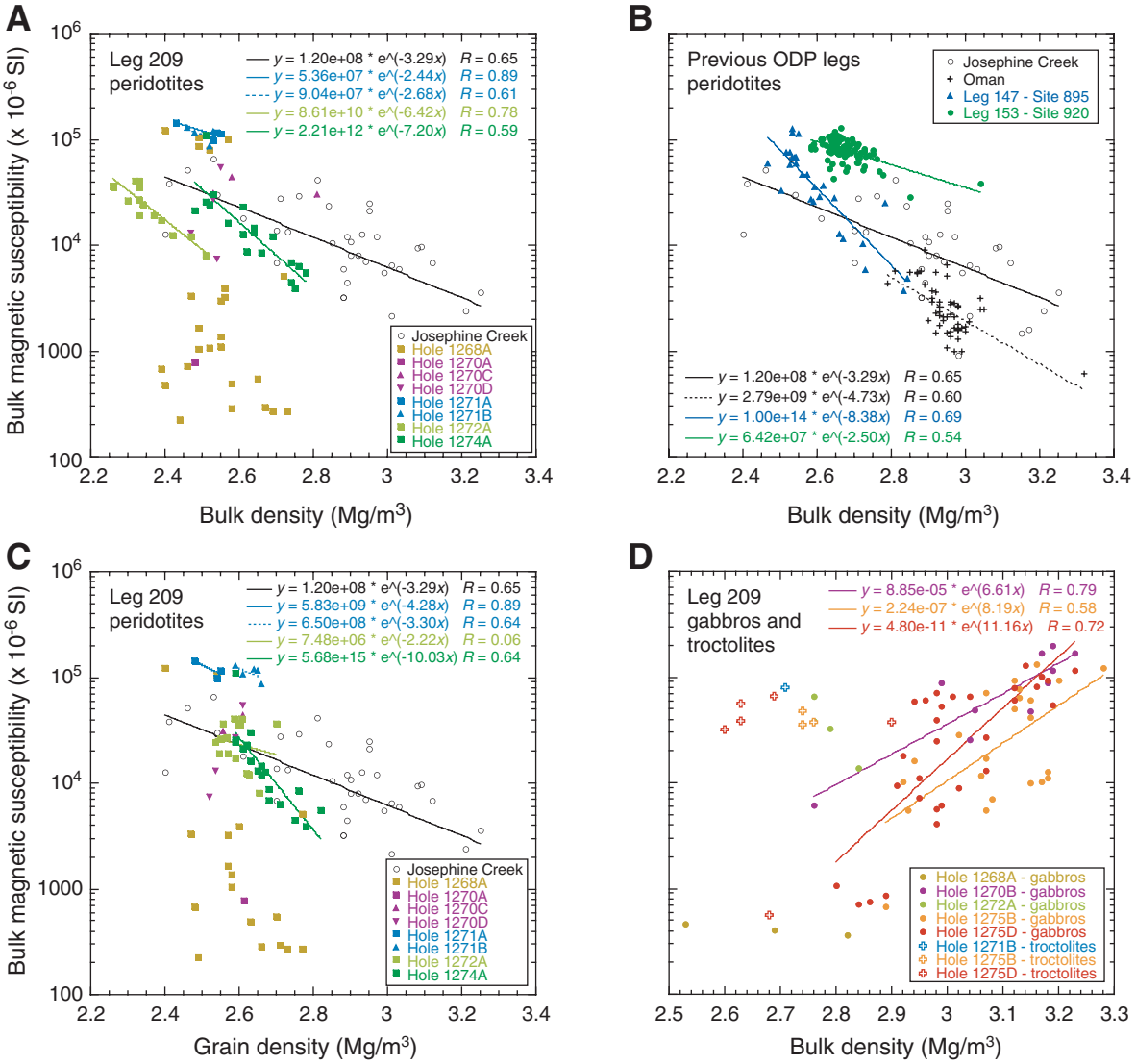

Figure F90. Archive-half magnetic measurements in Hole 1275B. From left: volume magnetic susceptibility; natural remanent magnetization (NRM) intensity (open red circles) and characteristic remanent magnetization (ChRM) intensity (solid circles); inclination of the NRM and the ChRM; and percentage of the NRM carried by the ChRM. Class A directions are indicated by gray solid circles. Blue solid circles represent Class C directions. Remanence and susceptibility data from within 4 cm of a piece end have been excluded. Note that susceptibility values are from whole-core measurements. TD = total depth.

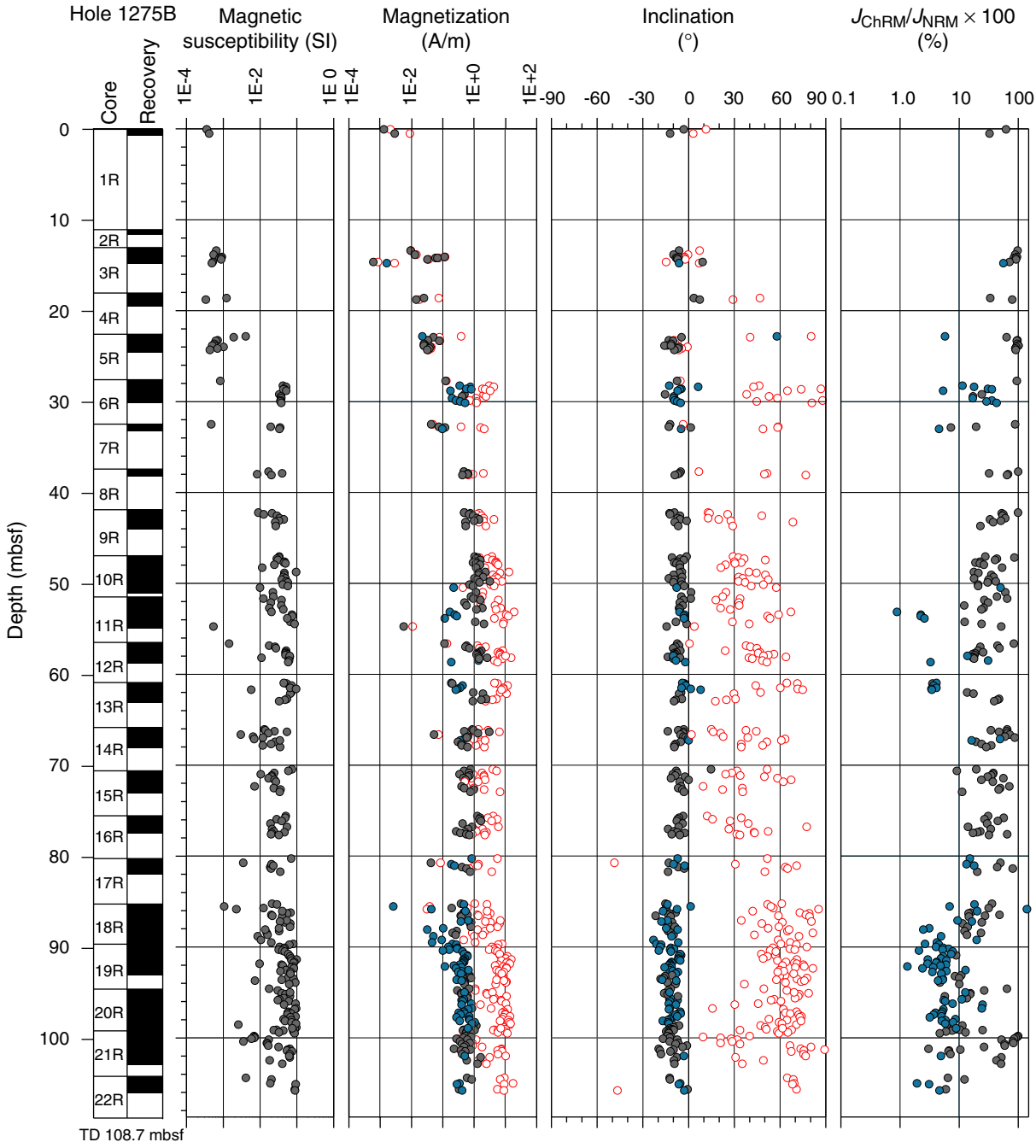

Figure F91. Archive-half magnetic measurements in Hole 1275D. From left: proportion of diabase; volume magnetic susceptibility; natural remanent magnetization (NRM) intensity (open red circles) and characteristic remanent magnetization (ChRM) intensity (solid circles); inclination of the NRM and the ChRM; and percentage of the NRM carried by the ChRM. Class A directions are indicated by gray solid circles. Blue solid circles represent Class C directions. Remanence and susceptibility data from within 4 cm of a piece end have been excluded. Note that susceptibility values are from archive-half measurements. TD = total depth.

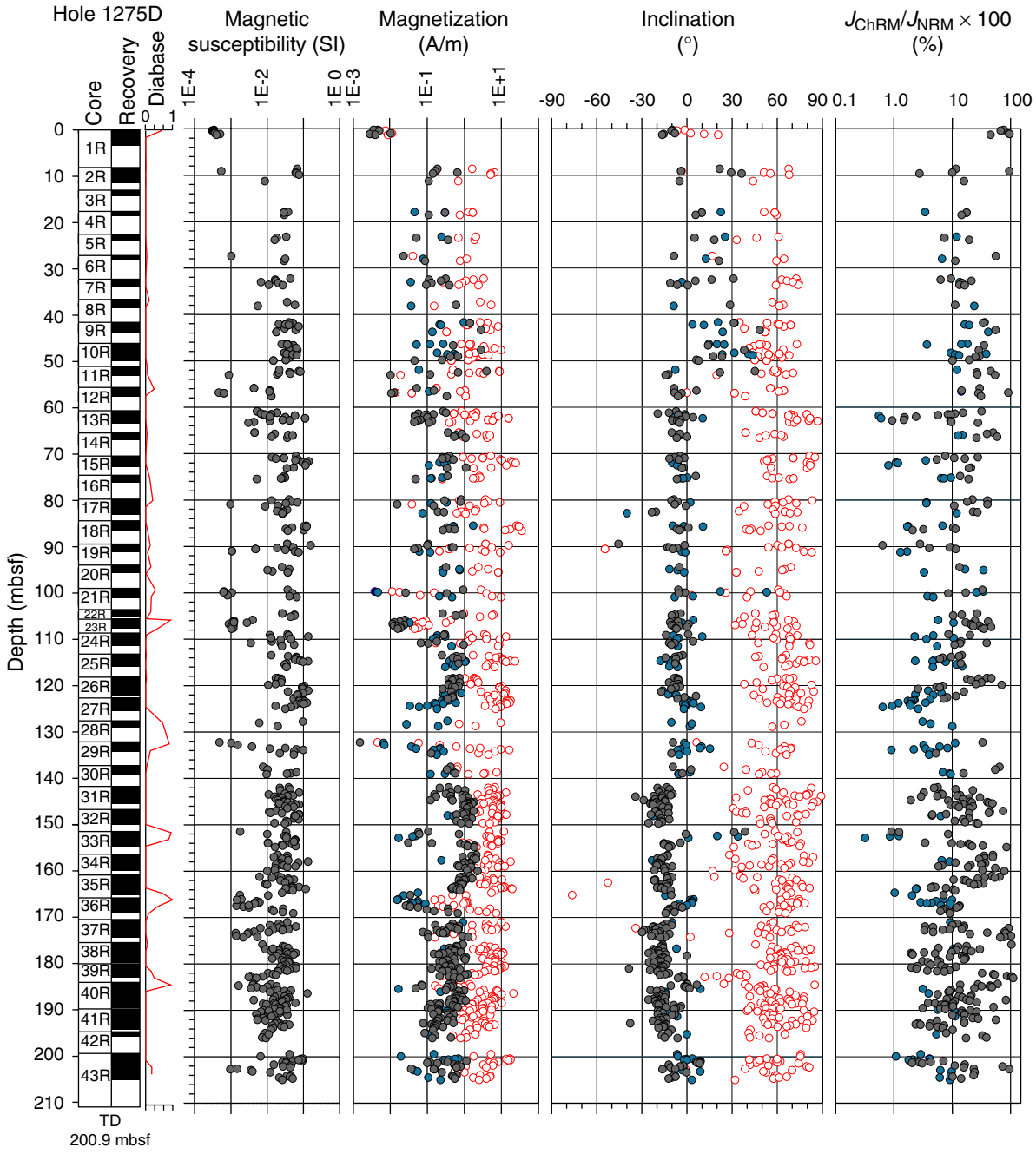

Figure F92. Comparison of representative vector endpoint diagrams for archive-half measurements (D–F) and discrete samples (A–C) from Hole 1275B. ***A.*** Sample 209-1275B-3R-1, 82–84 cm. **B.** Sample 209-1275B-10R-2, 44–46 cm. **C.** Sample 209-1275B-19R-1, 76–78 cm. **D.** Section 209-1275B-3R-1, 84 cm. **E.** Section 209-1275B-10R-2, 44 cm. **F.** Section 209-1275B-19R-1, 76 cm. NRM = natural remanent magnetization. Open circles = projections of the remanence onto the north–south vertical plane, solid circles are projections of the remanence onto the horizontal plane.

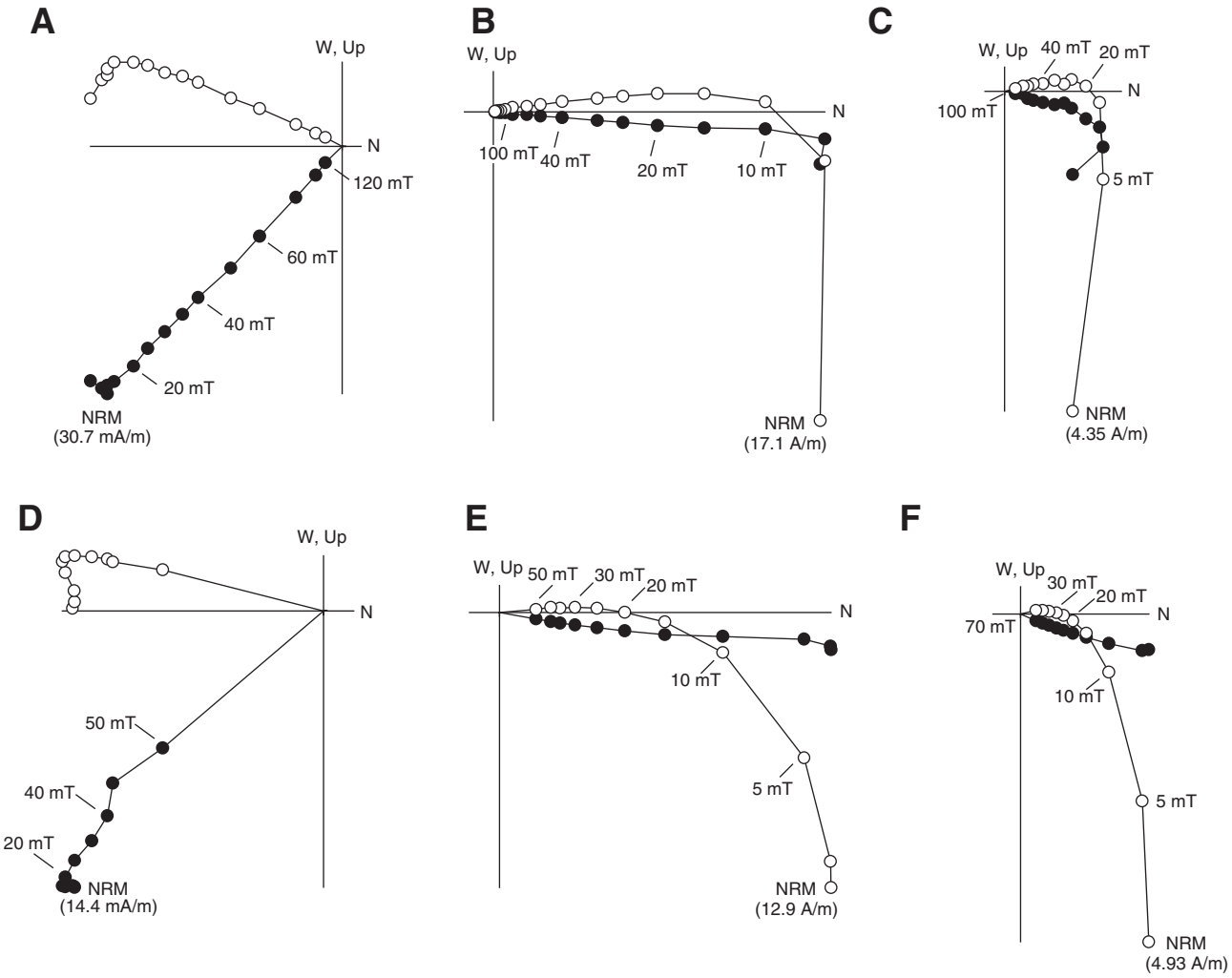

Figure F93. Comparison of representative vector endpoint diagrams for archive-half measurements (C, D) and discrete samples (A, B) of gabbros from Hole 1275D. **A.** Sample 209-1275D-26R-2, 95–97 cm. **B.** Sample 209-1275D-35R-2, 44–46 cm. **C.** Section 209-1275D-26R-2, 96 cm. **D.** Section 209-1275D-35R-2, 44 cm. NRM = natural remanent magnetization. Open circles = projections of the remanence onto the north–south vertical plane, solid circles are projections of the remanence onto the horizontal plane.

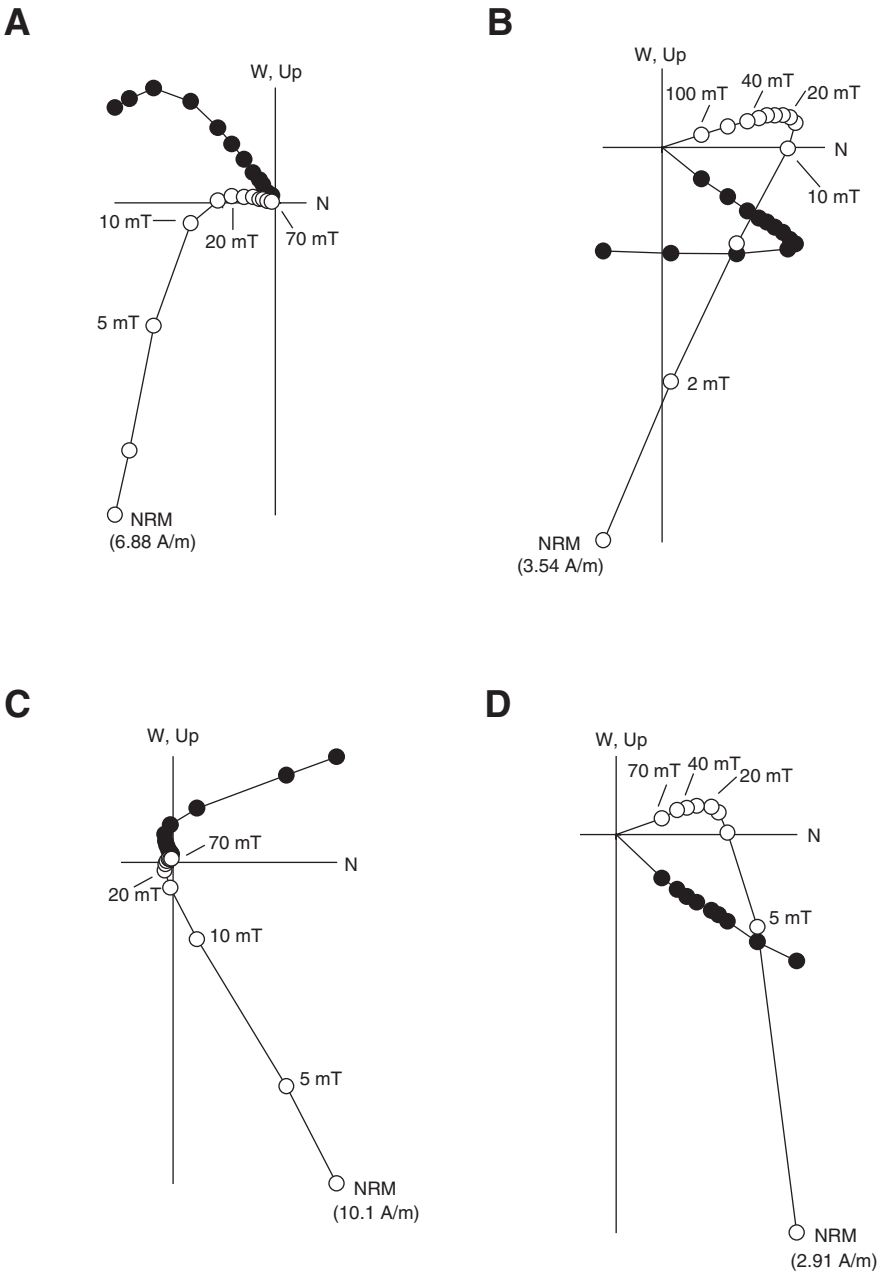

Figure F94. Vector endpoint diagrams for archive-half measurements (D–F) and discrete samples (A–C) of diabase and microgabbros from Hole 1275D showing positive inclinations (A, D), multicomponent magnetization (B, E), and very low coercivity remanence with positive inclinations (C, F). **A.** Sample 209-1275D-9R-1, 17–19 cm. **B.** Sample 209-1275D-10R-2, 95–97 cm. **C.** Sample 209-1275D-33R-1, 20–22 cm. **D.** Section 209-1275D-9R-1, 20 cm. **E.** Section 209-1275D-10R-2, 94 cm. **F.** Section 209-1275D-33R-1, 16 cm. NRM = natural remanent magnetization. Open circles = projections of the remanence onto the north–south vertical plane, solid circles are projections of the remanence onto the horizontal plane.

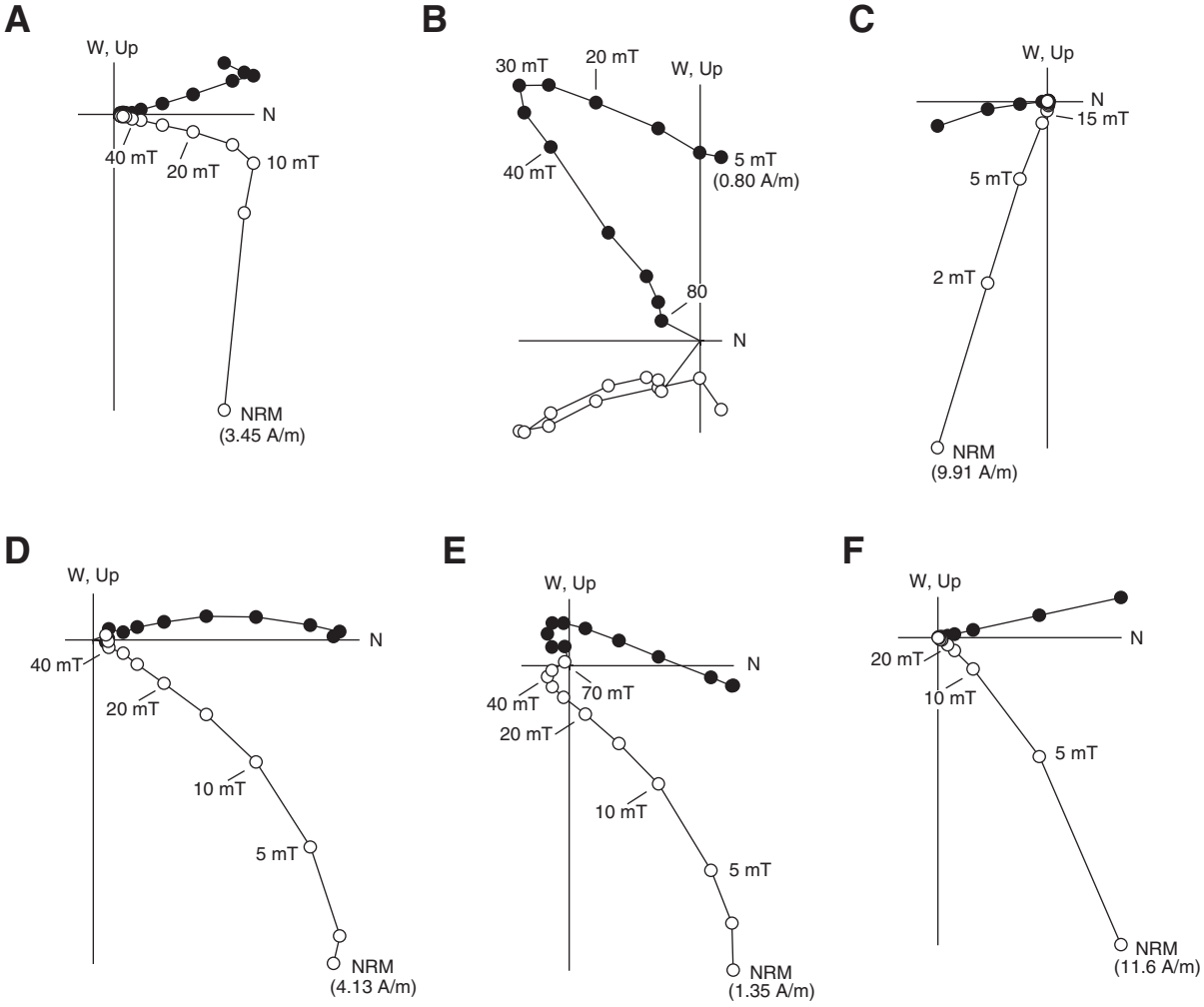

Figure F95. Anisotropy of magnetic susceptibility for discrete samples from (**A**) Hole 1275B and (**B**) Hole 1275D. Solid circles = the orientation of the eigenvector associated with the minimum eigenvalue of the susceptibility tensor. Red squares = the eigenvector associated with the maximum eigenvalue. All data have been restored to the geographic reference frame using the remanent declination (see text).

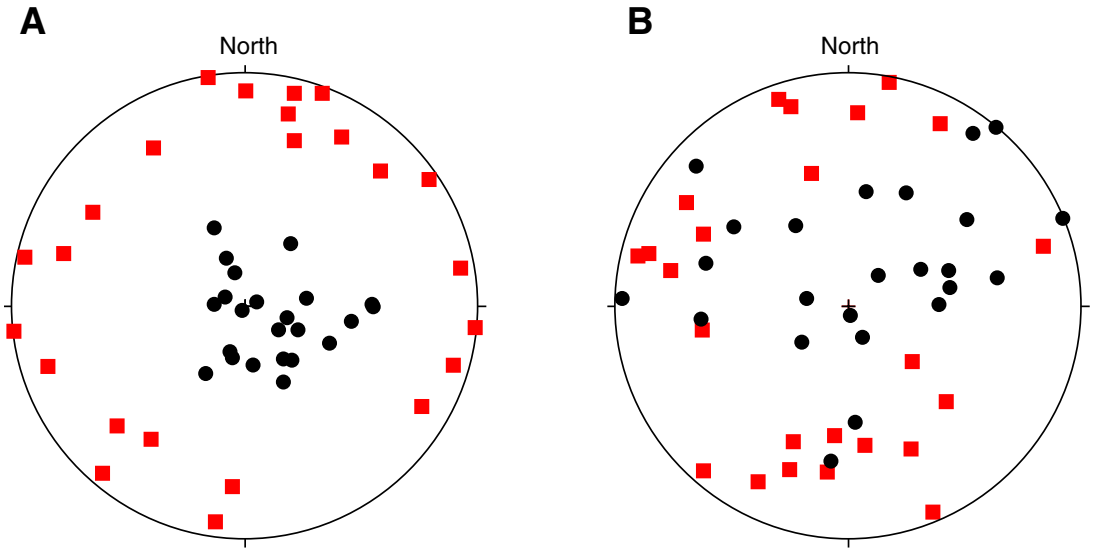

Figure F96. Histograms of inclinations for discrete samples (black bars) and archive halves (gray bars) from (**A**) Hole 1275B and (**B**) Hole 1275D.

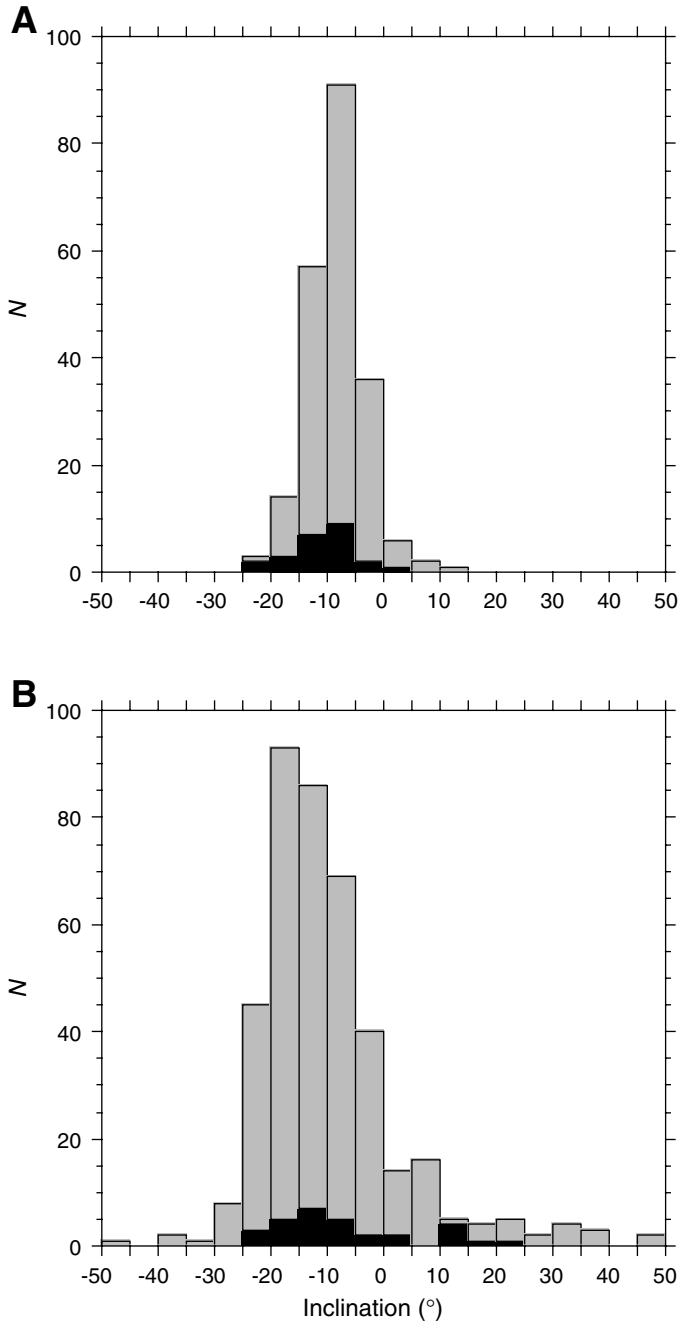

Figure F97. Original (right) and smoothed resistivity-at-the-bit (RAB)-8 resistivity images showing that the smoothing process removed most of the depth smear artifacts, notably between 10 and 15 mbsf.

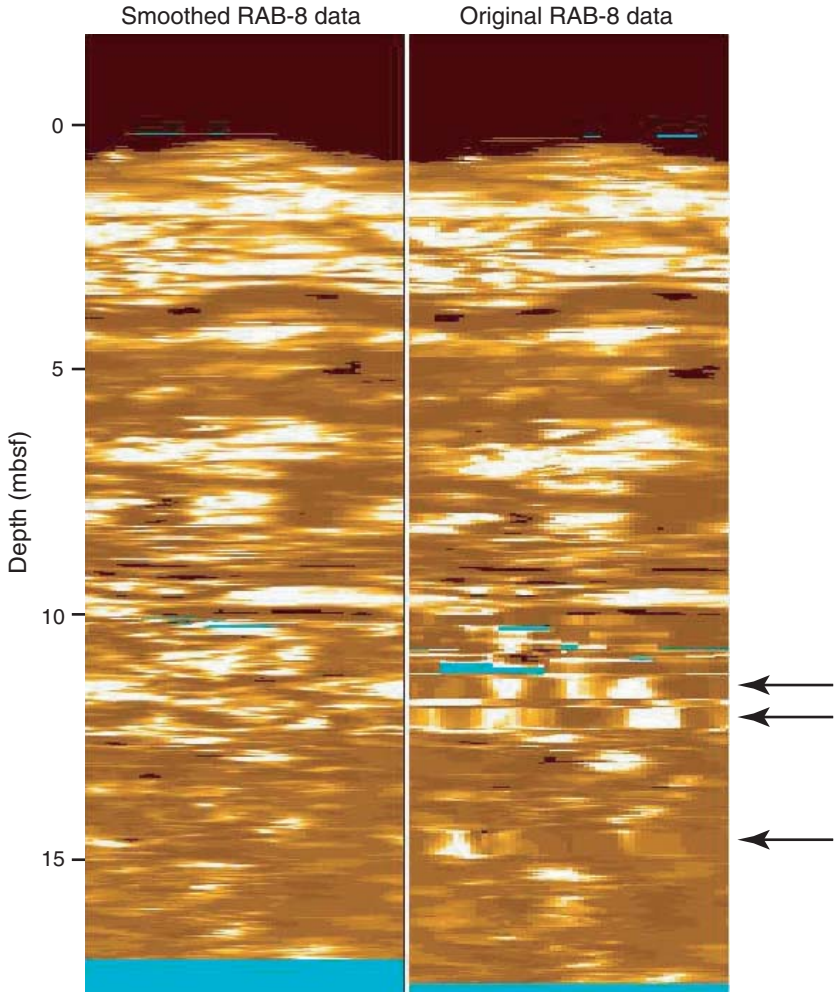

Figure F98. Diagram showing the original (blue upper curve) and smoothed (lower curve) RAB-8 time-depth file. The original curve has been offset +4 ft for clarity. Depth is in feet below rig floor and time is in seconds, time stamped at midnight on the previous day.

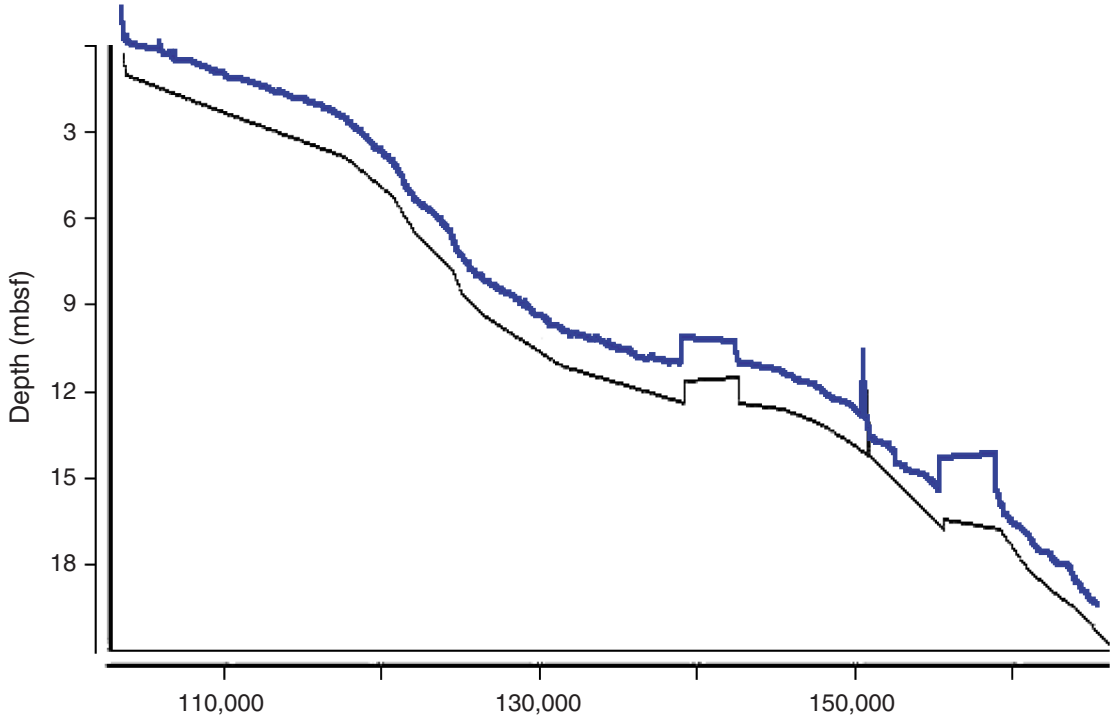

Figure F99. Static and dynamic images showing noticeable structures that likely represent fractures.

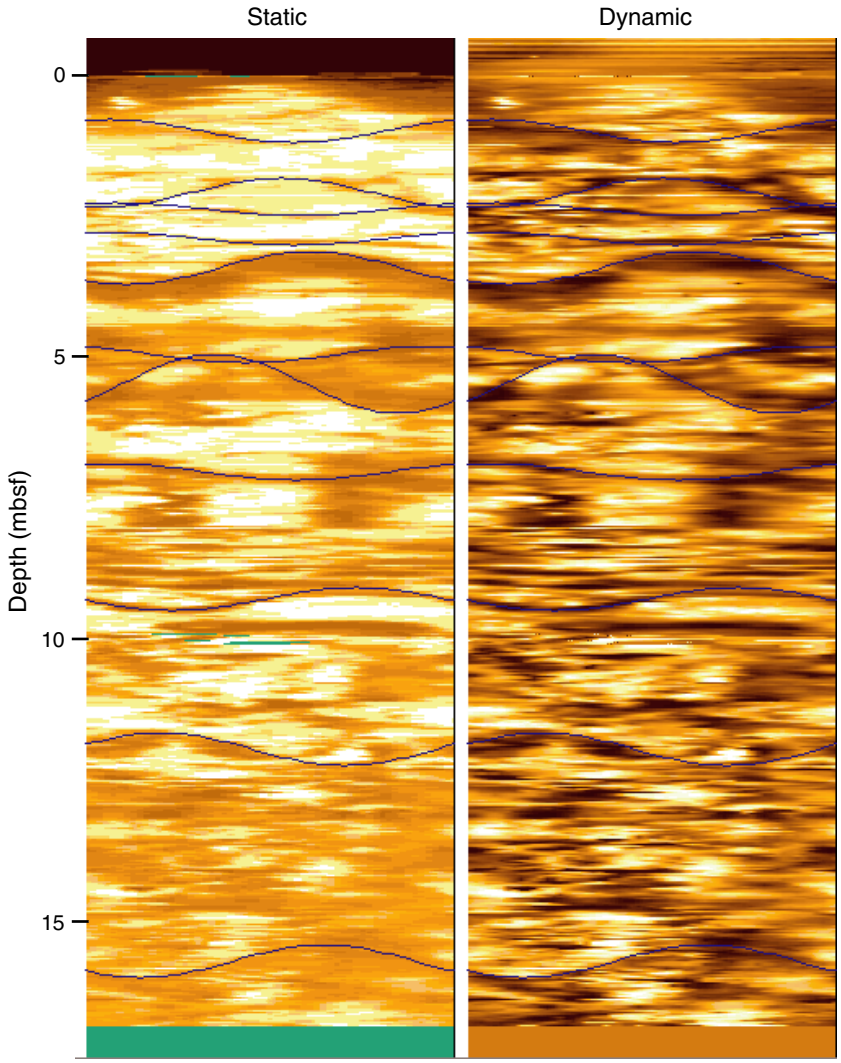

Figure F100. Three-dimensional display of dynamic resistivity-at-the-bit (RAB)-8 images with different geographical orientations. The images also show structures dipping at different azimuths.

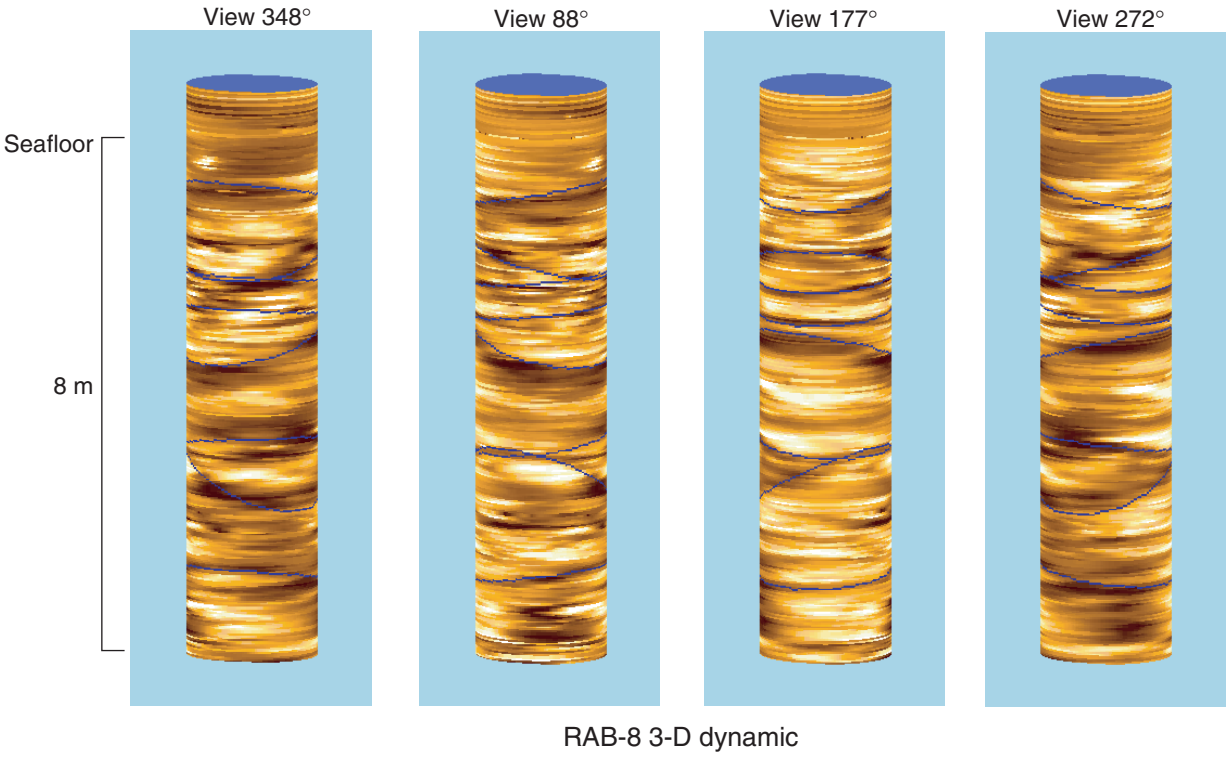

Figure F101. Total gamma ray and deep (BD), medium (BM), shallow (BS), ring (RRING), and bit (RBIT) resistivity logs recorded in Hole 1275C with the RAB-8.

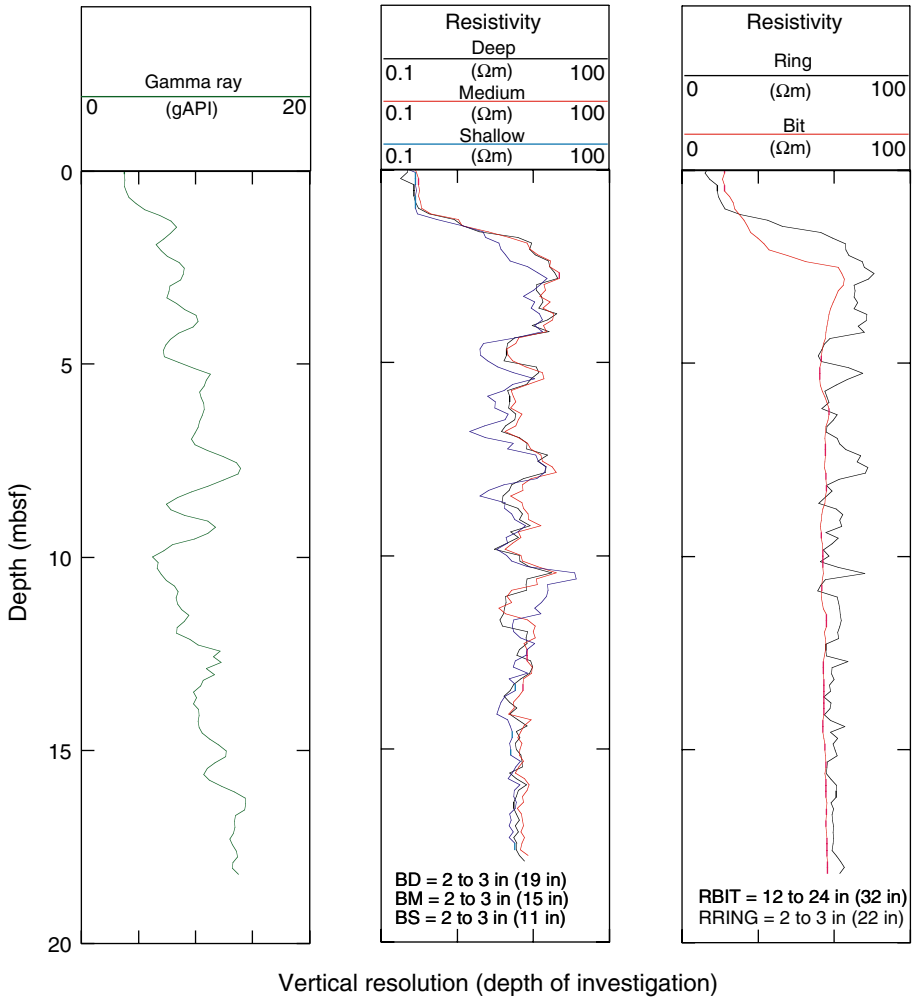

Figure F102. Core recovery, Formation MicroScanner (FMS) and Hostile Environment Litho-Density Sonde (HLDS) caliper, deep (IDPH) and shallow (SFLU) resistivity, and porosity logs from Hole 1275C. The interval highlighted in yellow shows a high-porosity interval. TD = total depth.

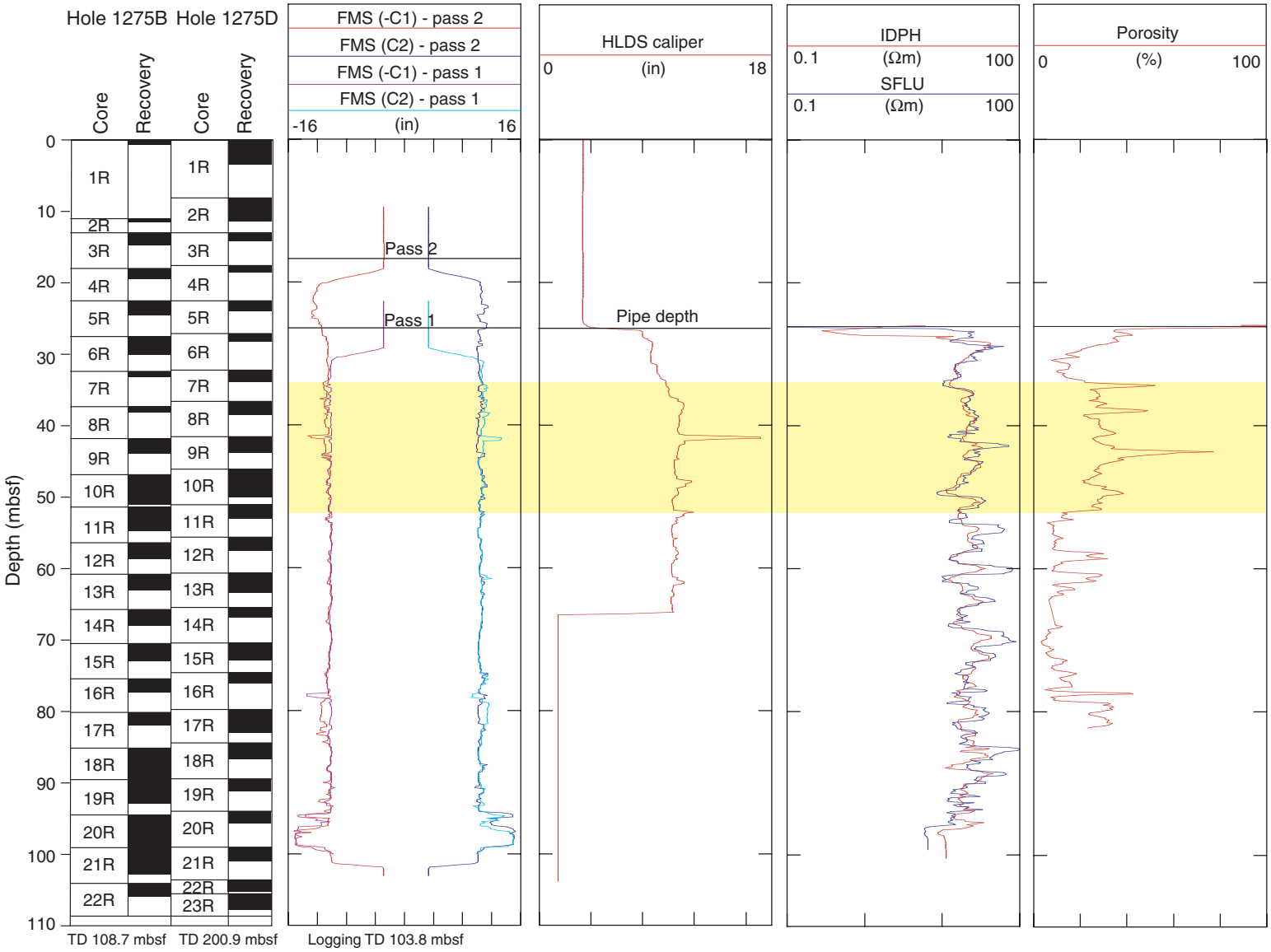

Figure F103. Core recovery, density, photoelectric effect (PEF), gamma ray intensity (total spectral gamma ray [HSGR] and environmentally corrected gamma ray [ECGR]), thorium, uranium, and potassium and compressional and shear wave velocity logs from Hole 1275D. The interval highlighted in yellow shows a low density, photoelectric effect, and potassium interval. This interval also corresponds to the high-porosity interval shown in Figure F102, p. 147. Shipboard laboratory measured HGR data are plotted with logging gamma ray data for comparison. Similarly, discrete sample velocity measurements are plotted with the logging data. TD = total depth.

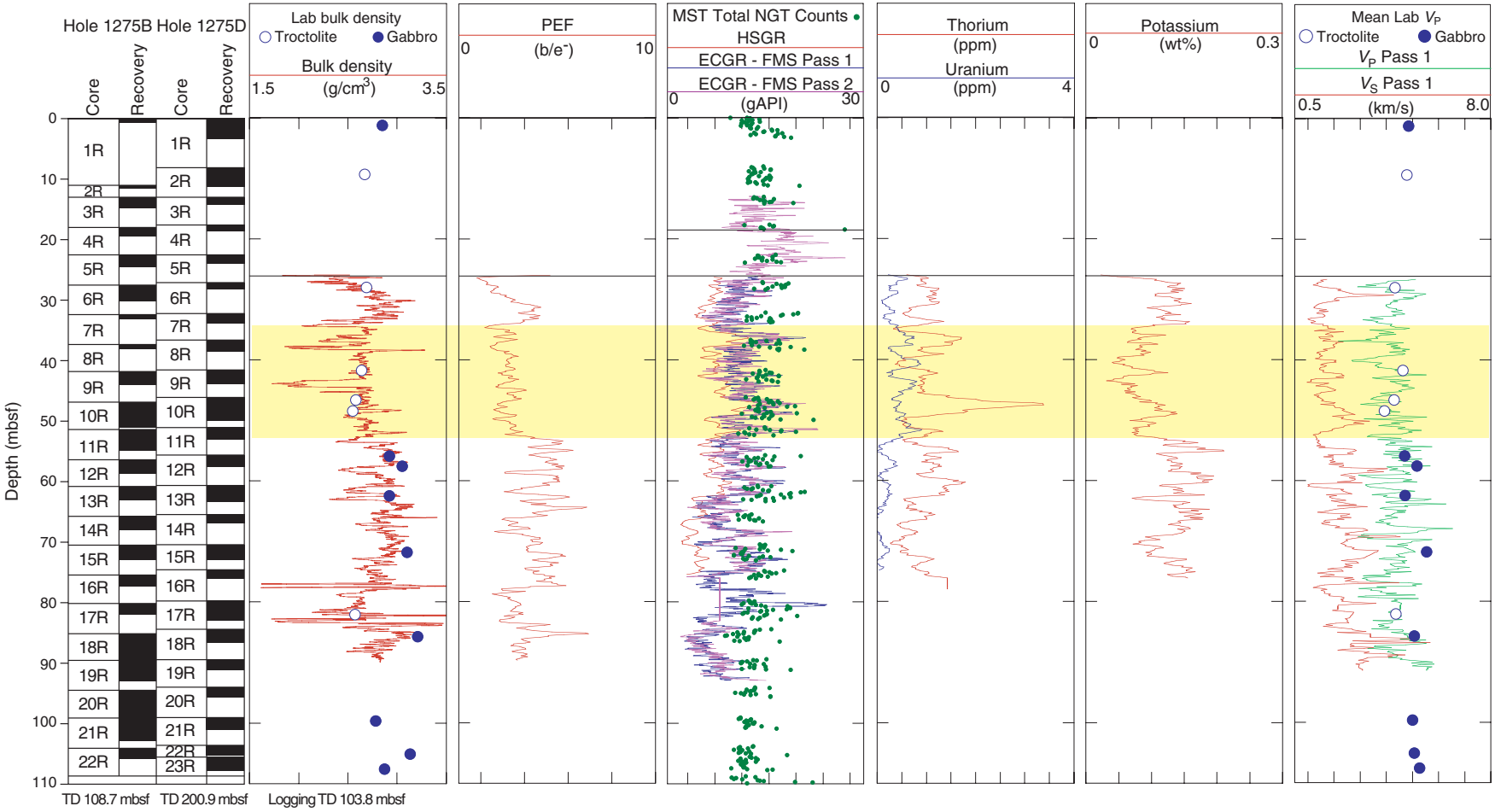

Figure F104. Logs obtained from the two GPIT passes in Hole 1275D showing the magnetic properties and orientation data. P1AZ = Pad 1 azimuth, Fx = horizontal magnetic field component, Fy = horizontal magnetic field component, Fz = vertical magnetic field component. FNOR = total magnetic field, FINC = magnetic inclination. HAZI = hole azimuth, DEVI = hole deviation.

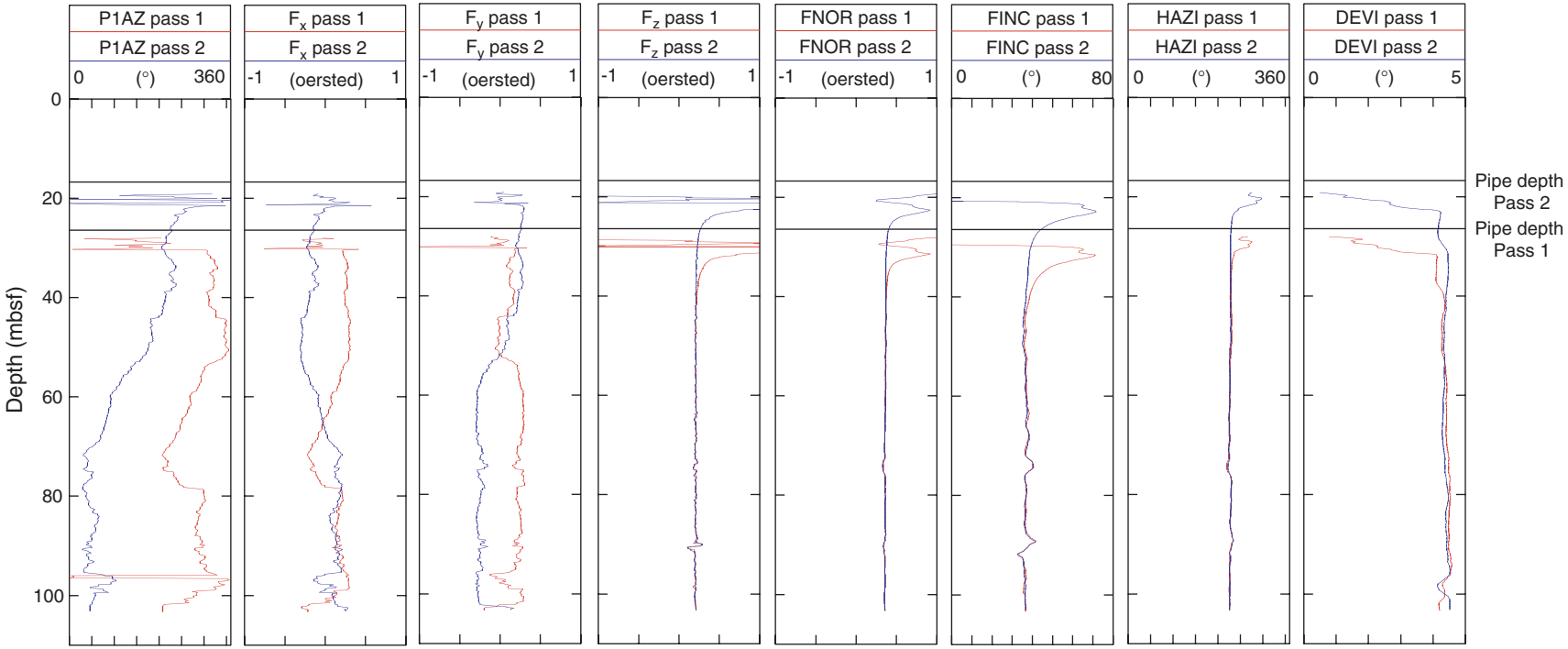

Figure F105. A. Downhole temperature and pressure profiles recorded with the TAP tool in Hole 1275D. **B.** Stationary temperature measurements made in Hole 1275 during a 5.4 station at 104 mbsf.

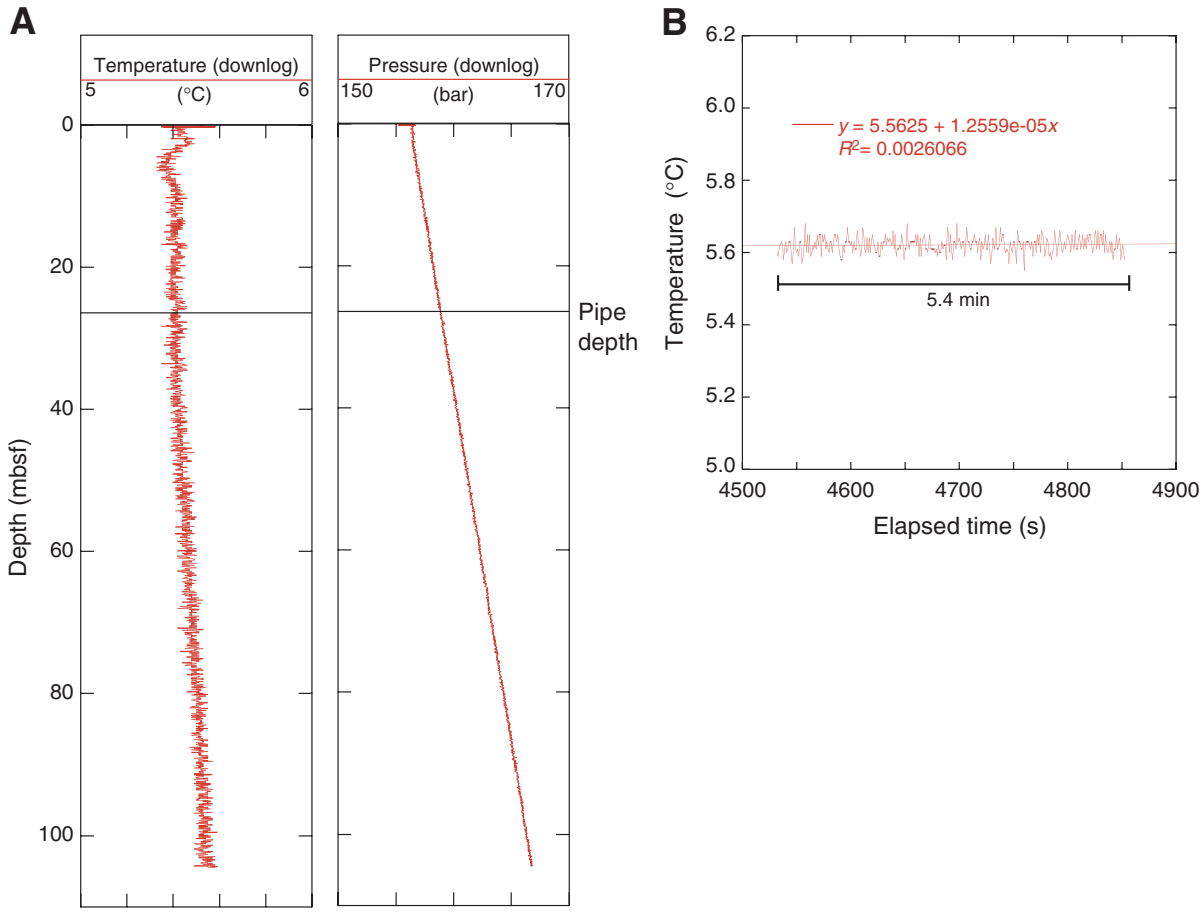

Figure F106. Formation MicroScanner (FMS) static images for 48–52 mbsf and 55.5–60 mbsf. A change in lithology or alteration is indicated at ~49.8 mbsf. Arrows indicate locations of probable fractures.

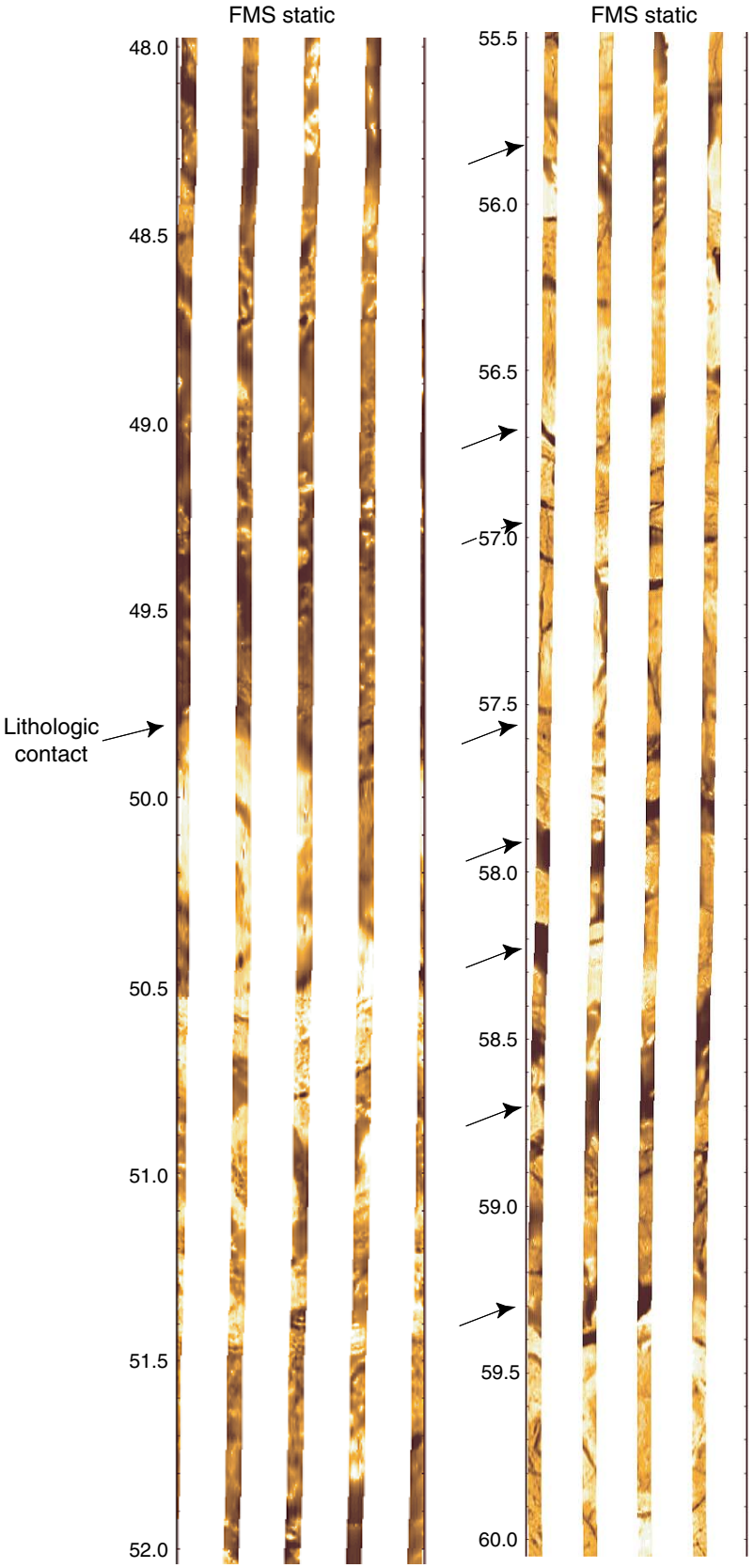

Figure F107. Formation MicroScanner (FMS) static images for 63–67 mbsf. Steep intervals of high resistivity contrast interpreted to represent fractures are evident between 65 and 66.6 mbsf. Arrows indicate the presence of probable shallower dipping fractures.

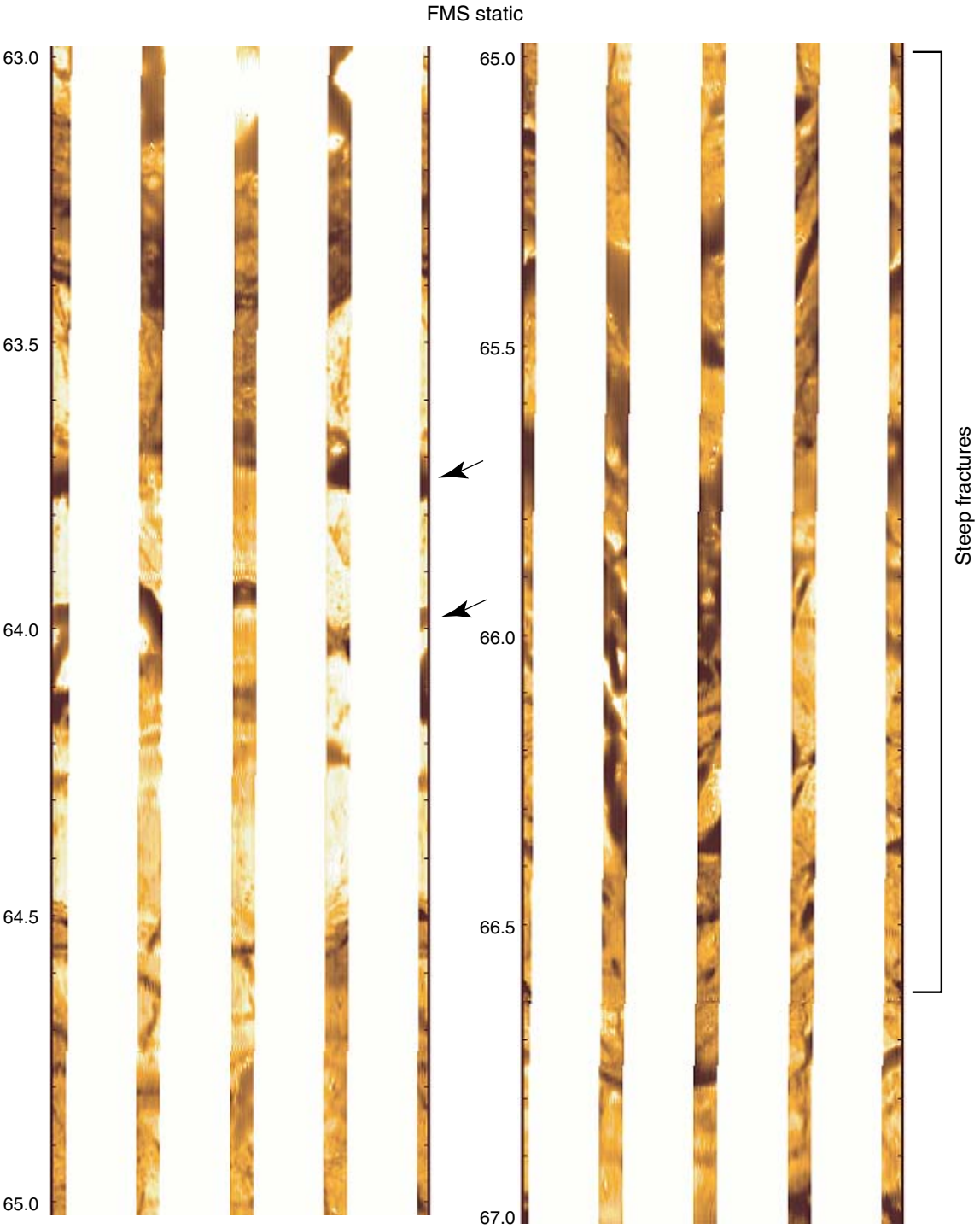

Figure F108. Formation MicroScanner (FMS) static images for 69–71 mbsf and 88–91 mbsf. Thin subvertical features resembling veins, large steep fractures, and resistivity contrasts suggesting lithologic contacts are also present throughout the entire logged interval.

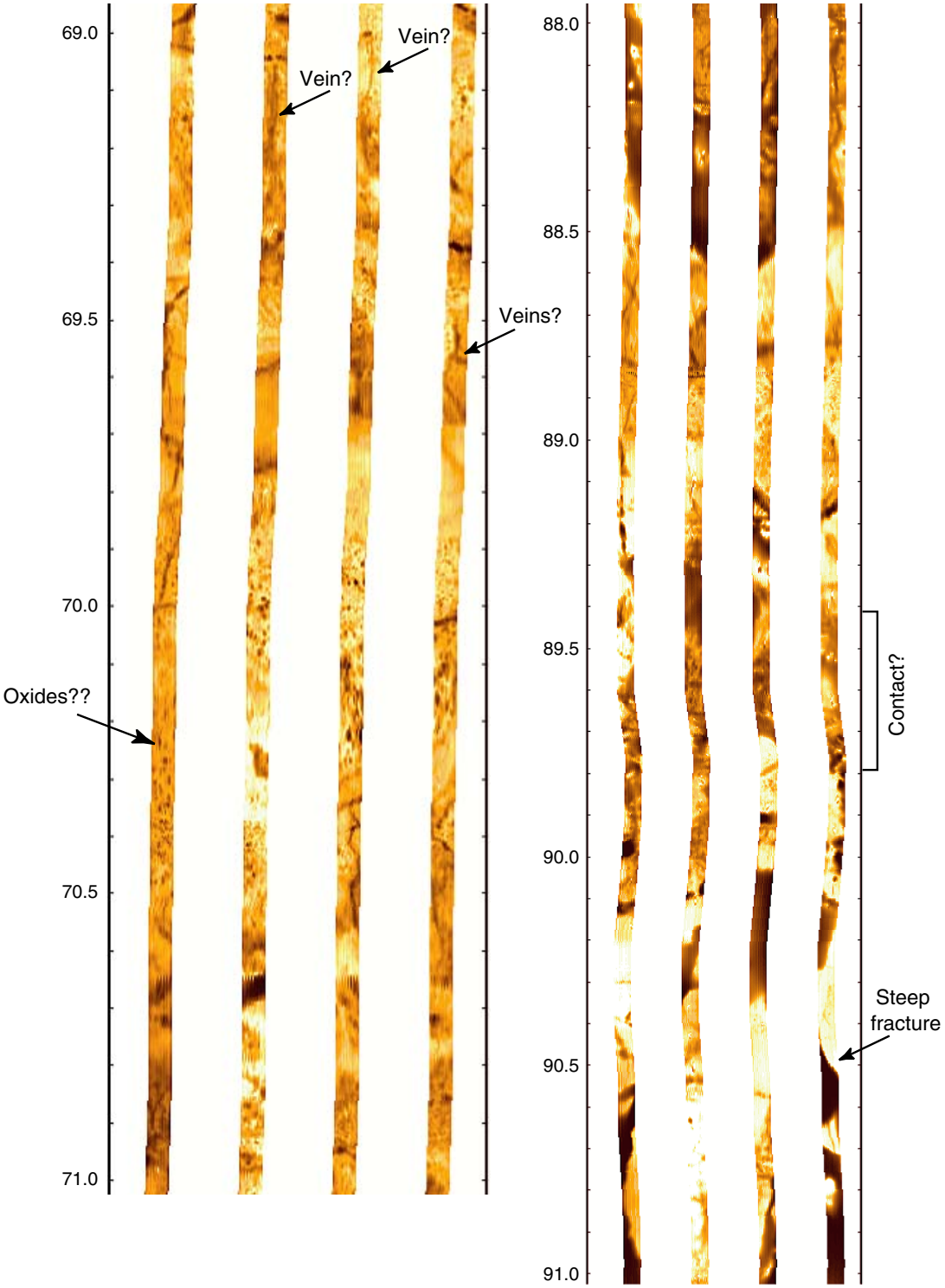

Table T1. Coring summary, Site 1275. (See table notes. Continued on next page.)

Hole 1275A
Latitude: 15°44.4892′N
Longitude: 46°54.2110′W
Time on site: 301.75 (2315 hr, 18 June–1300 hr, 1 July 2003)
Time on hole: 11.00 (2315 hr, 18 June–1015 hr, 19 June 2003)
Seafloor (drill pipe measurement from rig floor, mbrf): 1573.5
Distance between rig floor and sea level (m): 11.2
Water depth (drill pipe measurement from sea level, m): 1562.3
Total depth (drill pipe measurement from rig floor, mbrf): 1578.5
Total penetration (meters below seafloor, mbsf): 5.0
Total length of cored section (m): 5.0
Total core recovered (m): 0.13
Core recovery (%): 2.6
Total number of cores: 1

Hole 1275B
Latitude: 15°44.4858′N
Longitude: 46°54.2077′W
Time on hole: 102.50 (1015 hr, 19 June–1645 hr, 23 June 2003)
Seafloor (drill pipe measurement from rig floor, mbrf): 1573.0
Distance between rig floor and sea level (m): 11.3
Water depth (drill pipe measurement from sea level, m): 1561.7
Total depth (drill pipe measurement from rig floor, mbrf): 1681.7
Total penetration (meters below seafloor, mbsf): 108.7
Total length of cored section (m): 108.7
Total core recovered (m): 46.9
Core recovery (%): 43.2
Total number of cores: 22

Hole 1275C
Latitude: 15°44.4401′N
Longitude: 46°54.2178′W
Time on hole: 34.50 (1645 hr, 23 June–0315 hr, 25 June 2003)
Seafloor (drill pipe measurement from rig floor, mbrf): 1564.0
Distance between rig floor and sea level (m): 11.2
Water depth (drill pipe measurement from sea level, m): 1552.8
Total depth (drill pipe measurement from rig floor, mbrf): 1584.8
Total penetration (meters below seafloor, mbsf): 20.8
Total length of cored section (m): 20.8
Total core recovered (m): 0.17
Core recovery (%): 0.8
Total number of cores: 3
Comments: RAB-C (LWC) operation in this hole

Hole 1275D
Latitude: 15°44.4396′N
Longitude: 46°54.2173′W
Time on hole: 153.75 (0315 hr, 25 June–1300 hr, 1 July 2003)
Seafloor (drill pipe measurement from rig floor, mbrf): 1565.0
Distance between rig floor and sea level (m): 11.4
Water depth (drill pipe measurement from sea level, m): 1553.6
Total depth (drill pipe measurement from rig floor, mbrf): 1774.0
Total penetration (meters below seafloor, mbsf): 209.0
Total length of cored section (m): 209.0
Total core recovered (m): 104.63
Core recovery (%): 50.1
Total number of cores: 43

Core	Date (Jun 2003)	Local time (hr)	Depth (mbsf) Top	Depth (mbsf) Bottom	Length (m) Cored	Length (m) Recovered	Recovery (%)	Remarks
209-1275A-								
1R	19	1050	0.0	5.0	5.0	0.13	2.6	AHC
			Cored total:		5.0	0.13	2.6	
209-1275B-								
1R	19	2145	0.0	11.0	11.0	0.52	4.7	AHC, Whirl-Pak
2R	20	0250	11.0	13.0	2.0	0.40	20.0	Whirl-Pak
3R	20	0910	13.0	18.0	5.0	1.35	27.0	Whirl-Pak
4R	20	1920	18.0	22.6	4.6	1.10	23.9	Whirl-Pak
5R	20	2330	22.6	27.6	5.0	1.66	33.2	Whirl-Pak
6R	21	0305	27.6	32.3	4.7	2.15	45.7	Whirl-Pak
7R	21	0525	32.3	37.3	5.0	0.79	15.8	Whirl-Pak

Table T1 (continued).

Core	Date (Jun 2003)	Local time (hr)	Depth (mbsf) Top	Depth (mbsf) Bottom	Length (m) Cored	Length (m) Recovered	Recovery (%)	Remarks
8R	21	0745	37.3	41.8	4.5	0.77	17.1	Whirl-Pak
9R	21	1150	41.8	46.8	5.0	2.09	41.8	AHC, Whirl-Pak
10R	21	1730	46.8	51.3	4.5	3.60	80.0	Whirl-Pak
11R	21	2245	51.3	56.3	5.0	3.00	60.0	Whirl-Pak
12R	22	0205	56.3	60.8	4.5	2.19	48.7	Whirl-Pak
13R	22	0445	60.8	65.8	5.0	2.02	40.4	Whirl-Pak
14R	22	0625	65.8	70.4	4.6	1.76	38.3	Whirl-Pak
15R	22	0915	70.4	75.4	5.0	2.10	42.0	Whirl-Pak
16R	22	1145	75.4	80.1	4.7	1.90	40.4	Whirl-Pak
17R	22	1400	80.1	85.1	5.0	1.39	27.8	Whirl-Pak
18R	22	1820	85.1	89.4	4.3	3.86	89.8	Whirl-Pak
19R	22	2245	89.4	94.4	5.0	4.57	91.4	Whirl-Pak
20R	23	0255	94.4	99.0	4.6	4.56	99.1	Whirl-Pak
21R	23	0550	99.0	104.0	5.0	3.42	68.4	Whirl-Pak
22R	23	0955	104.0	108.7	4.7	1.70	36.2	Whirl-Pak
			Cored totals:		108.7	46.90	43.2	
209-1275C-								
1A	24	1515	0.0	12.3	12.3	0.00	0.0	AHC; no recovery
2A	24	1945	12.3	16.8	4.5	0.08	1.8	
3A	24	2240	16.8	20.8	4.0	0.09	2.3	
			Cored totals:		20.8	0.17	0.8	
209-1275D-								
1R	25	1650	0.0	8.0	8.0	2.50	31.3	
2R	25	2020	8.0	13.0	5.0	2.34	46.8	Whirl-Pak
3R	25	2245	13.0	17.6	4.6	0.78	17.0	Whirl-Pak
4R	26	0045	17.6	22.6	5.0	0.76	15.2	Whirl-Pak
5R	26	0300	22.6	27.1	4.5	1.07	23.8	Whirl-Pak
6R	26	0610	27.1	32.1	5.0	1.18	23.6	Whirl-Pak
7R	26	0900	32.1	36.6	4.5	1.50	33.3	Whirl-Pak
8R	26	1100	36.6	41.6	5.0	1.47	29.4	Whirl-Pak
9R	26	1325	41.6	46.1	4.5	1.74	38.7	Whirl-Pak
10R	26	1600	46.1	51.1	5.0	3.42	68.4	Whirl-Pak
11R	26	1835	51.1	55.7	4.6	1.91	41.5	
12R	26	2205	55.7	60.7	5.0	1.73	34.6	
13R	27	0020	60.7	65.4	4.7	2.25	47.9	
14R	27	0235	65.4	70.4	5.0	1.24	24.8	
15R	27	0515	70.4	74.7	4.3	2.44	56.7	
16R	27	0710	74.7	79.7	5.0	1.27	25.4	
17R	27	0855	79.7	84.4	4.7	2.65	56.4	
18R	27	1055	84.4	89.4	5.0	1.79	35.8	
19R	27	1250	89.4	94.0	4.6	1.50	32.6	
20R	27	1425	94.0	99.0	5.0	1.40	28.0	
21R	27	1725	99.0	103.7	4.7	1.64	34.9	
22R	27	2050	103.7	105.5	1.8	1.49	82.8	Core jam at catcher
23R	27	2315	105.5	108.7	3.2	1.92	60.0	
24R	28	0150	108.7	113.2	4.5	2.61	58.0	
25R	28	0430	113.2	118.2	5.0	2.66	53.2	
26R	28	0730	118.2	122.7	4.5	3.90	86.7	
27R	28	0940	122.7	127.7	5.0	2.57	51.4	Drilling break at 1688.7 m
28R	28	1145	127.7	132.2	4.5	1.29	28.7	
29R	28	1505	132.2	137.2	5.0	2.35	47.0	
30R	28	1730	137.2	141.8	4.6	1.92	41.7	
31R	28	2115	141.8	146.8	5.0	4.38	87.6	
32R	28	2315	146.8	151.3	4.5	2.79	62.0	
33R	29	0145	151.3	156.3	5.0	3.09	61.8	
34R	29	0355	156.3	160.8	4.5	3.38	75.1	
35R	29	0700	160.8	165.8	5.0	4.33	86.6	
36R	29	1010	165.8	170.5	4.7	2.88	61.3	
37R	29	1250	170.5	175.5	5.0	3.60	72.0	
38R	29	1530	175.5	180.1	4.6	4.13	89.8	
39R	29	1855	180.1	184.1	4.0	2.82	70.5	
40R	29	2345	184.1	189.8	5.7	5.44	95.4	
41R	30	0235	189.8	194.8	5.0	4.06	81.2	
42R	30	0440	194.8	199.3	4.5	1.01	22.4	
43R	30	0920	199.3	209.0	9.7	5.43	56.0	
			Cored totals:		209.0	104.63	50.1	

Notes: RAB-C = resistivity at the bit while coring, LWC = logging while coring. AHC = active heave compensation.

Table T2. XRD results, Holes 1275B and 1275D.

Core, section, interval (cm)	Depth (mbsf)	Piece	Rock type	Mineralogy			ICP-AES analyses	Thin section
				Major	Minor	Trace		
209-1275B-								
3R-1, 82–86	13.8	13	Gabbro	Plagioclase	Amphibole	Chlorite, ilmenite	Yes	Yes
3R-1, 103–107	14.0	17	Gabbro	Plagioclase	Amphibole	ilmenite	Yes	Yes
5R-1, 134–137	23.9	22	Gabbro	Plagioclase	Amphibole	Cpx, ilmenite, titanite	Yes	Yes
6R-1, 61–64	28.2	10	Troctolite	Lizardite	Olivine, magnetite	Cpx, plagioclase, aragonite	Yes	Yes
6R-2, 27–30	29.3	4A	Troctolite	Lizardite	Olivine	Amphibole, chlorite, talc	Yes	Yes
6R-2, 102–107	30.1	9	Troctolite	Lizardite	Olivine	Chlorite	Yes	Yes
9R-1, 109–112	42.9	15	Gabbro	Plagioclase	Cpx	Amphibole, ilmenite	Yes	Yes
10R-1, 74–76	47.5	10	Gabbro	Plagioclase	Cpx	Amphibole, ilmenite	Yes	Yes
12R-2, 89–92	58.4	1B	Gabbro	Plagioclase	Cpx	Amphibole, ilmenite	Yes	Yes
14R-1, 84–86	66.6	13	Gabbro	Plagioclase	Cpx, amphibole		Yes	Yes
15R-2, 68–71	72.5	11	Gabbro	Plagioclase	Cpx, ilmenite	Amphibole, pentlandite?	Yes	Yes
17R-1, 65–67	80.8	11	Gabbro	Plagioclase	Cpx	Amphibole	Yes	Yes
17R-1, 123–125	81.3	19	Gabbro	Plagioclase	Amphibole, cpx	ilmenite	Yes	Yes
19R-1, 48–50	89.9	5A	Gabbro	Plagioclase	Cpx	Amphibole	Yes	Yes
19R-1, 135–137	90.8	6B	Gabbro	Plagioclase	Cpx, ilmenite	Amphibole	Yes	Yes
20R-2, 105–107	96.6	7	Gabbro	Plagioclase	Cpx	Amphibole, ilmenite	Yes	Yes
20R-2, 117–119	96.7	8	Gabbro	Plagioclase	Cpx	Amphibole, ilmenite	Yes	Yes
21R-1, 26–28	99.3	1D	Gabbro	Plagioclase	Cpx, ilmenite	Amphibole	Yes	Yes
21R-1, 90–92	99.9	4C	Gabbro	Plagioclase	Cpx, ilmenite	Amphibole	Yes	Yes
21R-2, 0–4	100.5	1	Gabbro	Plagioclase	Cpx, amphibole	ilmenite	Yes	Yes
21R-2, 136–138	101.9	7B	Gabbro	Plagioclase	Cpx	Amphibole, ilmenite	Yes	Yes
209-1275D-								
1R-1, 113–115	1.1	19B	Diabase	Plagioclase	Amphibole	Titanite	Yes	Yes
2R-1, 137–140	9.4	27	Troctolite	Lizardite		Amphibole, chlorite, talc	Yes	Yes
6R-1, 89–91	28.0	17	Troctolite	Calcite	Talc, lizardite	Amphibole, chlorite, montmorillionite	Yes	Yes
10R-1, 50–52	46.6	6	Troctolite	Lizardite		Magnetite	Yes	Yes
10R-2, 104–106	48.6	14A	Troctolite	Lizardite		Magnetite, calcite	Yes	Yes
12R-2, 42–46	57.6	8	Gabbro	Plagioclase		Amphibole	Yes	Yes
13R-2, 49–51	62.5	1B	Gabbro	Plagioclase	Amphibole	Cpx	Yes	Yes
15R-2, 11–13	71.8	1A	Gabbro	Plagioclase		Amphibole, cpx	Yes	Yes
17R-2, 93–95	82.1	15A	Troctolite	Lizardite			Yes	Yes
18R-1, 133–135	85.7	17B	Gabbro	Plagioclase	Cpx	Amphibole	Yes	Yes
21R-1, 63–65	99.6	8A	Gabbro	Plagioclase	Cpx	Amphibole	Yes	Yes
22R-1, 145–147	105.2	20B	Gabbro	Plagioclase	Cpx	Amphibole	Yes	Yes
31R-2, 69–71	143.9	4F	Trondhjemite	Plagioclase	Quartz	Amphibole	Yes	Yes

Notes: Cpx = clinopyroxene. Due to peak overlap, samples with identified lizardite may also contain chrysotile. Qualifiers "major, minor, and trace" indicate relative abundances based on peak heights and do not necessarily reflect true relative proportions. ICP-AES = inductively coupled plasma–atomic emission spectrometry. ICP-AES data are available in Table **T4,** p. 158. This table is also available in **ASCII.**

Table T3. Vein mineralogy, Holes 1275B and 1275D.

Hole	1275B	1275D
Penetration depth (mbsf)	108.7	209.0
Recovery (%)	43.1	50.1
Length recovered (m)	46.9	104.6
Volume recovered (cm^3)	117,587	262,252
Veins in hole (cm^3/m)	10.8	16.2
Veins in hole (%)	0.43	0.65
Vein minerals in hole (cm^3/m):		
Picrolite	0.59	2.87
Amphibole	3.23	6.01
Chlorite	2.44	2.51
Talc	0.00	0.58
Quartz	0.41	0.24
Carbonates	0.62	3.71
Iron oxides	0.52	0.18
Clays	2.69	0.73
Others	0.27	0.30
Vein minerals in hole (%):		
Picrolite	0.02	0.11
Amphibole	0.13	0.24
Chlorite	0.10	0.10
Talc	0.00	0.02
Quartz	0.02	0.01
Carbonates	0.02	0.15
Iron oxides	0.02	0.01
Clays	0.11	0.03
Others	0.01	0.01
Vein minerals in veins (%):		
Picrolite	5.5	16.7
Amphibole	30.0	35.1
Chlorite	22.7	14.7
Talc	0.0	3.4
Quartz	3.8	1.4
Carbonates	5.8	21.6
Iron oxides	4.8	1.0
Clays	25.0	4.3
Others	2.5	1.8

Notes: The volume of veins is based on macroscopic observations of vein mineralogy and estimates of vein percentages by pieces. We computed volume percentage of veins by using the volume weighted average of the macroscopic estimates using the relative curated length and assuming a constant core radius throughout the site. This table is also available in **ASCII.**

Table T4. Major and trace element compositions of rocks, Holes 1275B and 1275D. (Continued on next page.)

Core, section, interval (cm)	Depth (mbsf)	Piece	Unit	Lithology	Gabbro group	Major element oxides (wt%)										Volatiles (wt%)	
						SiO_2	TiO_2	Al_2O_3	Fe_2O_3	MgO	MnO	CaO	Na_2O	K_2O	Total	LOI	CO_2	H_2O
209-1275B-																		
3R-1, 82–86	13.82	13	I	Diabase	1	51.76	1.26	15.07	10.66	9.00	0.18	10.36	2.90	0.07	101.26	1.23	0.28	1.92
3R-1, 103–107	14.03	17	I	Gabbro	2	51.78	3.63	13.84	12.41	6.19	0.21	8.99	4.04	0.12	101.21	0.72	0.10	1.13
5R-1, 134–137	23.94	22	I	Gabbro	2	50.04	6.85	11.86	14.91	4.99	0.26	9.34	3.71	0.17	102.12	0.56	0.08	1.13
6R-1, 61–64	28.21	10	II	Troctolite		40.74	0.17	3.80	10.26	37.55	0.15	5.91	0.14	0.12	98.83	12.16	3.20	8.46
6R-2, 27–30	29.33	4A	II	Troctolite		42.45	0.12	4.82	9.90	39.34	0.14	2.25	0.12	0.06	99.18	9.72	0.26	9.35
6R-2, 102–107	30.08	9	II	Troctolite		43.02	0.08	5.11	9.71	40.15	0.12	2.24	0.07	0.03	100.54	11.09	0.23	10.65
9R-1, 109–112	42.89	15	III	Fine-grained gabbro	2	44.79	5.36	11.88	18.71	5.68	0.27	9.45	3.20	0.12	99.47	–0.34	0.10	1.00
10R-1, 74–76	47.54	10	III	Coarse-grained gabbro	2	47.18	5.24	13.32	16.30	4.71	0.23	9.58	3.64	0.13	100.35	–0.38	0.17	1.08
12R-2, 89–92	58.36	1B	III	Gabbro	2	47.73	5.31	13.28	16.51	4.87	0.23	9.83	3.50	0.12	101.39	–0.97	0.11	0.98
14R-1, 84–86	66.64	13	III	Fine-grained diabase	1	47.87	1.24	15.35	12.78	9.16	0.20	11.06	2.29	0.10	100.04	2.33	0.34	2.28
15R-2, 68–71	72.54	11	III	Fine-grained gabbro	2	45.37	5.54	12.13	19.03	5.41	0.25	9.73	3.15	0.13	100.75	0.05	0.05	0.96
17R-1, 65–67	80.75	11	III	Fine-grained diabase	1	51.10	0.79	17.59	7.88	8.58	0.12	12.33	2.57	0.22	101.19	1.25	0.10	1.28
17R-1, 123–125	81.33	19	III	Coarse-grained gabbro	2	48.39	4.89	12.74	17.06	5.72	0.24	9.44	3.55	0.17	102.22	0.47	0.13	1.37
19R-1, 48–50	89.88	5A	III	Fine-grained gabbro	1	51.28	1.01	16.06	8.88	9.51	0.15	11.22	2.75	0.22	101.08	1.34	0.11	1.59
19R-1, 135–137	90.75	6B	III	Coarse-grained gabbro	2	45.19	6.60	13.07	16.38	4.90	0.22	9.47	3.41	0.16	99.40	–0.94	0.12	0.94
20R-2, 105–107	96.61	7	III	Fine-grained gabbro	2	50.79	2.00	13.50	14.35	6.91	0.23	10.75	3.10	0.18	101.83	0.00	0.13	0.99
20R-2, 117–119	96.73	8	III	Coarse-grained gabbro	2	45.14	4.07	12.85	19.68	5.14	0.23	9.41	3.21	0.25	99.99	–0.12	0.31	1.04
21R-1, 26–28	99.26	1D	III	Fine-grained gabbro	2	44.18	5.45	11.47	20.18	6.36	0.24	10.40	2.62	0.11	101.01	–0.05	0.16	1.24
21R-1, 90–92	99.90	4C	III	Coarse-grained gabbro	2	42.60	8.87	10.93	21.69	6.10	0.29	9.31	2.63	0.11	102.53	–0.42	0.08	0.90
21R-2, 0–4	100.50	1	III	Coarse-grained gabbro (altered)	2	45.42	5.25	11.53	19.13	6.45	0.25	10.77	2.72	0.12	101.63	–0.13	BDL	0.86
21R-2, 136–138	101.86	7B	III	Coarse-grained gabbro	2	47.43	4.23	12.19	18.70	6.04	0.24	10.55	3.02	0.14	102.54	–0.09	0.10	1.36
209-1275D-																		
1R-1, 113–115	1.13	19B	I	Gabbro	2	52.30	2.96	12.36	11.17	6.72	0.14	10.42	3.92	0.10	100.09	0.85	0.31	2.29
2R-1, 137–140	9.37	27	I	Troctolite		45.07	0.15	3.80	10.75	37.02	0.16	1.44	0.22	0.10	98.71	10.95	0.29	10.99
6R-1, 89–91	27.99	17	I	Troctolite		40.36	0.08	3.91	9.54	31.16	0.14	13.30	0.19	0.10	98.78	15.85	9.01	6.83
10R-1, 50–52	46.60	6	I	Troctolite		43.00	0.17	1.31	12.53	40.07	0.14	1.13	0.16	0.06	98.55	13.92	1.83	12
10R-2, 104–106	48.57	14A	I	Troctolite		41.48	0.14	2.24	10.44	40.65	0.17	2.72	0.13	0.07	98.03	15.65	2.97	12.47
12R-2, 42–46	57.58	8	II	Gabbro	2	44.36	5.86	12.24	18.69	5.31	0.26	9.87	3.08	0.11	99.77	0.09	0.20	1.38
13R-2, 49–51	62.45	1B	II	Gabbro	2	47.91	3.94	11.94	19.44	6.31	0.32	9.04	3.01	0.10	102.02	1.31	0.51	1.69
15R-2, 11–13	71.82	1A	II	Fine-grained gabbro	2	46.18	4.39	12.07	20.78	6.01	0.27	10.16	2.82	0.07	102.76	–0.24	0.28	1.25
17R-2, 93–95	82.05	15A	III	Troctolite		43.29	0.13	4.11	10.20	39.95	0.15	2.11	0.07	0.07	100.08	13.30	1.09	11.87
18R-1, 133–135	85.73	17B	III	Coarse-grained gabbro	2	45.81	4.08	12.52	22.01	5.66	0.23	9.78	2.87	0.11	103.07	–0.02	0.13	1.55
21R-1, 63–65	99.60	8A	IV	Diabase	1	53.30	1.00	16.02	9.27	8.31	0.17	11.89	2.81	0.05	102.81	1.40	0.24	2.27
22R-1, 145–147	105.15	20B	IV	Fine-grained gabbro	2	48.20	4.13	12.33	19.38	5.94	0.24	10.53	2.93	0.10	103.80	0.18	0.08	BDL
31R-2, 69–71	143.91	4F	IV	Granophyre		69.47	0.56	11.36	8.63	3.21	0.13	4.69	5.66	0.10	103.81	0.43	0.10	1.27

Note: This table is also available in **ASCII.**

Table T4 (continued).

Core, section, interval (cm)	Depth (mbsf)	Piece	Unit	Lithology	Gabbro group	Trace elements (ppm)									
						S	Cr	Ni	Ba	Sr	V	Y	Zr	Sc	Co
209-1275B-															
3R-1, 82–86	13.82	13	I	Diabase	1	<350	245	140	<39	140	244	28	89	38	53
3R-1, 103–107	14.03	17	I	Gabbro	2	<350	<41	<165	<39	178	321	23	44	55	74
5R-1, 134–137	23.94	22	I	Gabbro	2	<350	<41	<165	<39	146	539	28	76	64	110
6R-1, 61–64	28.21	10	II	Troctolite		<350	3738	1946	<39	30	44	6	21	7	123
6R-2, 27–30	29.33	4A	II	Troctolite		<350	3761	2008	<39	493	62	<2	10	9	129
6R-2, 102–107	30.08	9	II	Troctolite		<350	3389	1887	<39	13	45	2	8	9	126
9R-1, 109–112	42.89	15	III	Fine-grained gabbro	2	362	<41	<165	<39	130	596	20	47	56	117
10R-1, 74–76	47.54	10	III	Coarse-grained gabbro	2	1618	<41	<165	42	162	568	26	76	52	109
12R-2, 89–92	58.36	1B	III	Gabbro	2	778	<41	<165	<39	161	575	26	79	52	117
14R-1, 84–86	66.64	13	III	Fine-grained diabase	1	<350	325	165	<39	199	212	24	91	35	76
15R-2, 68–71	72.54	11	III	Fine-grained gabbro	2	<350	<41	<165	<39	134	866	23	66	57	106
17R-1, 65–67	80.75	11	III	Fine-grained diabase	1	<350	408	168	<39	123	188	17	44	32	79
17R-1, 123–125	81.33	19	III	Coarse-grained gabbro	2	<350	<41	<165	<39	149	765	25	63	52	108
19R-1, 48–50	89.88	5A	III	Fine-grained gabbro	1	<350	407	<165	<39	160	191	21	32	33	53
19R-1, 135–137	90.75	6B	III	Coarse-grained gabbro	2	1241	<41	<165	<39	159	663	19	73	53	128
20R-2, 105–107	96.61	7	III	Fine-grained gabbro	2	966	<41	<165	<39	154	589	15	31	52	94
20R-2, 117–119	96.73	8	III	Coarse-grained gabbro	2	1424	<41	<165	48	149	1038	35	66	44	127
21R-1, 26–28	99.26	1D	III	Fine-grained gabbro	2	<350	<41	<165	<39	130	1144	16	29	62	170
21R-1, 90–92	99.90	4C	III	Coarse-grained gabbro	2	<350	<41	<165	<39	125	1093	23	88	62	163
21R-2, 0–4	100.50	1	III	Coarse-grained gabbro (altered)	2	1521	<41	<165	<39	132	1053	24	61	64	111
21R-2, 136–138	101.86	7B	III	Coarse-grained gabbro	2	1546	<41	<165	<39	135	938	28	51	57	124
209-1275D-															
1R-1, 113–115	1.13	19B	I	Gabbro	2	<350	<41	<165	61	192	230	83	103	44	84
2R-1, 137–140	9.37	27	I	Troctolite		<350	3791	1691	<39	10	66	6	18	14	110
6R-1, 89–91	27.99	17	I	Troctolite		<350	4441	1596	<39	149	70	4	14	8	116
10R-1, 50–52	46.60	6	I	Troctolite		<350	4279	1790	48	16	67	5	17	12	130
10R-2, 104–106	48.57	14A	I	Troctolite		<350	3990	1912	<39	17	67	3	7	10	125
12R-2, 42–46	57.58	8	II	Gabbro	2	<350	<41	<165	<39	145	596	22	49	60	102
13R-2, 49–51	62.45	1B	II	Gabbro	2	1856	<41	<165	<39	128	539	34	47	53	101
15R-2, 11–13	71.82	1A	II	Fine-grained gabbro	2	2467	<41	<165	<39	127	922	23	33	60	119
17R-2, 93–95	82.05	15A	III	Troctolite		<350	3738	2048	<39	124	52	4	10	10	115
18R-1, 133–135	85.73	17B	III	Coarse-grained gabbro	2	1327	<41	<165	<39	128	1305	28	63	51	122
21R-1, 63–65	99.60	8A	IV	Diabase	1	<350	297	<165	<39	147	229	23	71	38	83
22R-1, 145–147	105.15	20B	IV	Fine-grained gabbro	2	<350	<41	<165	<39	133	1131	20	33	63	100
31R-2, 69–71	143.91	4F	IV	Granophyre		<350	<41	<165	63	91	99	110	1370	32	59

Table T5. Thermal conductivity measurements, Holes 1275B and 1275D.

Core, section, interval (cm)	Depth (mbsf)	Piece	Thermal conductivity* (W/[m·K])	Standard deviation	Standard error	Needle orientation	Apparent anisotropy (%)	Primary lithology
209-1275B-								
3R-1, 34–45	13.34	6	2.023	0.010	0.005	0	2.8	Diabase
3R-1, 34–45	13.34	6	2.018	0.004	0.002	1		Diabase
3R-1, 34–45	13.34	6	2.073	0.021	0.011	2		Diabase
5R-1, 16–27	22.76	4	2.226	0.004	0.002	0	5.8	Gabbro
5R-1, 16–27	22.76	4	2.188	0.033	0.017	1		Gabbro
5R-1, 16–27	22.76	4	2.101	0.025	0.013	2		Gabbro
6R-1, 57–68	28.17	10	3.385	0.027	0.014	0	1.5	Troctolite
6R-1, 57–68	28.17	10	3.428	0.028	0.014	1		Troctolite
6R-1, 57–68	28.17	10	3.388	0.013	0.007	2		Troctolite
9R-1, 110–122	42.90	15	2.106	0.008	0.004	0	0.7	Diabase
9R-1, 110–122	42.90	15	2.091	0.010	0.005	1		Diabase
9R-1, 110–122	42.90	15	2.108	0.022	0.011	2		Diabase
10R-3, 23–33	49.92	2B	2.023	0.018	0.009	0	1.7	Gabbro
10R-3, 23–33	49.92	2B	2.054	0.014	0.007	1		Gabbro
10R-3, 23–33	49.92	2B	2.025	0.013	0.007	2		Gabbro
10R-3, 121–132	50.90	15	2.112	0.028	0.014	0	4.4	Gabbro
10R-3, 121–132	50.90	15	2.019	0.010	0.005	1		Gabbro
10R-3, 121–132	50.90	15	2.058	0.006	0.003	2		Gabbro
12R-1, 106–116	57.36	16B	2.097	0.012	0.006	0	0.3	Gabbro
12R-1, 106–116	57.36	16B	2.103	0.013	0.006	1		Gabbro
12R-1, 106–116	57.36	16B	2.097	0.006	0.003	2		Gabbro
14R-1, 50–62	66.30	10	2.206	0.009	0.004	0	0.7	Gabbro
14R-1, 50–62	66.30	10	2.183	0.024	0.012	1		Gabbro
14R-1, 50–62	66.30	10	2.196	0.036	0.018	2		Gabbro
18R-3, 99–102	88.64	11B	2.271	0.026	0.013	0	1.9	Gabbro
18R-3, 99–102	88.64	11B	2.260	0.005	0.003	1		Gabbro
18R-3, 99–102	88.64	11B	2.228	0.007	0.004	2		Gabbro
19R-2, 13–23	90.99	2	2.238	0.006	0.003	0	1.2	Gabbro
19R-2, 13–23	90.99	2	2.226	0.011	0.006	1		Gabbro
19R-2, 13–23	90.99	2	2.258	0.009	0.004	2		Gabbro
20R-3, 51–65	97.45	1D	2.174	0.002	0.001	0	4.3	Gabbro
20R-3, 51–65	97.45	1D	2.168	0.010	0.005	1		Gabbro
20R-3, 51–65	97.45	1D	2.082	0.026	0.013	2		Gabbro
21R-2, 31–43	100.81	4	2.211	0.022	0.011	0		Gabbro
209-1275D-								
2R-2, 6–16	9.55	2	3.829	0.049	0.025	0		Gabbro/Troctolite
7R-2, 1–10	33.53	1	1.987	0.013	0.006	0		Gabbro
9R-1, 15–24	41.75	3	3.170	0.045	0.022	0		Troctolite
10R-3, 12–21	49.06	13	3.057	0.019	0.010	0		Troctolite
11R-2, 16–24	52.71	2	3.229	0.017	0.008	0		Troctolite
13R-1, 88–100	61.58	12C	1.992	0.025	0.012	0		Gabbro
17R-2, 86–102	81.98	15A	3.073	0.020	0.010	0		Troctolite
18R-2, 69–79	86.56	9	2.175	0.010	0.005	0		Gabbro
22R-1, 96–100	104.66	15	2.199	0.019	0.010	0		Gabbro
23R-2, 57–68	107.54	6	2.082	0.015	0.007	0		MicroGabbro
25R-1, 55–65	113.75	10	2.062	0.057	0.029	0		Gabbro
27R-1, 55–65	123.25	4	2.026	0.008	0.004	0		Gabbro
30R-1, 103–115	138.23	13	2.182	0.025	0.013	0		Gabbro
33R-1, 13–25	151.43	3A	3.355	0.035	0.018	0		Olivine Gabbro
34R-4, 33–45	159.91	2	2.191	0.009	0.004	0		Gabbro
37R-1, 100–110	171.5	12	2.128	0.012	0.006	0		Gabbro
41R-3, 89–100	193.48	4	1.969	0.016	0.008	0		Gabbro

Notes: * = average of four measurements. 0 = parallel to core axis, 1 = oblique to core axis (~35°), 2 = oblique to core axis (~35°) in opposite direction. This table is also available in **ASCII.**

Table T6. Porosity, density, and velocity on discrete samples, Holes 1275B and 1275D.

Core, section, interval (cm)	Depth (mbsf)	Volume measured in pycnometer: Density (Mg/m³) Bulk	Grain	Porosity (%)	Volume measured with caliper: Density (Mg/m³) Bulk	Grain	Porosity (%)	V_P (km/s) x	y	z	Mean	V_P apparent anisotropy (%)	Primary lithology
209-1275B-													
3R-1, 82–84	13.82	2.85	2.89	2.2	2.89	—	—	5.63	5.46	5.33	5.47	5.5	Diabase
3R-1, 107–109	14.07	2.87	2.93	3.2	—	—	—	—	—	—	—	—	Gabbro
4R-1, 57–59	18.57	2.97	3.04	3.3	2.93	—	—	4.55	4.59	4.18	4.44	9.3	Gabbro
5R-1, 17–19	22.77	3.11	3.22	4.8	3.07	—	—	4.74	4.65	4.48	4.62	5.8	Gabbro
6R-1, 59–61	28.19	2.68	2.75	4.3	2.74	—	—	4.64	4.45	4.35	4.48	6.5	Troctolite
6R-2, 31–33	29.37	2.72	2.75	1.7	2.74	—	—	5.15	4.81	4.97	4.98	6.8	Troctolite
6R-2, 106–108	30.12	2.70	2.73	1.6	2.76	—	—	5.01	4.89	4.79	4.90	4.6	Troctolite
9R-1, 114–116	42.94	3.07	3.11	1.7	3.02	—	—	5.41	5.36	5.31	5.36	1.9	Diabase
10R-1, 82–84	47.62	3.13	3.17	1.9	3.13	—	—	5.33	5.31	5.29	5.31	0.9	Gabbro
10R-2, 44–46	48.74	3.26	3.31	2.0	3.28	—	—	5.40	5.44	5.37	5.40	1.1	Gabbro
11R-1, 34–36	51.64	3.02	3.08	2.6	3.08	—	—	5.32	5.36	5.17	5.28	3.6	Gabbro
11R-2, 65–67	53.39	3.07	3.10	1.5	3.12	—	—	—	5.38	5.27	5.32	2.0	Gabbro
12R-1, 80–82	57.10	3.10	3.14	2.3	3.15	—	—	—	5.14	4.95	5.04	3.8	Gabbro
12R-2, 22–24	57.69	3.09	3.11	1.4	3.18	—	—	—	5.46	5.38	5.42	1.5	Gabbro
13R-1, 72–74	61.52	3.09	3.11	1.3	3.20	—	—	—	5.44	5.33	5.39	2.1	Gabbro
13R-2, 54–56	62.75	3.07	3.12	2.3	3.15	—	—	—	5.36	5.31	5.34	0.8	Gabbro
15R-1, 22–24	70.62	3.14	3.19	2.4	3.07	—	—	5.10	5.13	5.09	5.10	0.8	Gabbro
16R-1, 33–35	75.73	3.09	3.13	2.0	3.07	—	—	5.20	5.18	5.13	5.17	1.5	Gabbro
17R-1, 62–64	80.72	2.91	2.94	1.4	2.92	—	—	5.18	5.14	5.14	5.15	0.8	Microgabbro
18R-2, 5–7	86.22	3.10	3.16	2.5	3.13	—	—	5.19	5.23	5.14	5.19	1.7	Gabbro
18R-3, 108–110	88.73	2.92	2.95	1.5	2.94	—	—	5.41	5.25	5.23	5.30	3.3	Gabbro
19R-1, 76–78	90.16	3.11	3.14	1.5	3.12	—	—	—	5.33	5.35	5.34	—	Gabbro
19R-3, 113–115	92.68	3.17	3.21	1.6	3.15	—	—	—	5.29	5.19	5.24	1.8	Gabbro
20R-2, 6–8	95.62	3.02	3.06	1.5	3.17	—	—	5.35	5.44	5.33	5.37	2.1	Gabbro
21R-2, 6–8	100.56	3.18	3.25	3.2	3.18	—	—	5.03	5.01	4.97	5.00	1.1	Gabbro
21R-3, 54–56	102.47	3.11	3.18	3.0	3.06	—	—	4.74	—	4.61	4.67	—	Gabbro
22R-1, 105–107	105.05	3.06	3.11	2.4	3.16	—	—	—	—	5.15	5.15	—	Gabbro
209-1275D-													
1R-1, 127–129	1.27	2.85	2.93	3.9	2.86	—	—	4.95	4.87	4.77	4.86	3.7	Gabbro
2R-1, 139–141	9.39	2.67	2.70	1.6	2.69	—	—	4.83	4.70	4.84	4.79	2.9	Troctolite
6R-1, 93–95	28.03	2.69	2.79	5.7	2.90	—	—	4.41	4.41	4.21	4.34	4.6	Troctolite
9R-1, 17–19	41.77	2.64	2.68	3.0	2.68	—	—	4.77	4.58	4.54	4.63	4.9	Troctolite
10R-1, 52–54	46.62	2.58	2.65	4.6	2.63	—	—	4.34	4.29	4.30	4.31	1.2	Troctolite
10R-2, 95–97	48.48	2.55	2.64	5.6	2.60	—	—	3.90	3.93	3.97	3.93	1.6	Troctolite
12R-1, 20–22	55.90	2.92	3.02	4.8	2.99	—	—	4.74	4.71	4.68	4.71	1.1	Gabbro
12R-2, 41–43	57.57	3.05	3.11	2.8	3.12	—	—	5.22	5.15	5.18	5.18	1.4	Gabbro
13R-2, 54–56	62.50	2.92	3.01	4.8	3.07	—	—	4.82	4.69	4.70	4.73	2.8	Gabbro
15R-2, 8–11	71.79	3.10	3.12	1.0	3.14	—	—	5.58	5.51	5.54	5.54	1.3	Microgabbro
17R-2, 94–96	82.06	2.57	2.63	3.4	2.63	—	—	4.40	4.36	4.33	4.37	1.7	Microgabbro
18R-1, 136–138	85.76	3.21	3.25	1.9	3.17	—	—	5.08	5.13	5.05	5.08	1.6	Gabbro
21R-1, 67–69	99.67	2.78	2.85	3.8	2.84	—	—	5.01	5.02	4.99	5.01	0.6	Diabase
22R-1, 143–145	105.13	3.13	3.20	3.4	3.07	—	—	5.12	5.06	5.03	5.07	1.9	Gabbro
23R-2, 62–65	107.59	2.87	2.91	1.9	2.89	—	—	5.28	5.28	5.28	5.28	0.1	Microgabbro
24R-3, 22–24	111.48	3.11	3.15	1.8	3.19	—	—	5.30	5.30	5.22	5.28	1.5	Gabbro
25R-2, 40–42	114.65	3.18	3.22	1.7	3.12	—	—	5.43	5.35	5.30	5.36	2.6	Gabbro
26R-2, 95–97	120.46	3.16	3.22	2.8	3.18	—	—	5.25	5.21	5.20	5.22	0.9	Gabbro
27R-1, 25–27	122.95	3.08	3.12	1.8	3.16	—	—	5.46	5.39	5.39	5.41	1.3	Gabbro
29R-1, 62–64	132.82	2.95	2.97	1.3	2.98	—	—	5.53	5.51	5.55	5.53	0.6	Microgabbro
31R-3, 88–90	145.48	3.05	3.08	1.4	3.04	—	—	5.34	5.32	5.30	5.32	0.8	Gabbro
33R-1, 20–22	151.50	2.94	2.96	0.9	2.94	—	—	5.51	5.46	5.45	5.47	1.1	Olivine gabbro
33R-2, 69–71	153.43	2.97	2.98	0.4	2.99	—	—	5.62	5.63	5.61	5.62	0.3	Microgabbro
34R-2, 57–59	157.72	2.95	2.97	1.2	2.98	—	—	5.25	5.27	5.26	5.26	0.6	Gabbro
35R-2, 44–46	162.74	2.90	2.94	2.1	2.92	—	—	4.96	5.07	5.00	5.01	2.3	Gabbro
35R-4, 39–42	164.83	2.97	2.97	0.3	2.96	—	—	5.59	5.60	5.61	5.60	0.4	Microgabbro
36R-1, 58–60	166.38	2.93	2.96	1.1	2.98	—	—	5.69	5.67	5.72	5.69	0.9	Diabase
37R-1, 76–78	171.26	2.96	2.98	1.0	2.91	—	—	5.24	5.20	5.19	5.21	0.9	Gabbro
37R-3, 65–67	173.60	2.92	2.94	1.4	2.80	—	—	5.32	5.36	5.29	5.32	1.3	Gabbro
38R-3, 55–57	178.58	—	—	—	2.98	—	—	5.31	5.29	5.22	5.27	1.8	Gabbro
40R-1, 15–17	184.25	2.90	2.93	1.2	2.95	—	—	5.52	5.41	5.42	5.45	2.1	Diabase
40R-3, 52–54	187.40	2.92	2.95	1.3	3.01	—	—	5.46	5.48	5.41	5.45	1.3	Gabbro
41R-3, 71–73	193.30	2.95	2.97	1.0	2.95	—	—	5.34	5.42	5.33	5.36	1.5	Gabbro
43R-1, 96–98	200.26	3.24	3.27	1.5	3.23	—	—	5.59	5.50	5.44	5.51	2.7	Microgabbro
43R-2, 48–50	201.28	3.03	3.06	1.4	3.02	—	—	—	5.17	5.09	5.13	—	Gabbro
43R-4, 15–17	203.95	3.04	3.08	1.8	2.98	—	—	4.93	5.02	4.98	4.98	1.7	Gabbro

Note: This table is also available in **ASCII.**

Table T7. Summary of discrete sample data, Holes 1275B and 1275D. (**See table notes.** Continued on next page.)

Core, section, interval (cm)	Depth (mbsf)	Piece	NRM (A/m)	MDF (mT)	*N*	Decay type	MAD (°)	Remanence direction (°)		Demagnetization (mT)		*J* (A/m)	PCA (%)	PCA quality	Polarity
								Declination	Inclination	Low	High				
209-1275B-															
3R-1, 82	13.82	13	0.03	44.8	9	A	0.7	133.5	–16.5	25	120	0.0258	84.0	A	R
3R-1, 107	14.07	17	0.10	50.0	8	A	0.9	99.9	–12.8	25	120	0.0837	85.1	A	R
4R-1, 57	18.57	12	0.44	8.8	5	F	4.7	87.7	23.0	50	120	0.0201	4.6	C	I
5R-1, 17	22.77	4	0.16	11.6					*						
6R-1, 59	28.19	10	1.65	9.5	7	A	3.3	357.2	–20.2	20	60	0.5957	36.1	A	R
6R-2, 31	29.37	4A	1.48	53.9	3	A	1.0	237.8	–13	25	40	0.8650	58.4	C	R
6R-2, 106	30.12	9	1.56	23.4	7	A	1.5	161.1	–11.3	20	60	1.0799	69.2	A	R
9R-1, 114	42.94	15	4.37	20.6	10	A	1.4	71.4	–9.2	30	180	1.8397	42.1	A	R
10R-1, 82	47.62	10	8.14	18.3	10	A	0.9	25.0	–9	30	180	3.3700	41.4	A	R
10R-2, 44	48.74	8A	17.10	7.9	10	A	1.1	4.9	–8	30	180	3.9797	23.3	A	R
11R-1, 34	51.64	4	0.77	50.7	5	A	1.3	12.4	–6.9	50	120	0.5289	69.1	A	R
11R-2, 65	53.39	5	18.60	3.4	7	A	5.5	311.3	0.3	30	120	0.4756	2.6	A	R
12R-1, 80	57.10	13	2.94	4.8	9	A	1.3	311.1	–15.3	20	120	1.2697	43.2	A	R
12R-2, 22	57.69	1B	11.50	7.1	8	A	0.7	227.0	–8.6	25	120	2.3498	20.4	A	R
13R-1, 72	61.52	6B	17.00	4.4	5	A	3.5	62.3	–12.9	40	100	0.6587	3.9	A	R
13R-2, 54	62.75	8	8.78	20.7	7	A	0.6	159.6	–3.9	25	100	3.9199	44.6	A	R
15R-1, 22	70.62	3	10.30	4.0	6	A	1.0	38.5	–10.9	30	100	0.7469	7.3	A	R
16R-1, 33	75.73	5	2.07	22.1	7	A	1.2	157.9	–8.7	25	100	1.1700	56.5	A	R
17R-1, 62	80.72	11	0.12	6.3	7	A	1.5	36.9	–20.4	25	100	0.0487	42.3	A	R
18R-2, 5	86.22	1A	3.74	9.7	8	A	2.6	149.3	–3.7	20	100	1.5799	42.2	A	R
18R-3, 108	88.73	11B	1.38	3.4	6	A	3.6	17.1	–7.5	30	100	0.0342	2.5	A	R
19R-1, 76	90.16	5A	4.35	4.6	8	A	3.2	14.1	–9.9	20	100	0.9060	20.8	A	R
19R-3, 113	92.68	2	2.73	4.5	4	A	1.4	358.5	–13.8	50	100	0.4569	16.7	A	R
20R-2, 6	95.62	1A	12.50	3.6	6	A	1.6	37.3	–10.5	30	100	1.1799	9.4	A	R
21R-2, 6	100.56	1	1.26	89.7	5	A	0.4	311.1	–10.8	30	80	1.2800	101.6	A	R
21R-3, 54	102.47	6	1.18	80.1	4	A	0.3	47.2	–16.3	20	40	1.2700	107.6	A	R
22R-1, 105	105.05	9	15.70	3.8	3	A	3.4	12.1	–7.1	30	50	0.7213	4.6	A	R
209-1275D-															
1R-1, 127	1.27	21	0.02	29.8	4	A	1.5	310.7	–21.4	35	60	0.0141	78.3	A	I
2R-1, 139	9.39	27	3.35	17.8	4	F	2.3	56.6	22.6	30	50	0.5506	16.4	A	I
6R-1, 93	28.03	17	0.56	4.8	4	F	2.8	205.7	–2.2	30	50	0.0832	14.9	A	I
9R-1, 17	41.77	3	3.45	5.8	10	F	2.1	345.5	12.0	20	100	0.7991	23.2	A	I
10R-1, 52	46.62	6	1.80	8.9	5	F	3.1	12.2	19.8	30	60	0.3842	21.3	A	I
10R-2, 95	48.48	14A	NA	NA	5	F	3.4	235.6	14.4	30	60	0.3007	NA	A	I
12R-1, 20	55.90	3	NA	NA	5	A	1.0	77.7	–14.5	40	80	0.0322	NA	A	R
12R-2, 41	57.57	8	NA	NA	6	A	0.6	8.5	–16.3	40	100	0.4400	NA	A	R
13R-2, 54	62.50	1C	NA	NA	3	A	1.9	4.5	4.1	40	60	0.1760	NA	A	R
15R-2, 8	71.79	1A	NA	NA	9	A	7.2	222.0	10.4	25	120	0.2170	NA	A	R
17R-2, 94	82.06	15A	NA	NA					*						
18R-1, 136	85.76	17B	NA	NA	6	A	5.3	356.5	–5.6	35	100	0.5452	NA	A	R
21R-1, 67	99.67	8A	NA	NA					*						
22R-1, 143	105.13	20B	NA	NA	4	A	1.3	178.1	2.0	60	120	0.1350	NA	A	R
23R-2, 62	107.59	6	NA	NA	8	A	1.4	239.6	–11.4	30	120	0.0273	NA	A	R
24R-3, 22	111.48	1	NA	NA	7	A	2.0	323.8	–9.3	35	120	0.7319	NA	A	R
25R-2, 40	114.65	1A	NA	NA	9	A	1.7	139.7	–10.4	25	120	1.1897	NA	A	R
26R-2, 95	120.46	8C	6.88	6.3	6	A	2.4	234.7	–8.3	30	100	0.7198	10.5	A	R
27R-1, 25	122.95	4A	12.90	4.0	6	A	2.3	69.4	–9.4	30	100	0.8319	6.4	A	R
29R-1, 62	132.82	7	0.43	6.1	4	A	1.6	167.3	–15.6	40	100	0.0592	13.8	A	R
31R-3, 88	145.48	2H	17.50	3.9	5	A	0.8	223.0	–21.6	35	100	1.9299	11.0	A	R
33R-1, 20	151.50	3A	9.91	2.3	6	F	20.5	346.4	40.2	30	100	0.0495	0.5	C	I
33R-2, 69	153.43	3C	11.90	1.8	3	A	8.3	252.2	28.8	30	40	0.0732	0.6	C	I
34R-2, 57	157.72	1E	4.75	3.6	3	A	2.2	65.2	–18.2	30	40	0.2040	4.3	C	R
35R-2, 44	162.74	3C	3.54	4.8	6	A	0.9	36.0	–13.6	30	100	1.2198	34.5	A	R
35R-4, 39	164.83	1C	17.20	1.8	4	A	6.8	140.3	30.5	25	40	0.1448	0.8	C	I
36R-1, 58	166.38	10A	2.06	NA	4	A	2.0	160.7	–16.3	80	140	0.0686	3.3	A	R
37R-1, 76	171.26	9B	2.25	NA	7	A	0.5	30.0	–17	50	140	0.5310	23.6	A	R
37R-3, 65	173.60	2	0.08	NA	5	A	2.6	18.7	–12.1	40	70	0.0128	15.8	A	R
38R-3, 55	178.58	1B	21.70	4.2	3	A	0.9	71.9	–22.6	60	100	0.4000	1.8	A	R
40R-1, 15	184.25	3A	0.97	NA	7	A	1.3	11.2	–5	50	140	0.5099	52.5	A	R
40R-3, 52	187.40	4	15.90	3.6	4	A	0.6	230.0	–17.3	40	100	0.7519	4.7	A	R
41R-3, 71	193.30	2	2.47	4.0	4	A	1.8	183.6	–14.9	40	100	0.1799	7.3	A	R
43R-1, 96	200.26	8B	21.40	4.7	4	A	1.5	28.2	13.9	25	60	2.3899	11.2	A	R
43R-2, 48	201.28	1A	2.14	NA	8	A	2.5	88.4	–9.8	40	120	0.0982	4.6	A	R
43R-4, 15	203.95	4	NA	NA	5	F	1.7	243.1	–10.8	30	100	0.8177	NA	A	R

Table T7 (continued).

Notes: NRM = natural remanent magnetization. MDF = median destructive field for vector difference sum. *N* = number of points. Decay type: A = anchored to origin, F = free of origin. Principal component analysis (PCA) (%) = percentage of NRM intensity. MAD = maximum angular deviation. PCA quality: A = considered to be a reliable record of stable remanence, C = significant overlap between ChRM and drilling overprint result in less reliable inclinations. Polarity: R = rotate to 180°, I = indeterminate. NA = data not available. * = no stable direction. This table is also available in **ASCII.**

Table T8. Piece orientation from archive-half data, Hole 1275B.

Core, section, interval (cm)	Length (cm)	Piece	PCA interval (cm)	Depth (mbsf)	*N*	Decay type	MAD (°)	Remanence direction (°)		Demagnetization (mT)		*J* (A/m)	PCA (%)	PCA quality
								Declination	Inclination	Low	High			
209-1275B-														
1R-1, 1–7	6	1	4	0.04	2	A	1.4	160.6	–3.3	40	50	0.0013	62.3	A
1R-1, 47–54	7	9	50	0.50	3	A	0.7	55.8	–12.2	35	50	0.0029	32.8	A
3R-1, 34–56	22	6	38	13.38	2	A	0.2	121.5	–6.4	30	35	0.0093	97.5	A
3R-1, 79–88	9	13	84	13.84	4	A	2.3	137.5	–10	30	50	0.0128	89.0	A
3R-1, 103–112	9	17	108	14.08	4	A	0.3	105.3	–6.6	20	35	0.1130	95.4	A
3R-1, 114–130	16	18	118	14.18	3	A	0.1	339.8	–8.3	25	35	0.0586	84.2	A
3R-1, 114–130	16	18	120	14.20	4	A	0.3	346.4	–7.5	20	35	0.0671	90.7	A
3R-1, 131–140	9	19	136	14.36	5	A	0.7	144.8	–7.2	25	50	0.0322	91.8	A
3R-2, 12–19	7	3	14	14.64	2	A	0.1	181.0	9.2	40	50	0.0006	71.1	A
3R-2, 21–31	10	4	26	14.76	2	A	0.9	334.2	–6.4	40	50	0.0016	56.2	C
4R-1, 55–65	10	12	60	18.60	4	A	0.7	65.5	3.5	50	80	0.0249	33.6	A
4R-1, 70–80	10	14	78	18.78	6	A	1	228.9	7.3	35	80	0.0141	79.0	A
5R-1, 15–27	12	4	22	22.82	2	A	4.1	335.7	57.9	40	50	0.0222	5.8	C
5R-1, 28–37	9	5	32	22.92	3	A	0.5	21.6	–4.7	35	50	0.0496	63.6	A
5R-1, 60–67	7	10	64	23.24	6	A	0.1	169.1	–13	20	50	0.0331	97.2	A
5R-1, 68–74	6	11	70	23.30	6	A	0.8	196.4	–10.3	20	50	0.0767	94.9	A
5R-1, 99–106	7	17	104	23.64	7	A	0.6	225.2	–11.5	15	50	0.0251	96.8	A
5R-1, 120–126	6	20	122	23.82	6	A	0.5	218.1	–14.1	20	50	0.0269	101.1	A
5R-1, 120–126	6	20	124	23.84	6	A	0.4	218.8	–15.9	20	50	0.0251	101.0	A
5R-1, 134–144	10	22	138	23.98	6	A	0.6	303.8	–6.5	20	50	0.0396	92.4	A
5R-2, 0–16	16	1	10	24.15	6	A	0.5	281.8	–7.1	20	50	0.0371	89.2	A
5R-2, 23–31	8	3	26	24.31	6	A	0.1	56.2	–9.4	20	50	0.0318	90.6	A
6R-1, 6–15	9	2	12	27.72	6	A	0.6	234.9	–7.6	20	50	0.1230	94.5	A
6R-1, 57–69	12	10	64	28.24	2	A	0.7	349.8	–12.8	35	40	0.3470	11.4	C
6R-1, 69–80	11	11	76	28.36	6	A	6	0.1	6.3	20	50	0.7576	17.9	C
6R-1, 96–112	16	15	100	28.60	3	A	3.6	168.3	–4.8	30	40	0.5618	30.6	C
6R-1, 96–112	16	15	104	28.64	3	A	2.1	171.3	–5.7	30	40	0.8087	35.9	C
6R-1, 116–124	8	17	120	28.80	2	A	4.4	171.1	–7.3	35	40	0.1737	5.4	C
6R-2, 10–24	14	3	14	29.20	2	A	1.8	259.1	–15.5	40	50	0.4909	24.2	A
6R-2, 25–51	26	4	36	29.42	2	A	2.5	249.6	–9.7	40	50	0.4118	17.2	A
6R-2, 52–71	19	5	56	29.62	2	A	5.6	172.8	–10.1	35	40	0.1961	17.1	C
6R-2, 76–85	9	7	82	29.88	2	A	1.1	149.1	–9.3	30	35	0.2600	35.9	C
6R-2, 87–101	14	8	92	29.98	2	A	5	235.5	–7.5	40	50	0.3583	29.1	C
6R-2, 103–112	9	9	108	30.14	2	A	2.5	169.3	–5.3	35	40	0.5137	43.2	C
7R-1, 17–23	6	5	20	32.50	5	A	2.3	48.4	–12.2	20	40	0.0423	88.4	A
7R-1, 42–48	6	9	46	32.76	4	A	2.6	164.2	–13	30	50	0.0737	19.4	A
7R-1, 49–60	11	10	54	32.84	4	A	2.9	152.1	1.4	30	50	0.1169	7.2	A
7R-1, 65–74	9	12	70	33.00	3	A	2.4	134.7	–5	35	50	0.0957	4.6	C
8R-1, 35–43	8	7	40	37.70	5	A	0.1	246.3	–5.3	25	50	0.4660	99.7	A
8R-1, 56–63	7	11	58	37.88	2	A	0.7	251.9	–6.1	40	50	0.6380	32.3	A
8R-1, 65–72	7	12	68	37.98	2	A	0.4	178.5	–7.3	40	50	0.6110	67.2	A
8R-1, 74–81	7	13	78	38.08	2	A	0.6	176.5	–9.1	40	50	0.4210	64.4	A
9R-1, 37–42	5	8	40	42.20	5	A	0.7	293.7	–9.3	25	50	0.4809	99.1	A
9R-1, 44–68	24	9	48	42.28	4	A	0.6	278.6	–12.6	30	50	0.7590	52.7	A
9R-1, 44–68	24	9	60	42.40	3	A	1	283.5	–12.2	35	50	0.6909	56.2	A
9R-1, 70–76	6	10	74	42.54	2	A	0.3	269.0	–5.7	40	50	0.9230	54.0	A
9R-1, 97–108	11	14	102	42.82	5	A	0.7	327.2	–7.2	25	50	1.2199	60.4	A
9R-1, 110–126	16	15	116	42.96	3	A	0.5	86.3	–5.7	35	50	1.4300	33.2	A
9R-1, 128–133	5	16	130	43.10	5	A	0.9	359.0	–1.3	25	50	0.9999	50.9	A
9R-2, 1–25	24	1	12	43.26	4	A	0.4	151.5	–9.1	50	80	0.5320	37.7	A
9R-2, 50–57	7	7	54	43.68	4	A	1.2	317.2	–6.9	50	80	0.5398	22.9	A
10R-1, 21–29	8	5	24	47.04	4	A	1.1	19.9	–1.4	30	50	1.0299	27.7	A
10R-1, 30–43	13	6	34	47.14	4	A	0.6	107.6	–11	30	50	1.2599	86.1	A
10R-1, 44–53	9	7	48	47.28	3	A	0.6	35.4	–5.6	35	50	1.1600	43.5	A
10R-1, 54–66	12	8	62	47.42	3	A	0.7	216.5	–3.3	35	50	1.5800	40.7	A
10R-1, 73–106	33	10	80	47.60	3	A	0.6	34.2	–7.6	35	50	1.1300	22.5	A
10R-1, 73–106	33	10	90	47.70	3	A	0.8	35.2	–9.5	35	50	0.9160	18.9	A
10R-1, 73–106	33	10	100	47.80	3	A	0.7	39.8	–8	35	50	1.1700	22.4	A
10R-1, 109–120	11	11	114	47.94	3	A	0.8	341.9	–5.8	35	50	1.5400	26.3	A
10R-1, 138–150	12	15	146	48.26	3	A	0.4	266.6	–5.7	35	50	1.1600	53.4	A

Notes: Principal component analysis (PCA) interval = level at which PCA analysis was performed. *N* = number of samples. Decay type: A = anchored to origin, F = free of origin, + = includes origin as point. MAD = maximum angular deviation. PCA (%) = percentage of natural remanent magnetization intensity. PCA quality: A = considered to be a reliable record of stable remanence, C = significant overlap between ChRM and drilling overprint results in less reliable inclination. Only a sample of this table appears here. The complete table is available in **ASCII.**

Table T9. Anisotropy of magnetic susceptibility data, Holes 1275B and 1275D. (Continued on next page.)

Core, section, interval (cm)	Depth (mbsf)	Piece	Susceptibility (SI)	1 σ	Maximum*			Intermediate*			Minimum*		
					Value	Dec (°)	Inc (°)	Value	Dec (°)	Inc (°)	Value	Dec (°)	Inc (°)
209-1275B-													
3R-1, 82	13.82	13	6.82E–04	0.00058	0.3337	198.4	32.3	0.3335	108.4	0.0	0.3328	18.4	57.7
3R-1, 107	14.07	17	1.06E–03	0.00049	0.3369	39.5	13.6	0.3342	132.1	10.8	0.3289	259.3	72.5
4R-1, 57	18.57	12	5.54E–03	0.00015	0.3432	324.5	11.2	0.3368	232.5	10.3	0.3200	100.8	74.7
5R-1, 17	22.77	4	5.40E–03	0.00009	0.3383	79.4	17.7	0.3354	170.5	3.6	0.3263	271.5	71.9
6R-1, 59	28.19	10	4.63E–02	0.00019	0.3538	177.5	8.7	0.3320	85.7	11.8	0.3142	303.3	75.3
6R-2, 31	29.37	4A	3.51E–02	0.00008	0.3457	245.4	7.0	0.3299	342.5	45.0	0.3245	148.6	44.1
6R-2, 106	30.12	9	3.64E–02	0.00017	0.3508	358.0	26.7	0.3288	90.7	5.4	0.3205	191.2	62.6
9R-1, 114	42.94	15	2.83E–02	0.00023	0.3410	357.2	7.4	0.3389	87.3	1.0	0.3201	184.8	82.5
10R-1, 82	47.62	10	6.34E–02	0.00041	0.3431	127.3	3.8	0.3400	37.2	2.0	0.3169	280.1	85.7
10R-2, 44	48.74	8A	1.22E–01	0.00052	0.3421	175.8	0.7	0.3349	85.5	21.7	0.3230	267.7	68.3
11R-1, 34	51.64	4	7.16E–03	0.00018	0.3372	85.1	12.9	0.3353	177.0	8.0	0.3276	298.1	74.7
11R-2, 65	53.39	5	9.32E–02	0.00036	0.3507	34.9	0.7	0.3349	125.2	21.0	0.3144	303.2	69.0
12R-1, 80	57.10	13	4.24E–02	0.00075	0.3425	186.6	4.5	0.3334	94.0	29.8	0.3241	284.3	59.8
12R-2, 22	57.69	1B	6.47E–02	0.00037	0.3413	127.2	6.4	0.3350	220.7	28.6	0.3237	25.8	60.6
13R-1, 72	61.52	6B	9.46E–02	0.00028	0.3473	337.7	0.8	0.3399	247.7	1.5	0.3129	96.4	88.2
13R-2, 54	62.75	8	6.13E–02	0.00028	0.3443	309.7	23.0	0.3347	218.8	2.2	0.3210	123.5	66.8
15R-1, 22	70.62	3	7.21E–02	0.0002	0.3483	42.4	23.4	0.3370	138.2	13.3	0.3147	255.3	62.7
16R-1, 33	75.73	5	3.78E–02	0.00017	0.3451	279.4	24.4	0.3380	12.5	6.7	0.3169	116.8	64.5
17R-1, 62	80.72	11	3.34E–03	0.00025	0.3393	229.6	16.9	0.3359	319.9	1.1	0.3248	53.6	73.0
18R-2, 5	86.22	1A	7.66E–02	0.00033	0.3401	359.2	17.7	0.3310	267.5	5.1	0.3289	162.1	71.5
18R-3, 108	88.73	11B	1.61E–02	0.00039	0.3451	123.0	20.3	0.3312	214.0	2.6	0.3236	311.0	69.5
19R-1, 76	90.16	5A	5.10E–02	0.00036	0.3419	60.9	25.9	0.3326	164.6	26.0	0.3255	292.7	51.8
19R-3, 113	92.68	2	2.24E–02	0.00039	0.3445	191.7	7.0	0.3387	97.4	31.6	0.3168	292.7	57.4
20R-2, 6	95.62	1A	9.31E–02	0.00044	0.3448	77.6	6.6	0.3345	346.4	10.1	0.3207	200.3	77.9
21R-2, 6	100.56	1	1.09E–02	0.00064	0.3364	176.4	19.2	0.3323	70.8	37.5	0.3313	287.6	46.2
21R-3, 54	102.47	6	1.21E–02	0.00023	0.3349	247.2	3.3	0.3335	337.8	9.9	0.3316	138.7	79.6
22R-1, 105	105.05	9	1.30E–01	0.00032	0.3455	47.3	30.7	0.3332	157.1	29.6	0.3213	281.3	44.7
209-1275D-													
1R-1, 127	1.27	21	7.37E–04	0.0006	0.3347	188.6	48.7	0.3338	301.2	18.6	0.3314	45.0	35.3
2R-1, 139	9.39	27	6.44E–02	0.0002	0.3498	352.3	1.0	0.3280	261.9	19.4	0.3221	85.1	70.6
6R-1, 93	28.03	17	3.63E–02	0.00032	0.3565	237.3	18.3	0.3350	143.5	11.3	0.3085	23.3	68.2
9R-1, 17	41.77	3	5.45E–02	0.00028	0.3479	332.8	33.9	0.3327	64.0	1.8	0.3194	156.6	56.1
10R-1, 52	46.62	6	5.53E–02	0.00045	0.3399	29.2	33.1	0.3353	204.1	56.8	0.3248	297.7	2.3
10R-2, 95	48.48	14A	3.09E–02	0.00023	0.3360	61.3	37.2	0.3343	261.5	51.1	0.3297	158.9	10.0
12R-1, 20	55.90	3	6.02E–03	0.00018	0.3411	32.1	40.8	0.3326	275.6	27.3	0.3264	162.7	37.0
12R-2, 41	57.57	8	1.29E–02	0.00006	0.3346	191.4	18.1	0.3331	360.0	71.6	0.3322	100.2	3.4
13R-2, 54	62.50	1C	7.83E–02	0.00017	0.3408	105.9	23.5	0.3380	9.0	15.6	0.3212	248.4	61.3
15R-2, 8	71.79	1A	1.26E–01	0.00039	0.3605	228.1	43.5	0.3265	328.5	10.8	0.3130	69.3	44.5
17R-2, 94	82.06	15A	3.72E–02	0.00019	0.3408	132.1	14.0	0.3366	222.9	3.3	0.3226	325.9	75.6
18R-1, 136	85.76	17B	1.01E–01	0.00023	0.3436	77.0	36.7	0.3294	346.8	0.2	0.3270	256.6	53.3
21R-1, 67	99.67	8A	6.99E–04	0.00036	0.3340	336.3	13.2	0.3335	233.2	44.0	0.3325	78.9	43.1
22R-1, 143	105.13	20B	2.65E–02	0.00014	0.3356	339.7	7.5	0.3331	72.3	19.0	0.3313	229.2	69.5
23R-2, 62	107.59	6	8.38E–04	0.00058	0.3348	280.0	12.7	0.3331	34.5	61.5	0.3321	183.9	25.1
24R-3, 22	111.48	1	5.34E–02	0.00012	0.3417	68.5	12.5	0.3343	176.1	53.8	0.3240	330.1	33.4
25R-2, 40	114.65	1A	5.93E–02	0.00011	0.3373	304.5	40.7	0.3342	39.6	5.9	0.3285	136.4	48.7
26R-2, 95	120.46	8C	9.19E–02	0.00032	0.3404	185.5	59.9	0.3329	3.8	30.1	0.3267	94.3	0.7
27R-1, 25	122.95	4A	8.02E–02	0.00017	0.3427	45.4	33.4	0.3325	312.7	4.1	0.3249	216.5	56.2
29R-1, 62	132.82	7	4.11E–03	0.00015	0.3387	208.5	6.7	0.3323	90.6	75.8	0.3291	300.0	12.4
31R-3, 88	145.48	2H	6.48E–02	0.00013	0.3454	339.5	31.3	0.3358	222.2	37.1	0.3188	97.0	37.3
33R-1, 20	151.50	3A	5.88E–02	0.00012	0.3376	73.4	19.7	0.3349	163.8	1.1	0.3276	256.9	70.2
33R-2, 69	153.43	3C	5.21E–02	0.00009	0.3395	10.7	16.1	0.3322	279.8	3.0	0.3283	179.6	73.6
34R-2, 57	157.72	1E	2.44E–02	0.00024	0.3583	229.2	11.9	0.3496	138.8	1.7	0.2921	41.0	77.9
35R-2, 44	162.74	3C	1.78E–02	0.00018	0.3526	158.6	19.1	0.3257	7.2	68.5	0.3216	252.0	9.5
35R-4, 39	164.83	1C	6.05E–02	0.00016	0.3462	195.5	15.7	0.3403	99.0	22.1	0.3135	318.0	62.4
36R-1, 58	166.38	10A	5.63E–03	0.00011	0.3427	167.9	29.0	0.3347	53.7	36.4	0.3226	285.5	40.0
37R-1, 76	171.26	9B	9.50E–03	0.00027	0.3472	49.5	26.1	0.3386	152.9	25.3	0.3142	280.5	52.2
37R-3, 65	173.60	2	1.06E–03	0.00046	0.3381	122.1	7.9	0.3373	30.3	12.7	0.3247	243.2	75.0
38R-3, 55	178.58	1B	7.14E–02	0.00024	0.3580	278.6	13.5	0.3313	25.5	50.3	0.3106	178.4	36.4
40R-1, 15	184.25	3A	7.29E–03	0.00021	0.3408	348.9	5.0	0.3330	162.2	84.9	0.3262	258.9	0.6
40R-3, 52	187.40	4	6.46E–02	0.0002	0.3490	60.5	3.1	0.3376	330.5	1.3	0.3134	218.3	86.7
41R-3, 71	193.30	2	1.12E–02	0.00021	0.3509	76.7	13.2	0.3389	168.2	6.5	0.3103	283.7	75.3
43R-1, 96	200.26	8B	1.15E–01	0.00017	0.3399	50.2	37.2	0.3342	170.1	33.3	0.3259	287.8	35.2
43R-2, 48	201.28	1A	9.07E–03	0.00015	0.3397	115.3	16.3	0.3311	213.7	26.7	0.3292	357.3	58.0
43R-4, 15	203.95	4	3.95E–02	0.00035	0.3474	236.1	39.7	0.3298	332.9	8.2	0.3228	72.5	49.1

Notes: σ = 1 standard deviation for normalized eigenvalues. Total anisotropy critical value = 3.4817. * = unrotated core coordinates (double line on working half = 360°, inclination positive down). Dec = declination, inc = inclination. F12 = max, min eigenvalues, F23 = int, min eigenvalues (critical value = 4.2565 for F12 and F23). *P* (degree of anisotropy) = max/min eigenvalues, *F* (magnetic foliation) = int/min eigenvalues, *L* (magnetic lineation) = max/int eigenvalues. † = anisotropy of magnetic susceptibility core coordinates rotated to 180°. This table is also available in **ASCII.**

Table T9 (continued).

Core, section, interval (cm)	Depth (mbsf)	Piece	Total anisotropy	F12	F23	*P*	*F*	*L*	Minimum† Dec (°)	Minimum† Inc (°)	Maximum† Dec (°)	Maximum† Inc (°)
209-1275B-												
3R-1, 82	13.82	13	0.5	0.1	0.7	1.003	1.002	1.001				
3R-1, 107	14.07	17	54.8	15.9	56.9	1.024	1.016	1.008	339.40	72.5	119.6	13.6
4R-1, 57	18.57	12	5062.6	910.0	6205.9	1.072	1.052	1.019				
5R-1, 17	22.77	4	4201.0	569.0	5533.5	1.037	1.028	1.009				
6R-1, 59	28.19	10	8816.1	6615.8	4474.0	1.126	1.057	1.066	126.10	75.3	0.3	8.7
6R-2, 31	29.37	4A	9999.9	9999.9	2445.8	1.065	1.017	1.048	90.80	44.1	187.6	7.0
6R-2, 106	30.12	9	6585.8	8130.7	1154.2	1.094	1.026	1.067	210.10	62.6	16.9	26.7
9R-1, 114	42.94	15	1961.8	40.5	3273.9	1.065	1.059	1.006	293.40	82.5	105.8	7.4
10R-1, 82	47.62	10	977.0	30.0	1584.1	1.083	1.073	1.009	75.10	85.7	282.3	3.8
10R-2, 44	48.74	8A	275.0	96.3	260.8	1.059	1.037	1.022	82.80	68.3	350.9	0.7
11R-1, 34	51.64	4	664.1	60.2	946.3	1.029	1.024	1.006	105.70	74.7	252.7	12.9
11R-2, 65	53.39	5	2064.5	979.6	1628.4	1.116	1.065	1.047	171.90	69.0	263.6	0.7
12R-1, 80	57.10	13	120.2	73.5	76.7	1.057	1.029	1.027	153.20	59.8	55.5	4.5
12R-2, 22	57.69	1B	472.0	147.9	472.7	1.054	1.035	1.019	338.80	60.6	80.2	6.4
13R-1, 72	61.52	6B	3392.6	350.6	4723.5	1.110	1.086	1.022	214.10	88.2	95.4	0.8
13R-2, 54	62.75	8	1442.1	607.8	1231.1	1.073	1.043	1.029	143.90	66.8	330.1	23.0
15R-1, 22	70.62	3	5880.0	1606.1	6250.5	1.107	1.071	1.033	36.80	62.7	183.9	23.4
16R-1, 33	75.73	5	5705.5	826.8	7397.9	1.089	1.067	1.021	138.90	64.5	301.5	24.4
17R-1, 62	80.72	11	742.1	93.7	992.66	1.04	1.03	1.010	196.70	73.0	12.7	16.9
18R-2, 5	86.22	1A	257.9	374.9	20.63	1.03	1.01	1.028	192.80	71.5	29.9	17.7
18R-3, 108	88.73	11B	634.3	644.2	192.81	1.07	1.02	1.042	113.90	69.5	285.9	20.3
19R-1, 76	90.16	5A	414.6	330.4	193.85	1.05	1.02	1.028	98.60	51.8	226.8	25.9
19R-3, 113	92.68	2	1102.3	107.5	1551.05	1.09	1.07	1.017	114.20	57.4	13.2	7.0
20R-2, 6	95.62	1A	614.6	279.1	499.81	1.08	1.04	1.031	343.00	77.9	220.3	6.6
21R-2, 6	100.56	1	14.0	19.8	1.34	1.02	1.00	1.012			45.3	19.2
21R-3, 54	102.47	6	42.8	18.7	35.80	1.01	1.01	1.004	271.50	79.6	20.0	3.3
22R-1, 105	105.05	9	1146.2	743.9	689.27	1.08	1.04	1.037	89.20	44.7	215.2	30.7
209-1275D-												
1R-1, 127	1.27	21	6.3	1.1	7.78	1.01	1.01	1.003				
2R-1, 139	9.39	27	4457.9	6216.2	456.96	1.09	1.02	1.066				
6R-1, 93	28.03	17	4473.9	2221.2	3413.76	1.16	1.09	1.064				
9R-1, 17	41.77	3	2078.7	1472.6	1133.16	1.09	1.04	1.046				
10R-1, 52	46.62	6	230.4	51.1	264.70	1.05	1.03	1.014				
10R-2, 95	48.48	14A	158.4	25.5	200.06	1.02	1.01	1.005				
12R-1, 20	55.90	3	1269.7	1056.5	557.04	1.04	1.02	1.026	265.0	37.0	134.4	40.8
12R-2, 41	57.57	8	339.0	316.2	122.60	1.01	1.00	1.004	271.7	3.4	2.9	18.1
13R-2, 54	62.50	1C	3026.5	140.2	4720.93	1.06	1.05	1.009	63.9	61.3	281.4	23.5
15R-2, 8	71.79	1A	3074.2	3697.9	589.64	1.15	1.04	1.104	27.3	44.5	186.1	43.5
17R-2, 94	82.06	15A	2120.6	267.3	2837.91	1.06	1.04	1.013				
18R-1, 136	85.76	17B	1236.7	1927.1	57.82	1.05	1.01	1.043	80.1	53.3	260.5	36.7
21R-1, 67	99.67	8A	3.3	0.8	3.62	1.00	1.00	1.001				
22R-1, 143	105.13	20B	185.8	151.3	84.18	1.01	1.01	1.007	231.1	69.5	341.6	7.5
23R-2, 62	107.59	6	4.2	4.1	1.39	1.01	1.00	1.005				
24R-3, 22	111.48	1	4303.2	1825.5	3658.64	1.05	1.03	1.022	186.3	33.4	284.7	12.5
25R-2, 40	114.65	1A	1387.4	432.2	1393.16	1.03	1.02	1.009	176.7	48.7	344.8	40.7
26R-2, 95	120.46	8C	366.6	275.6	185.60	1.04	1.02	1.023	39.6	0.7	130.8	59.9
27R-1, 25	122.95	4A	2198.1	1795.3	991.72	1.05	1.02	1.031	327.1	56.2	156.0	33.4
29R-1, 62	132.82	7	804.8	867.2	212.50	1.03	1.01	1.019	312.7	12.4	221.2	6.7
31R-3, 88	145.48	2H	8799.6	2751.4	8821.30	1.08	1.05	1.028	54.0	37.3	296.5	31.3
33R-1, 20	151.50	3A	1446.4	241.9	1808.65	1.03	1.02	1.008				
33R-2, 69	153.43	3C	3189.0	3247.0	963.55	1.03	1.01	1.022				
34R-2, 57	157.72	1E	9999.9	666.4	9999.90	1.23	1.20	1.025	155.8	77.9	344.0	11.9
35R-2, 44	162.74	3C	7129.8	9999.9	266.67	1.10	1.01	1.083	36.0	9.5	302.6	19.1
35R-4, 39	164.83	1C	9188.7	648.7	9999.90	1.10	1.09	1.017				
36R-1, 58	166.38	10A	6174.1	2427.4	5496.49	1.06	1.04	1.024	304.8	40.0	187.2	29.0
37R-1, 76	171.26	9B	3298.2	516.4	4195.80	1.11	1.08	1.025	70.5	52.2	199.5	26.1
37R-3, 65	173.60	2	217.5	1.5	382.80	1.04	1.04	1.002	44.5	75.0	283.4	7.9
38R-3, 55	178.58	1B	8042.7	6355.0	3806.63	1.15	1.07	1.081	286.5	36.4	26.7	13.5
40R-1, 15	184.25	3A	973.6	698.1	523.08	1.04	1.02	1.023	67.7	0.6	157.7	5.0
40R-3, 52	187.40	4	6906.8	1695.2	7653.18	1.11	1.08	1.034	168.3	86.7	10.5	3.1
41R-3, 71	193.30	2	7823.3	1625.7	9179.74	1.13	1.09	1.036	280.1	75.3	73.1	13.2
43R-1, 96	200.26	8B	1305.6	530.9	1139.25	1.04	1.03	1.017	79.6	35.2	202.0	37.2
43R-2, 48	201.28	1A	1084.8	1603.9	77.53	1.03	1.01	1.026	88.9	58.0	206.9	16.3
43R-4, 15	203.95	4	1030.9	1233.2	201.34	1.08	1.02	1.053	9.4	49.1	173.0	39.7

Table T10. Surface water and atmospheric microbiology results, 20–30 June 2003.

Sample	Date (Jun 2003)	Surface water (counts/mL)		Air growth* (CFU)		Atmospheric condition†
		Bacteria	Virus	Bacteria	Fungi	
a	20	5.66×10^5	5.30×10^6	0/0	0/3	10.3: light dust
b	21	6.79×10^5	4.79×10^6	0/0	0/1	7.6: light cloud
c	22	5.85×10^5	4.45×10^6	0/0	0/2	No data
d	23	4.72×10^5	3.96×10^6	0/0	0/0	10.3: light dust
e	24	5.09×10^5	4.24×10^6	0/0	0/1	11.2: light dust
f	25	5.47×10^5	6.22×10^6	0/0	0/0	8.6: light dust
g	26	7.17×10^5	5.33×10^6	0/0	0/3	6.5: light cloud/dust in photo but obscured by clouds
h	27	7.36×10^5	4.81×10^6	0/0	0/1	No data
I	28	6.23×10^5	4.53×10^6	0/2	0/5	9.7: light dust
j	29	5.85×10^5	5.53×10^6	0/0	0/3	9.5: light dust
k	30	6.98×10^5	5.36×10^6	0/0	0/0	5.6: light cloud

Notes: * = colony-forming units (CFU) growth is measured at 48/96 hr. † = SeaWiFS image values.